AN ABSTRACT OF THE DISSERTATION OF

Sean R. Tachibana for the degree of Doctor of Philosophy in Chemistry presented on July 14, 2021.

Title: Revealing Ultrafast Dynamics and Functional Basis of Potential Biomedical Tools from Calcium Sensing to Optogenetics

Abstract approved:

_____

Chong Fang

"The journey of 1000 miles begins with a single step." – Miyamoto Musashi

Photoactivated biomedical tools like fluorescent biosensors and optogenetic proteins have increased in popularity due to the precision targeting and activation used for *in vivo* applications. In nature, the initially discovered parent proteins exhibit properties such as fluorescence quantum yield (FQY), fluorescence color, and photoswitching dynamics that are unfavorable in mammalian applications. Tailoring these proteins for specific applications typically requires high-throughput random mutagenesis, which commonly lacks a photophysical understanding of the chromophore (or cofactor) interaction with the protein environment. Such "microscopic" interactions between the protein pocket and the embedded chromophore are crucial as removing or mutating a single residue inside the pocket could drastically change the "macroscopic" function. To fully understand the exact roles of the protein pocket and chromophore play in governing the biomolecular functionality, insights on the intrinsic molecular timescales (e.g., femtosecond/10^{-15} s to nanosecond/10^{-9} s) must be obtained. Ultrafast spectroscopic techniques such as femtosecond transient

absorption (fs-TA) and femtosecond stimulated Raman spectroscopy (FSRS), aided by quantum calculations, can illustrate the molecular mechanism upon photoexcitation (photophysics and photochemistry) via ground- and excited-state potential energy surfaces (PESs). The combination of time-resolved electronic and vibrational spectroscopies thus allows the elucidation of intrinsically coupled electronic and nuclear motions during a photoinduced process, and typically provides a non-invasive experimental platform to study biomolecular systems in physiological conditions. Furthermore, the use of light not only allows characterization but also enables potential strategies from photochroism, photodynamic therapy, to light-induced modulation or gain of functionality.

First, I investigated a green fluorescent protein (GFP) based calcium biosensor named GEM-GECO1-P377R (P377R for short) in collaboration with the Campbell Lab at the University of Alberta, Canada. Previously, the elucidated excited state proton transfer (ESPT) of the parent biosensor, GEM-GECO1, is crucial in understanding the green and blue fluorescence when calcium ions are free and bound, respectively. This property makes it a powerful emission-ratiometric biosensor. However, mutation of a single proline residue to an arginine changed the prominent blue fluorescence to green upon calcium binding, essentially making it an excitation ratiometric biosensor. In addition, the single-site mutation changed the more hydrophobic environment of the embedded protein chromophore to a hydrophilic and compact environment, promoting a faster ESPT reaction but also creating a trapped excited state population that becomes more photosensitive and photodegradable. One unique spectroscopic finding was the out-of-phase oscillations of the 1265 cm^{-1} (C–O stretch) and 1575 cm^{-1} (C=C/C=O

stretch) mode intensities in the excited-state FSRS data of the Ca^{2+}-free biosensor following photoexcitation. These oscillations from coherently generated vibrational intensity quantum beats, after Fourier transform analysis, correspond to a low-frequency mode at ~180 cm^{-1} that intrinsically modulates these higher frequency vibrations via anharmonic coupling, which governs the initial energy transfer between these nuclear motions of the chromophore prior to fluorescence events.

Later, I brought my P377R experience of studying the equilibrium dynamics of a calcium-bound versus calcium-free state to dissect the non-equilibrium dynamics of a photoswitchable cyanobacteriochrome (CBCR) called AnPixJg2. This project stemmed from my NSF East Asia and Pacific Summer Institutes for U.S. Graduate Students (EAPSI) and Japan Society for the promotion of Science (JSPS) Fellowship in Summer 2017, and related protein engineering work performed in the Sato Lab at University of Tokyo, Japan. Additional AnPixJg2 sample were provided by the Narikawa Lab at Shizuoka University, Japan. Using fs-TA spectroscopy, we captured the initial reversible photoswitching events between the thermally stable, red-absorbing state (P_r) and the meta-stable, green absorbing conformer (P_g) in real-time. Before converting to the final photoproduct, many photoswitchable proteins like CBCRs generate intermediate Lumi states which are partially-twisted conformers that resemble the photoproduct. The P_r-to-P_g conversion was found to be a more uphill reaction requiring a two-step process (~13 and 217 ps) before reaching an S_1/S_0 conical intersection (CI). In contrast, the largely downhill P_g-to-P_r conversion requires a much faster (~3 ps) process to reach an S_1/S_0 CI with a significant rise of the Lumi-G species on the ~30 ps timescale.

One of the drawbacks of AnPixJg2 was the incorporation of phycocyanobilin (PCB) as the cofactor. PCB is not biologically available in mammalian cells, which makes it difficult for biomedical applications (e.g., optogenetic for human subjects). Biliverdin (BV) is a known mammalian derivative where the aforementioned Narikawa and Sato Groups incorporated into AnPixJg2 with just four key mutations (AnPixJg2_BV4). Using the field-proven experimental and computational platform that mainly constitutes steady-state and time-resolved electronic and vibrational spectroscopies, aided by density-functional-theory (DFT) calculations, we systematically compared the parent AnPixJg2 with PCB (Apcb) to the mutant AnPixJg2_BV4 with PCB (Bpcb) and BV (Bbv). Upon comparison between Apcb and Bpcb, the overall initial photoswitching process remains largely intact, but the mutated pocket allows more room for larger twisting motions to occur faster. The incorporation of BV red-shifts the ground-state absorption bands from P_r/P_g to P_{fr}/P_o due to the extended conjugation of the cofactor. The integrated BV and mutated pocket drastically change the initial photoswitching processes, with both conversions with in either direction (Bbv P_o to P_{fr} and P_{fr} to P_o) requiring a two-step mechanism to reach the CI. Surprisingly, both conversions display similar spectral patterns with almost identical decay constants of ~5 and 35 ps. The major difference was identified to be the relative amplitude weights associated with each temporal component in the fs-TA spectral fitting, which indicates a unique clockwise/counterclockwise reaction pathway (e.g., reversible photoswitching of Bbv inside an engineered CBCR).

Notable, I have also contributed to the group research mission and experimental toolset by developing home-built instruments such as a 3D-printed LED box, low-

volume flow cell, low-temperature flow cell, and miscellaneous tools to help mix the solution samples in thin quartz cuvettes. Future project investigations include a photodimerizing protein named Vivid and its engineered variants named nMag and pMag. These proteins are flavin adenine dinucleotide (FAD) based proteins with nMag and pMag engineered to have electrostatically charged residues at the interface, which can prevent homodimerization and promote heterodimerization. In addition, these proteins have been implemented with other split proteins like GFP and CRISPR-Cas-9 for specific light activation applications, which could be facilitated and expedited with a molecular mechanistic understanding in real time as shown above by our “Molecular Movie” technology on photosensitive chromophores and cofactors in protein matrix after photons hit.

Revealing Ultrafast Dynamics and Functional Basis of Potential Biomedical Tools from Calcium Sensing to Optogenetics

by
Sean R. Tachibana

A DISSERTATION

submitted to

Oregon State University

in partial fulfillment of
the requirements for the
degree of

Doctor of Philosophy

Presented July 14, 2021
Commencement June 2022

Doctor of Philosophy dissertation of Sean R. Tachibana presented on July 14, 2021

APPROVED:

Major Professor, representing Chemistry

Head of the Department of Chemistry

Dean of the Graduate School

I understand that my dissertation will become part of the permanent collection of Oregon State University libraries. My signature below authorizes release of my dissertation to any reader upon request.

Sean R. Tachibana, Author

ACKNOWLEDGEMENTS

I would like to first and foremost thank my graduate advisor, Dr. Chong Fang, for supporting and guiding me through my academic career. Dr. Fang has built a highly collaborative research family that thrives on helping everyone succeed. I want to express my dearest gratitude to the past and present Fang group members for the enlightening discussions throughout the years. I would also like to thank my senior group members, Dr. Weimen Liu, Dr. Breland Oscar, Dr. Liangdong Zhu, Dr. Yanli Wang, and Dr. Cheng Chen, for teaching and training me as a young graduate student. I would especially like to thank Dr. Longteng Tang, who has mentored me and is constantly showing me what it means to be a great researcher and lifelong learner. My success in the group is a direct reflection of the support and encouragement from the Fang lab family.

To my committee members, I would first like to thank Dr. Wei Kong, who has taught me the fundamentals of P-Chem in many of my graduate courses at Oregon State. I would also like to thank Dr. Yun-Shik Lee, Dr. Mas Subramanian, Dr. Michael Lerner, and Dr. Gregory Herman for serving on my committee and provide me with insightful and thought-provoking suggestions.

I want to thank all of my collaborators, especially Dr. Robert Campbell, Dr. Morotoshi Sato, Dr. Rei Narikawa, and their groups, for the opportunity to study exciting and complex systems that have the chance to make a difference in the world. Dr. Campbell provided our group with all of the calcium ion biosensors where I was fortunate enough to join in for my first project. I would also like to thank the U.S.

National Science Foundation and the Japanese Society for the Promotion of Science for the East Asia and Pacific Summer Institutes fellowship. In 2017, I spent the summer in Dr. Sato's lab at the University of Tokyo and learned molecular biology techniques for protein engineering and in vivo studies.

I would like to thank the Department of Chemistry at Oregon State University for offering me assistantships, resources, awards, and fellowships. Without this support, my success in my graduate studies would not have been possible. I would also like to thank Dr. Ryan Mehl and the Unnatural protein facility for allowing me to synthesize protein samples for our lab.

I want to thank the friends I made during my time at OSU, where many conversations sparked creativity in my personal life and research. Taking my mind off school and my research allowed me to distress, refresh, and overcome many obstacles during my graduate career. I will never forget all the good times and good vibes we shared exploring Oregon.

Last but not least, I would like to thank my Ohana for all the love and support they have shown me in my life. My parents taught me what it means to be successful, and the hard work and dedication needed to achieve your dreams. I want to thank my brother for always being an outstanding role model and the person I learned everything from growing up as a kid. I would also like to thank my grandparents, who are my biggest fans and constantly check in on me to make sure I am doing fine. To Aimy Ung Pharm.D., thank you for putting up with me while pursuing our doctorate degrees. We made it, and I can't wait to start our next journey together! Without the love and support

of my family and friends, I would not be the person I am today. Words cannot express my gratitude and I can’t wait to celebrate with all of you in the future!

TABLE OF CONTENTS

Page

TABLE OF CONTENTS (Continued)

Page

TABLE OF CONTENTS (Continued)

Page

TABLE OF CONTENTS (Continued)

Page

LIST OF FIGURES

Figure Page

LIST OF FIGURES (Continued)

Figure Page

LIST OF FIGURES (Continued)

Figure Page

LIST OF TABLES

Table Page

Chapter 1 General introduction

"It is necessary to know ten thousand things by knowing one well. If you are to practice the way of strategy, nothing must escape your eyes." – Miyamoto Musashi

1.1 Green Fluorescent Protein (GFP) Based Calcium Biosensors

Before discovering green fluorescent protein (GFP), scientists lacked the tools to visualize biological processes that have no fluorescent properties. It was not until Shimomura and co-workers first purified GFP from the jellyfish *Aequorea Victoria* in the Pacific Northwest (**Fig. 1.1**),[1] where scientists could start to develop a tool to express a fluorescent tag genetically.[2] This feat ignited the development of GFP-based fluorescent tags and sensors to understand the biological working mechanisms better. One of the most surprising qualities of GFP is its high fluorescent quantum yield (FQY) efficiency with photostability.[3] GFP has remained as the current gold standard when comparing new biological fluorescent tags. Protein engineers have tried to tailor GFP for specific applications over the years by tuning the absorption and emission color, photobleaching, and attaching other proteins to act as biosensors. Many of these discoveries have required a high throughput, randomized screening to make GFP an efficient fluorescent toolset, however, a fundamental understanding of the fluorescence generation and modulation mechanism remains lacking due to the experimental challenges to resolve correlated electronic and nuclear motions of the protein chromophore in real time.

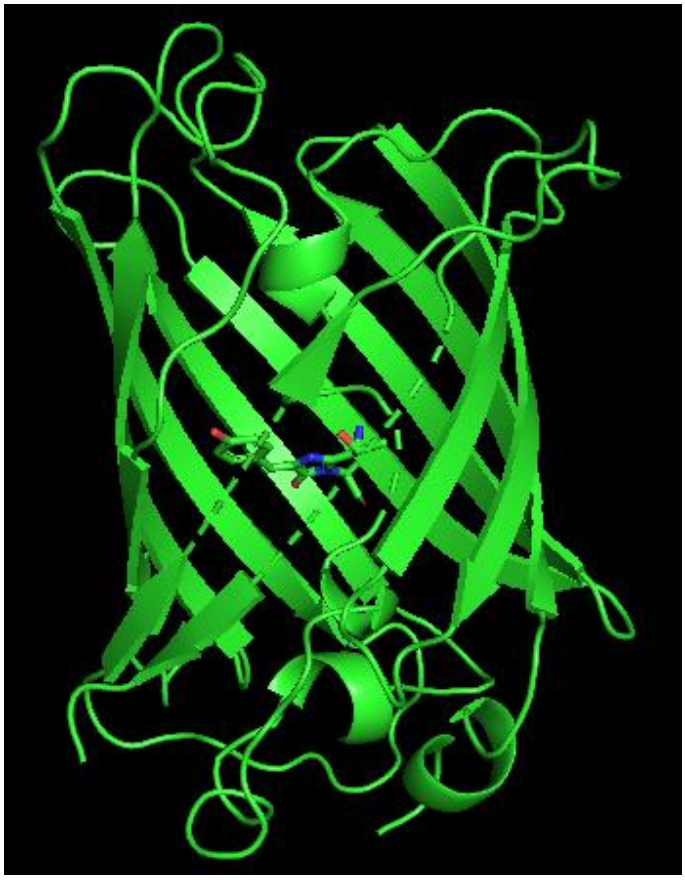

Fig. 1.1. The crystal structure of green fluorescent protein (GFP, PDB 1EMA[4]) with the SYG chromophore shown (center) embedded in the β-barrel. The superficial β-strands have been hidden to better visualize the chromophore.

It was not until the development of ultrafast spectroscopy techniques such as femtosecond transient absorption (fs-TA) and femtosecond stimulated Raman spectroscopy (FSRS) that scientists could readily track how photosensitive systems, like GFP, dissipate their energy after photoexcitation.[5] The combination of vibrational and electronic spectroscopic techniques can also elucidate the essential motions and interactions responsible for the biomolecular function. In 2009, Fang and co-workers first described the key functional motions responsible for GFP's green fluorescence using the newly developed FSRS methodology (**Fig 1.2**).[6] Upon 397 nm excitation,

the GFP three-residue (serine, tyrosine, and glycine, or SYG) chromophore (CRO) rapidly undergoes an ultrafast excited-state proton transfer (ESPT) reaction on the ~5 ps time scale.[7,8] The initially excited protonated CRO transfers the phenolic proton to a nearby conserved water molecule that is hydrogen-bonded with Ser 205, Glu 222, and Ser 65 down the stream (**Fig. 1.2**), while pronounced vibrational intensity quantum beats were observed between coupled motions on the ~1 ps timescale that facilitate ESPT.[6,9] Interestingly, the conserved water molecule in the ESPT chain is slightly out of plane with the CRO. The CRO exhibits a low-frequency wagging motion that can bring the proton closer to the conserved water to transfer the proton while the CRO vicinity "slowly" adjusts to better accommodate the deprotonated CRO as the main emission species. The efficient and dominant ESPT reaction inside wild-type (wt)GFP allows for the high FQY of 0.79 (the highest among natural emitters) with the famous green fluorescence.[3,6]

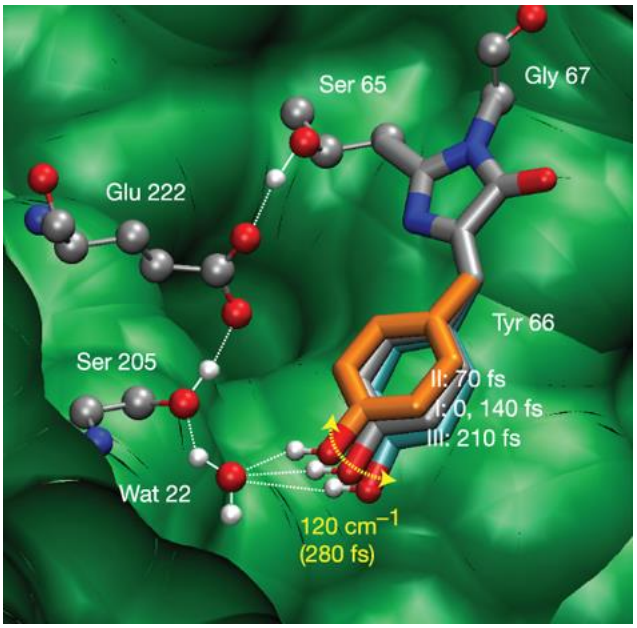

Fig. 1.2. The excited-state proton transfer (ESPT) chain of the Ser-Try-Gly chromophore inside the green fluorescent protein (GFP) pocket. Reproduced from Fang et. al. *Nature* 2009.[6]

After discovering GFP, protein engineers started to attach calmodulin (CaM) to detect calcium ions (Ca^{2+}) *in vivo*.[4,10,11] Ca^{2+} plays an essential role as a biological regulator of electrical and mechanical actions.[12] In 2011, Zhao and coworkers developed an expandable palette of Ca^{2+} biosensors that can be genetically encoded.[11] Here, GEM-GECO1 (GECO stands for genetically encoded calcium ion indicators for optical imaging) was found to exhibit the best contrast ratio between the Ca^{2+}-free vs. bound states, achieved by attaching a circularly permutated (cp)GFP to CaM with a peptide derived from myosin light chain kinase (M13). Upon four Ca^{2+} ions binding to one subunit, CaM undergoes a global conformational change, wrapping around the M13 peptide (**Fig. 1.3A**). While GEM-GECO1 is in the Ca^{2+}-free state, it exhibits green fluorescence (**Fig. 1.3B**, dashed green), however, upon Ca^{2+} binding, GEM-GECO1 emits blue fluorescence (**Fig. 1.3B**, dashed blue). Possessing two distinct emission

wavelengths allows GEM-GECO1 to exhibit a high contrast ratio for bioimaging applications.

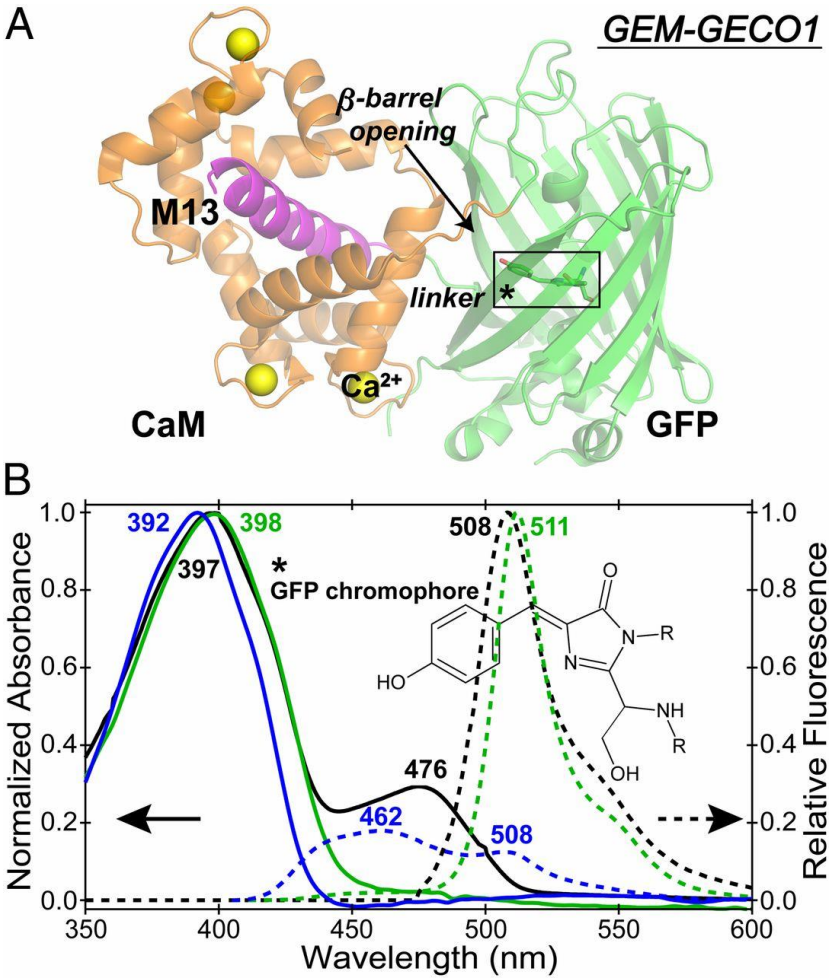

Fig. 1.3. (A) Crystal structure of GEM-GECO1 in the calcium-bound state (PDB 3EVR[13]) that includes a (cp)GFP (green), calmodulin (orange), M13 peptide (magenta), and calcium ions (yellow). (B) The corresponding absorption (solid traces) and emission (dashed traces) of *wt*-GFP (black), GEM-GECO1 in the Ca^{2+}-free state (green), and GEM-GECO1 in the Ca^{2+}-bound state (blue). Reproduced from Oscar et. al. *PNAS* 2014.[14]

To understand the root cause for the green and blue fluorescence for the Ca^{2+}-free and bound state of the protein biosensor, respectively, Oscar and coworkers implemented FSRS to elucidate the ultrafast reaction mechanisms.[14] In the Ca^{2+}-free

state, GEM-GECO1 behaves similar to *wt*-GFP but the (cp)GFP has a natural "opening" on one side of the β-barrel to genetically attach CaM. The interfacial cavity exposes the CRO to the solvent, making the internal water molecules more inhomogeneous and flexible than those inside wtGFP (or standalone GFP derivatives with a largely intact β-barrel structure). The less conserved water slows the ESPT time constant to ~30 ps, significantly larger than the ~5 ps time constant inside wtGFP. Upon Ca^{2+} binding, the prominent conformational change of CaM brings a hydrophobic proline to reside proximal to the phenolic hydrogen of the cpGFP chromophore. The resulting proline interaction effectively inhibits the ESPT pathway, causing the trapped neutral CRO to emit blue fluorescence. The importance of this hydrophobic proline 377, sparked the question: how would a hydrophilic residue such as arginine affect the ESPT pathway? This line of inquiry has been addressed in two of my publications (see Chapters 2 and 3).[15,16]

1.2 Optogenetic tools

Cyanobacteriochromes (CBCRs) are a part of a superfamily of photoreceptors that bind a linear tetrapyrrole cofactor.[17-31] Many photoreceptors have propelled advances in optogenetics due to their efficient photoswitching characteristics, consisting of a naturally occurring thermally stable state and a metastable state.[32-37] Both the thermally stable and metastable states have their own separated ground state absorption peaks. By exciting the thermally stable or equilibrium state, the cofactor undergoes an isomerization reaction along the C15=C16 bond, flipping the D-ring.[22,26,27,32,38-42] The metastable state can then convert back to the thermally stable

state through a slower thermal conversion over time or through a faster photoconversion process. The photoconversion from the thermally stable or metastable state typically introduces an intermediate state known as a Lumi state. The Lumi state resembles photophysical characteristics more similar to the converted (photoproduct) state rather than the initial (photoreactant) state.[19,22,23,26,31-34,38,39,43-47]

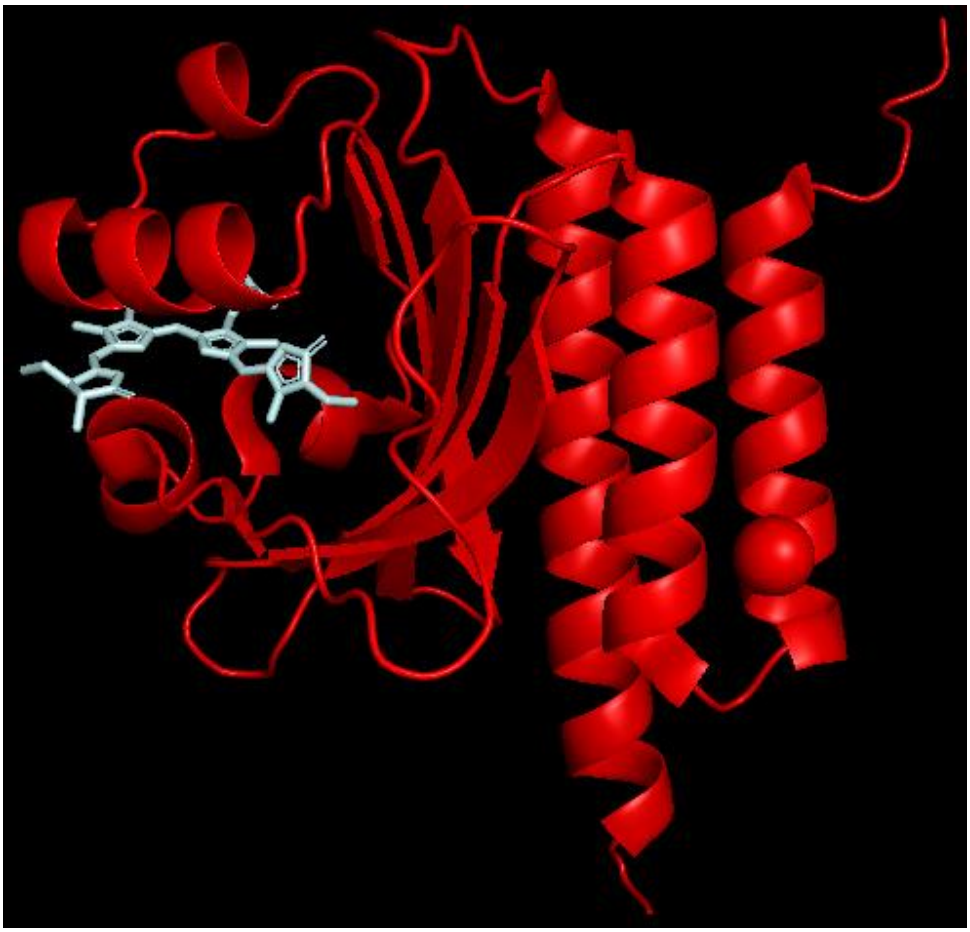

Fig. 1.4. Crystal structure of AnPixJg2 in the thermally stable Pr conformer (PDB 3W2Z)[48]. The phycocyanobilin (PCB) cofactor is shown in gray with the D-ring deviating from the tetrapyrrole ring plane.

A CBCR that has gained attention is AnPixJg2[19,22,26,31,44-47] (**Fig. 1.4**), which was derived from *Anabaena sp. PCC 7120* and only needs a small, 177 amino acids,

compact GAF (cGMP-phosphodiesterase/adenylate cyclase/formate hydrogen lyase transcription activator FhlA) domain for cofactor incorporation and function. Other photoreceptors in the superfamily like phytochromes and bacteria phytochromes require two or more domains ranging from 316 – 908 amino acids.[27,34,44] AnPixJg2 is a hypsochromic photoreceptor with a thermal stable state absorbing at 648 nm (P_r) and a metastable state at 544 nm (P_g). Phytochromes were studied initially because they incorporate a more mammalian available cofactor named biliverdin (BV). In 2019, Fushimi and coworkers were able to find four key mutations that would allow for efficient BV binding in AnPixJg2 named AnPixJg2_BV4 (**Fig. 1.5**).[44] The four mutated residues are His293Tyr, Phe308Thr, His318Tyr, and Ile336Val. The Thr308 and Val336 were shown to be the most crucial for BV incorporation, allowing for a ~ 0.75 Å shift of the cofactor location inside the binding pocket. One of the major differences between PCB and BV is the extended conjugation in the latter cofactor. Such an extended conjugation over the cofactor ring system is responsible for the red-shifted absorption profiles and shifting the cofactor attachment by one bond. AnPixJg2_BV4 with the BV cofactor goes from a P_r/P_g absorption with the protein pocket attachment at the $C3^1$ carbon to a P_{fr}/P_o absorption attaching at the $C3^2$ carbon.

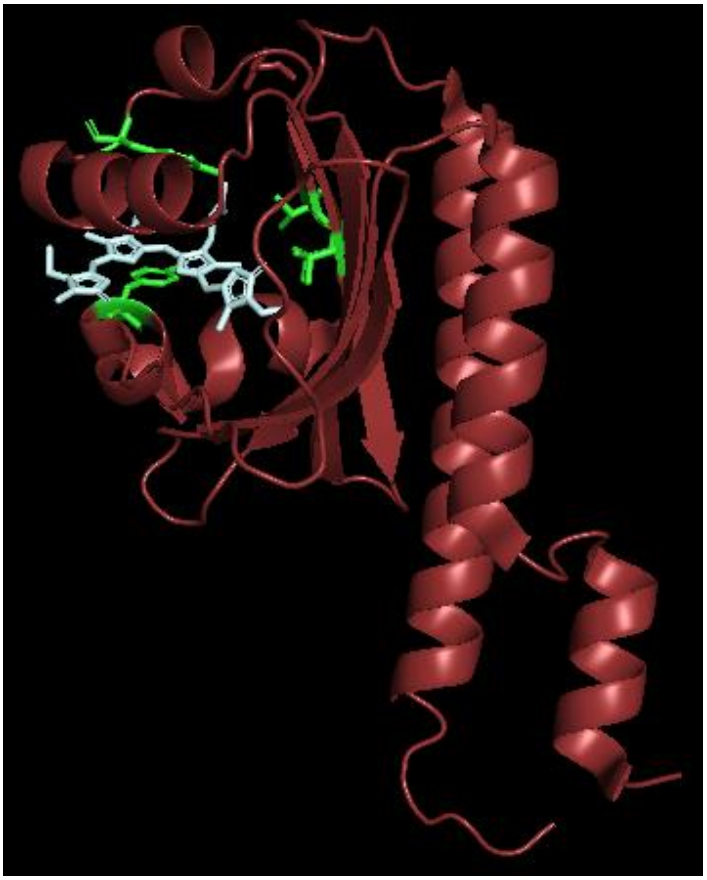

Fig. 1.5. Crystal structure of AnPixJg2_BV4 in the thermally stable P_{fr} conformer (PDB 5ZOH)[44]. The biliverdin (BV) cofactor is shown in gray with the BV4 mutations (His293Tyr, Phe308Thr, His318Tyr, and Ile336Val) shown in green.

To understand the high photoswitching efficiency of AnPixJg2 with the PCB cofactor (Apcb) and the effects of the four key mutations with the BV cofactor, a systematic study of three samples was performed. The first is to understand the ultrafast photoswitching mechanism of the parent Apcb protein. The second is to understand how the four mutations affect the photoswitching dynamics on the intrinsic molecular timescale (typically on the fs-to-ps timescale). This aim can be achieved by studying AnPixJg2_BV4 with the BV cofactor (Bpcb). Third, we will study AnPixJg2_BV4 with the BV cofactor to understand how the different cofactors interact with protein

pocket to achieve their macroscopic functions (see our results in Chapters 4 and 5 below).

1.3 Ultrafast Electronic Spectroscopy

1.3.1 Femtosecond transient absorption (fs-TA)

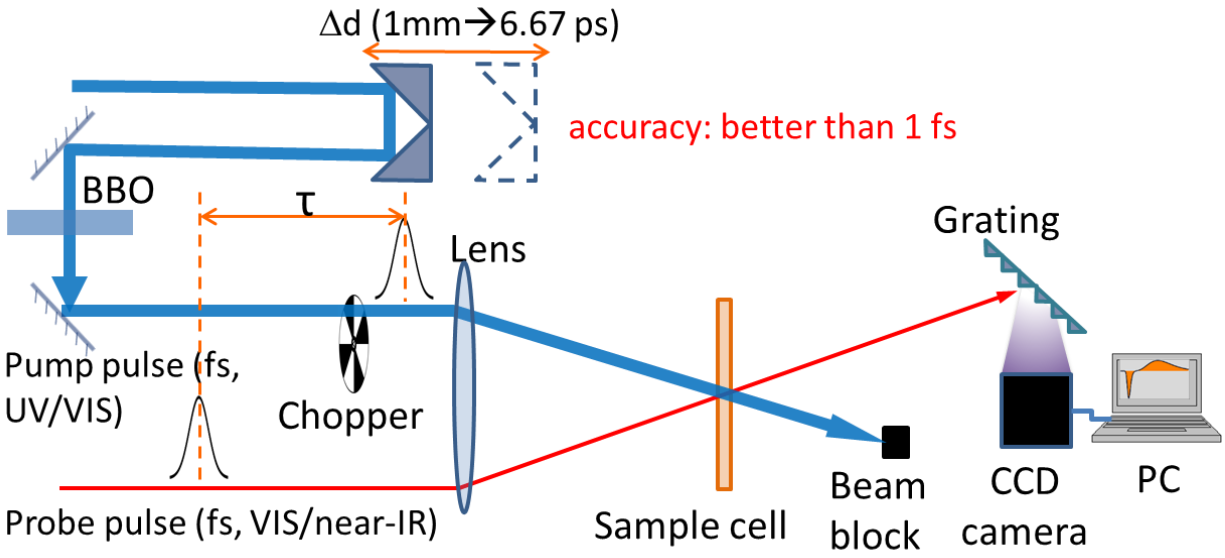

Fig. 1.6. Fs-TA schematic of the actinic pump (blue) and probe pulse (red). Past the sample the transmitted probe pulse is spatially dispersed with its the photons being detected on a CCD camera.

In this section, theoretical basics and analysis for femtosecond transient absorption (fs-TA) spectroscopy and global analysis using Glotaran software will be briefly described. For further details, individual research papers with an extended Methods section can be referenced.[15,16,31,49]

Fs-TA is one of the generally available ultrafast spectroscopy techniques as a time-resolved version of steady-state absorption and fluorescence on the excited state.

Fs-TA can achieve its time resolution on the electronically excited state by implementing two pulses: An actinic pump and a supercontinuum white light (SCWL) probe (**Fig. 1.6**).[50] The actinic pump is responsible for exciting the sample from the singlet ground state (S_0) to a higher-lying excited state, typically S_1. The probe pulse carries the signal from the photoexcited molecule and gets dispersed by a reflective grating, before being imaged onto an array detector (CCD camera) that outputs the spectra (**Fig. 1.6**). A motorized delay line determines the time delay of the actinic pump that controls when the pump pulse hits the sample with respect to the probe pulse. The time resolution is governed by the cross-correlation time between the two fs (pump and probe) pulses at the sample spot, typically solvent in a 1-mm-pathlength quartz cuvette if the sample solution is measured therein.

A significant advantage of fs-TA is its ability to study both fluorescent and non-fluorescent systems, unlike time-resolved fluorescence.[31,51] The resulting signal is a difference of absorption (ΔA) based on the Beer-Lambert's Law $\Delta A = A_{ex} - A_{gd} = \left(-log\frac{I_{ex}}{I_0}\right) - \left(-log\frac{I_{gd}}{I_0}\right) = -log\frac{I_{ex}}{I_{gd}}$. The I_{ex} and I_{gd} are the probe intensities after passing through the sample cuvette with and without the actinic pump, respectively. The I_0 is the incident probe intensity before hitting the sample. The typical fs-TA signals observed are ground-state bleaching (GSB), stimulated emission (SE), excited-state absorption (ESA), and hot ground-state absorption (HGSA). The negative GSB signal is due to a depletion of the ground-state population upon excitation. The SE signal results from a probe photon matching the frequency and direction of a photon emitted from the molecule. This causes the SE feature to be negative as it represents a downward transition between the excited state and a lower-lying state, and a gain of

probe intensity after electronic excitation by the pump. The ESA signal is similar to the ground state absorption as the molecule absorbs photons from the probe (i.e., a loss of probe intensity), which results in a positive signal (see the equation above). Opposite to SE, ESA samples upward transitions to higher-lying states. In addition, the HGSA signal arise from ground-state intermediates. HGSA is typically associated with photoswitching or photoconverting systems that isomerize on the ultrafast timescales (e.g. GFP CRO in solution). Due to the unrelaxed nature of molecules contributing to HGSA, the signal appears on the red side of the ground-state absorption peak.

The fs-actinic pump in our optical setup can be tuned from 267 nm, 400 nm, 480 – 720 nm, to 800 nm. The 800 nm pulse is the fundamental output of the Ti:Sapphire laser amplifier system. The 400 nm pulse is produced through second harmonic generation (SHG) of two 800 nm pulses through a nonlinear β-barium borate (BBO) crystal. Similarly, the 267 nm pulse is generated through sum frequency generation of the 400 and 800 nm pulses. The tunable range from 480 – 720 nm is achieved by a home-built two-stage fs noncollinear optical parametric amplifier (NOPA). In brief, each NOPA is comprised of a 400 nm pump that overlaps noncollinearly with a seed on a BBO crystal. The first NOPA determines the actinic pump wavelength by amplifying a region of the supercontinuum white light (SCWL), which is generated by focusing an 800 nm pulse onto a thin sapphire plate (typically 2 or 3-mm-thick). The resulting wavelength-tuned pulse acts as the seed in the second NOPA to mainly amplify its power. As for the fs probe pulse, the broadband SCWL is generated by focusing an 800 nm pulse on a thin sapphire plate or a 2-mm-thick quartz cell filled with deionized water (for bluer probe photons).[52]

Probe-dependent wavelength analysis in fs-TA can be performed to fit the kinetic intensity dynamics of the aforementioned transient electronic bands. Typically, multi-exponential decay fits can retrieve relevant time components of the photoinduced processes. One of the significant downsides of fs-TA spectra is the highly overlapped, broad electronic features. Such a high degree of overlap introduces challenges in the probe-dependent fits with the resulting time constants being represented as weighted averages. To facilitate the kinetic analysis and resolve the overlapping transient electronic bands, mathematical programs can be implemented.

1.3.2 Glotaran for global analysis

Fs-TA spectra are highly overlapped because of the broad peak width characteristic of electronic spectra. This makes it difficult to reliably fit the dynamics of the overlapped features which cause the resulting dynamics to be influenced by each other. To better resolve and fit the highly convoluted spectra, a mathematical software called Glotaran has been commonly used. Glotaran implements matrix calculations to fit the superposition models to multidimensional data from TA and also other ultrafast techniques like time-resolved fluorescence spectroscopy.[53-55] In Glotaran, global analysis simultaneously processes the entire spectrum in both time and wavelength. By analyzing both dimensions at the same time, it helps to disentangle overlapped processes that correspond to kinetically evolving spectral components of a photoexcited molecule.

Global analysis requires the input of an initial kinetic model that needs to be iteratively manipulated, reducing the root mean square fit to raw spectra. The resulting

analysis outputs two series of spectra: an evolution-associated difference spectrum (EADS) and decay-associated difference spectrum (DADS). In general, EADS represents a linear model with each component evolving from the first to the last. DADS is a parallel model with each component exponentially decaying away. After completing these two global analysis methods, target analysis can be further implemented to apply specific kinetic analysis of species evolution. This is achieved by buillding a K matrix that controls the species evolution, such as pathway branching. Successful target analysis is rather challenging and requires prior knowledge of the system and multiple test models. The most reliable global and target analysis should output the most distinguishable spectral properties with a minimal number of components, which could lead to the most reasonable physical insights of the photophysical/photochemical processes under investigation.

1.4 Ultrafast Vibrational Spectroscopy

1.4.1 Femtosecond stimulated Raman spectroscopy

Since the 2000's, femtosecond stimulated Raman spectroscopy (FSRS) has increasingly gained popularity because of its simultaneously high temporal and spectral resolutions.[38] This is possible due to spectral data collection in the mixed time-frequency domain with the short fs-actinic pump and the narrowband ps-Raman pump attributing to the high time and spectral resolution, respectively (**Fig. 1.7**). The fs broadband Raman probe not only achieves a short cross-correlation with the fs actinic pump (determining time resolution) but also enables spectral detection across a broad spectral window. Dynamic resonance enhancement from FSRS also allow for higher

signal-to-noise ratios that lead to reliable data collection in low-concentration samples or with low pump powers.[5,56,57] The basic concept of FSRS is to create a molecular movie wherein each vibrational peak at each time delay acts as a molecular snapshot in a stop-motion film. These vibrational motions are constantly influenced by the surrounding environment and physical changes of the molecule itself. An overview of how the molecule dissipates its energy upon photoexcitation can be made in a potential energy surface diagram by observing each motion over time when the photoinduced processes are "in action".

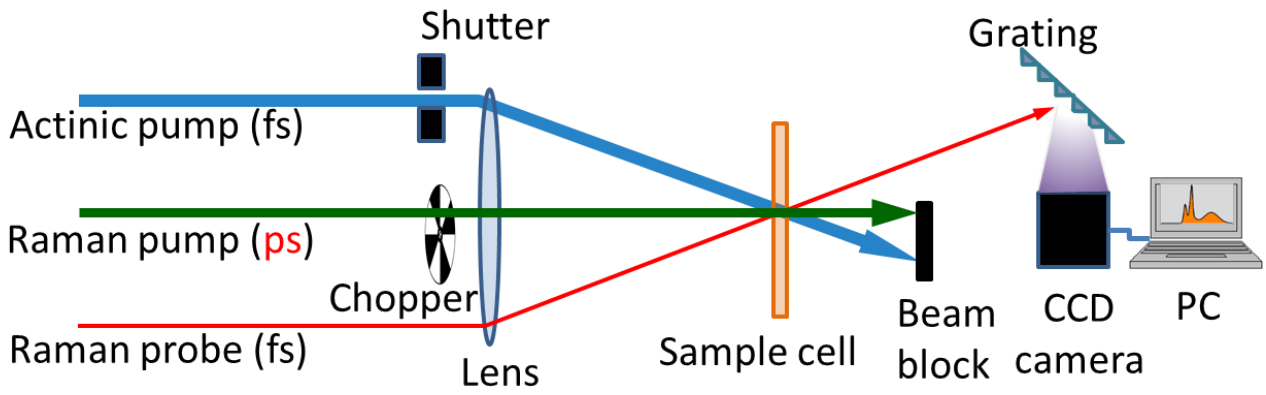

Fig. 1.7. General schematic of the actinic pump (blue) as well as the Raman pump (green) and probe (red) pair. The transmitted probe pulse past the sample cell is spatially dispersed before the probe spectrum is recorded on a CCD camera.

In general, the FSRS setup is the same as fs-TA with the addition of a Raman pump. The fs actinic pump excites the molecule to the excited state, which is controlled by a mechanical shutter and motorized delay line. The ps Raman pump is generated by implementing a home-built second harmonic bandwidth compressor (SHBC) to create a ps pump pulse and fs-NOPA and spectral filter for a ps seed pulse. To create a 400

nm ps pump from an 800 nm fs pulse, the SHBC splits the 800 nm pulse into two arms with a positive and negative chirp. The two arms are then combined in a BBO crystal, resulting in a 400 nm ps-pump to be used in the subsequent two-stage ps-NOPA. The first fs-NOPA and spectral filter uses a 400 nm fs-pump and fs-SCWL to generate a wavelength-tunable fs-pulse. This pulse is spatially dispersed on a narrow slit that selects only a narrow bandwidth (a specific color) to go through. The result is a much weaker ps-seed that can be amplified using a two-stage ps-NOPA (similar to the aforementioned actinic pump amplified in a two-stage fs-NOPA) to be amplified for the wavelength-tunable ps-Raman pump. Such a wavelength-tunable setup was not implemented in the early stage of our lab, so only an 800 nm ps-Raman pump was used for some of the early FSRS measurements on GFP-based calcium sensors.[14,15] This is what is known as conventional FSRS and tunable FSRS, with the latter technique including the rest of the tunable range for the ps Raman pump to enable studies of a wide array of molecular systems from biomolecules to materials.[9,57,58]

For data analysis, the baseline removal is one of the most challenging aspects in processing excited-state FSRS. Although, in theory, the excited-state vibrational modes should appear on top of the fs-TA signal as the background, the effects induced by the Raman pump with the excited-state population prevent a 1-to-1 subtraction (i.e., Raman-pump-induced change to the TA profile at each time delay point). Currently, the most reliable approach to removing the background is through systematic manual baseline drawing. A general rule is to have featureless, broad, and smooth baselines for the entire spectral window to remain consistent in drawing baselines. Some of the difficulties stem from fs laser fluctuations, and experimental conditions like resonance

enhancement (the specific Raman pump and probe overlap with transient spectral features) or temperature and humidity fluctuations in the laser lab can all cause inconsistencies or dispersive line shapes. Overall, the time-stacked plot is a powerful guide to identifying significant peaks and drawing the baseline; previous literature including our publications on related proteins or protein biosensors could provide a useful comparison. A semi-automated baseline fitting function or software could reduce human error and has been used to corroborate the manual baseline drawing.[57,59]

1.4.2 Quantum calculations for mode assignment

Quantum calculation software like Gaussian 09 or 16 allows for the visualization of specific vibrational modes (normal modes).[60] Although quantum calculations are not our main area of expertise, the commonly used density functional theory (DFT) calculations allow for trend analysis and mode assignment. For larger, more complex molecules, sidechain R-groups that do not influence the conjugation or electron distribution can be methyl capped to help the calculation converge faster (e.g., CBCR work)[31,61]. Also, if a molecule has a hard time converging to a geometrically optimized state, starting with a lower level calculation and working your way up (with higher theory level and expanded basis sets) usually helps to find the global minimum.

1.5 References

(1) Shimomura, O.; Johnson, F. H.; Saiga, Y. *Journal of Cellular and Comparative Physiology* **1962**, *59*, 223.

(2) Chalfie, M.; Tu, Y.; Euskirchen, G.; Ward, W. W.; Prasher, D. C. *Science (New York, N.Y.)* **1994**, *263*, 805.

(3) Morise, H.; Shimomura, O.; Johnson, F. H.; Winant, J. *Biochemistry* **1974**, *13*, 2656.

(4) Ormö, M.; Cubitt, A. B.; Kallio, K.; Gross, L. A.; Tsien, R. Y.; Remington, S. J. *Science (New York, N.Y.)* **1996**, *273*, 1392.

(5) Kukura, P.; McCamant, D. W.; Mathies, R. A. *Annual Review of Physical Chemistry* **2007**, *58*, 461.

(6) Fang, C.; Frontiera, R. R.; Tran, R.; Mathies, R. A. *Nature* **2009**, *462*, 200.

(7) Chattoraj, M.; King, B. A.; Bublitz, G. U.; Boxer, S. G. *Proc. Natl. Acad. Sci. U.S.A.* **1996**, *93*, 8367.

(8) Kennis, J. T. M.; Larsen, D. S.; van Stokkum, I. H. M.; Vengris, M.; van Thor, J. J.; van Grondelle, R. *Biophys. J.* **2004**, *86*, 168A.

(9) Fang, C.; Tang, L. *Annual Review of Physical Chemistry* **2020**, *71*, 239.

(10) Yang, F.; Moss, L. G.; Phillips, G. N. *Nature biotechnology* **1996**, *14*, 1246.

(11) Zhao, Y.; Araki, S.; Wu, J.; Teramoto, T.; Chang, Y.-F.; Nakano, M.; Abdelfattah, A. S.; Fujiwara, M.; Ishihara, T.; Nagai, T.; Campbell, R. E. *Science (New York, N.Y.)* **2011**, *333*, 1888.

(12) Fijorek, K.; Püsküllüoğlu, M.; Tomaszewska, D.; Tomaszewski, R.; Glinka, A.; Polak, S. *Folia medica Cracoviensia* **2014**, *54*, 53.

(13) Wang, Q.; Shui, B.; Kotlikoff, M. I.; Sondermann, H. *Structure* **2008**, *16*, 1817.

(14) Oscar, B. G.; Liu, W.; Zhao, Y.; Tang, L.; Wang, Y.; Campbell, R. E.; Fang, C. *Proceedings of the National Academy of Sciences* **2014**, 201403712.

(15) Tachibana, S. R.; Tang, L.; Wang, Y.; Zhu, L.; Liu, W.; Fang, C. *Physical Chemistry Chemical Physics* **2017**, *19*, 7138.

(16) Tachibana, S. R.; Tang, L.; Zhu, L.; Liu, W.; Wang, Y.; Fang, C. *The Journal of Physical Chemistry B* **2018**, *122*, 11986.

(17) Bussell, A. N.; Kehoe, D. M. *Proceedings of the National Academy of Sciences* **2013**, *110*, 12834.

(18) Enomoto, G.; Ni-Ni-Win; Narikawa, R.; Ikeuchi, M. *Proceedings of the National Academy of Sciences* **2015**, *112*, 8082.

(19) Fushimi, K.; Enomoto, G.; Ikeuchi, M.; Narikawa, R. *Photochemistry and Photobiology* **2017**, *93*, 681.

(20) Gottlieb, S. M.; Kim, P. W.; Corley, S. C.; Madsen, D.; Hanke, S. J.; Chang, C.-W.; Rockwell, N. C.; Martin, S. S.; Lagarias, J. C.; Larsen, D. S. *Biochemistry* **2014**, *53*, 1029.

(21) Hirose, Y.; Rockwell, N. C.; Nishiyama, K.; Narikawa, R.; Ukaji, Y.; Inomata, K.; Lagarias, J. C.; Ikeuchi, M. *Proceedings of the National Academy of Sciences* **2013**, *110*, 4974.

(22) Kim, P. W.; Freer, L. H.; Rockwell, N. C.; Martin, S. S.; Lagarias, J. C.; Larsen, D. S. *Biochemistry* **2012**, *51*, 619.

(23) Kim, P. W.; Freer, L. H.; Rockwell, N. C.; Martin, S. S.; Lagarias, J. C.; Larsen, D. S. *Biochemistry* **2012**, *51*, 608.

(24) Narikawa, R.; Fushimi, K.; Ni Ni, W.; Ikeuchi, M. *Biochemical and biophysical research communications* **2015**, *461*, 390.

(25) Oliinyk, O. S.; Chernov, K. G.; Verkhusha, V. V. *Int J Mol Sci* **2017**, *18*, 1691.

(26) Rao, A. G.; Wiebeler, C.; Sen, S.; Cerutti, D. S.; Schapiro, I. *bioRxiv* **2020**, 2020.08.21.260158.

(27) Rockwell, N. C.; Lagarias, J. C. *ChemPhysChem* **2010**, *11*, 1172.

(28) Rockwell, N. C.; Martin, S. S.; Feoktistova, K.; Lagarias, J. C. *Proc. Natl. Acad. Sci. U.S.A.* **2011**, *108*, 11854.

(29) Rockwell, N. C.; Martin, S. S.; Lagarias, J. C. *Biochemistry* **2012**, *51*, 9667.

(30) Song, C.; Narikawa, R.; Ikeuchi, M.; Gärtner, W.; Matysik, J. *The Journal of Physical Chemistry B* **2015**, *119*, 9688.

(31) Tachibana, S. R.; Tang, L.; Chen, C.; Zhu, L.; Takeda, Y.; Fushimi, K.; Seevers, T. K.; Narikawa, R.; Sato, M.; Fang, C. *Spectrochimica Acta Part A: Molecular and Biomolecular Spectroscopy* **2020**, *250*, 119379.

(32) Fukushima, Y.; Iwaki, M.; Narikawa, R.; Ikeuchi, M.; Tomita, Y.; Itoh, S. *Biochemistry* **2011**, *50*, 6328.

(33) Fukushima, Y.; Okajima, K.; Shibata, Y.; Ikeuchi, M.; Itoh, S. *Biochemistry* **2005**, *44*, 5149.

(34) Ikeuchi, M.; Ishizuka, T. *Photochem. Photobiol. Sci.* **2008**, *7*, 1159.

(35) Ishizuka, T.; Kamiya, A.; Suzuki, H.; Narikawa, R.; Noguchi, T.; Kohchi, T.; Inomata, K.; Ikeuchi, M. *Biochemistry* **2011**, *50*, 953.

(36) Ishizuka, T.; Narikawa, R.; Kohchi, T.; Katayama, M.; Ikeuchi, M. *Plant Cell Physiol.* **2007**, *48*, 1385.

(37) Ishizuka, T.; Shimada, T.; Okajima, K.; Yoshihara, S.; Ochiai, Y.; Katayama, M.; Ikeuchi, M. *Plant Cell Physiol.* **2006**, *47*, 1251.

(38) Dasgupta, J.; Frontiera, R. R.; Taylor, K. C.; Lagarias, J. C.; Mathies, R. A. *Proceedings of the National Academy of Sciences* **2009**, *106*, 1784.

(39) Liu, Y.; Chen, Z.; Wang, X.; Cao, S.; Xu, J.; Jimenez, R.; Chen, J. *Physical Chemistry Chemical Physics* **2020**, *22*, 19903.

(40) Song, C.; Psakis, G.; Lang, C.; Mailliet, J.; Gartner, W.; Hughes, J.; Matysik, J. *Proc. Natl. Acad. Sci. U.S.A.* **2011**, *108*, 3842.

(41) Toh, K. C.; Stojkovic, E. A.; van Stokkum, I. H. M.; Moffat, K.; Kennis, J. T. M. *Proc. Natl. Acad. Sci. U.S.A.* **2010**, *107*, 9170.

(42) Xu, X.; Höppner, A.; Wiebeler, C.; Zhao, K.-H.; Schapiro, I.; Gärtner, W. *Proceedings of the National Academy of Sciences* **2020**, *117*, 2432.

(43) Kim, P. W.; Freer, L. H.; Rockwell, N. C.; Martin, S. S.; Lagarias, J. C.; Larsen, D. S. *Journal of the American Chemical Society* **2012**, *134*, 130.

(44) Fushimi, K.; Miyazaki, T.; Kuwasaki, Y.; Nakajima, T.; Yamamoto, T.; Suzuki, K.; Ueda, Y.; Miyake, K.; Takeda, Y.; Choi, J.-H.; Kawagishi, H.; Park, E. Y.; Ikeuchi, M.; Sato, M.; Narikawa, R. *Proceedings of the National Academy of Sciences* **2019**, *116*, 8301.

(45) Scarbath-Evers, L. K.; Jähnigen, S.; Elgabarty, H.; Song, C.; Narikawa, R.; Matysik, J.; Sebastiani, D. *Physical Chemistry Chemical Physics* **2017**, *19*, 13882.

(46) Velazquez Escobar, F.; Utesch, T.; Narikawa, R.; Ikeuchi, M.; Mroginski, M. A.; Gärtner, W.; Hildebrandt, P. *Biochemistry* **2013**, *52*, 4871.

(47) Xu, X. L.; Gutt, A.; Mechelke, J.; Raffelberg, S.; Tang, K.; Miao, D.; Valle, L.; Borsarelli, C. D.; Zhao, K. H.; Gärtner, W. *Chembiochem : a European journal of chemical biology* **2014**, *15*, 1190.

(48) Narikawa, R.; Ishizuka, T.; Muraki, N.; Shiba, T.; Kurisu, G.; Ikeuchi, M. *Proceedings of the National Academy of Sciences* **2013**, *110*, 918.

(49) Tachibana, S. R.; Tang, L. **2021**, *22*.

(50) Berera, R.; van Grondelle, R.; Kennis, J. T. M. *Photosynthesis Research* **2009**, *101*, 105.

(51) Tang, L.; Fang, C. *The Journal of Physical Chemistry B* **2019**, *123*, 4915.

(52) Tang, L.; Wang, Y.; Zhu, L.; Lee, C.; Fang, C. *The Journal of Physical Chemistry Letters* **2018**, *9*, 2311.

(53) van Stokkum, I. H. M.; Larsen, D. S.; van Grondelle, R. *Biochim. Biophys. Acta* **2004**, *1657*, 82.

(54) Kim, P. W.; Rockwell, N. C.; Martin, S. S.; Lagarias, J. C.; Larsen, D. S. *Biochemistry* **2014**, *53*, 4601.

(55) Dedecker, P. *Journal of Chemometrics* **2014**, *28*, 137.

(56) Oscar, B. G.; Chen, C.; Liu, W.; Zhu, L.; Fang, C. *The Journal of Physical Chemistry A* **2017**, *121*, 5428.

(57) Fang, C.; Tang, L.; Oscar, B. G.; Chen, C. *The Journal of Physical Chemistry Letters* **2018**, *9*, 3253.

(58) Dietze, D. R.; Mathies, R. A. *ChemPhysChem* **2016**, *17*, 1224.

(59) Taylor, M. A.; Zhu, L.; Rozanov, N. D.; Stout, K. T.; Chen, C.; Fang, C. *Physical Chemistry Chemical Physics* **2019**, *21*, 9728.

(60) Frisch, M. J.; Trucks, G. W.; Schlegel, H. B.; Scuseria, G. E.; Robb, M. A.; Cheeseman, J. R.; Scalmani, G.; Barone, V.; Petersson, G. A.; Nakatsuji, H.; Li, X.; Caricato, M.; Marenich, A. V.; Bloino, J.; Janesko, B. G.; Gomperts, R.; Mennucci, B.; Hratchian, H. P.; Ortiz, J. V.; Izmaylov, A. F.; Sonnenberg, J. L.; Williams; Ding, F.; Lipparini, F.; Egidi, F.; Goings, J.; Peng, B.; Petrone, A.; Henderson, T.; Ranasinghe, D.; Zakrzewski, V. G.; Gao, J.; Rega, N.; Zheng, G.; Liang, W.; Hada, M.; Ehara, M.; Toyota, K.; Fukuda, R.; Hasegawa, J.; Ishida, M.; Nakajima, T.; Honda, Y.; Kitao, O.; Nakai, H.; Vreven, T.; Throssell, K.; Montgomery Jr., J. A.; Peralta, J. E.; Ogliaro, F.; Bearpark, M. J.; Heyd, J. J.; Brothers, E. N.; Kudin, K. N.; Staroverov, V. N.; Keith, T. A.; Kobayashi, R.; Normand, J.; Raghavachari, K.; Rendell, A. P.; Burant, J. C.; Iyengar, S. S.; Tomasi, J.; Cossi, M.; Millam, J. M.; Klene, M.; Adamo, C.; Cammi, R.; Ochterski, J. W.; Martin, R. L.; Morokuma, K.; Farkas, O.; Foresman, J. B.; Fox, D. J. Wallingford, CT, 2016.

(61) Wiebeler, C.; Rao, A. G.; Gärtner, W.; Schapiro, I. *Angewandte Chemie International Edition* **2019**, *58*, 1934.

Chapter 2 Tuning calcium biosensors with a single-site mutation: Structural dynamics insights from femtosecond Raman spectroscopy

Published in: **Sean R. Tachibana**, Longteng Tang, Yanli Wang, Liangdong Zhu, Weimin Liu, and Chong Fang **(2017)** "Tuning calcium biosensors with a single-site mutation: Structural dynamics insights from femtosecond Raman spectroscopy", *Phys. Chem. Chem. Phys.*, 19 (10), 7138-7146. DOI: 10.1039/C6CP08821J.

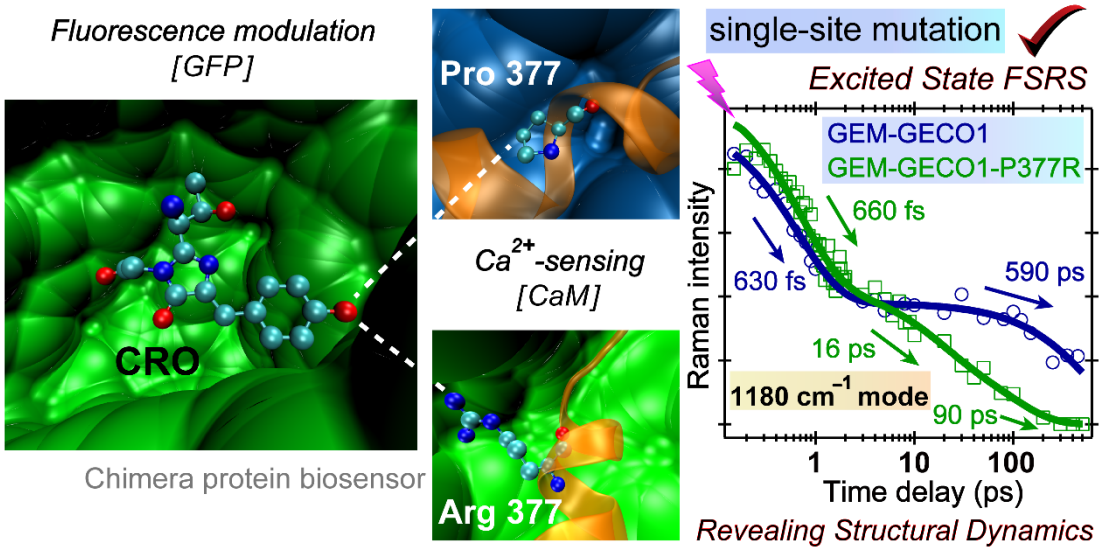

"If you are not progressing along the true way, a slight twist in the mind can become a major twist. This must be pondered well." – Miyamoto Musashi

2.1 Abstract

Fluorescent protein biosensors are popular reporters for biological processes and life sciences, but their fundamental working mechanisms remain unclear. To characterize the functional fluorescence events on their native timescales, we implemented the wavelength-tunable femtosecond stimulated Raman spectroscopy (FSRS) to shed light on a blue-green emission-ratiometric fluorescent protein based Ca^{2+} biosensor with a single Pro377Arg mutation. The transient Raman modes of the embedded chromophore from ca. 1000—1650 cm^{-1} exhibit characteristic intensity and frequency dynamics which infer the underlying atomic motions and photochemical reaction stages. Our experimental study reveals the hidden structural inhomogeneity of the protein local environment upon Ca^{2+} binding with the mutated arginine residue trapping multiple chromophore subpopulations, which manifest distinct time constants of ~16 and 90 ps for excited state proton transfer (ESPT) following 400 nm photoexcitation. The altered ESPT reaction pathways and emission properties of the Ca^{2+} biosensor represent the foundational step of rationally designing advanced fluorescent protein biosensors to tune their functionalities by site-specifically altering the local environment (e.g., active site) of the embedded chromophore.

2.2 Introduction

Modern biological imaging and life sciences have benefited tremendously from the development of fluorescent proteins (FPs) and the FP-based biosensors.[1-5] Among them, genetically encoded calcium indicators for optical imaging (GECOs) belong to a family of circularly permuted (cp)FP-based biosensors.[6,7] The GECOs consist of three

major subunits, calmodulin (CaM), a binding client such as M13 peptide from myosin light chain kinase, and cpGFP. As CaM binds calcium ions (Ca^{2+}), it wraps itself around M13 and blocks the adjacent β-barrel opening which affects the emission properties of the biosensor. These highly functional protein biosensors have enabled advanced bioimaging with different scanning and modelling procedures, but their intrinsic fluorescence mechanisms remain one of the crucial and governing aspects for future rational design. The challenges to achieve such level of fundamental understanding lie at the experimental difficulty of tracking atomic motions in the electronic excited state.[8] When such information becomes available with the invent of suitable techniques, it is desirable to examine the molecular structural dynamics basis with site specificity so detailed reaction coordinates can be dissected without overlapping contributions from a crowded protein environment.[9-13] This unique line of inquiry is thus biophysical chemistry in nature with a fundamental focus, making it an indispensable integral part of chemical sciences. Furthermore, instead of being a specialized effort to benchmark a model system, the practical implications of our results in revealing fluorescence modulation mechanisms and how they govern the biosensor imaging properties are directly applicable and beneficial for the broad science and engineering community.

To provide such mechanistic insights, we have developed femtosecond stimulated Raman spectroscopy (FSRS)[10,14-16] to study a dual-emission ratiometric Ca^{2+} biosensor, GEM-GECO1, with an autocatalytically formed Ser-Tyr-Gly (SYG) chromophore.[6,7] The FSRS technique enables us to go beyond the UV-Visible and fluorescence spectroscopy showing that the Ca^{2+}-free biosensor emits green but changes to blue upon Ca^{2+} binding. Our key finding was that excited state proton

transfer (ESPT) in an "open" β-barrel on a ~30 picosecond (ps) timescale generates a deprotonated chromophore that emits green photons. With Ca^{2+} binding, conformationally changed CaM pushes its Pro377 to the interface, creating a hydrophobic environment near the GFP chromophore and inhibiting proton transfer.[17,18] The dominant structural motion that guides GEM-GECO1 out of the Franck-Condon (FC) region is a phenolic ring rocking.[17] This vibrational motion facilitates ESPT in the Ca^{2+}-free GEM-GECO1 biosensor as evinced by spectral oscillations. Because ESPT is a ubiquitous process in FPs which determines their overall function of fluorescence, this work holds a broad impact for the FP researchers, engineers as well as users.

To delineate the role played by Pro377, Campbell and co-workers performed single-site mutagenesis at residue position 377 in GEM-GECO1, replacing proline with arginine (P377R).[17] Our experimental approach is to collect the conventional FSRS with an 800 nm Raman pump[10,17,19] to track the protonated chromophore A* modes after photoexcitation of the P377R (short for GEM-GECO1-P377R) biosensor, and then tune the Raman pump to visible range[16,20,21] to track the deprotonated chromophore I* modes as the ESPT reaction progresses. The comparison between the Ca^{2+}-free and bound biosensors infers calcium sensing mechanisms, while the contrast to GEM-GECO1 biosensor elucidates the functional role of residue 377. Notably, our recent results on an intensiometric biosensor G-GECO1.1 concern a different TYG chromophore which has an extra methyl group at the imidazolinone end.[20] That is why we focus our comparative analysis between GEM-GECO1 and its P377R mutant (i.e., change of one residue) so we can reliably discern the main effect of a single-site

mutation in the vicinity of the conserved SYG chromophore. The conformational states and dynamics insights clearly involve the SYG chromophore and ESPT time constants which underlie intrinsic fluorescence modulation mechanism of the overall P377R biosensor.

2.3 Experimental

2.3.1 Protein sample preparation

The GEM-GECO1-P377R biosensor sample preparation follows previously published procedures starting from *E. coli* DH10B cells (Invitrogen) transformed with the pTorPE plasmid harbouring the 6-histidine tagged GEM-GECO1.[17] For the single site-specific mutagenesis in this work, the synthetic DNA oligonucleotides with the corresponding sequence were purchased from Integrated DNA Technologies and used with the QuickChange Lightning Single kit (Agilent Technologies). These P377R proteins are harvested, purified, and dissolved in buffer solutions, before finally exchanged into the desired MOPS buffer solution (pH=7.2) with either 10 mM EGTA (for the Ca^{2+}-free sample) or 10 mM Ca-EGTA (for the Ca^{2+}-bound sample). The protein biosensors are characterized by *in vitro* steady-state electronic spectroscopy including the UV-Visible (Thermo Scientific Evolution 201) and fluorescence (Hitachi F-2500) spectrophotometers. To avoid protein destabilization or denaturing, we keep buffer conditions, pH and temperature unchanged and verify the sample integrity using UV-Vis before and after each ultrafast spectroscopic measurement.

We found that three separately prepared batches of purified P377R samples exhibit a weak response to Ca^{2+} in emission under 395 nm excitation. The excitation

spectra of P377R suggest this mutant chimeric protein has essentially become an excitation ratiometric (green) indicator, which differs from the original GEM-GECO1 that is a blue-green emission ratiometric biosensor.[17] This result highlights the critical role of residue 377 in the absorption and fluorescence properties of the GCaMP-type indicators for Ca^{2+} sensing.[6,7]

2.3.2 Tunable FSRS optical setup

The femtosecond stimulated Raman spectroscopy (FSRS) setup with technical advances in our laboratory has been reported.[15-17,31,46] In brief, a femtosecond (fs) mode-locked Ti:sapphire oscillator (Mantis-5) and regenerative laser amplifier (Legend Elite-USP-1K-HE, Coherent, Inc.) provide ~35 fs, 4 mJ, 800 nm fundamental pulses with a 1 kHz repetition rate. The stimulated Raman pump–probe pair and a preceding actinic pump are separately generated via nonlinear light conversion processes. The 400 nm actinic pulse of ~400 μW arises from the frequency doubling of a portion of the fundamental pulse in a 0.3-mm-thick type-I β-barium borate (BBO) crystal. For conventional FSRS, the 800 nm Raman pump with ~4 mW power and ~3 ps pulse duration is generated by passing the fundamental pulse through a home-built spectral filter.[14,15] The ~100 nJ Raman probe pulse is a supercontinuum white light (ca. 840—960 nm) generated in a 2-mm-thick *Z*-cut sapphire crystal, followed by the prism-pair compression and a long-pass filter (RG830, Newport). For tunable FSRS, the 553 nm Raman pump is produced by a home-built two-stage ps noncollinear optical parametric amplifier (NOPA) which is seeded by an fs NOPA with a spectral filter and pumped by a home-built second harmonic bandwidth compressor.

For the exited state FSRS data collection, the actinic pump is controlled by a motorized translation stage while the Raman pump and probe pulses remain temporally coincident. The three beams are focused on the protein sample solution (OD≈1/mm at 400 nm), continuously flowed through a 1-mm path length quartz cell to avoid thermal effect and provide a fresh spot for pulsed laser irradiation. While the Raman pump and actinic pump pulses are blocked after the sample, the transmitted probe beam carrying the collinear stimulated Raman signal goes through a pinhole and enters an imaging spectrograph (SP-2356, Princeton Instruments). The signal is then dispersed by a 1000 nm blaze, 600 grooves/mm grating in conventional FSRS setup (and a 500 nm blaze, 1200 grooves/mm grating in tunable FSRS) and imaged onto a front-illuminated 1340×100 CCD camera array system (PIXIS 100F; Princeton Instruments). At least 10 sets of excited state FSRS spectra are collected from –5 to 650 ps with various time steps as small as 50 fs. For each time delay point in each spectral data set, 1500 Raman spectra are collected and averaged. Therefore, for the final spectra presented (e.g., Figs. 2.2 and 2.4b as well as Fig. 2.6 in Section 2.7 below), each one data trace represents an average of at least 15000 experimental Raman spectra following photoexcitation. The flowing protein sample spot and incident laser fluctuations within the entire data scan could sporadically exert some small, unwanted effects but the extensive, periodic averaging of the same spectrum at a certain time delay after photoexcitation, being collected at various time during the experiment, could effectively cancel out most of the random noises. The ground state spectrum of the protein biosensor sample is also recorded periodically throughout the excited state data scan to monitor the protein sample and laser stability.[10,15,17,47] The UV-Vis spectra of the samples in buffer solution

are collected before and after each FSRS experiment to verify sample integrity (acceptable if the absorption peak intensity variation is within 10% after the entire FSRS experiment on protein samples which typically lasts for 1–2 hours).

2.4 Results and Discussion

2.4.1 Steady-state and time-resolved spectroscopic characterization of the protein chimera biosensor in solution

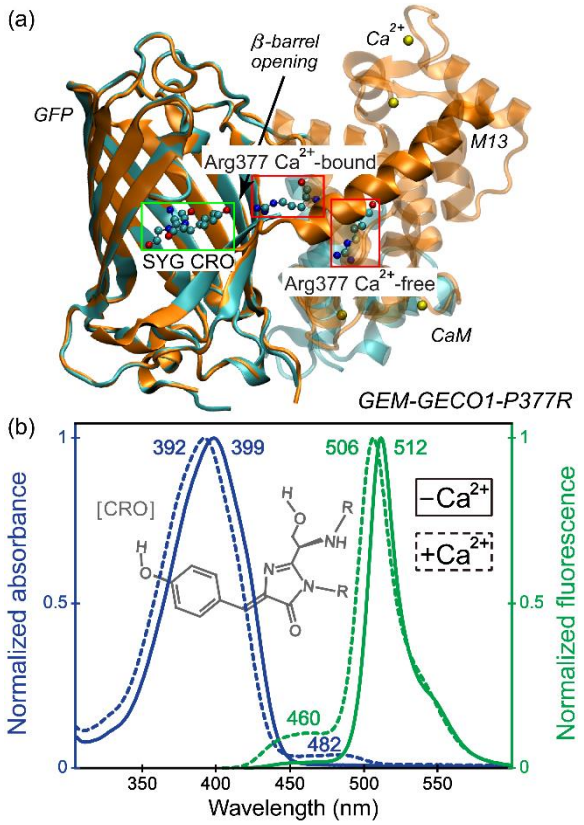

Fig. 2.1 Structure and optical properties of the GEM-GECO1-P377R biosensor. (a) The Ca^{2+}-free (cyan, PDB ID 3EKJ) and bound (orange, ID 3EVR) parent GCaMP2 structures modelling GFP chromophore [CRO] and CaM interfacial arginine residue highlighted by the coloured boxes. Four Ca^{2+} binding sites are shown. (b) Normalized absorption (blue) and emission (green) spectra of the biosensor in the Ca^{2+}-free (solid) and bound (dashed) state. The peak wavelengths are noted. The chemical structure of the SYG chromophore (gray) is depicted in the insert.

Based on the parent GCaMP crystal structures in the Ca^{2+}-free state,[22,23] Arg377 is located in the CaM domain, far from the β-barrel opening and the embedded GFP chromophore (Fig. 2.1a). The Ca^{2+}-free P377R biosensor resembles GEM-GECO1 with the absorption maximum at 399 nm and the fluorescence maximum at 512 nm (Fig. 2.1b). Upon Ca^{2+} binding, the peaks blue-shift to 392 and 506 nm, respectively, and the absorption shoulder at ~482 nm shows a slightly increased deprotonated chromophore (B) population in ground state (S_0). This blueshift of electronic features is commonly observed in GECOs,[7,17,20] indicating a stabilized chromophore in the Ca^{2+}-bound state with more electrostatic interactions including H-bonding. This creates a larger gap between S_0 to the first singlet excited state (S_1). Meanwhile, the 460 nm emission shoulder represents a subpopulation of protonated chromophore (A) that does not undergo ESPT. This sharp contrast to GEM-GECO1 confirms the importance of Pro377 for dominant blue emission with Ca^{2+} as the chromophore is effectively trapped in A*. With Arg377, such a trapping effect diminishes and the P377R mutant becomes excitation ratiometric. The resultant biosensor can achieve high imaging contrast by taking the ratio of excitation ratios (e.g., emission at 512 nm with excitations at 450 or 395 nm) of the Ca^{2+}-bound over the Ca^{2+}-free biosensor.[7]

Though the biosensors are thermally equilibrated prior to our spectroscopic measurement, the time-resolved FSRS setup allows the collection of the non-equilibrium chromophore conformational dynamics within the protein pocket following 400 nm photoexcitation. The 800 nm Raman pump is far away from the absorption peaks of both A and B states, so the S_0 Raman peaks are weak (see Fig. 2.2). However, the A* peaks are pre-resonantly enhanced due to the excited state absorption

band around ~900 nm in FPs, previously observed by transient absorption.[10,17,20] This makes it possible to record the excited state spectra without interference from the significant ground state bleaching, and track the evolution of excited state Raman modes during the A*→I* conversion as ESPT occurs.

The time-stacked spectral plot in Fig. 2.2 contains essential information about transient structural motions during ESPT, and the ~1180, 1545, and 1575 cm^{-1} vibrational bands are analysed to infer the photochemical reaction coordinate that governs biosensor function. The broad baselines for raw data (see Fig. 2.6 in Section 2.7) validate the enhanced S_1 Raman features, while weaker peaks upon Ca^{2+} binding may be due to lower sample concentration, laser pumping efficiency, and varied resonance Raman conditions of the altered chromophore environment. We therefore focus on the kinetic analysis of Fig. 2.2a and 2.2b individually. Moreover, in contrast to some other background subtraction methods assuming a one-to-one correspondence to transient absorption features or using complex filters that lead to sharp turns in spectral baselines,[24] our spline fitting method has been field proven to yield reliable results for wild-type GFP and the GEM-GECO1 biosensor,[10,17] which can be compared and cross-checked with the current results.

2.4.2 Frequency and intensity dynamics of vibrational marker bands reveal structural inhomogeneity affecting the ESPT pathways

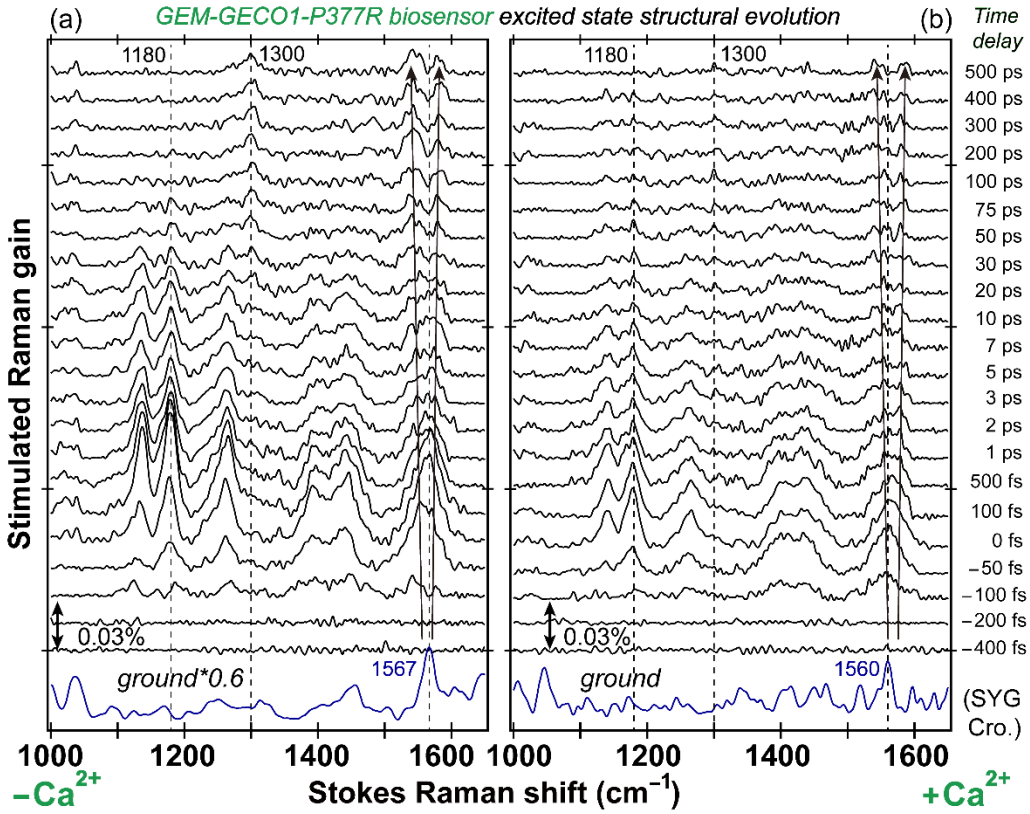

Fig. 2.2 Time-resolved excited state FSRS of GEM-GECO1-P377R biosensor in the (a) Ca^{2+}-free and (b) Ca^{2+}-bound state from –400 fs to 500 ps after 400 nm photoexcitation. The Raman pump is at 800 nm. The bottom blue trace is the S_0 spectrum with buffer subtracted. The black traces are the excited state spectra with both the ground state and buffer subtracted. The Ca^{2+}-free ground state is scaled by 0.6. The double-headed arrow shows the Raman gain of 0.03%. Peak frequency shifts below 1600 cm^{-1} are denoted by black arrows. Marker bands are labelled by dashed lines.

In the electronic ground state S_0, the 1567 cm^{-1} peak is attributed to the phenolic C=C and imidazolinone C=N stretching motions of the chromophore. After 400 nm photoexcitation, this mode shifts and significantly broadens, which can be fit with two

peaks and they gradually split with time in S_1. The lower-frequency mode redshifts while the higher-frequency mode blue-shifts (Fig. 2.3). From comparative Gaussian TD-DFT calculations[17,19,25] of the protonated and deprotonated chromophore to assign the observed frequency position and trend, besides the common C=C stretch, the 1545 cm^{-1} mode involves the imidazolinone ring C=N stretch while the 1575 cm^{-1} mode involves the C=O stretch (Table 2.1, see Section 2.7 below).

This latter mode is newly observed in this work but not in GEM-GECO1,[17] indicating that the excited state C=O stretching mode is enhanced and further redshifted from its S_0 peak location (~1660 cm^{-1}) due to the P377R mutation. The photoinduced electron redistribution could weaken the double bond and cause the mode frequency redshift. The modified local environment in S_1 may provide additional H-bonding to the C=O bond and also increase its electronic polarizability. After photoexcitation of the Ca^{2+}-free biosensor, this S_1 mode blue-shifts from ~1572 to 1584 cm^{-1} with a 37 ps time constant (Fig. 2.3b). In comparison, the Ca^{2+}-bound biosensor shows a similar blueshift from ~1571 to 1582 cm^{-1} with a 44 ps time constant. Both the trend and rate of the vibrational peak frequency change are consistent with an ESPT reaction that leads to deprotonation of the chromophore. The resultant migration of the negative charge back to the conjugated ring system (see the chromophore chemical structure in the Fig. 2.1b insert) could increase the C=O double bond character hence the apparent mode frequency blueshift. The ~1 ps dwell time for the exponential fit of the frequency dynamics is similar to other FP biosensors,[17,19-21] confirming that the blueshift is preceded by an initial structural "preparation" stage.[10,26] We consider that during the first 1 ps, the molecular system needs to move out of the FC region with significant

electron redistribution and small-scale nuclear motions, which lead to many competing factors and could complicate robust interpretation of the overall unchanged frequency dynamics that are experimentally observed. As I* accumulates, the mode frequency blueshift could involve vibrational cooling in I* state, typically on ps timescale.[27-30] Notably, the 1575 cm^{-1} mode intensity exemplifies complex dynamics (Fig. 2.7, see Section 2.7 below) which suggest contributions from both A* and I* states with overlapping vibrational peaks. The double-exponential decay time constants of ~600 fs (16% weight) and 32 ps (84%) are accompanied by a 35 ps rise in the Ca^{2+}-free P377R biosensor.

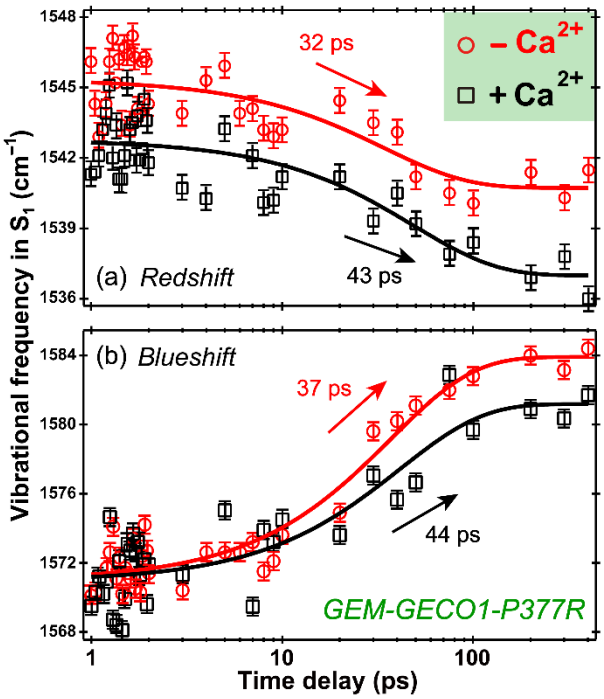

Fig. 2.3 Time-dependent S_1 vibrational frequency shift tracks transient conformational dynamics. (a) The redshift of the ~1545 cm^{-1} mode in the Ca^{2+}-free and bound P377R biosensor with the 32 and 43 ps time constant, respectively. (b) The blueshift of the ~1575 cm^{-1} mode in the Ca^{2+}-free and bound biosensor with the 37 and 44 ps time constant. The error bars (1 s.d.) are shown. The solid curves are exponential fits.

The lower-frequency mode of this peak doublet redshifts from 1545 to 1541 cm^{-1} and 1543 to 1537 cm^{-1} in the Ca^{2+}-free and bound biosensors, respectively (Fig. 2.3a). The redshift time constants from the least-squares exponential fit are 32 and 43 ps, which closely match the aforementioned blueshift time constants thus support a common structural dynamics origin.

For further corroboration, we analyze the 1180 cm^{-1} mode intensity dynamics which is also one of the most prominent spectral features in such FP biosensors (see raw data in Fig. 2.6, Section 2.7 below).[17,20] Notably, the Ca^{2+}-free biosensor exhibits

a double-exponential decay with 800 fs (60%) and 36 ps (40%) time constants (Fig. 2.4a) whereas the Ca^{2+}-bound biosensor exhibits a triple-exponential decay with time constants of 660 fs (59%), 16 ps (19%), and 90 ps (22%) (for a less satisfactory double-exponential fit, see Fig. 2.8, in section 2.7 below). The sub-ps time constants are attributed to FC dynamics.[10,17] The 36 ps time constant in the Ca^{2+}-free sample is due to ESPT reaction,[17] similar to the redshift and blueshift time constants in Fig. 2.3. In comparison, the two ps time constants of the Ca^{2+}-bound biosensor likely arise from two different ESPT pathways. The faster component is attributed to the slightly more deprotonated chromophore population in A* (see the steady-state absorption spectrum in Fig. 2.1b) and its stabilization by the positively charged Arg377. Our previous work[20,21] on an intensiometric FP biosensor G-GECO1.1 lends support in that a more deprotonated chromophore in the Ca^{2+}-bound state exhibits faster ESPT time constants. The longer, 90 ps time constant is due to the A* subpopulation that is more protonated in S_0, reflected by the blue-shifted electronic absorption peak at 392 nm. The apparent time constant of ~44 ps in Fig. 2.3 is largely consistent with a weighted average of these two distinct ps time constants. We note that these subpopulations arise from the multiple A species underneath a common electronic absorption band with a broad and asymmetric lineshape.

The structural inhomogeneity in the Ca^{2+}-bound biosensor is also inferred in peak widths (Fig. 2.2). The Ca^{2+}-free peaks are narrower than the Ca^{2+}-bound peaks in general. Because FSRS measures the ensemble average, the observed broader peaks indicate multiple subpopulations. For further comparison, we implement the wavelength-tunable FSRS by keeping the photoexcitation at 400 nm but tuning the

Raman pump to 553 nm.[20,31] Due to the pre-resonance match to the stimulated emission band, the I* modes are enhanced (Fig. 2.4b). Similar to the conventional FSRS data, the Ca^{2+}-free peaks are narrower and close in frequency (1336 and 1370 cm^{-1}) whereas the Ca^{2+}-bound peaks are broader and more separated (1331 and 1383 cm^{-1}) (see the peak width comparison from the least-squares fits in Fig. 2.9, and major Raman mode assignment in Table 2.2, in Section 2.7 below). This result indicates that the two ESPT pathways are largely independent of each other and the resultant transient I* modes do not mix on the ps timescale. Molecular dynamics simulations of GEX-GECO1, a similar excitation-ratiometric Ca^{2+} biosensor with an SYG chromophore and Arg377,[7] support the inhomogeneity seen in P377R biosensor due to two different O⋯O distances between the chromophore phenolic hydroxyl group and the adjacent Ser118 along the ESPT chain.[17,21] Further analysis of enhanced I* modes will yield insights into the ESPT reaction barrier crossing, vibrational cooling within the I* state, and energy relaxation back to the ground state.

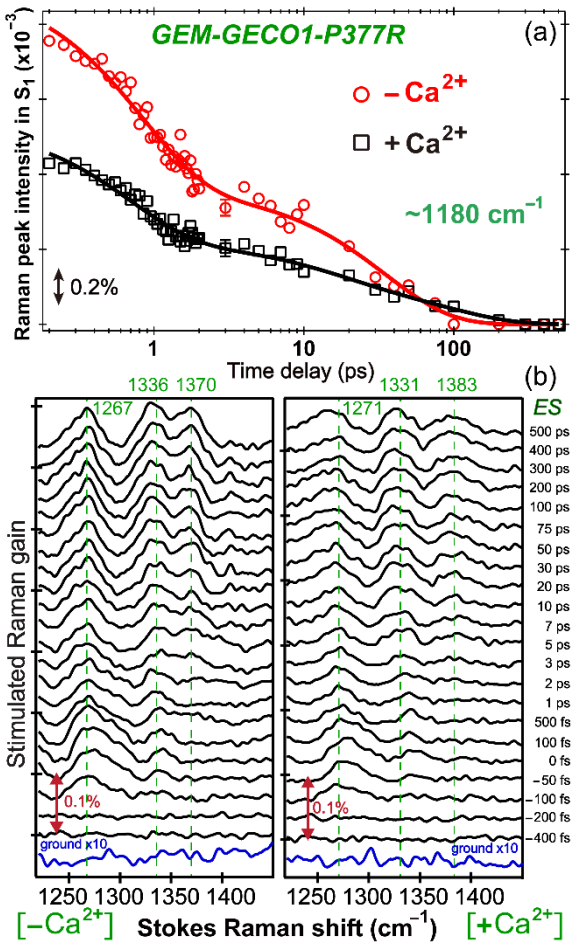

Fig. 2.4 Intensity dynamics of A* in contrast to I* modes enhanced by tunable FSRS methodology. (a) Integrated intensity plot of the ~1180 cm^{-1} marker bands in Ca^{2+}-free (red circles) and bound (black squares) P377R biosensor from 200 fs to 500 ps. (b) Time-resolved excited state FSRS data of the Ca^{2+}-free and bound biosensor from 1220—1450 cm^{-1} with the Raman pump tuned to 553 nm. The buffer and baseline-subtracted S_0 spectra (blue) are plotted at the bottom and multiplied by 10 to compare with the enhanced transient S_1 spectra (black).

It is clear from the stationary absorption spectrum (Fig. 2.1) that the P377R biosensor exhibits different ground state chromophore populations including the protonated A (major) and deprotonated B (minor) states. However, that is not the structural inhomogeneity which can be ascertained from the time-resolved FSRS (Figs.

2.2–2.4). In fact, because of the choice of actinic pump wavelength at 400 nm, our FSRS spectra only probe the excited state of the protonated species (A* state). In consequence, the above-mentioned A subpopulations govern the ESPT reaction pathways starting from photoexcitation time zero and are thus highly relevant for the biosensor function.

2.4.3 Vibrational intensity oscillations on ultrafast timescales dissect the ESPT reaction coordinates

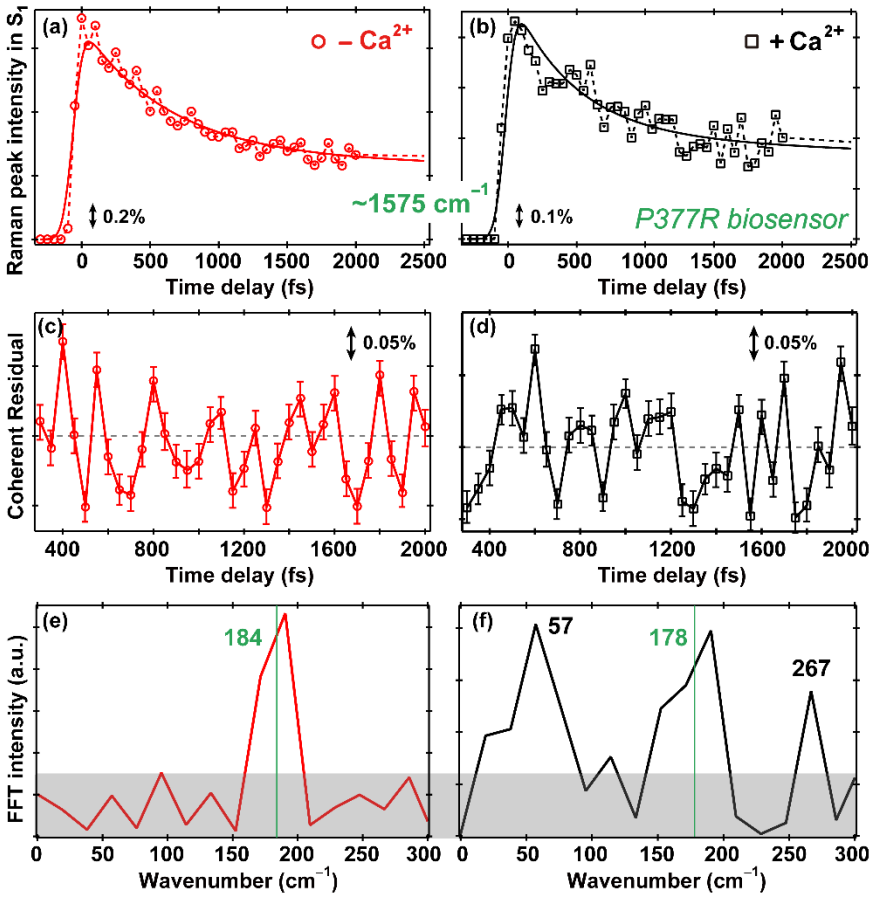

Fig. 2.5 Transient Raman intensity quantum beats probe low-frequency modulation modes. Integrated intensity dynamics of the ~1575 cm^{-1} mode in (a) Ca^{2+}-free and (b) Ca^{2+}-bound P377R biosensor with data in red circles and black squares, respectively. The corresponding Raman gain magnitude of 0.2% and 0.1% is denoted by the double-arrowed line. After removal of the incoherent rise and decay, e.g., red and black solid fit curves in (a) and (b), the coherent residuals within ~2 ps for (c) Ca^{2+}-free and (d) Ca^{2+}-bound biosensor are displayed. Clearer oscillations occur in (c). Error bars are shown (1 s.d.). The FFT results of the residuals yield dominant modulation modes below ~300 cm^{-1} in the (e) Ca^{2+}-free and (f) Ca^{2+}-bound P377R biosensor, with a conserved low-frequency mode at ~180 cm^{-1} . The FFT experimental noise level is indicated by gray shades.

One of the unique resolving powers of excited state FSRS is the direct observation of vibrational quantum beats.[10,13,32-34] Because the Ca^{2+}-free GEM-GECO1 exhibits a dominant 174 cm^{-1} phenolic ring rocking mode that gates ESPT by modulating the distance between proton donor (chromophore hydroxyl) and acceptor (e.g., bridging water molecules), we expect the Ca^{2+}-free P377R biosensor to maintain this pronounced oscillation because the mutation site is far away from the chromophore pocket (Fig. 2.1a). Indeed, the 1265 cm^{-1} C–O stretch and 1575 cm^{-1} C=C/C=O stretch mode intensities exhibit out-of-phase oscillations that yield a ~184 cm^{-1} mode after fast Fourier transform (FFT) analysis (Fig. 2.5e). The frequency difference from the 174 cm^{-1} mode in GEM-GECO1 may be due to some long-range interactions in the protein mutant. In contrast, the Ca^{2+}-bound P377R biosensor exhibits weaker and less clear oscillatory patterns with low-frequency modulation modes retrieved at 57, 178, and 267 cm^{-1} (Fig. 2.5f). The 57 and 267 cm^{-1} modes have phenol ring wagging characters as corroborated by DFT calculations (see below). These modes differ from those in the Ca^{2+}-bound GEM-GECO1 wherein the Pro377 residue inhibits ESPT and leads to significant blue fluorescence,[17] which indicates that P377R not only allows the biosensor green fluorescence, it also provides (1) an increased structural inhomogeneity due to less solvent access and less averaging in the chromophore vicinity,[35] (2) multiple ESPT pathways for the chromophore to lose its proton as evidenced by the spectral data analysis of Figs. 2.2-2.5, and (3) a more hydrophilic environment with stronger H-bonds involving the positively charged Arg377 residue to help stabilize the deprotonated FP chromophore after ESPT.[20,36]

Notably, the FFT analysis of the Ca^{2+}-free P377R biosensor reveals only one dominant ~184 cm^{-1} mode, which closely matches the chromophore phenol ring rocking mode at ~174 cm^{-1} mode that we observed in the Ca^{2+}-free GEM-GECO1 biosensor (i.e., with the Pro377 residue distant from the GFP chromophore pocket, see structural constraints in Fig. 2.1a).[17] Since the P377R mutation is far away from the chromophore, it exerts little effect on the local environment around the SYG chromophore, leading to the survival of this functional low-frequency mode with a similar ESPT time constant (~30 ps in the Ca^{2+}-free GEM-GECO1 and 36 ps in the Ca^{2+}-free P377R). In contrast, the FFT analysis of the Ca^{2+}-bound P377R yields a more complex pattern with three low-frequency modes below 300 cm^{-1}. Besides the 178 cm^{-1} mode that is largely conserved and confirms the importance of this in-plane phenol ring rocking motion, the 57 and 267 cm^{-1} modes both have phenol ring out-of-plane wagging character based on DFT calculations in Gaussian.[25] This result indicates that as the Ca^{2+}-bound CaM subunit moves closer, shields the nearby GFP β-barrel opening and increases the inhomogeneity of chromophore pocket (Fig. 2.1a), additional ESPT pathways are opened because a variety of low-frequency modes are activated and further involved in the vibrational anharmonic coupling matrix.[9,37-39] Because the chromophore conformational states govern the potential energy surface from the electronic ground to excited state, different low-frequency modes are coupled to photoexcitation (starting from the FC region) to various degrees. Their activity in relation to the other anharmonically coupled vibrational motions (e.g., the 1575 cm^{-1} mode in Fig. 2.5) could act as a molecular gate[10,17,34] and contribute to the observed multiple ESPT rates in the Ca^{2+}-bound biosensor.

In other words, the interplay between the chromophore photoacidity[16,40,41] and the protein local environment particularly the H-bonding network[42-44] determines the dominant photoexcitation energy dissipation pathways along the characteristic vibrational coordinates, out of the FC region, and toward the fluorescent state in these FP-based biosensors.

2.4.4 Comparative analysis to previous FP biosensors and within the same biosensor yields key mechanistic underpinnings

A general rule of thumb is that fundamental knowledge could be effectively gained if only one parameter is changed that leads to an observed functionality change. The direct comparison of current work to our previous report[17] on GEM-GECO1 with an identical SYG chromophore provides such a rare opportunity to elucidate the fluorescence modulation mechanism affected by just one strategic interfacial residue between CaM (Ca^{2+}-sensing domain) and GFP (fluorescence domain). We recognize that a multitude of effects could be introduced by one amino acid mutation, from the short-range to long-range interactions, however, we emphasize that this specific mutation close to the protein active site is key to establish the biosensor structure-function relationship because the interfacial residue at position 377 is in close proximity to the embedded chromophore. Our results reveal why GEM-GECO1 is dual-emission ratiometric whereas the P377R mutant is effectively tuned to become single-emission excitation ratiometric, which substantiate the originality and significance of this spectroscopic work.

In a previous report on a green intensiometric G-GECO1.1 biosensor[20] we correlated the consumption of reactant and generation of product state on the tens of ps timescales to a common photochemical reaction coordinate. Similarly, the concomitant observation of A* peak decay and I* peak rise (Fig. 2.4) in the P377R biosensor well supports the assignment of vibrational dynamics to an ESPT process. Meanwhile, the least-squares fit of the peak frequency shift is considered a reliable way to track the ultrafast photochemical reaction progress particularly when the potentially overlapping Raman modes are along the ESPT reaction coordinate. Alternatively, we can model the observed broad Raman bands near 1545 or 1575 cm^{-1} with two adjacent peaks assigned to A* and I* and fit the apparent frequency shift as a gradual exchange of two distinctive spectral patterns. However, the experimental signal-to-noise ratio and inevitable assumption of the individual peak width could hinder quantitative analysis while the accuracy for such modelling may not surpass the direct fit of peak centre frequency shift.[10,13,45] Therefore, the ensemble nature of FSRS experiments requires a consistent, multifaceted approach to dissect spectral data and deduce reaction mechanisms: the multiple mode frequency dynamics in Fig. 2.3 need to be compared and discussed in concert with the intensity dynamics of other modes in Fig. 2.4 so we can firmly attribute the retrieved time constants to the ESPT reaction along with distinguishable conformational states.

Based on these recent findings, we expect that an increase of the hydrophilicity of the protein chromophore pocket with an extended and more flexible H-bonding network could reduce the specific A* subpopulation with the ~90 ps ESPT time constant. The other A* subpopulation that yields the 460 nm emission shoulder band

in Fig. 2.1b (i.e., incapable of undergoing ESPT reaction) could also be decreased. In consequence, the overall fluorescence quantum yield of the Ca^{2+}-bound P377R biosensor can be effectively improved upon 400 nm photoexcitation with the resultant improved biosensor brightness and sensitivity defined as the ratio of excitation ratios for Ca^{2+} sensing.[7]

2.5 Conclusion

In this work, we have developed and implemented the wavelength-tunable excited state FSRS to elucidate the structural dynamics basis for the fluorescence modulation of a single-site P377R mutant of the emergent GEM-GECO1 calcium biosensor. This contribution represents the first time that a targeted single mutant of a functional biosensor is studied by an advanced time-resolved vibrational spectroscopic toolset, especially after the steady-state electronic spectroscopy shows a noticeable difference in its emission properties from the parent biosensor. The transient Raman modes following 400 nm photoexcitation report on the characteristic ESPT time constants of 36 ps in the Ca^{2+}-free biosensor versus 16, 90 ps in the Ca^{2+}-bound state. This covert structural inhomogeneity is a direct consequence of positioning a positively charged residue (like arginine) close to the cpGFP chromophore in response to the Ca^{2+}-binding-induced conformational change at the nearby CaM domain. The altered ESPT pathways based on different H-bonding configurations govern the functionality change from a green-blue emission ratiometric biosensor (GEM-GECO1) to a green excitation ratiometric biosensor (GEM-GECO1-P377R) for Ca^{2+} imaging. Such a quantitative examination of the molecular mechanism provides previously unavailable

knowledge about this emerging calcium biosensor family, particularly regarding the intrinsic conformational states and molecular motions of the functional chromophore.

Furthermore, from the integrated Raman peak intensity oscillations, a chromophore in-plane ring rocking mode at ~180 cm^{-1} is found to dominate in the Ca^{2+}-free biosensor but is joined by two other out-of-plane low-frequency modes in gating the multidimensional ESPT reaction coordinate upon Ca^{2+} binding. We expect that such targeted mutation(s) around the protein active site, in conjunction with the genetic code expansion methods to incorporate various non-canonical amino acids[48,49] as well as chemical modification of the chromophores,[41,50] can efficiently translate the rational design principles uncovered by ultrafast Raman spectroscopy into better FP biosensors for advanced bioimaging applications.

2.6 References

1 O. Shimomura, *FEBS Lett.*, 1979, **104**, 220-222.

2 M. Chalfie, Y. Tu, G. Euskirchen, W. W. Ward and D. C. Prasher, *Science*, 1994, **263**, 802-805.

3 R. Y. Tsien, *Annu. Rev. Biochem.*, 1998, **67**, 509-544.

4 H.-w. Ai, K. L. Hazelwood, M. W. Davidson and R. E. Campbell, *Nat. Methods*, 2008, **5**, 401-403.

5 G. Jung, (Ed.), *Fluorescent Proteins II: Application of Fluorescent Protein Technology*, Springer-Verlag, Berlin Heidelberg, 2012.

6 A. Miyawaki, J. Llopis, R. Heim, J. M. McCaffery, J. A. Adams, M. Ikura and R. Y. Tsien, *Nature*, 1997, **388**, 882-887.

7 Y. Zhao, S. Araki, J. Wu, T. Teramoto, Y.-F. Chang, M. Nakano, A. S. Abdelfattah, M. Fujiwara, T. Ishihara, T. Nagai and R. E. Campbell, *Science*, 2011, **333**, 1888-1891.

8 R. J. D. Miller, *Science*, 2014, **343**, 1108-1116.

9 R. M. Hochstrasser, *Proc. Natl. Acad. Sci. U.S.A.*, 2007, **104**, 14190-14196.

10 C. Fang, R. R. Frontiera, R. Tran and R. A. Mathies, *Nature*, 2009, **462**, 200-204.

11 H. Kuramochi, S. Takeuchi and T. Tahara, *J. Phys. Chem. Lett.*, 2012, **3**, 2025-2029.

12 J. T. M. Kennis, I. H. M. van Stokkum, D. S. Peterson, A. Pandit and R. M. Wachter, *J. Phys. Chem. B*, 2013, **117**, 11134-11143.

13 D. P. Hoffman and R. A. Mathies, *Acc. Chem. Res.*, 2016, **49**, 616-625.

14 D. W. McCamant, P. Kukura, S. Yoon and R. A. Mathies, *Rev. Sci. Instrum.*, 2004, **75**, 4971-4980.

15 W. Liu, F. Han, C. Smith and C. Fang, *J. Phys. Chem. B*, 2012, **116**, 10535-10550.

16 W. Liu, Y. Wang, L. Tang, B. G. Oscar, L. Zhu and C. Fang, *Chem. Sci.*, 2016, **7**, 5484-5494.

17 B. G. Oscar, W. Liu, Y. Zhao, L. Tang, Y. Wang, R. E. Campbell and C. Fang, *Proc. Natl. Acad. Sci. U.S.A.*, 2014, **111**, 10191-10196.

18 D. Zhong, A. Douhal and A. H. Zewail, *Proc. Nat. Acad. Sci. U.S.A.*, 2000, **97**, 14056-14061.

19 Y. Wang, L. Tang, W. Liu, Y. Zhao, B. G. Oscar, R. E. Campbell and C. Fang, *J. Phys. Chem. B*, 2015, **119**, 2204-2218.

20 L. Tang, W. Liu, Y. Wang, Y. Zhao, B. G. Oscar, R. E. Campbell and C. Fang, *Chem. Eur. J.*, 2015, **21**, 6481-6490.

21 L. Tang, W. Liu, Y. Wang, L. Zhu, F. Han and C. Fang, *J. Phys. Chem. Lett.*, 2016, **7**, 1225-1230.

22 J. Akerboom, J. D. V. Rivera, M. M. R. Guilbe, E. C. A. Malavé, H. H. Hernandez, L. Tian, S. A. Hires, J. S. Marvin, L. L. Looger and E. R. Schreiter, *J. Biol. Chem.*, 2009, **284**, 6455-6464.

23 J. Akerboom, T.-W. Chen, T. J. Wardill, L. Tian, J. S. Marvin, S. Mutlu, N. C. Calderón, F. Esposti, B. G. Borghuis, X. R. Sun, A. Gordus, M. B. Orger, R. Portugues, F. Engert, J. J. Macklin, A. Filosa, A. Aggarwal, R. A. Kerr, R. Takagi, S. Kracun, E. Shigetomi, B. S. Khakh, H. Baier, L. Lagnado, S. S.-H. Wang, C. I. Bargmann, B. E. Kimmel, V. Jayaraman, K. Svoboda, D. S. Kim, E. R. Schreiter and L. L. Looger, *J. Neurosci.*, 2012, **32**, 13819-13840.

24 M. Quick, A. L. Dobryakov, S. A. Kovalenko and N. P. Ernsting, *J. Phys. Chem. Lett.*, 2015, **6**, 1216-1220.

25 M. J. Frisch, G. W. Trucks, H. B. Schlegel, G. E. Scuseria, M. A. Robb, J. R. Cheeseman, G. Scalmani, V. Barone, B. Mennucci, G. A. Petersson, H. Nakatsuji, M. Caricato, X. Li, H. P. Hratchian, A. F. Izmaylov, J. Bloino, G. Zheng, J. L. Sonnenberg, M. Hada, M. Ehara, K. Toyota, R. Fukuda, J. Hasegawa, M. Ishida, T. Nakajima, Y. Honda, O. Kitao, H. Nakai, T. Vreven, J. J. A. Montgomery, J. E. Peralta, F. Ogliaro, M. Bearpark, J. J. Heyd, E. Brothers, K. N. Kudin, V. N. Staroverov, R. Kobayashi, J. Normand, K. Raghavachari, A. Rendell, J. C. Burant, S. S. Iyengar, J. Tomasi, M. Cossi, N. Rega, J. M. Millam, M. Klene, J. E. Knox, J. B. Cross, V. Bakken, C. Adamo, J. Jaramillo, R. Gomperts, R. E. Stratmann, O. Yazyev, A. J. Austin, R. Cammi, C. Pomelli, J. W. Ochterski, R. L. Martin, K. Morokuma, V. G. Zakrzewski, G. A. Voth,

P. Salvador, J. J. Dannenberg, S. Dapprich, A. D. Daniels, Ö. Farkas, J. B. Foresman, J. V. Ortiz, J. Cioslowski and D. J. Fox, *Gaussian 09, Revision B.1*, Gaussian, Inc., Wallingford, CT, 2009.

26 F. Han, W. Liu and C. Fang, *Chem. Phys.*, 2013, **422**, 204-219.

27 T. Lian, B. Locke, Y. Kholodenko and R. M. Hochstrasser, *J. Phys. Chem.*, 1994, **98**, 11648-11656.

28 P. Hamm, S. M. Ohline and W. Zinth, *J. Chem. Phys.*, 1997, **106**, 519-529.

29 Y. Mizutani and T. Kitagawa, *Science*, 1997, **278**, 443-446.

30 S. A. Kovalenko, R. Schanz, H. Hennig and N. P. Ernsting, *J. Chem. Phys.*, 2001, **115**, 3256-3273.

31 L. Zhu, W. Liu and C. Fang, *Appl. Phys. Lett.*, 2014, **105**, 041106.

32 A. H. Zewail, *Femtochemistry: Ultrafast Dynamics of the Chemical Bond*, World Scientific, Singapore, 1994.

33 D. B. Turner, K. E. Wilk, P. M. G. Curmi and G. D. Scholes, *J. Phys. Chem. Lett.*, 2011, **2**, 1904-1911.

34 P. J. M. Johnson, A. Halpin, T. Morizumi, V. I. Prokhorenko, O. P. Ernst and R. J. D. Miller, *Nature Chem.*, 2015, **7**, 980-986.

35 C. Fang, A. Senes, L. Cristian, W. F. DeGrado and R. M. Hochstrasser, *Proc. Natl. Acad. Sci. U.S.A.*, 2006, **103**, 16740-16745.

36 X. Shi, P. Abbyad, X. Shu, K. Kallio, P. Kanchanawong, W. Childs, S. J. Remington and S. G. Boxer, *Biochemistry*, 2007, **46**, 12014-12025.

37 M. H. Vos, F. Rappaport, J.-C. Lambry, J. Breton and J.-L. Martin, *Nature*, 1993, **363**, 320-325.

38 Q. Wang, R. W. Schoenlein, L. A. Peteanu, R. A. Mathies and C. V. Shank, *Science*, 1994, **266**, 422-424.

39 L. Zhu, J. T. Sage and P. M. Champion, *Science*, 1994, **266**, 629-632.

40 R. Simkovitch, S. Shomer, R. Gepshtein and D. Huppert, *J. Phys. Chem. B*, 2015, **119**, 2253-2262.

41 S. P. Laptenok, J. Conyard, P. C. B. Page, Y. Chan, M. You, S. R. Jaffrey and S. R. Meech, *Chem. Sci.*, 2016, **7**, 5747-5752.

42 A. Douhal, F. Lahmani and A. H. Zewail, *Chem. Phys.*, 1996, **207**, 477-498.

43 M. Rini, B.-Z. Magnes, E. Pines and E. T. J. Nibbering, *Science*, 2003, **301**, 349-352.

44 E. R. Young, J. Rosenthal, J. M. Hodgkiss and D. G. Nocera, *J. Am. Chem. Soc.*, 2009, **131**, 7678-7684.

45 Y.-C. Wu, B. Zhao and S.-Y. Lee, *J. Chem. Phys.*, 2016, **144**, 054104.

46 W. Wang, W. Liu, I.-Y. Chang, L. A. Wills, L. N. Zakharov, S. W. Boettcher, P. H.-Y. Cheong, C. Fang and D. A. Keszler, *Proc. Natl. Acad. Sci. U.S.A.*, 2013, **110**, 18397-18401.

47 R. R. Frontiera, C. Fang, J. Dasgupta and R. A. Mathies, *Phys. Chem. Chem. Phys.*, 2012, **14**, 405-414.

48 L. Wang, J. M. Xie, A. A. Deniz and P. G. Schultz, *J. Org. Chem.*, 2003, **68**, 174-176.

49 J. C. Peeler and R. A. Mehl, in *Unnatural Amino Acids*, eds. L. Pollegioni and S. Servi, Humana Press, 2012, ch. 8, pp. 125-134.

50 C. L. Walker, K. A. Lukyanov, I. V. Yampolsky, A. S. Mishin, A. S. Bommarius, A. M. Duraj-Thatte, B. Azizi, L. M. Tolbert and K. M. Solntsev, *Curr. Opin. Chem. Biol.*, 2015, **27**, 64-74.

2.7 Supplemental Information

Fluorescent proteins and their derivatives are critically important in the bioimaging field and life sciences. The elucidation of the underlying conformational dynamics of a recently developed Ca^{2+} biosensor GEM-GECO1-P377R (Fig. 2.1a) involves transient Raman modes in the electronic excited state,[1,2] exhibiting distinct frequency and intensity evolution on the crucial femtosecond to picosecond timescales (Figs. 2.2–2.5) before the fluorescence events. As a result, we can mechanistically understand green fluorescence (i.e., biosensor functionality) in both the Ca^{2+}-free and bound state of the biosensor and how the pertaining excited state proton transfer (ESPT) reaction progresses on the intrinsic molecular timescales. In particular, we have implemented the emergent wavelength-tunable FSRS methodology to dissect the intricate H-bonding network (e.g., ESPT chain) around the chromophore,[3-6] in systematic comparison to other functional calcium biosensors studied by FSRS in our laboratory.[2,7,8] The comparative analysis and comprehension of crucial and multidimensional photochemical reaction coordinates about how the chromophore responds to light and transfers the proton forms *the structural dynamics basis* for the biosensor fluorescence, and in particular, the fluorescence modulation in response to Ca^{2+} binding. In contrast to more technically demanding time-resolved electron or X-ray diffraction to capture chemistry in action,[9] our line of inquiry on a table-top optical apparatus is filling a current knowledge gap (besides practical applications) in understanding the structural motions that power or accompany molecular fluorescence (i.e., an intrinsic ultrafast photochemical event). This work thus opens the door to targeted mutation(s) at strategic site(s) to achieve the desired biofunctions,

transcending the boundaries of modern physical chemistry, biophysics and biochemistry, protein engineering, nonlinear optics, spectroscopy, and biological imaging.

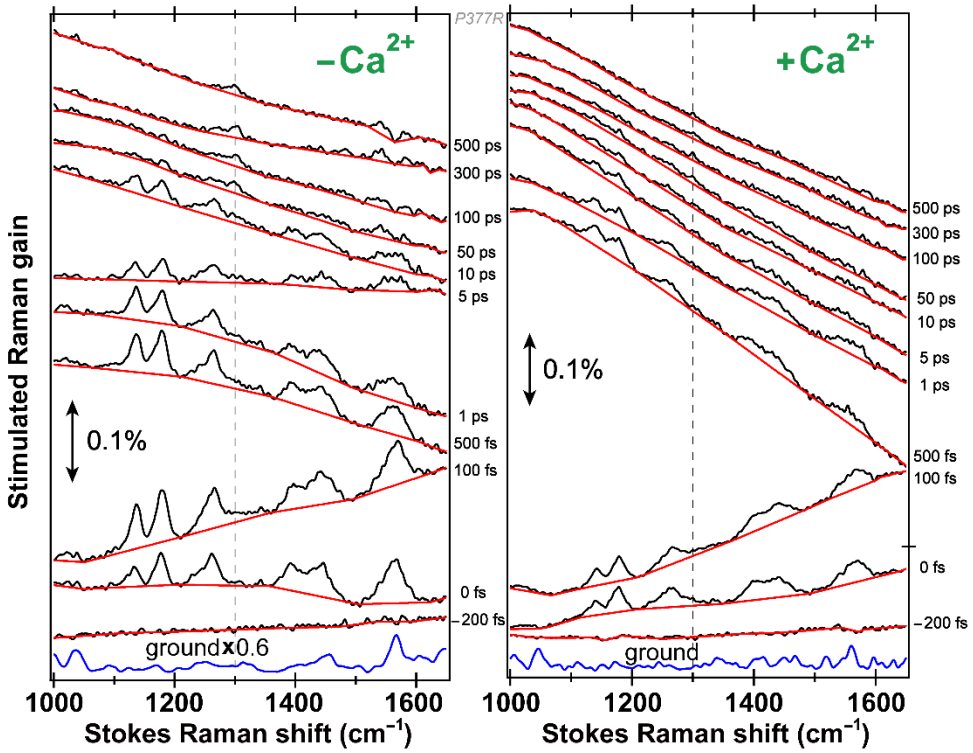

Fig. 2.6. Time-resolved excited state FSRS spectra of the Ca^{2+}-free (left) and Ca^{2+}-bound (right) GEM-GECO1-P377R biosensor with the spline baseline drawn for each time-delayed trace following 400 nm photoexcitation. Representative *raw experimental data* traces with evolving Raman peaks (black) are shown between –200 fs and 500 ps, while the baselines (red) are clearly broad and featureless. The double-arrowed vertical line denotes the stimulated Raman gain magnitude of 0.1%. The ground-state spectra (blue) are plotted at the bottom for comparison. The dashed lines highlight the emergence of transient I* peaks at ~1300 cm^{-1} on the ps timescale.

We note that the Raman peak intensity in the Ca^{2+}-bound biosensor is smaller than its Ca^{2+}-free counterpart, which may be due to some difference in sample

concentration, laser power, resonance conditions,[10] electronic polarizability,[11] and photoexcitation pumping efficiency.[1,12] Therefore, instead of directly comparing peak intensities, we focus on analyzing the vibrational dynamics in each sample and retrieve the time constants to infer the effect of Ca^{2+} binding.

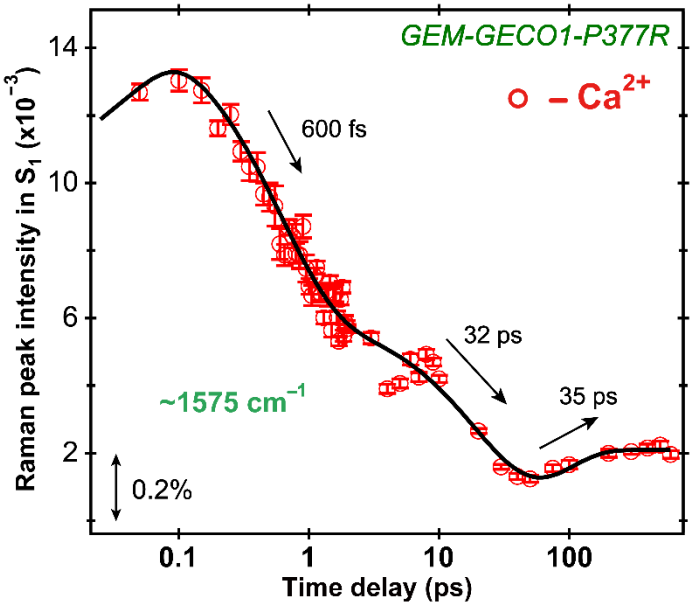

Fig. 2.7. Time-dependent integrated intensity of the ~1575 cm^{-1} mode in the Ca^{2+}-free P377R biosensor after 400 nm photoexcitation (an independent dataset to check the experimental reproducibility). The double-arrowed line indicates the stimulated Raman gain magnitude of 0.2%. The retrieved decay and rise time constants from the least-squares fit (black solid curve) are noted against the logarithmic time delay axis. The error bars (1 s.d.) are shown for all the time-dependent data points (red circles).

The initial 600 fs peak intensity decay is attributed to the protonated chromophore A* wavepackets moving out of the Franck-Condon region, which likely results in a rapid change of the resonance Raman conditions and the electronic polarizability change.[1,2] Because we least-squares fit the data trace from a common time zero, the 32

ps decay dynamics and the 35 ps rise dynamics can be associated with an ESPT reaction leading to the A* depletion and the concomitant deprotonated I* accumulation, respectively. These characteristic time constants match well with the ultrafast vibrational frequency dynamics shown in Fig. 2.3 (Section 2.4).

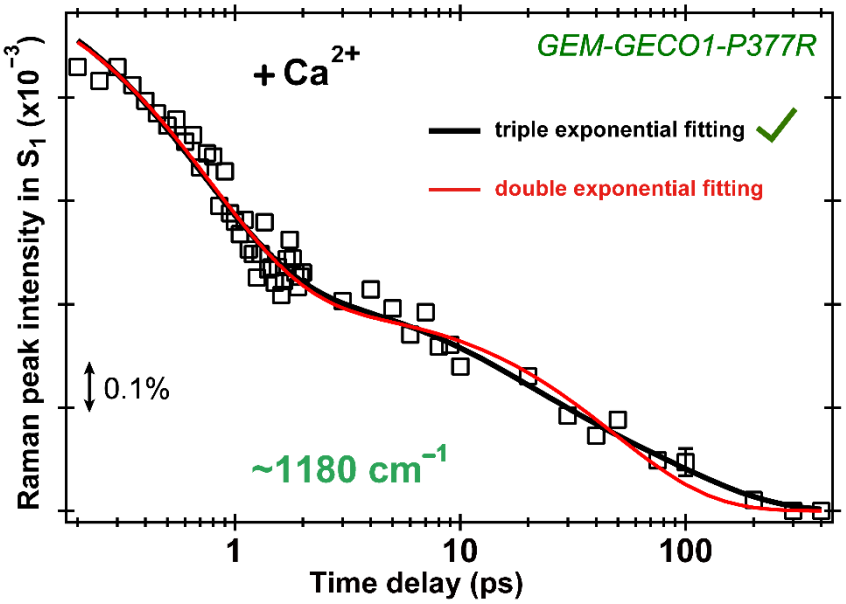

Fig. 2.8. Time-dependent integrated intensity of the ~1180 cm^{-1} mode in the Ca^{2+}-bound P377R biosensor after 400 nm photoexcitation. The data points (black squares) are overlaid with the triple-exponential (black solid curve) and double-exponential (red solid curve) least-squares fit from 200 fs to 400 ps (shown in logarithmic scales along the time axis). The double-arrowed line indicates the stimulated Raman gain magnitude of 0.1%. A representative error bar is shown at 100 ps time delay (with high signal-to-noise ratio), and the red curve is outside the error bar.

We select the 1180 cm^{-1} mode, one of the strongest Raman peaks in Figs. 2.2 and 2.6, to perform detailed analysis and to further minimize the effect of small uncertainties that could be associated with any kind of background subtraction method. The semi-logarithmic time-dependent peak intensity plot exhibits clear difference in

the fit and the triple-exponential fit better matches the spectral data particularly for the later dynamics part beyond ~1 ps. This result is consistent with the largely conserved nature of initial A* structural dynamics that prepare the system for undergoing the ESPT reaction on the ps timescale, which in this case, consists of two pathways with the exponential time constants of 16 and 90 ps (see Section 2.4 above) to reach I*.

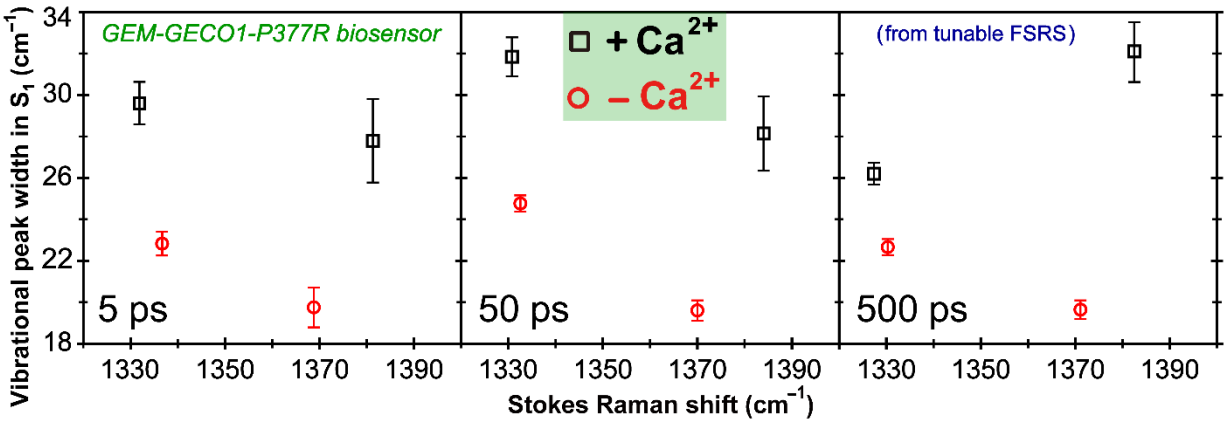

Fig. 2.9. Comparison of two excited state vibrational marker bands between the Ca^{2+}-free (red circles) and Ca^{2+}-bound (black squares) GEM-GECO1-P377R biosensors after 400 nm photoexcitation. The Raman pump is at 553 nm and the data points are selected from the time-resolved spectral traces in Fig. 4b. The representative time delay of 5, 50, and 500 ps is noted in each panel of the figure. The error bars (1 s.d.) for the least-squares fit peak widths (full width at half maximum of the Raman band, see the vertical axis) are shown. The horizontal axis records the Raman shift on the Stokes side in the spectral region of interest (in cm^{-1} unit).

Notably, the lower-frequency peak arises from a mixture of A* and I* modes as we observe the complex intensity dynamics starting from around the photoexcitation time zero in Fig. 2.4b. The associated peak width shows an interesting rise-drop pattern on the ps timescale as ESPT converts A* to I* species. In contrast, the higher-frequency

mode emerges after ~2 ps and is likely attributed to an I* peak as a result of the ESPT reaction. In general, the Ca^{2+}-bound biosensor displays broader and further separated Raman peaks in this spectral region (ca. 1320—1400 cm^{-1}) than the Ca^{2+}-free biosensor (see Section 2.4 for discussion and implications). The time-resolved peak frequency redshift and blueshift of the lower and higher frequency Raman band, respectively, is also notable in this figure (from the left to right panel).

Table 2.1. Representative ground and excited state vibrational frequencies of P377R biosensor

	Expt. freq. [a] (cm^{-1})	Calc. freq. [b] (cm^{-1})	Major peak assignment
Ground state (S_0)	1567/1560	1571 (1552)	Phenolic ring C=C stretching and imidazolinone ring C=N stretching
Excited state (S_1)	1545 (1541) / 1543 (1537)	1511 (1502)	Phenolic COH rocking with phenolic ring C=C stretching, and imidazolinone ring C=N stretching
	1572 (1584) / 1571 (1582)	1587 (1619)	Phenolic ring C=C stretching and imidazolinone ring C=O stretching

[a] Observed Raman frequency of the ground and excited state peaks of P377R using an 800 nm Raman pump. In the excited state S_1 as mode frequency shift occurs (see Fig. 2.3), the average peak frequency from ca. 1—3 ps is followed by the average frequency from ca. 100—500 ps in parentheses. The Ca^{2+}-free and bound biosensor peak frequencies are separated by "/".

[b] The ground state calculations are performed using density functional theory (DFT) RB3LYP with 6-31G+(d,p) basis sets on the protonated and (deprotonated) chromophore *in vacuo* in Gaussian.[13] The excited state calculations are performed using the time-dependent DFT (TD-DFT) RB3LYP and the same basis sets (more related calculation results and comparisons can be found in our previous reports),[2,7,8,14] with the deprotonated chromophore results in parentheses. The frequency scaling factor is 0.96. Note that the observed frequency change matches the calculated redshift of the 1571 cm^{-1} mode in S_0 and 1511 cm^{-1} mode in S_1, as well as the blueshift of the 1587 cm^{-1} mode in S_1. This multi-mode correlation supports the assignment of the photochemical event revealed by FSRS (Figs. 2.2 and 2.4b) to the ESPT reaction which induces the chromophore deprotonation.

To assess the effect of ring twisting motion that makes the chromophore lose its two-ring coplanarity, we also perform a series of DFT calculations on the protonated chromophore in the electronic ground state.[8] The frequency scaling factor is 0.96. The phenolic ring C=C stretching and imidazolinone ring C=N stretching mode frequency redshifts from ~1571, 1569 to 1567 cm^{-1} as the dihedral angle around the bridge C=C bond (i.e., adjacent to the imidazolinone ring, see Fig. 2.1b insert for the chromophore structure depiction) is fixed and varied from 0º, 20º to 40º. This trend is consistent with the observed redshift of the ~1545 cm^{-1} mode in S_1 (Fig. 2.3a), which suggests that ring twisting may accompany the ESPT reaction.[8,15,16]

Table 2.2. Mode assignment for the representative excited state vibrational peaks in tunable FSRS of the GEM-GECO1-P377R biosensor aided by quantum calculations

Expt. freq. (cm^{-1}) [a]	Calc. freq. (cm^{-1}) [b]	Major peak assignment
1267/1271	1286 (1289)	Phenolic C–O stretching, ring H rocking with asymmetric ring C=C stretching, and imidazolinone ring breathing
1336/1331	1343 (1348)	Bridge and phenol ring H out-of-phase rocking, imidazolinone ring C–N stretching
1370/1383	1393 (1390)	Phenolic C–O stretching, bridge C–C (close to phenol ring) stretching, bridge and phenol ring H in-phase rocking with imidazolinone ring C–N stretching

[a] Observed Raman frequency of the excited state peaks of the P377R biosensor using a 553 nm Raman pump. We average the peak frequencies from ca. 1—500 ps in Fig. 2.4b to highlight the I* contribution as a result of the chromophore deprotonation. The Ca^{2+}-free and bound biosensor peak frequencies are separated by "/".

[b] The excited state vibrational frequencies of a geometrically optimized protonated and (deprotonated) SYG chromophore are calculated using TD-DFT RB3LYP 6-31G+(d,p) *in vacuo* in Gaussian. The frequency scaling factor is 0.96. Tunable FSRS enhances the deprotonated chromophore more than the protonated chromophore,[8] and we expect that after photoexcitation, the transient A* features in Fig. 4b have partially deprotonated character prior to ~1 ps, followed by the I* species being accumulated on the ps timescale as a result of the ESPT reaction inside the biosensor protein pocket. The level of mismatch between the experimental and calculated peak frequency trend associated with chromophore deprotonation may arise from the incomplete modelling of inhomogeneous subpopulations which adopt non-uniform structural configurations.

2.8 Supplemental References

1 C. Fang, R. R. Frontiera, R. Tran and R. A. Mathies, *Nature*, 2009, **462**, 200-204.

2 B. G. Oscar, W. Liu, Y. Zhao, L. Tang, Y. Wang, R. E. Campbell and C. Fang, *Proc. Natl. Acad. Sci. U.S.A.*, 2014, **111**, 10191-10196.

3 M. Chattoraj, B. A. King, G. U. Bublitz and S. G. Boxer, *Proc. Natl. Acad. Sci. U.S.A.*, 1996, **93**, 8362-8367.

4 K. Brejc, T. K. Sixma, P. A. Kitts, S. R. Kain, R. Y. Tsien, M. Ormö and S. J. Remington, *Proc. Natl. Acad. Sci. U.S.A.*, 1997, **94**, 2306-2311.

5 S. R. Meech, *Chem. Soc. Rev.*, 2009, **38**, 2922-2934.

6 P. J. Tonge and S. R. Meech, *J. Photochem. Photobiol. A: Chemistry*, 2009, **205**, 1-11.

7 L. Tang, W. Liu, Y. Wang, Y. Zhao, B. G. Oscar, R. E. Campbell and C. Fang, *Chem. Eur. J.*, 2015, **21**, 6481-6490.

8 L. Tang, W. Liu, Y. Wang, L. Zhu, F. Han and C. Fang, *J. Phys. Chem. Lett.*, 2016, **7**, 1225-1230.

9 R. J. D. Miller, *Science*, 2014, **343**, 1108-1116.

10 A. B. Myers and R. A. Mathies, in *Biological Applications of Raman Spectroscopy*, ed. T. G. Spiro, John Wiley & Sons, Inc., New York, 1987, vol. 2, pp. 1-58.

11 J. L. McHale, *Molecular Spectroscopy*, Prentice-Hall, Upper Saddle River, NJ, 1999.

12 W. Liu, F. Han, C. Smith and C. Fang, *J. Phys. Chem. B*, 2012, **116**, 10535-10550.

13 M. J. Frisch, G. W. Trucks, H. B. Schlegel, G. E. Scuseria, M. A. Robb, J. R. Cheeseman, G. Scalmani, V. Barone, B. Mennucci, G. A. Petersson, H. Nakatsuji, M. Caricato, X. Li, H. P. Hratchian, A. F. Izmaylov, J. Bloino, G. Zheng, J. L. Sonnenberg, M. Hada, M. Ehara, K. Toyota, R. Fukuda, J. Hasegawa, M. Ishida, T. Nakajima, Y. Honda, O. Kitao, H. Nakai, T. Vreven, J. J. A. Montgomery, J. E. Peralta, F. Ogliaro, M. Bearpark, J. J. Heyd, E. Brothers, K. N. Kudin, V. N. Staroverov, R. Kobayashi, J.

Normand, K. Raghavachari, A. Rendell, J. C. Burant, S. S. Iyengar, J. Tomasi, M. Cossi, N. Rega, J. M. Millam, M. Klene, J. E. Knox, J. B. Cross, V. Bakken, C. Adamo, J. Jaramillo, R. Gomperts, R. E. Stratmann, O. Yazyev, A. J. Austin, R. Cammi, C. Pomelli, J. W. Ochterski, R. L. Martin, K. Morokuma, V. G. Zakrzewski, G. A. Voth, P. Salvador, J. J. Dannenberg, S. Dapprich, A. D. Daniels, Ö. Farkas, J. B. Foresman, J. V. Ortiz, J. Cioslowski and D. J. Fox, *Gaussian 09, Revision B.1*, Gaussian, Inc., Wallingford, CT, 2009.

14 Y. Wang, L. Tang, W. Liu, Y. Zhao, B. G. Oscar, R. E. Campbell and C. Fang, *J. Phys. Chem. B*, 2015, **119**, 2204-2218.

15 N. Y. A. Baffour-Awuah and M. Zimmer, *Chem. Phys.*, 2004, **303**, 7-11.

16 S. Rafiq, B. K. Rajbongshi, N. N. Nair, P. Sen and G. Ramanathan, *J. Phys. Chem. A*, 2011, **115**, 13733-13742.

Chapter 3 Watching an Engineered Calcium Biosensor Glow: Altered Reaction Pathways before Emission

Published in: **Sean R. Tachibana**, Longteng Tang, Liangdong Zhu, Weimin Liu, Yanli Wang, and Chong Fang **(2018)** "Watching an Engineered Calcium Biosensor Glow: Altered Reaction Pathways before Emission", *J. Phys. Chem. B*, 122 (50), 11986–11995. DOI: 10.1021/acs.jpcb.8b10587.

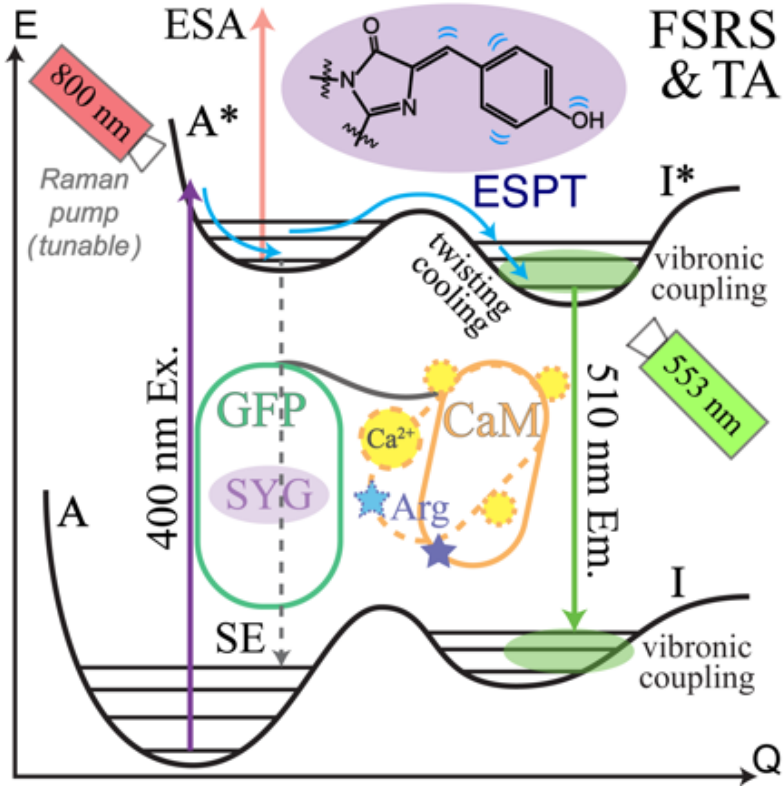

"You must understand that there is more than one path up to the top of the mountain." – Miyamoto Musashi

3.1 Abstract

Biosensors have become an indispensable toolset in life sciences. Among them, fluorescent protein based biosensors have great biocompatibility and tunable emission properties, but their development is largely trial and error. To facilitate rational design, we implement tunable femtosecond stimulated Raman spectroscopy (FSRS), aided by transient absorption and quantum calculations, to elucidate the working mechanisms of a single-site Pro377Arg mutant of an emission ratiometric Ca^{2+} biosensor based on a GFP-calmodulin complex. Comparisons with the parent protein and the Ca^{2+}-free/bound states unveil more structural inhomogeneity yet an overall faster excited state proton transfer (ESPT) reaction inside the Ca^{2+}-bound biosensor. The correlated photoreactant and photoproduct vibrational modes in the excited state reveal more chromophore twisting and trapping in the Ca^{2+}-bound state during ESPT, and the largely conserved chromophore dynamics in the Ca^{2+}-free state from parent protein. The uncovered structural dynamics insights throughout an ESPT reaction inside a calcium biosensor provide important design principles in maintaining a hydrophilic, less compact, and more homogeneous environment with directional H-bonding (from the chromophore to surrounding protein residues) via bioengineering methods to improve the ESPT efficiency and quantum yield while maintaining photostability.

3.2 Introduction

Biosensor technology creates powerful tools to probe and understand complex biological processes in real time, which has greatly advanced bioimaging and life sciences.[1-6] Among them, fluorescent protein (FP) biosensors utilize the photosensitive

FP unit as part of a nanomachine to image cellular components of interest due to their high signal-to-noise ratios, biocompatibility, versatile engineerability, and tunable emission properties that span the UV to visible range. The large Stokes shift between absorption and emission of the FP-based biosensors stems from excited state proton transfer (ESPT) that allows the protein chromophore to relax to a lower energy state before radiative emission. Therefore, ESPT is a crucial step in governing their main functions,[7-11] which represents an archetypal biomolecular system to reveal the structure-function relationships on their intrinsic time scales. By understanding the ESPT reaction and competing pathways on the native femtosecond (fs) to picosecond (ps) time scales, one can rationally suggest specific single or multi-site mutations in tailoring new FPs and FP-based biosensors for advanced applications. The fundamental knowledge about how a chromophore interacts with its local environment inside a protein matrix also affords a rare opportunity to investigate conformational states and dynamics, energy relaxation pathways, and key atomic motions when a bioluminescent complex is in action.

In this study, we synergistically implemented the tunable femtosecond stimulated Raman spectroscopy (FSRS),[12-14] transient absorption (TA), and quantum calculations[15] to uncover the effects of a single-site Pro377Arg (P377R) mutation of a parent green fluorescent protein (GFP) based calcium biosensor GEM-GECO1 (GECO stands for genetically encoded calcium indicator for optical imaging).[16,17] The integral platform of electronic and vibrational spectroscopies, aided by normal mode assignment using computational chemistry methods, enables us to reveal the structure-energy-function relationships of a biomolecular system on the basis of time-resolved

spectra starting from the time zero of electronic excitation. For the recently engineered GECO series, this platform has been proven effective in dissecting the fluorescence mechanisms.[17-20]

Since calcium ions play essential regulatory roles in cellular systems from gene expression, metabolism, hormone release, neuron firing, muscle contraction, to pathology, the importance to develop better calcium biosensors cannot be overstated. These fluorescent biosensors consist of a circularly permuted GFP (cpGFP), an adjacent calmodulin (CaM) subunit and a chicken kinase M13 peptide as its binding client.[2,16] The cpGFP, unlike wtGFP, has an opening in the β-barrel that exposes the phenolic end of the embedded serine-tyrosine-glycine (SYG) chromophore to the environment. During directed evolution,[16] one residue stands out to be crucial for blue emission from the Ca^{2+}-bound biosensor: Pro377 in the CaM subunit that largely shields the β-barrel opening and inhibits ESPT from the cpGFP chromophore. On the basis of a previous report that the Pro377Arg (P377R) mutation converts the parent biosensor from green-blue emission ratiometric to green excitation ratiometric,[19] the elucidation of fluorescence modulation mechanisms of this engineered calcium ion (Ca^{2+}) biosensor requires a much improved sensitivity to track the photoproduct species I* after excitation of the photoreactant species A* in different local environments, induced by the Ca^{2+}-binding events at allosteric sites away from the photosensitive chromophore (see Figure 3.1 for illustration).

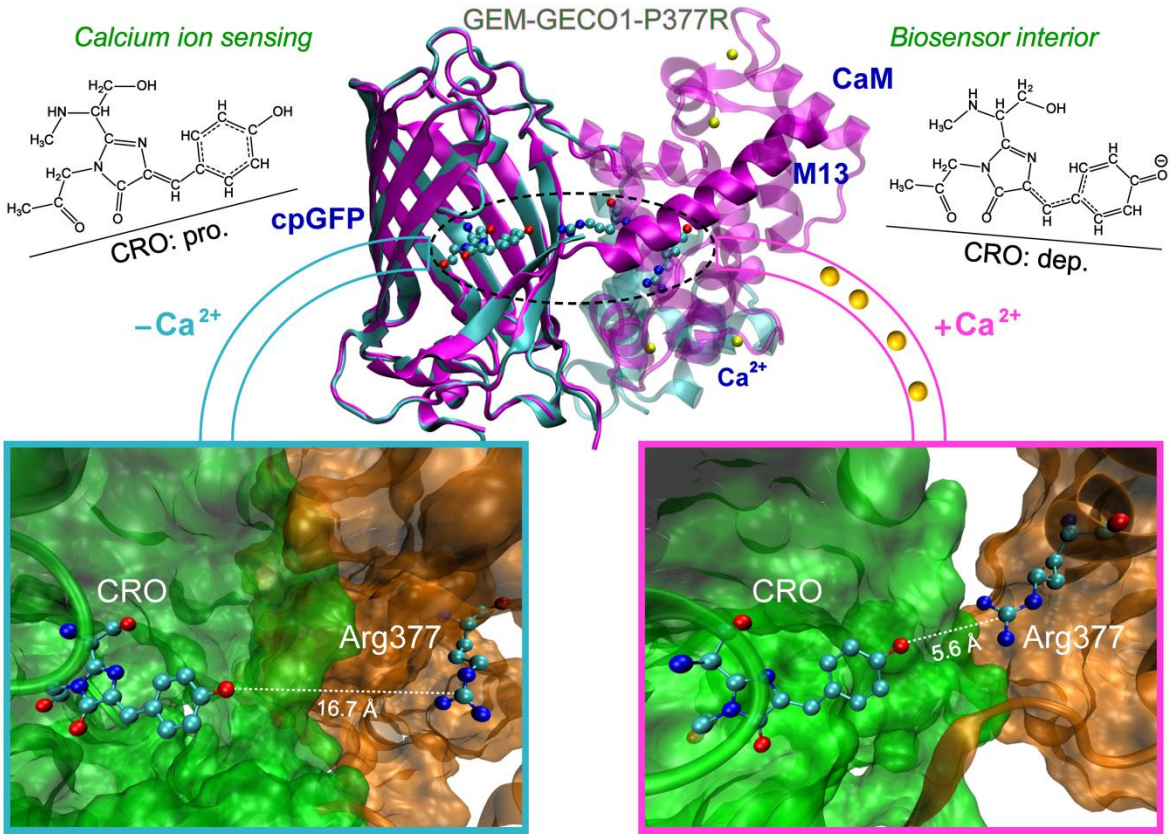

Figure 3.1. Protein structural illustration of the Ca^{2+}-free (cyan) and bound (magenta) GEM-GECO1-P377R calcium biosensor. The four Ca^{2+} ions bound to each biosensor are represented by yellow spheres. The SYG chromophore (CRO) and interfacial R377 residue (black dashed ellipse) are highlighted in the enlarged windows (lower panels), depicting the relative positions, orientations, and distances between the CRO phenolic oxygen in cpGFP (green) and R377 guanidinium carbon in the CaM (orange) subunit that notably change upon Ca^{2+} binding. The chemical structures of the protonated (pro.) and deprotonated (dep.) chromophores are also shown.

Given the photoresponse of the biosensor spanning multiple time scales, femtosecond transient absorption (fs-TA) is an effective first step to bring the steady-state electronic spectroscopy (e.g., UV/Visible absorption and fluorescence) into the time domain and starting from the time zero of photoexcitation. The excited-state electronic dynamics such as excited state absorption (ESA, $S_1 \rightarrow S_n$), stimulated

emission (SE, $S_1 \rightarrow S_0$), and ground state bleaching (GSB) provide a holistic picture of the potential energy surface (PES) involving the excited or relaxed chromophore in its microenvironment.[21] In practice, FSRS can be readily achieved in the same setup as fs-TA by incorporating an additional picosecond (ps) Raman pump to stimulate a Raman scattering process in a resonantly or pre-resonantly enhanced excited state population (sometimes even at off-resonant conditions but with a reduced signal-to-noise ratio), tracking the vibrational dynamics of interest.[10,22,23] Conventional FSRS spectrally filters the 800 nm laser output as Raman pump to overlap with a broad ESA band of FPs, enhancing the photoreactant in S_1.[10,17] Tunable FSRS expands research capability by positioning the Raman pump across a wide range so transient excited state species can be selectively enhanced on molecular time scales.[18,19,24,25] In comparison to the time-resolved IR studies on proteins,[26-28] the main experimental observables for FPs and FP-based biosensors in tunable FSRS are the vibrational dynamics of the chromophore immediately following electronic excitation, which underlie the protein main function in emitting light.

3.3 Materials and Methods

3.3.1 Protein sample preparation

The GEM-GECO1-P377R biosensor (referred as P377R) sample was synthesized according to previously reported procedures, which started with *E. coli* DH10B cells (Invitrogen) transformed using the pTorPE plasmid with 6-histadine-tagged GEM-GECO1 protein.[16,17] For the P377R mutation, synthetic DNA oligonucleotides (Integrated DNA Technologies) and QuikChange Lighting Single kit

(Agilent Technologies) were used. The final P377R protein samples were prepared in pH=7.2 MOPS buffer solution with 10 mM EGTA (Ca^{2+}-free) and 10 mM Ca-EGTA (Ca^{2+}-bound). The steady-state electronic absorption and emission spectroscopy is performed at room temperature using a Thermo Scientific Evolution 201 UV-Visible (UV-Vis) and a Hitachi F-2500 fluorescence spectrophotometer, respectively.

3.3.2 Femtosecond transient absorption (fs-TA)

Our ultrafast laser source originates from a regenerative amplifier (Legend Elite-USP-1K-HE) seeded by a mode-locked Ti:Sapphire oscillator (Mantis-5, Coherent, Inc.). The fundamental pulse (FP) at 800 nm has ~35 fs duration, ~4 mJ energy, and 1 kHz repetition rate. About 75 mW of the FP goes through a β-barium borate (BBO) crystal for second harmonic generation to obtain the 400 nm pulse, followed by temporal compression using a prism pair (Suprasil-1, CVI Melles Griot). Its intensity is attenuated to ~0.2 mW to act as the actinic pump. About 25 mW of the FP passes through a pinhole and a neutral density filter before being focused on a 2-mm-thick *Z*-cut sapphire plate to generate a supercontinuum white light (SCWL) as the probe (ca. 430—700 nm).[18,23] The P377R sample concentration was made to reach OD=1/mm at 400 nm (also for femtosecond Raman measurement, see below). The protein biosensor solution was housed in a 1-mm-pathlength quartz flow cell (48-Q-1, Starna Cells) using a peristaltic pump, to minimize photodamage of the sample as well as reduce thermal effect during data collection. The pump and probe pulses focus at the sample while the time delay (up to 600 ps in this work) between them is regulated by a motorized delay stage (NRT150, Thorlabs, Inc.) where the pump beam traverses. We

also performed a TA measurement with a compressed probe using a chirped mirror pair (DCM-9, 450—950 nm, Laser Quantum, Inc.). With the reduced pulse duration to ~50 fs, the main dynamics of interest remain unchanged, yet the bluer ESA region (see Figure 3.2b below) gets cut off due to the DCM-9 optical coating. Therefore, the fs-TA data in Figures 3.2b and 3.3 in Section 3.4 were collected without the chirped mirror pair to analyze the broader spectral region and compare the excited state proton transfer (ESPT) dynamics on the ps or longer time scales.

3.3.3 Tunable femtosecond stimulated Raman spectroscopy (FSRS)

The recently developed tunable FSRS setup in our laboratory has been reported.[12-14,23] In brief, half of the aforementioned laser FP is used to power the fs actinic pump, the picosecond (ps) Raman pump, and the fs Raman probe. The tunable (~480—750 nm) Raman pump is achieved by a two-stage ps noncollinear optical parametric amplifier (NOPA), pumped by a ps 400 nm pulse out of a homebuilt second harmonic bandwidth compressor (SHBC).[12] Based on the electronic profiles of P377R biosensor, we tuned the Raman pump to 553 nm (~4 μJ, ~2 ps duration) to achieve pre-resonance condition with both the photoreactant and photoproduct TA bands while keeping the 400 nm actinic pump (0.1—0.2 μJ pulse energy),[23,25] to compare with conventional FSRS wherein the 800 nm Raman pump was used.[13,19] A control experiment using a 580 nm Raman pump led to a much reduced signal-to-noise ratio for the deprotonated chromophore species of interest, hence confirming the advantage of using the 553 nm Raman pump for pre-resonance Raman enhancement.[19,23] The fs broadband probe (ca. 560—630 nm) is generated by focusing ~2 μJ of the FP onto a 2-

mm-thick sapphire plate (see above) and selecting the target region from the SCWL. All three incident pulses are focused to overlap at the sample spot in a 1-mm-pathlength flow cell (see above) that ensured sample integrity during a typical FSRS experiment lasting for ~2.5 hours. The FSRS signal collinear with the Raman probe is dispersed by a 1200 grooves per mm grating at 500 nm blaze in a spectrograph (Acton SpectraPro SP-2356, Princeton Instruments) before being imaged on a CCD array camera (PIXIS:100F, Princeton Instruments). Fifteen excited-state data sets were collected and within each data set, 1500 stimulated Raman spectra were averaged at each time delay point (>75 time points across the detection time window of 600 ps) by the LabVIEW custom-made suite of programs. The UV/Vis spectra were checked before and after the excited state TA and FSRS experiments with 400 nm pump to confirm the sample integrity (i.e., within 5%/10% spectral difference for the Ca^{2+}-free/bound P377R absorption profile, see Figure 3.2a for example).

3.4 Results and Discussion

To achieve a high contrast for Ca^{2+} imaging, a ratio of excitation ratios can be taken due to the small deprotonated (B form) absorbance in the Ca^{2+}-bound state (Figure 3.2a). Using conventional FSRS, the hydrophilic Arg377 was found to create a less homogeneous chromophore environment inside the Ca^{2+}-bound biosensor with A* decay time constants of ~16 and 90 ps, which differ from the single time constant of 36 ps in the Ca^{2+}-free biosensor.[19] However, an important question regarding the biosensor mechanism remains: which characteristic nuclear motions respond to the key single-site mutation that alters the photochemical reaction pathways and outcomes?

Such mechanistic insights require a structural dynamics technique that can track transient molecular species during (not just before and after) a photoinduced process.[14] The main experimental evidence to support any rational design principles need to include the site-specific information on molecular time scales, which typically span the fs to ps range when primary structural events occur and govern the molecular fate as well as the “downstream” macroscopic functions of interest.[13,17,29]

3.4.1 Steady-state absorption and fluorescence spectroscopy

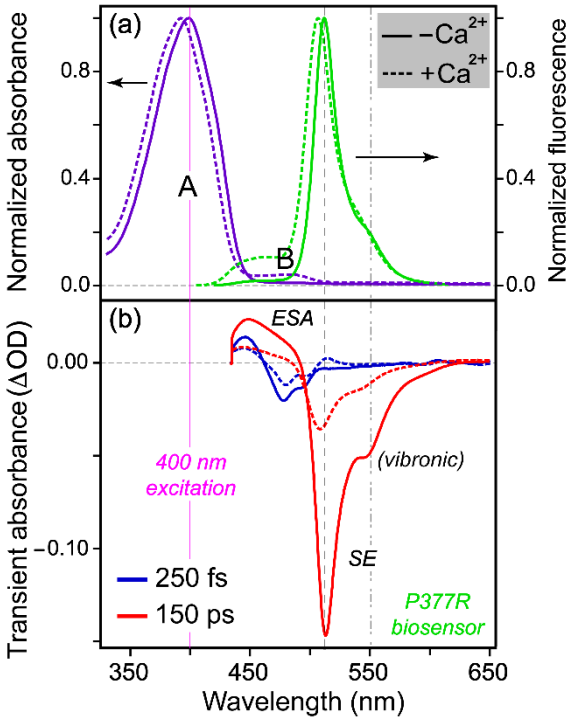

Figure 3.2. Electronic spectroscopy of the P377R biosensor in aqueous buffer solution. (a) Normalized steady-state absorption (violet) and emission (green) spectra of the Ca^{2+} free (solid) and bound (dashed) states. The protonated and deprotonated chromophore is denoted by A and B, respectively. (b) Fs-TA spectra at 250 fs (blue) and 150 ps (red). The actinic pump was set to 400 nm (vertical magenta line). The main SE band and a prominent red shoulder are marked by the vertical dashed and dash-dotted lines, likely indicative of vibronic coupling. The evolution from the A* SE peak at ~478 nm (blue dip) to the I* SE peak at ~510 nm (red dip) is apparent.

Figure 3.2a displays the steady-state absorption and emission spectra that are reminiscent of a GFP chromophore except that the B form has a much smaller contribution in the biosensor than wtGFP.[7,8,10] A 400 nm actinic pump was selected for TA and FSRS to effectively pump the dominant A form. Interestingly, the Ca^{2+}-bound

biosensor shows an increased B absorption peak at ~480 nm and also an increased A* emission peak at ~460 nm which indicates structural inhomogeneity in the ground and excited state,[17,30] while its absorption and emission peaks (392 and 506 nm) are both blue shifted from the Ca^{2+}-free counterparts (399 and 512 nm). Such a blue shift of electronic features upon Ca^{2+} binding is commonly observed in the GECO family, likely due to an increase of electrostatic interaction stabilizing the photoacidic chromophore better in the ground state (S_0) than that in the excited state (e.g., S_1) with a reduced dipole after the photoinduced ultrafast intramolecular charge transfer across the chromophore two-ring conjugated system.[16,17,19,31-33]

3.4.2 Time-resolved electronic spectroscopy

Upon 400 nm excitation, Figures 3.2b and 3.3 provide clear evidence that some chromophore S_0 populations reach a transient S_1 state, and the initial protonated photoreactant (A*) converts to a deprotonated photoproduct (I*) on ultrafast time scales. Robust assignment of two chromophore species (i.e., change of protonation states) before and after ESPT is corroborated by a close match between the A* and I* SE peaks and fluorescence peaks (Figure 3.2). At early times (e.g., 250 fs), the main negative peak at 478/479 nm for the Ca^{2+}-free/bound biosensor corresponds to the A* SE band, located to the red side of the A* fluorescence peak (~460 nm), which is in accord with the aforementioned charge transfer characteristics in the transient electronic excited state.[11,32,34] Since the ground state B population is very small with an absorption peak at ~480 nm, we do not expect a significant GSB contribution from the B species after 400 nm excitation. At late times (e.g., 150 ps), the Ca^{2+}-free/bound

biosensor SE band grows and red shifts to 513/508 nm that is attributed to I* after ESPT, confirmed by the spontaneous emission peaks at 512/506 nm.

In addition, a prominent red shoulder appears in both fluorescence and SE bands. To elucidate its origin, we took a 1-nm slice from the main SE band (513/508 nm) and shoulder (550/544 nm) for the Ca^{2+}-free/bound biosensors (see Figure 3.6 in Section 3.7 below), which exhibit nearly identical dynamics between their respective main SE band and red shoulder, indicating that both peaks arise from the same transient deprotonated chromophore species. In particular, the shoulder observed in the fluorescence band is associated with a vibrational mode in S_0 that is coupled to the downward electronic transition, whereas the SE shoulder could involve a similar vibrational mode in S_1 as the I* species relax in a non-equilibrium electronic excited state.[25,35,36] The choice of tunable Raman pump at the red side of main SE band potentially enhances the vibrational modes associated with these vibronic transitions (see below).

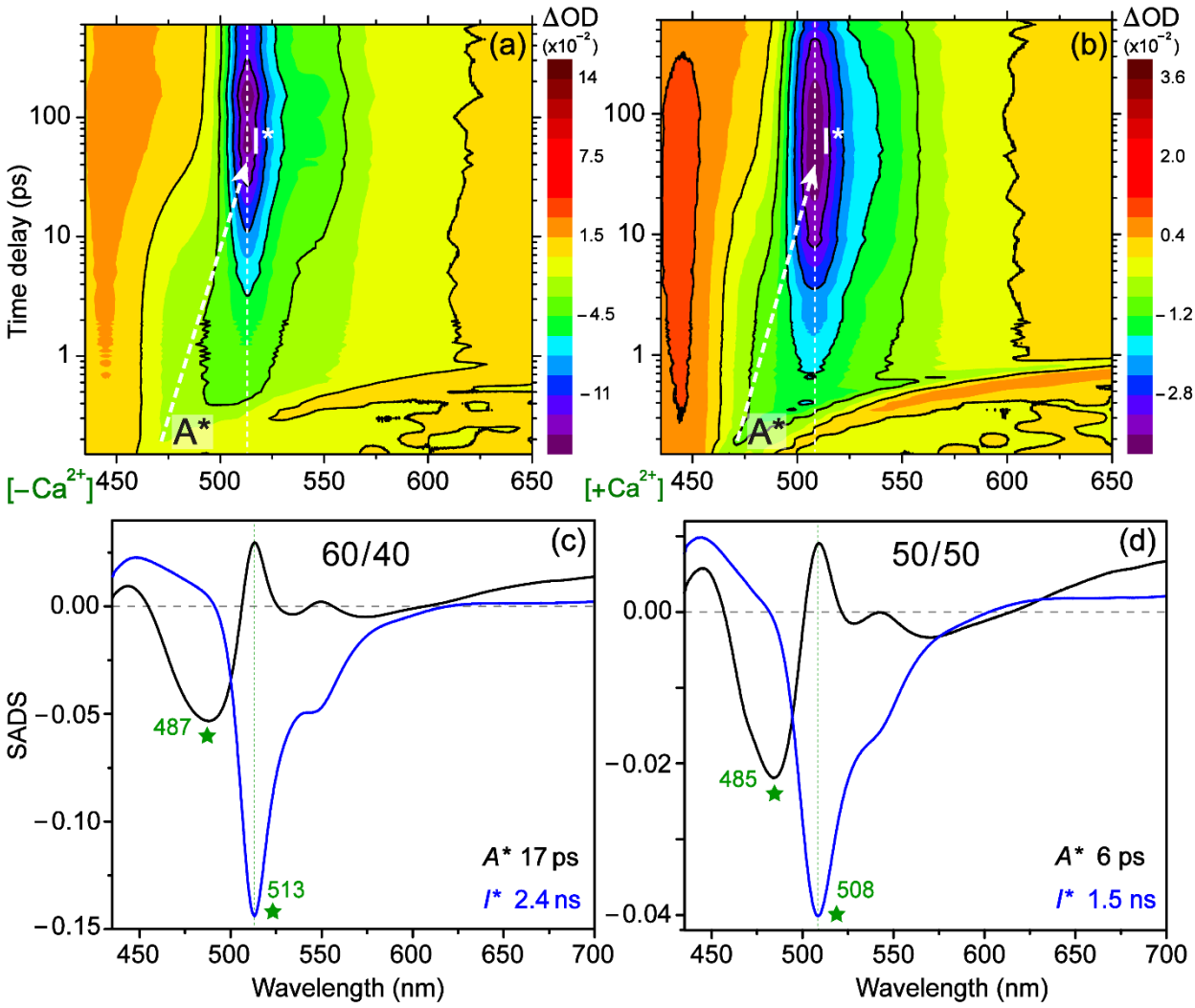

Figure 3.3. Fs-TA contour plot of the Ca^{2+}-free (a) and bound (b) states after 400 nm excitation. The A*→I* transition through ESPT reaction is highlighted by the white dashed line across SE bands. Target analysis of the Ca^{2+}-free (c) and bound (d) states adopts a two-component (A*→I*) model. To correct for fluorescence background (FB), the optimal A*/FB initial population is denoted in black. The 17 ps ESPT time constant and 2.4 ns green fluorescence lifetime were derived for the Ca^{2+}-free state whereas the Ca^{2+}-bound state analysis converges to lifetimes of 6 ps and 1.5 ns.

The experimental TA spectra are typically convoluted due to overlapping electronic bands associated with multiple populations (Figure 3.3a and b). To better

understand how each population evolves with time, global and target analyses are typically used to dissect complex systems.[37] For the Ca^{2+}-free and bound biosensors, multiple components were tested via target analysis (see Figure 3.7 in Section 3.7 below) to examine the validity of signal deconvolution. Figure 3.3c and d present the simplest reasonable model (i.e., two-component sequential model, A*→I*→I) with the 17/6 ps and 2.4/1.5 ns time constants for the Ca^{2+}-free/bound states, respectively. The initial process corresponds to the main ESPT reaction with a clear transition of SE bands (i.e., A*→I*), revealing that the hydrophilic Arg377 in the Ca^{2+}-bound biosensor facilitates a faster ESPT channel. The nanosecond process is associated with the green fluorescence lifetime as the SE band diminishes (i.e., I*→I). We note that a fluorescence background (FB) signal is present at negative time points due to an intrinsic difference of the probe spectrum between the pump on and pump off cases with laser repetition rate at 1 kHz, while the CCD camera records the signal non-stop within the 1 ms data collection window for each laser shot. To correct for FB contribution and elucidate the dynamic ESPT reaction pathway, an initial population ratio (A*/FB) of 60/40 and 50/50 was optimized to least-squares fit the TA data of the Ca^{2+}-free/bound states to retrieve the target analysis species.

3.4.3 Time-resolved vibrational spectroscopy using tunable FSRS

Because the main ESPT reaction occurs on the picosecond time scale, we implement the tunable FSRS methodology to track nuclear motions during the photoproduct formation. Using a Raman pump at 553 nm that is preresonant with the I* SE band at ~510 nm (Figure 3.3), we effectively capture the essence of ESPT

because (1) it is the only pathway converting A* to I*, (2) the Raman pump is >40 nm away from the SE peak so the Raman-pump-induced depletion of I* population is insignificant,[23,38] (3) the observed vibrational dynamics of I* provide unambiguous information about the rise and decay of deprotonated chromophore species before returning to S_0. In Figure 3.4a and b, excited state FSRS contour plot of the Ca^{2+}-free/bound biosensor is contrasted with the buffer-subtracted ground state spectra: the frequency and intensity change of the Raman modes between S_0 and S_1 is conspicuous. In particular, the ground state chromophore only exhibits one prominent peak at ~1565 cm^{-1}, while an array of peaks from ~700 to 1700 cm^{-1} manifest interesting dynamics (e.g., peak integrated intensity and center frequency, vide infra) in the excited state in close association with ESPT reaction (Figure 3.4) that warrants detailed analysis.

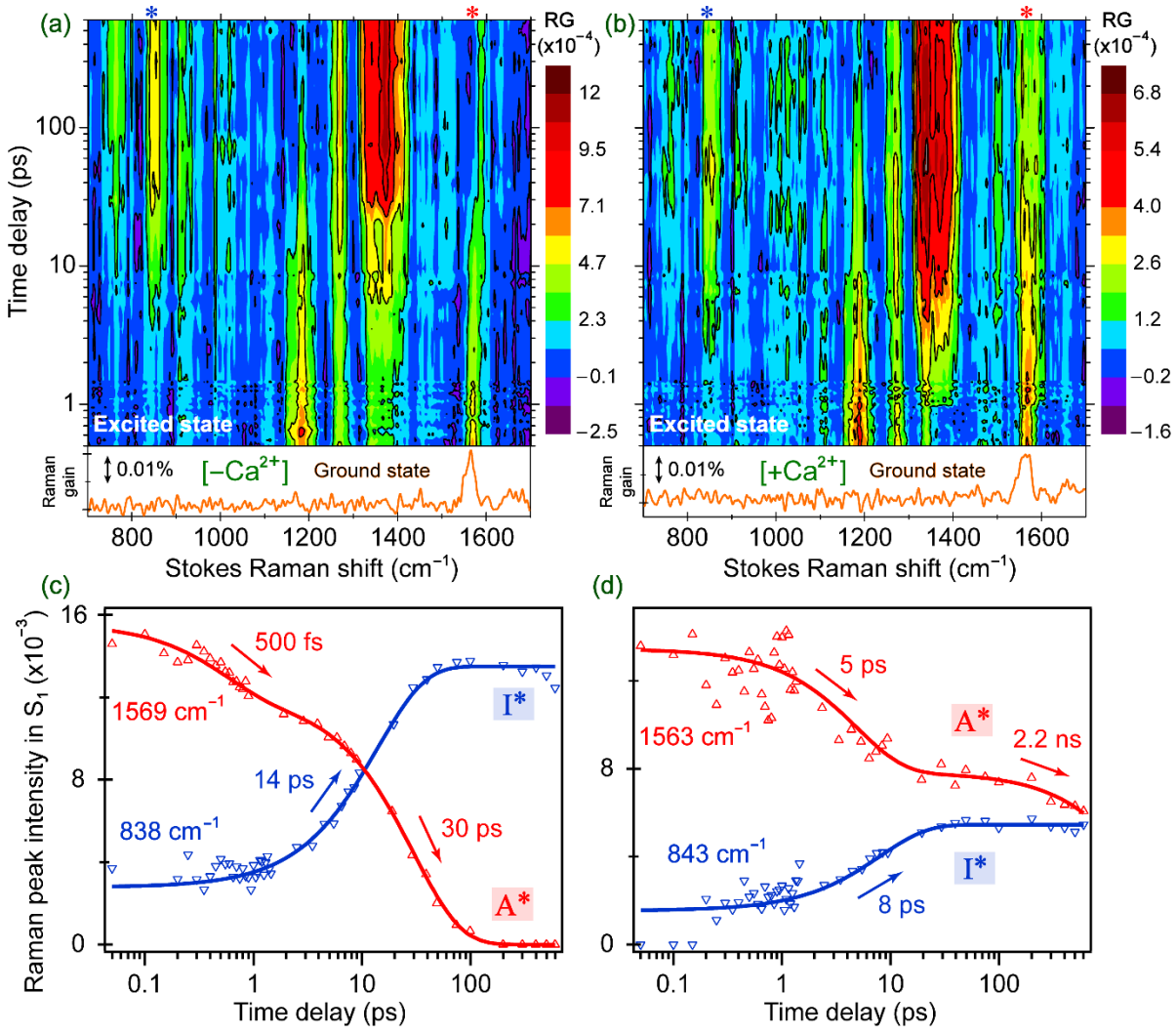

Figure 3.4. Tunable FSRS 2D contour plot of the Ca^{2+}-free (a) and bound (b) P377R biosensor from 10 fs to 600 ps with 400 nm actinic pump and 553 nm Raman pump. The ground state spectra are displayed below (orange). For vibrational intensity dynamics of the Ca^{2+}-free (c) and bound (d) biosensor in S_1, the I* 838/843 cm^{-1} mode intensity rise (blue) is contrasted with the A* 1569/1563 cm^{-1} mode intensity decay (red) with the multiexponential fits in solid curves and time constants.

First, the Ca^{2+}-free and bound biosensors show similar peak positions and dynamic patterns (see Figure 3.8 in Section 3.7 for the raw experimental spectra with baselines drawn across the detection window). This is expected because they share the

same SYG chromophore (see Figure 3.1 inset for the chemical structures with different protonation states) and both emit green light upon 400 nm excitation, and the major difference in the chromophore local environment is the proximity to an interfacial R377 residue located on a different protein subunit.[10,17,19] This allows an effective spectroscopic platform to track the chromophore response at the biosensor active site as the Ca^{2+}-binding events occur allosterically at the nearby CaM domain (Figure 3.1), and reveal key differences between the excited state vibrational motions.

Second, the I* modes at ~840, 860 and 1340 cm^{-1} appear earlier in Figure 3.4b than 3.4a, indicative of a faster ESPT channel in the Ca^{2+}-bound biosensor wherein the I* population rises with an 8 ps time constant (Figure 3.4d) versus 14 ps in the Ca^{2+}-free biosensor (Figure 3.4c, while the fit of the adjacent 860 cm^{-1} mode yields a similar 12 ps rise time constant). Quantum calculations show that the ~840 and 860 cm^{-1} modes mainly consist of the phenolic ring out-of-plane deformation (see Table 3.1 in Section 3.7) and the imidazolinone ring deformation,[24] respectively, hence these ring motions are a sensitive vibrational probe for the accumulation of I* species due to the increased electric polarizability over the two-ring system and pre-resonance enhancement (i.e., the I* SE peaks at ~510 nm while the Raman pump is at 553 nm, see Figure 3.2b). This dynamic trend also matches a previous report on the TYG chromophore in the Ca^{2+}-free/bound G-GECO1.1 biosensors, wherein tunable FSRS with a 529 nm Raman pump allowed the tracking of I* ~1370 cm^{-1} mode intensity rise with 42/22 ps time constants.[18] Notably, the Ca^{2+}-free over bound ratio of I* intensity rise time constants (14 ps/8 ps ≈ 1.8) in the P377R biosensor matches that in the G-GECO1.1 biosensor (42 ps/22 ps ≈ 1.9). It is thus plausible that the protonated SYG chromophore is more

prone to ESPT upon 400 nm photoexcitation than the TYG chromophore,[3,8] but the effect of Ca^{2+} binding on the ESPT rate is comparable in both biosensors.

Third, a faster reaction may lead to less complete ESPT if an inhomogeneous population consists of significant subpopulations that cannot undergo ESPT (e.g., trapped in A*). This point is evinced by the prolonged A* 1563 cm^{-1} mode intensity decay that differs from the I* 843 cm^{-1} mode intensity rise in the Ca^{2+}-bound biosensor (Figure 3.4d). The ~5 ps (with 43% amplitude weight in the least-squares fit) initial A* decay is an average of Franck-Condon (FC) relaxation and ESPT dynamics which is in accord with the ~8 ps I* rise. The much longer 2.2 ns (with 57% amplitude weight) A* decay likely reflects a mixture of fluorescence lifetime and nonradiative decay pathways so the trapped chromophore subpopulation could return to the ground state. Due to our experimental pre-resonance condition favoring the I* modes, the A* mode dynamics become more convoluted thus exhibiting averaged dynamics; the cleaner A* decay dynamics can be observed using conventional FSRS with an 800 nm Raman pump.[10,19] Using ultrafast vibrational spectroscopy, similar conformational inhomogeneity has been observed in a membrane protein environment due to a slower exchange between different H-bonding configurations.[26]

Fourth, the Ca^{2+}-free biosensor exhibits similar dynamics as the previous conventional FSRS results (Figure 3.4c).[19] Unlike the Ca^{2+}-bound state, the Ca^{2+}-free biosensor reveals a more homogeneous and efficient ESPT channel that allows the A* 1569 cm^{-1} mode decay to zero, suggesting that the resonance conditions for A* species diminish more dramatically as the Ca^{2+}-free biosensor chromophore undergoes ESPT

reaction. It also shows that energy dissipation via competing pathways (e.g., nonradiative relaxation) is more significant in the Ca^{2+}-free case.

With this enhanced sensitivity for certain A* species, the initial 500 fs decay (with 41% amplitude weight) in Figure 3.4c shows the A* population moving out of the FC region[10,17,20] while the 30 ps decay (with 59% amplitude weight) represents an ensemble average of ESPT (~14 ps for the I* 839 cm^{-1} mode rise in Figure 3.4c) and other A* nonradiative relaxation processes on the tens of ps time scale.[20,39] We note that this 30 ps time constant is also retrieved from other A* modes at ~1155, 1183, and 1208 cm^{-1}. Since the fluorescent quantum yield for such biosensors is typically around 0.2 with 400 nm excitation,[16,17,20] the nonradiative relaxation channels effectively compete with ESPT on ultrafast time scales to deplete the A* population. This also explains the negligible A* spontaneous emission peak in the Ca^{2+}-free state (Figure 3.2a).

3.4.4 Characteristic vibrational motions differ in the Ca^{2+} free and bound biosensors

To better understand the observed and potentially functional structural motions of the biosensor chromophore, we analyze the Raman mode frequency dynamics in S_1 (Figure 3.5) to correlate with mode assignments aided by density functional theory (DFT) calculations. The peak doublet between 800 and 900 cm^{-1} displays different frequency dynamics upon Ca^{2+} binding. In the Ca^{2+}-free state, the ~838 cm^{-1} mode shows a 4 ps blue shift from 832 to 845 cm^{-1} (Figure 3.5a), which can be attributed to vibrational cooling (VC) within the I* state after the ultrafast ESPT reaction barrier

crossing.[29,40-42] The adjacent 864 cm^{-1} mode exhibits a similar blue shift from 859 to 870 cm^{-1} with a 6 ps time constant. This observation represents the first time that a frequency shift is tracked in a photoproduct, instead of a photoreactant species or a mixed A*/I* species inside a protein pocket.[20,24,39] However, the Ca^{2+}-bound state does not show a clear blue shift (Figure 3.5b), which could be due to a less steep PES or competing pathways. In both the parent GEM-GECO1 (SYG chromophore, adjacent P377) and a related G-GECO1.1 biosensor (TYG chromophore, adjacent R377), the Ca^{2+}-bound state hosts a more twisted chromophore in the ground state.[24,43] To estimate how twisting affects vibrational frequency in the excited state with reasonable computational costs, the DFT calculation of a 20º-twisted SYG chromophore was compared to the coplanar two-ring-system case (see Table 3.1 in Section 3.7 and Figure 3.4 for the pertinent mode assignment). For the calculated 828 cm^{-1} mode, the deprotonated chromophore shows a 4 cm^{-1} red shift as it twists by 20º. The close-in of the long side chain and positively charged R377 toward the chromophore in the Ca^{2+}-bound biosensor is expected to create a compact microenvironment (Figure 3.1) which allows the deprotonated chromophore after ESPT to further twist.[43] As a result, the VC-induced blue shift mixed with the twisting-induced red shift of the I* mode can lead to an overall stagnant Raman band center frequency (Figure 3.5b).

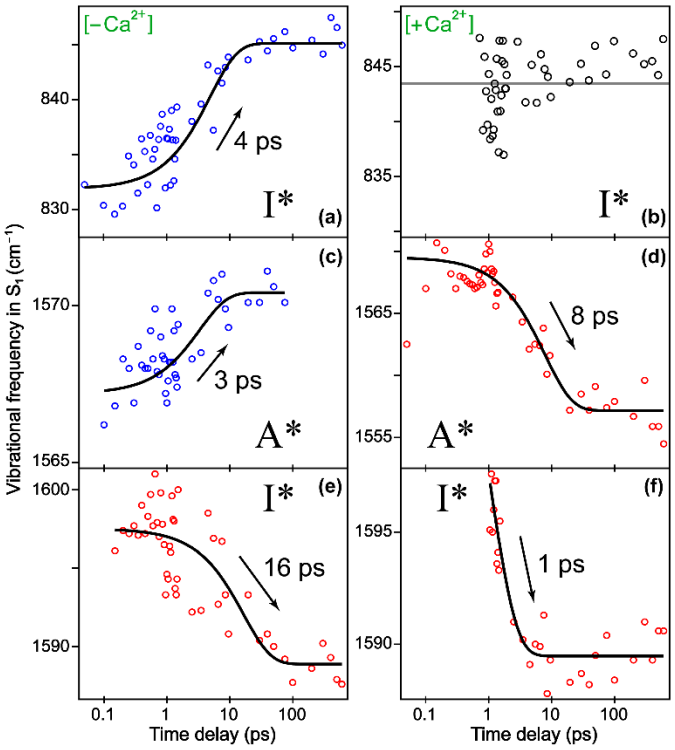

Figure 3.5. Excited state vibrational mode frequency dynamics of the P377R biosensor chromophore. In the Ca^{2+}-free state, the ~838 cm^{-1} I* mode, 1569 cm^{-1} A* mode, and 1594 cm^{-1} I* mode shifts are shown in (a), (c), and (e), respectively, with the single-exponential fits in solid black curves. Time constants are denoted. For comparison in the Ca^{2+}-bound state, the ~843 cm^{-1} I* mode, 1563 cm^{-1} A* mode, and 1593 cm^{-1} I* mode shifts are shown in (b), (d), and (f), respectively. The ~1540 cm^{-1} I* shoulder peak affects the ~1569/1563 cm^{-1} A* peak dynamics.

When comparing the A* marker band frequency shift in the C=C, C=N, and C=O stretching region, the 1569/1563 cm^{-1} mode for the Ca^{2+}-free/bound biosensor is overlapped with the emerging I* modes at 1594/1593 and 1540/1540 cm^{-1}, essentially forming a "Y" spectral pattern as delay time increases (see Figure 3.4a and b). Given the challenge to retrieve mode dynamics from this congested high-frequency region,[24] we fit the spectra using multi-gaussian peaks and record the peak center frequencies. The 1540 cm^{-1} mode is dispersive in the FSRS spectra along with the 1300 cm^{-1} mode

(Figure 3.8 in Section 3.7), indicating that both modes are coupled to the I* SE transition (i.e., vibronic coupling) thus involve hot luminescence pathways in the FSRS signal generation.[44,45] Furthermore, these specific modes project strongly along the ESPT reaction coordinate and are sensitive trackers for the I* formation.[10,18,39] Detailed fitting with dispersive line shape can also be performed[46] to retrieve more information about these modes, but the focus here is to monitor an adjacent mode frequency change. The frequency red shift from the ~1565 cm^{-1} A* mode has been observed in wild-type GFP and GEM-GECO1 biosensor (with a common SYG chromophore) after ESPT reaction and the resultant change of the H-bonding network around the nascent deprotonated chromophore (I*).[10,17] Such a red shift is observed for the Ca^{2+}-bound biosensor A* mode, ca. 1570→1557 cm^{-1}, with a time constant of 8 ps (Figure 3.5d), matching the I* 843 cm^{-1} mode intensity rise time constant of 8 ps (Figure 3.4d), hence confirming their concomitant tracking of ESPT. This result shows that the shoulder peak with a dispersive line shape may not affect the apparent dynamics of a nearby dominant mode with a non-dispersive line shape, and the intensity "pulling" effect to exhibit a marker band red shift is still evident when the ESPT reaction occurs. The general red shift trend of this vibrational mode frequency is also reproduced by TD-DFT calculations wherein the protonated chromophore motion at 1587 cm^{-1} becomes 1536 and 1572 cm^{-1} in the deprotonated chromophore (see Table 3.1 in Section 3.7).

In sharp contrast, the Ca^{2+}-free biosensor A* mode manifests a small blue shift, ca. 1567→1571 cm^{-1}, with a time constant of 3 ps (Figure 3.5c) that does not match the I* 839 cm^{-1} mode intensity rise time constant of 14 ps (Figure 3.4d). To rationalize this intriguing observation, we note that the ~1565 cm^{-1} marker band lasts much longer in

the Ca^{2+}-bound than Ca^{2+}-free biosensor, so beyond tens of ps in the latter case, the I* modes at ~1540 and 1594 cm^{-1} dominate (Figure 3.4b). Indeed, the 1594 cm^{-1} I* mode (Figure 3.5e) exhibits a frequency red shift, ca. 1600→1588 cm^{-1}, with a time constant of 16 ps that is consistent with the ESPT rate in the Ca^{2+}-free biosensor. Our DFT calculations show that the deprotonated chromophore twisting leads to a mode frequency red shift of 3 cm^{-1} (i.e., 1581→1578 cm^{-1}, see Table 3.1 in Section 3.7) so the effect is additive to ESPT, i.e., the aforementioned intensity pulling from a nascent ~1540 cm^{-1} mode at the lower frequency side which also red shifts with the chromophore ring twisting (i.e., 1552→1546 cm^{-1}, see Table 3.1 in Section 3.7). In consequence, a blue shift for the "middle" 1569 cm^{-1} mode in the excited state (Figure 3.5c) could arise from a VC process in A* partially mixed with ESPT as well as the chromophore twisting-induced red shift of adjacent I* modes.

Furthermore, the 1593 cm^{-1} mode is attributed to I* due to its intensity rise after a short dwell of ~1 ps, while its frequency exhibits a 9 cm^{-1} red shift (ca. 1598→1589 cm^{-1}) with a ~1 ps time constant (Figure 3.5f) in the Ca^{2+}-bound state. This ultrafast time constant with a delayed onset of ~1 ps is unique among all the mode frequency dynamics in Figure 3.5, and is likely associated with the I* species responding to the rapidly rearranging bridge water molecules (i.e., between the chromophore phenolate oxygen end and the R377 side chain guanidinium end) on the typical molecular water reorientation time scale.[38,47] This process is consistent with the deprotonated chromophore twisting in a more compact environment with certain H-bonding configurations in support of faster ESPT on the few ps time scale, so such a structural step adjusting the bridge water orientation is important to stabilize the nascent I*

species and enlarge the "quantum box" for pertinent vibrational motions (i.e., leading to the observed mode frequency red shift). Meanwhile, a significant A* population does not undergo ESPT and remains trapped in the Ca^{2+}-bound biosensor, which explains the A* 1563 cm^{-1} mode intensity decay component of 2.2 ns in Figure 3.4d, as well as the increased A* spontaneous emission peak at ~460 nm (Figure 3.2a). In addition, our experiments showed that the Ca^{2+}-bound biosensor is more sensitive to laser irradiation (i.e., susceptible to photodamage reflected by a larger change of UV/Vis spectra before and after the FSRS data collection, see the Materials and Methods above) than the Ca^{2+}-free biosensor. This observation indicates that some trapped A* populations do not experience an efficient and/or effective relaxation pathway to achieve desirable molecular photoprotection properties for the Ca^{2+}-bound biosensor.[42,48]

3.4.5 Formulating the design principles of fluorescent biosensors from a molecular perspective

These mechanistic insights uncover a key design principle for the Ca^{2+} biosensor based on the cpGFP-CaM complex: reduce conformational inhomogeneity and increase the ESPT propensity in the Ca^{2+}-bound state. Since conserved arginine residues (e.g., Arg96 in wtGFP)[3,8] with a positively charged side chain are considered important in stabilizing the charge-transfer excited state of a protein chromophore, we envision that modification of a key residue in the vicinity of the chromophore may provide a directional force to interact with R377 via water bridges and/or electrostatic interactions,[14,49] thus limiting the orientations of the R377 side chain relative to the chromophore phenolate oxygen in the Ca^{2+}-bound state. The replacement of R377 with

a negatively charged residue such as Glu or Asp represents an alternative strategy by maintaining the hydrophilic environment while providing directional H-bonding and proton acceptors to potentially "reroute" the ESPT chain in the Ca^{2+}-bound state, hence making an ratiometric or intensiometric biosensor with improved sensing capabilities.[50,51]

On the other hand, a thiol bridge or some H-bonding partners could be incorporated to restrict the chromophore phase space[52] around the ESPT-prone region so a more homogeneous A* population can effectively proceed to I*. Previous work on the GFP model chromophore such as the widely studied *p*-hydroxybenzylidene-imidazolidinone (HBDI) in solution has shown that chromophore twisting around the ethylenic bridge region leads to the dominant energy relaxation pathway (i.e., nonradiative internal conversion from S_1 to S_0),[14,53,54] which is greatly suppressed for the locked chromophores or inside a protein pocket.[10,39,55] The chromophore surroundings can thus be carefully tuned to provide sufficient structural constraints to increase the nonradiative isomerization energy barrier[56,57] so the fluorescence pathway becomes more favored.

In addition, implementing a hydrophilic canonical (e.g., Lys, His) or noncanonical amino acid (NCAA)[58] that interacts with the chromophore from a slightly larger distance could help promote ESPT in a less crowded environment with a higher fluorescence quantum yield, which also reduces the trapped A* population by allowing more efficient relaxation pathways of A*, thereby leading to improved photostability of the overall biosensor. Since the P377R biosensor acts in an excitation ratiometric manner, increasing the B population in the Ca^{2+}-bound state is also beneficial, and the

aforementioned strategies are expected to shift the ground state equilibrium from A to B due to a more favorable H-bonding environment with a better positioned and more homogeneous R377 (or another hydrophilic residue after the bioengineering step as stated above) interacting with the phenolic end of the chromophore. It is interesting to note that a previous two-photon absorption spectroscopic study showed a blue-shifted absorption peak for the lowest-energy band in the one-photon absorption spectrum (see Figure 3.2a for example) of the anionic form of an enhanced GFP chromophore, which led to a proposed hidden electronic excited state (e.g., S_2) with a large two-photon absorptivity.[59] Though this result was specifically tied to a deprotonated TYG chromophore either in solution or inside enhanced GFP, not the protonated SYG chromophore in a GFP-based calcium biosensor mutant as reported herein, we consider it as further evidence that the elucidation of multidimensional electronic PES of the protein chromophore is non-trivial and requires a careful assessment of the observed spectral data on various time scales and under specific experimental conditions. This exertion is especially pertinent when two-photon absorption is desired for greater penetration depth and/or higher resolutions in advanced bioimaging applications.[51,60]

3.5 Conclusions

Understanding how fluorescent protein based Ca^{2+} biosensors work is of fundamental interest and use for applications in bioimaging and life sciences. In this contribution, we have implemented the tunable FSRS technique, aided by fs-TA and computations, to elucidate how a single-site P377R mutation affects the main function (i.e., fluorescence) of a GFP-based calcium ion biosensor. The Ca^{2+}-free state has a

largely homogeneous chromophore environment due to the unrestricted β-barrel opening with labile water molecules and a distant R377 residue. Direct tracking of deprotonated I* species reveals a ~14 ps ESPT reaction and ~4 ps vibrational cooling time constant in the I* state, while the protonated A* species shows biexponential decay time constants of 500 fs and 30 ps. Upon Ca^{2+} binding, R377 impedes the β-barrel opening and yields a more compact biosensor interior with restricted water molecules as the bridge for ESPT and subsequent relaxation. The resultant chromophore population becomes more inhomogeneous: one subpopulation undergoes faster ESPT to I* than its Ca^{2+}-free counterpart with an 8 ps time constant for green emission, while another subpopulation favors a trapped A* species that yields more emission in the blue. Moreover, the nascent I* population adopts a more twisted conformation as it vibrationally cools and stabilizes within a dynamic H-bonding network before fluorescence, reflected by the correlated Raman marker band frequency dynamics including the ~8 (1) ps red shift of the 1563 cm^{-1} A* (1593 cm^{-1} I*) mode.

The altered reaction pathways underlie the overall decreased green emission with more photodegradation after 400 nm excitation of the Ca^{2+}-bound biosensor, which substantiates the spectroscopy-aided rational design strategies to reduce conformational inhomogeneity by modifying the chromophore-R377 interaction to be more directional, less compact, and with improved plasticity. The incorporation of specific functional groups to the protein chromophore via NCAA methodology and characterization by tunable FSRS technique to dissect fluorescence properties is currently underway in our lab.

3.6 References

(1) Shimomura, O.; Johnson, F. H.; Saiga, Y. Extraction, Purification and Properties of Aequorin, a Bioluminescent Protein from the Luminous Hydromedusan, Aequorea. *J. Cell. Comp. Physiol.* **1962**, *59*, 223-239.

(2) Miyawaki, A.; Llopis, J.; Heim, R.; McCaffery, J. M.; Adams, J. A.; Ikura, M.; Tsien, R. Y. Fluorescent Indicators for Ca^{2+} Based on Green Fluorescent Proteins and Calmodulin. *Nature* **1997**, *388*, 882-887.

(3) Tsien, R. Y. The Green Fluorescent Protein. *Annu. Rev. Biochem.* **1998**, *67*, 509-544.

(4) Prevarskaya, N.; Skryma, R.; Shuba, Y. Calcium in Tumour Metastasis: New Roles for Known Actors. *Nat. Rev. Cancer* **2011**, *11*, 609-618.

(5) Grienberger, C.; Konnerth, A. Imaging Calcium in Neurons. *Neuron* **2012**, *73*, 862-885.

(6) Akerboom, J.; Carreras Calderon, N.; Tian, L.; Wabnig, S.; Prigge, M.; Tolo, J.; Gordus, A.; Orger, M. B.; Severi, K. E.; Macklin, J. J.; et al. Genetically Encoded Calcium Indicators for Multi-Color Neural Activity Imaging and Combination with Optogenetics. *Front. Mol. Neurosci.* **2013**, *6*, 2.

(7) Chattoraj, M.; King, B. A.; Bublitz, G. U.; Boxer, S. G. Ultra-fast Excited State Dynamics in Green Fluorescent Protein: Multiple States and Proton Transfer. *Proc. Natl. Acad. Sci. U. S. A.* **1996**, *93*, 8362-8367.

(8) Brejc, K.; Sixma, T. K.; Kitts, P. A.; Kain, S. R.; Tsien, R. Y.; Ormö, M.; Remington, S. J. Structural Basis for Dual Excitation and Photoisomerization of

the *Aequorea victoria* Green Fluorescent Protein. *Proc. Natl. Acad. Sci. U. S. A.* **1997**, *94*, 2306-2311.

(9) Zimmer, M. Green Fluorescent Protein (GFP): Applications, Structure, and Related Photophysical Behavior. *Chem. Rev.* **2002**, *102*, 759-781.

(10) Fang, C.; Frontiera, R. R.; Tran, R.; Mathies, R. A. Mapping GFP Structure Evolution During Proton Transfer with Femtosecond Raman Spectroscopy. *Nature* **2009**, *462*, 200-204.

(11) Meech, S. R. Excited State Reactions in Fluorescent Proteins. *Chem. Soc. Rev.* **2009**, *38*, 2922-2934.

(12) Zhu, L.; Liu, W.; Fang, C. A Versatile Femtosecond Stimulated Raman Spectroscopy Setup with Tunable Pulses in the Visible to Near Infrared. *Appl. Phys. Lett.* **2014**, *105*, 041106.

(13) Dietze, D. R.; Mathies, R. A. Femtosecond Stimulated Raman Spectroscopy. *ChemPhysChem* **2016**, *17*, 1224-1251.

(14) Fang, C.; Tang, L.; Oscar, B. G.; Chen, C. Capturing Structural Snapshots During Photochemical Reactions with Ultrafast Raman Spectroscopy: From Materials Transformation to Biosensor Responses. *J. Phys. Chem. Lett.* **2018**, *9*, 3253–3263.

(15) Frisch, M. J.; Trucks, G. W.; Schlegel, H. B.; Scuseria, G. E.; Robb, M. A.; Cheeseman, J. R.; Scalmani, G.; Barone, V.; Mennucci, B.; Petersson, G. A.; et al. *Gaussian 09*, Revision B.1; Gaussian, Inc.: Wallingford, CT, 2009.

(16) Zhao, Y.; Araki, S.; Wu, J.; Teramoto, T.; Chang, Y.-F.; Nakano, M.; Abdelfattah, A. S.; Fujiwara, M.; Ishihara, T.; Nagai, T.; Campbell, R. E. An Expanded Palette of Genetically Encoded Ca^{2+} Indicators. *Science* **2011**, *333*, 1888-1891.

(17) Oscar, B. G.; Liu, W.; Zhao, Y.; Tang, L.; Wang, Y.; Campbell, R. E.; Fang, C. Excited-State Structural Dynamics of a Dual-Emission Calmodulin-Green Fluorescent Protein Sensor for Calcium Ion Imaging. *Proc. Natl. Acad. Sci. U. S. A.* **2014**, *111*, 10191-10196.

(18) Tang, L.; Liu, W.; Wang, Y.; Zhao, Y.; Oscar, B. G.; Campbell, R. E.; Fang, C. Unraveling Ultrafast Photoinduced Proton Transfer Dynamics in a Fluorescent Protein Biosensor for Ca^{2+} Imaging. *Chem. Eur. J.* **2015**, *21*, 6481-6490.

(19) Tachibana, S. R.; Tang, L.; Wang, Y.; Zhu, L.; Liu, W.; Fang, C. Tuning Calcium Biosensors with a Single-Site Mutation: Structural Dynamics Insights from Femtosecond Raman Spectroscopy. *Phys. Chem. Chem. Phys.* **2017**, *19*, 7138-7146.

(20) Tang, L.; Wang, Y.; Liu, W.; Zhao, Y.; Campbell, R. E.; Fang, C. Illuminating Photochemistry of an Excitation Ratiometric Fluorescent Protein Calcium Biosensor. *J. Phys. Chem. B* **2017**, *121*, 3016-3023.

(21) Berera, R.; van Grondelle, R.; Kennis, J. T. M. Ultrafast Transient Absorption Spectroscopy: Principles and Application to Photosynthetic Systems. *Photosynth. Res.* **2009**, *101*, 105-118.

(22) McCamant, D. W.; Kukura, P.; Yoon, S.; Mathies, R. A. Femtosecond Broadband Stimulated Raman Spectroscopy: Apparatus and Methods. *Rev. Sci. Instrum.* **2004**, *75*, 4971-4980.

(23) Liu, W.; Wang, Y.; Tang, L.; Oscar, B. G.; Zhu, L.; Fang, C. Panoramic Portrait of Primary Molecular Events Preceding Excited State Proton Transfer in Water. *Chem. Sci.* **2016**, *7*, 5484-5494.

(24) Tang, L.; Liu, W.; Wang, Y.; Zhu, L.; Han, F.; Fang, C. Ultrafast Structural Evolution and Chromophore Inhomogeneity inside a Green-Fluorescent-Protein-Based Ca^{2+} Biosensor. *J. Phys. Chem. Lett.* **2016**, *7*, 1225-1230.

(25) Tang, L.; Wang, Y.; Zhu, L.; Kallio, K.; Remington, S. J.; Fang, C. Photoinduced Proton Transfer Inside an Engineered Green Fluorescent Protein: A Stepwise-Concerted-Hybrid Reaction. *Phys. Chem. Chem. Phys.* **2018**, *20*, 12517–12526.

(26) Fang, C.; Senes, A.; Cristian, L.; DeGrado, W. F.; Hochstrasser, R. M. Amide Vibrations Are Delocalized Across the Hydrophobic Interface of a Transmembrane Helix Dimer. *Proc. Natl. Acad. Sci. U. S. A.* **2006**, *103*, 16740-16745.

(27) Laptenok, S. P.; Lukacs, A.; Gil, A.; Brust, R.; Sazanovich, I. V.; Greetham, G. M.; Tonge, P. J.; Meech, S. R. Complete Proton Transfer Cycle in GFP and Its T203V and S205V Mutants. *Angew. Chem. Int. Ed.* **2015**, *54*, 9303-9307.

(28) Laptenok, S. P.; Gil, A. A.; Hall, C. R.; Lukacs, A.; Iuliano, J. N.; Jones, G. A.; Greetham, G. M.; Donaldson, P.; Miyawaki, A.; Tonge, P. J.; Meech, S. R. Infrared Spectroscopy Reveals Multi-Step Multi-Timescale Photoactivation in the Photoconvertible Protein Archetype Dronpa. *Nat. Chem.* **2018**, *10*, 845-852.

(29) Nibbering, E. T. J.; Fidder, H.; Pines, E. Ultrafast Chemistry: Using Time-Resolved Vibrational Spectroscopy for Interrogation of Structural Dynamics. *Annu. Rev. Phys. Chem.* **2005**, *56*, 337-367.

(30) McAnaney, T. B.; Park, E. S.; Hanson, G. T.; Remington, S. J.; Boxer, S. G. Green Fluorescent Protein Variants as Ratiometric Dual Emission pH Sensors. 2. Excited-State Dynamics. *Biochemistry* **2002**, *41*, 15489-15494.

(31) Henderson, J. N.; Remington, S. J. Crystal Structures and Mutational Analysis of amFP486, A Cyan Fluorescent Protein from Anemonia majano. *Proc. Natl. Acad. Sci. U. S. A.* **2005**, *102*, 12712-12717.

(32) Spry, D. B.; Fayer, M. D. Charge Redistribution and Photoacidity: Neutral versus Cationic Photoacids. *J. Chem. Phys.* **2008**, *128*, 084508.

(33) Olsen, S. Locally-Excited (LE) versus Charge-Transfer (CT) Excited State Competition in a Series of Para-Substituted Neutral Green Fluorescent Protein (GFP) Chromophore Models. *J. Phys. Chem. B* **2015**, *119*, 2566-2575.

(34) Chen, C.; Liu, W.; Baranov, M. S.; Baleeva, N. S.; Yampolsky, I. V.; Zhu, L.; Wang, Y.; Shamir, A.; Solntsev, K. M.; Fang, C. Unveiling Structural Motions of a Highly Fluorescent Superphotoacid by Locking and Fluorinating the GFP Chromophore in Solution. *J. Phys. Chem. Lett.* **2017**, *8*, 5921–5928.

(35) Lochbrunner, S.; Wurzer, A. J.; Riedle, E. Ultrafast Excited-State Proton Transfer and Subsequent Coherent Skeletal Motion of 2-(2'-hydroxyphenyl)benzothiazole. *J. Chem. Phys.* **2000**, *112*, 10699-10702.

(36) Spillane, K. M.; Dasgupta, J.; Lagarias, J. C.; Mathies, R. A. Homogeneity of Phytochrome Cph1 Vibronic Absorption Revealed by Resonance Raman Intensity Analysis. *J. Am. Chem. Soc.* **2009**, *131*, 13946-13948.

(37) Snellenburg, J. J.; Laptenok, S.; Seger, R.; Mullen, K. M.; van Stokkum, I. H. M. Glotaran: A Java-Based Graphical User Interface for the R Package TIMP. *J. Stat. Softw.* **2012**, *49*, 1-22.

(38) Tang, L.; Zhu, L.; Wang, Y.; Fang, C. Uncovering the Hidden Excited State toward Fluorescence of an Intracellular pH Indicator. *J. Phys. Chem. Lett.* **2018**, *9*, 4969-4975.

(39) Tang, L.; Zhu, L.; Taylor, M. A.; Wang, Y.; Remington, S. J.; Fang, C. Excited State Structural Evolution of a GFP Single-Site Mutant Tracked by Tunable Femtosecond-Stimulated Raman Spectroscopy. *Molecules* **2018**, *23*, 2226.

(40) Mizutani, Y.; Kitagawa, T. Direct Observation of Cooling of Heme Upon Photodissociation of Carbonmonoxy Myoglobin. *Science* **1997**, *278*, 443-446.

(41) Liu, W.; Tang, L.; Oscar, B. G.; Wang, Y.; Chen, C.; Fang, C. Tracking Ultrafast Vibrational Cooling During Excited State Proton Transfer Reaction with Anti-Stokes and Stokes Femtosecond Stimulated Raman Spectroscopy. *J. Phys. Chem. Lett.* **2017**, *8*, 997–1003.

(42) Tang, L.; Wang, Y.; Zhu, L.; Lee, C.; Fang, C. Correlated Molecular Structural Motions for Photoprotection After Deep-UV Irradiation. *J. Phys. Chem. Lett.* **2018**, *9*, 2311-2319.

(43) Wang, Y.; Tang, L.; Liu, W.; Zhao, Y.; Oscar, B. G.; Campbell, R. E.; Fang, C. Excited State Structural Events of a Dual-Emission Fluorescent Protein Biosensor for Ca^{2+} Imaging Studied by Femtosecond Stimulated Raman Spectroscopy. *J. Phys. Chem. B* **2015**, *119*, 2204-2218.

(44) Lee, S.-Y.; Zhang, D.; McCamant, D. W.; Kukura, P.; Mathies, R. A. Theory of Femtosecond Stimulated Raman Spectroscopy. *J. Chem. Phys.* **2004**, *121*, 3632-3642.

(45) Oscar, B. G.; Chen, C.; Liu, W.; Zhu, L.; Fang, C. Dynamic Raman Line Shapes on an Evolving Excited-State Landscape: Insights from Tunable Femtosecond Stimulated Raman Spectroscopy. *J. Phys. Chem. A* **2017**, *121*, 5428-5441.

(46) Ellis, S. R.; Hoffman, D. P.; Park, M.; Mathies, R. A. Difference Bands in Time-Resolved Femtosecond Stimulated Raman Spectra of Photoexcited Intermolecular Electron Transfer from Chloronaphthalene to Tetracyanoethylene. *J. Phys. Chem. A* **2018**, *122*, 3594-3605.

(47) Agmon, N. Elementary Steps in Excited-State Proton Transfer. *J. Phys. Chem. A* **2005**, *109*, 13-35.

(48) Pecourt, J.-M. L.; Peon, J.; Kohler, B. DNA Excited-State Dynamics: Ultrafast Internal Conversion and Vibrational Cooling in a Series of Nucleosides. *J. Am. Chem. Soc.* **2001**, *123*, 10370-10378.

(49) Park, J. W.; Rhee, Y. M. Electric Field Keeps Chromophore Planar and Produces High Yield Fluorescence in Green Fluorescent Protein. *J. Am. Chem. Soc.* **2016**, *138*, 13619-13629.

(50) Shu, X.; Kallio, K.; Shi, X.; Abbyad, P.; Kanchanawong, P.; Childs, W.; Boxer, S. G.; Remington, S. J. Ultrafast Excited-State Dynamics in the Green Fluorescent Protein Variant S65T/H148D. 1. Mutagenesis and Structural Studies. *Biochemistry* **2007**, *46*, 12005-12013.

(51) Wu, J.; Abdelfattah, A. S.; Miraucourt, L. S.; Kutsarova, E.; Ruangkittisakul, A.; Zhou, H.; Ballanyi, K.; Wicks, G.; Drobizhev, M.; Rebane, A.; Ruthazer, E. S.; Campbell, R. E. A Long Stokes Shift Red Fluorescent Ca^{2+} Indicator Protein for Two-Photon and Ratiometric Imaging. *Nat. Commun.* **2014**, *5*, 5262.

(52) Burgie, E. S.; Vierstra, R. D. Phytochromes: An Atomic Perspective on Photoactivation and Signaling. *Plant Cell* **2014**, *26*, 4568-4583.

(53) Mandal, D.; Tahara, T.; Meech, S. R. Excited-State Dynamics in the Green Fluorescent Protein Chromophore. *J. Phys. Chem. B* **2004**, *108*, 1102-1108.

(54) Usman, A.; Mohammed, O. F.; Nibbering, E. T. J.; Dong, J.; Solntsev, K. M.; Tolbert, L. M. Excited-State Structure Determination of the Green Fluorescent Protein Chromophore. *J. Am. Chem. Soc.* **2005**, *127*, 11214-11215.

(55) Baranov, M. S.; Lukyanov, K. A.; Borissova, A. O.; Shamir, J.; Kosenkov, D.; Slipchenko, L. V.; Tolbert, L. M.; Yampolsky, I. V.; Solntsev, K. M. Conformationally Locked Chromophores as Models of Excited-State Proton Transfer in Fluorescent Proteins. *J. Am. Chem. Soc.* **2012**, *134*, 6025-6032.

(56) Polyakov, I. V.; Grigorenko, B. L.; Epifanovsky, E. M.; Krylov, A. I.; Nemukhin, A. V. Potential Energy Landscape of the Electronic States of the GFP Chromophore in Different Protonation Forms: Electronic Transition Energies and Conical Intersections. *J. Chem. Theory Comput.* **2010**, *6*, 2377-2387.

(57) Kumpulainen, T.; Lang, B.; Rosspeintner, A.; Vauthey, E. Ultrafast Elementary Photochemical Processes of Organic Molecules in Liquid Solution. *Chem. Rev.* **2017**, *117*, 10826-10939.

(58) Peeler, J. C.; Mehl, R. A. Site-Specific Incorporation of Unnatural Amino Acids as Probes for Protein Conformational Changes. In *Unnatural Amino Acids: Methods and Protocols*; Pollegioni, L., Servi, S., Eds.; Humana Press: New York, NY, 2012; pp 125-134.

(59) Hosoi, H.; Yamaguchi, S.; Mizuno, H.; Miyawaki, A.; Tahara, T. Hidden Electronic Excited State of Enhanced Green Fluorescent Protein. *J. Phys. Chem. B* **2008**, *112*, 2761-2763.

(60) Drobizhev, M.; Makarov, N. S.; Tillo, S. E.; Hughes, T. E.; Rebane, A. Two-Photon Absorption Properties of Fluorescent Proteins. *Nat. Meth.* **2011**, *8*, 393-399.

3.7 Supplemental Information

In this work, we report the altered reaction pathways inside an engineered calcium biosensor with transient electronic and vibrational spectroscopies. Besides ESPT, we identified vibrational cooling and other relaxation pathways in the excited state as proton departs from the chromophore. Resolving the intensity and frequency dynamics of Raman marker bands before and after ESPT reaction holds the key to elucidate the photochemical reaction coordinates, despite competing pathways including nonradiative decay, which leads to the rational design strategies for better Ca^{2+} biosensors (see Section 3.4). Given the complexity of a biomolecular complex in sensing calcium ions and emitting characteristic photons, the elucidation of distinct species during a photochemical reaction inside a protein pocket remains a formidable challenge — that is the reason why tunable FSRS[1-5] has been developed to become a powerful toolset in monitoring transient molecular species, especially when they are only differed by a single proton. This current study on a well-defined allosteric biosensor also provides a model system for theoreticians and computational scientists to further refine and deepen our understanding of the intrinsic structure-energy-function relationships of functional biomolecules.

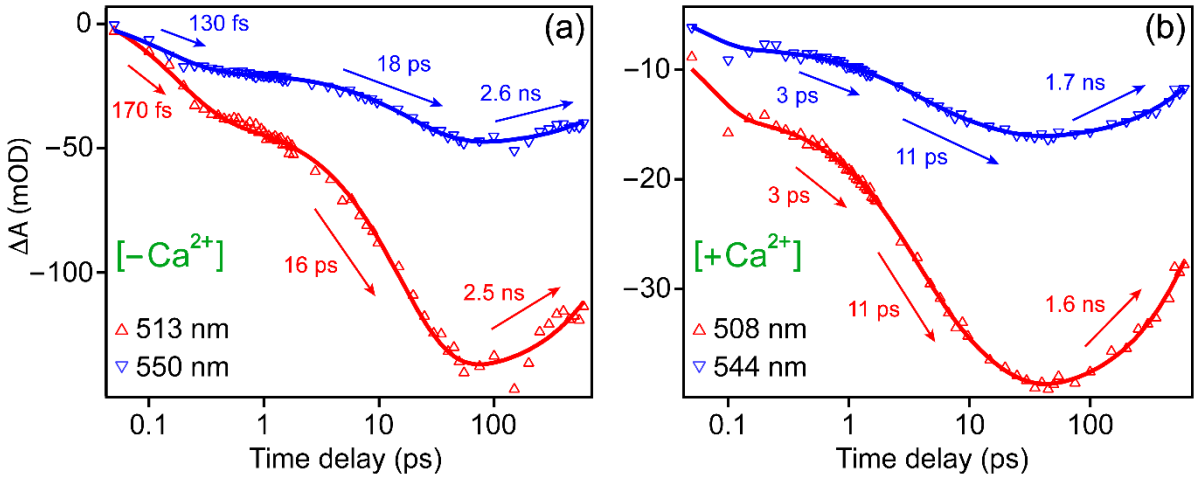

Figure 3.6. Fs-TA data traces of the Ca^{2+}-free (a) and bound (b) GEM-GECO1-P377R biosensor. A 1-nm slice was taken from the I* SE main band at 513/508 nm (red triangles) and red-side shoulder at 550/544 nm (blue triangles) for the Ca^{2+}-free and bound biosensor, respectively.

By integrating and fitting the main and shoulder SE bands, we infer the origin of the pertinent species by observing their evolution over time. Regardless of the Ca^{2+}-free or bound state, the main and shoulder bands exhibit similar rise and decay dynamics in their characteristic environment, suggesting that both bands represent the same species and the observed energy gap corresponds to a vibrational mode at ~1300 cm^{-1} (see Figure 3.4, and Figure 3.8 in Section 3.7 below) that is coupled to the downward electronic transition. The steady-state emission in Figure 3.2a also exhibits a similar vibronic band in the electronic ground state. For the SE band, the 16 and 18 ps rise time constants in the Ca^{2+}-free state resemble the 14 ps ESPT time constant retrieved from the excited state FSRS spectra (Figure 3.4c). Similarly, the 8 ps ESPT time constant from FSRS analysis of the Ca^{2+}-bound biosensor (Figure 3.4d) falls in

between the two SE rise time constants of ~3 and 11 ps, which could be considered as an ensemble average of the conformationally inhomogeneous distribution of chromophore species contributing to the observed vibrational dynamics.[4]

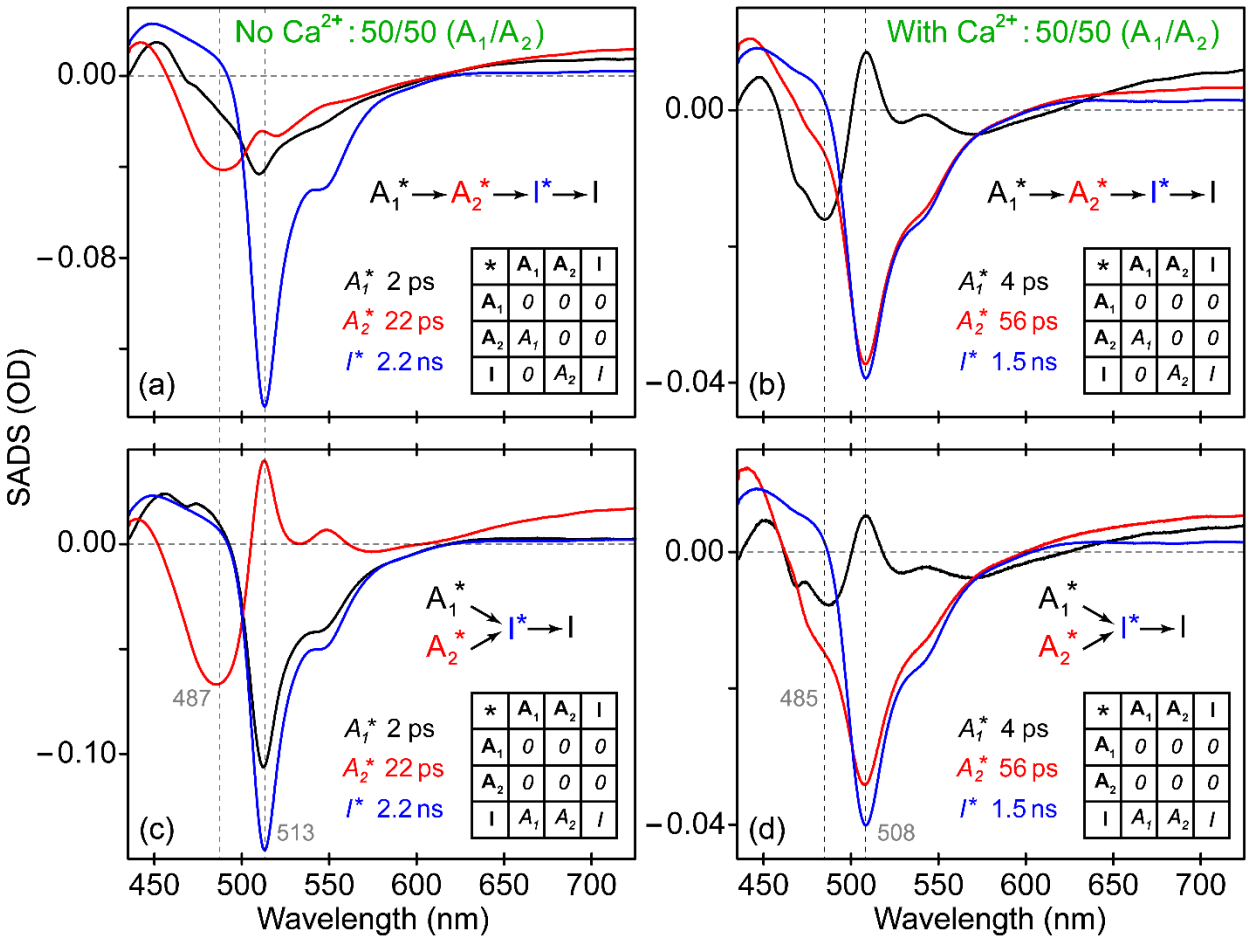

Figure 3.7. Three-component target analysis of the fs-TA spectra of the P377R biosensor. The Ca^{2+}-free/bound biosensor is fit using a sequential model in (a)/(b) or parallel model in (c)/(d). For these illustrated models, a 50%, 50% initial population of A_1*, A_2* species was used to exemplify the pertinent time constants and species dynamics. Transfer matrices are shown in the insets: the non-zero off-diagonal elements correspond to the compartmental transitions from one electronic state to the other, and the non-zero diagonal elements denote relaxation to the ground state of I.

The three-component species-associated difference spectra (SADS via target analysis) for the Ca^{2+}-free and bound samples could separate the spectra from transient

chromophore species. Multiple analysis schemes with different A* initial subpopulation ratios from 90/10 to 10/90 were implemented and compared. Also, the four, five, or six-component models do not significantly improve the root-mean-square (RMS) value and the very early species end up fitting coherent artifacts around time zero. In the Ca^{2+}-free state three-component sequential model as shown in (a), the A_1* species (more deprotonated, black) must become more protonated (A_2*, red) in 2 ps before undergoing ESPT to I* (blue), which is highly unlikely. From the experimental TA and FSRS analysis (see Section 3.4) the Ca^{2+}-free biosensor does not involve a 2 ps time constant, while the A_1* (black) trace exhibits multiple SE features in (a), which suggest that a three-component sequential model is not optimal or better than the two-component model (see Figure 3.3c). For the parallel model in (c) to analyze the Ca^{2+}-free biosensor chromophore, the time constants of 2 and 22 ps remain while the component feature resembles single species, but the A_1* species has an almost identical TA line shape to the I* species, which cannot be rationalized.

In the Ca^{2+}-bound state, the three-component sequential model in (b) yields the A_2* and I* species having similar profiles while A_2* is still convoluted with some A_1* SE at ~485 nm. This is more prevalent for the A_2* species in the Ca^{2+}-bound state parallel model in (d). Given the goal of target analysis in uncovering single species as an evolving temporal component, the multiple and unnecessarily mixed SE features in (b) and (d) are indicative of less optimal modeling.

Furthermore, the ESPT time constants of ~14/8 ps retrieved from FSRS for the Ca^{2+}-free/bound biosensor (see Figure 3.4c and d in Section 3.4) are consistent with a weighted average of the two A* species time constants in the three-component models.

However, due to distinct spectral features of A* and I* especially in the SE region, the two-component sequential model as presented in Figure 3.3 (see Section 3.4) is simpler, reasonable, and effective in retrieving the time constants of electronic population dynamics.

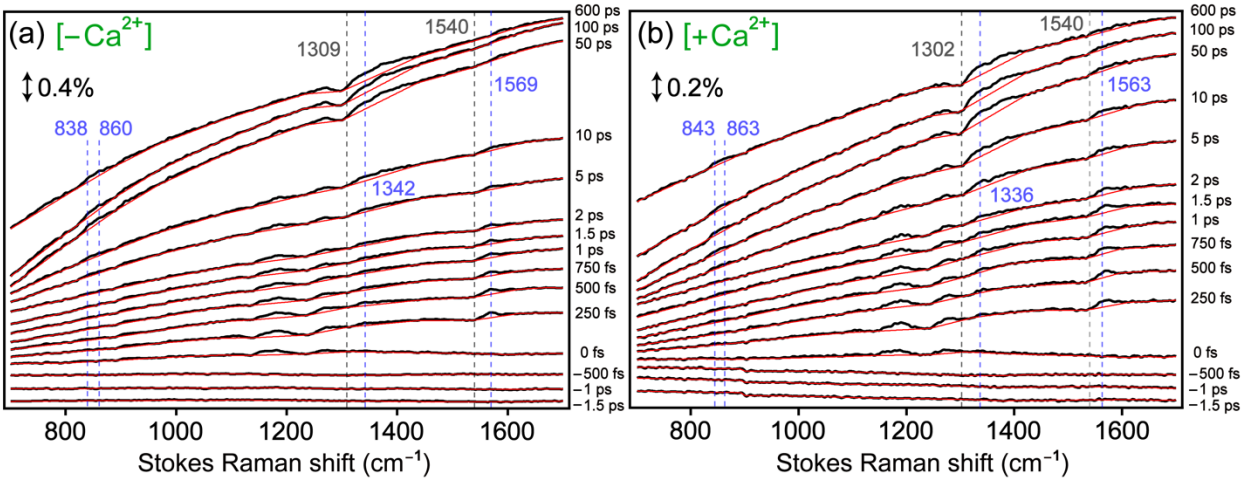

Figure 3.8. Experimental time-resolved FSRS of the Ca^{2+} (a) free and (b) bound P377R biosensor after 400 nm photoexcitation. The ground-state-subtracted excited state spectra (black) are shown with their spline baselines drawn (red). The vibronically coupled peaks are identified by the gray dashed lines at ca. 1309/1302 and 1540/1540 cm^{-1} for the Ca^{2+}-free/bound biosensor, respectively. The blue dashed lines denote the other transient Raman modes with largely absorptive line shapes (discussed in Section 3.4). The Raman gain magnitude is depicted by the vertical arrowed line.

The Raman peak intensities in (a) and (b) are not directly comparable due to different pumping efficiencies using a 400 nm actinic pump (see Figure 3.2a) and the pre-resonance conditions using a 553 nm Raman pump with respect to the I* SE band (Figure 3.3). Therefore, vibrational dynamics and the retrieved time constants from

each case were used to elucidate the effects of Ca^{2+} binding on the biosensor fluorescence properties. We also note that the broad baseline drawing around the dispersive peaks is illustrative in nature to highlight the mode intensity change due to transient accumulation of I* species, so the absolute peak line shape is not the focus[6,7] and we did not present the intensity dynamics of those spectral components to avoid potential baseline issues. Instead, we fit and display the Raman band dynamics with absorptive line shapes, e.g., ~840 and 1565 cm^{-1} in Figure 3.4c and d (frequency dynamics in Figure 3.5), to track the ESPT reaction progress.

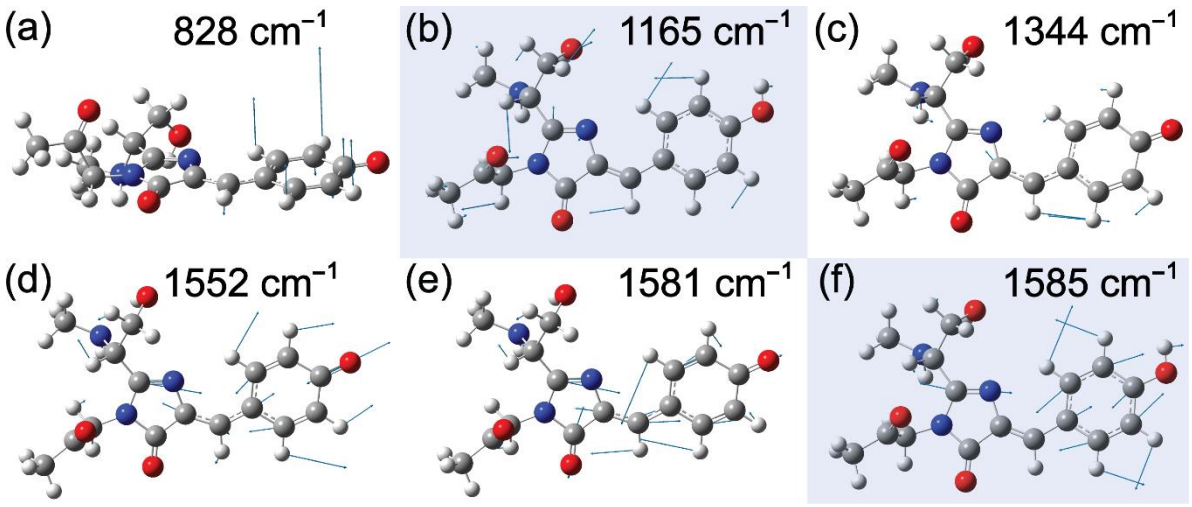

Figure 3.9. Depiction of the calculated vibrational normal modes of the protein chromophore of the GEM-GECO1-P377R biosensor. The density functional theory (DFT) calculations with the RB3LYP exchange-correlation functional and the 6-31G+(d,p) basis sets (see below Table 3.1 for details) of the geometrically optimized SYG chromophore (with methyl caps at the imidazolinone ends where the connections to the protein backbone occur) *in vacuo* were used to perform the normal mode

analysis. The mode frequencies are listed for the protonated (b and f, highlighted by the cyan shades) and deprotonated (a, c, d, and e) chromophore with a frequency scaling factor of 0.96 to help match the experimentally observed frequencies.

These Raman marker bands exhibit characteristic atomic motions that can aid the assignment of the excited state Raman modes observed by time-resolved FSRS (see Figure 3.4), especially because the time-dependent (TD-)DFT methodology only computes the vibrational energy levels without accurate information about transient electric polarizabilities.[8-10] Therefore, the focus of our calculations has been on the main atomic composition of the observed vibrational motions, and the trend of mode frequency shift upon photoexcitation (e.g., from $S_0 \rightarrow S_1$), deprotonation, conformational twisting, or a change of environment (e.g., from water to the protein interior).[4,9,11] Such a systematic approach aids the mode assignment and interpretation of the FSRS data sets.

Table 3.1. Key Raman mode assignment of the Ca^{2+}-free/bound P377R biosensor chromophore

–/+ Ca^{2+} FSRS [a] (cm^{-1})	**TD-DFT Pro. [b] (cm^{-1})**	**DFT Pro. [c] (cm^{-1})**	**DFT Pro. [d] 20° twisted**	**Vibrational motions (major)**
838 / 843				
1183 / 1185	1178	1165	1174	Phenolic ring-H scissor and bridge-H rocking with imidazolinone ring in-plane deformation
1340 / 1336				
1569/1563 [e]	1587	1585	1593	Phenolic C=C stretch with imidazolinone C=N and C=O stretch
1594 / 1593				

–/+ Ca^{2+} FSRS [a] (cm^{-1})	**TD-DFT Dep. [b] (cm^{-1})**	**DFT Dep. [c] (cm^{-1})**	**DFT Dep. [d] 20° twisted**	**Vibrational motions (major)**
838 / 843	836	828	824	Phenolic ring OOP deformation
1183 / 1185				
1340 / 1336	1348	1344	1345	Bridge-H rocking and C=C stretch with phenolic ring-H rocking
1569/1563 [e]	1536	1552	1546	Phenolic C=C and C=O stretch and imidazolinone C=N stretch with small-scale bridge C=C stretch
1594 / 1593	1572	1581	1578	Phenolic C=C stretch and bridge C=C stretch with imidazolinone C=N stretch

[a] Observed Raman mode frequencies of the Ca^{2+}-free and bound GEM-GECO1-P377R biosensor, separated by "/", using 553 nm Raman pump. The excited state mode frequency is an average value from the mid-point of the frequency dynamics fit (e.g., Figure 3.5a for the ~838 cm^{-1} mode).

[b] The excited state (S_1) normal mode frequencies of the SYG chromophore *in vacuo* were calculated using time-dependent density functional theory (TD-DFT) with the RB3LYP exchange-correlation functional[12,13] and the 6-31G+(d,p) basis sets[12] using Gaussian 09 software on a geometrically optimized protonated (Pro., A*) or deprotonated (Dep., I*) chromophore (see Figure 3.1 inset for the corresponding chemical structures with methyl caps at the imidazolinone end).[14] The vacuum environment of the chromophore during calculations is to capture the essence of protein interior wherein water molecules are scarce when compared with aqueous solution.[4,15] Previously, a reasonable match between calculated and experimental Raman mode frequencies of the embedded chromophore has been found for a number of fluorescent proteins and fluorescent protein based biosensors.[4,11,15] Since we did not directly calculate the excited-state Raman spectrum by numerical differentiation methods in a non-equilibrium state,[16] the quantized vibrational energy levels are used to assign the observed Raman modes to characteristic nuclear motions of the chromophore. A frequency scaling factor of 0.96 was applied to the calculation results to compare with the time-resolved FSRS experimental values (see Figures 3.4 and 3.5).

[c] The ground state (S_0) Raman mode frequencies of the coplanar SYG chromophore *in vacuo* were calculated using the DFT RB3LYP/6-31G+(d,p) level of theory for the geometrically optimized protonated (A) or deprotonated (B) chromophore in the electronic ground state. A frequency scaling factor of 0.96 was applied to the calculation results to compare with the ground state FSRS (Figure 3.4a and b, bottom panels). For the calculated modes in a spectrally congested region, an average of adjacent modes may be used to better match the experimentally observed band center

frequency with intrinsic conformational inhomogeneity.[4,5,11] For example, the calculated mode frequencies of B at ~1628.3 and 1665.5 cm^{-1} with similar nuclear motions yield an average frequency of 1646.9 cm^{-1} which, after applying the aforementioned scaling factor, leads to ~1581 cm^{-1}. Such mode mixing seems to be more prominent for the calculated chromophore modes in water (e.g., IEFPCM=water used in Gaussian).[9] Notably, the pertinent vibrational motions listed in this column are illustrated in Figure 3.9 for the protonated and deprotonated SYG chromophores, which could aid the excited state Raman mode assignment after TD-DFT calculations. The methyl caps do not noticeably affect such calculations regarding the mode composition and frequency so the modeling of the region connecting the chromophore to the protein backbone is reasonable.[1,4,11]

[d] To assess the effect of chromophore twisting, the same ground-state DFT calculations were implemented for the protonated (upper table) and deprotonated (lower table) chromophore as the dihedral angle along the ethylenic bridge C=C bond is set at 20º, which is a reasonable value considering the structural constraints exerted by the protein matrix on the embedded chromophore.[11,15] The overall trend is that the protonated/deprotonated chromophore responds to the chromophore ring twisting with the Raman mode frequency blueshift/redshift, respectively.

[e] This mode is present throughout our experimental detection time window (see Figure 3.4 and Figure 3.8 above), which likely corresponds to a mixture of (spectrally overlapping) A* and I* species, hence the experimentally observed mode frequency red shift and intensity complex dynamics as ESPT reaction occurs inside the protein

pocket.[9,15] This is in contrast to the other Raman marker bands which exhibit clear decay (~1184 cm^{-1}, A*) or rise (~840, 1340, 1590 cm^{-1}, I*) dynamics.

3.8 Supplemental References

(1) Tang, L.; Liu, W.; Wang, Y.; Zhao, Y.; Oscar, B. G.; Campbell, R. E.; Fang, C. Unraveling Ultrafast Photoinduced Proton Transfer Dynamics in a Fluorescent Protein Biosensor for Ca^{2+} Imaging. *Chem. Eur. J.* **2015**, *21*, 6481-6490.

(2) Dietze, D. R.; Mathies, R. A. Femtosecond Stimulated Raman Spectroscopy. *ChemPhysChem* **2016**, *17*, 1224-1251.

(3) Liu, W.; Wang, Y.; Tang, L.; Oscar, B. G.; Zhu, L.; Fang, C. Panoramic Portrait of Primary Molecular Events Preceding Excited State Proton Transfer in Water. *Chem. Sci.* **2016**, *7*, 5484-5494.

(4) Tachibana, S. R.; Tang, L.; Wang, Y.; Zhu, L.; Liu, W.; Fang, C. Tuning Calcium Biosensors with a Single-Site Mutation: Structural Dynamics Insights from Femtosecond Raman Spectroscopy. *Phys. Chem. Chem. Phys.* **2017**, *19*, 7138-7146.

(5) Fang, C.; Tang, L.; Oscar, B. G.; Chen, C. Capturing Structural Snapshots During Photochemical Reactions with Ultrafast Raman Spectroscopy: From Materials Transformation to Biosensor Responses. *J. Phys. Chem. Lett.* **2018**, *9*, 3253–3263.

(6) Oscar, B. G.; Chen, C.; Liu, W.; Zhu, L.; Fang, C. Dynamic Raman Line Shapes on an Evolving Excited-State Landscape: Insights from Tunable Femtosecond Stimulated Raman Spectroscopy. *J. Phys. Chem. A* **2017**, *121*, 5428-5441.

(7) Ellis, S. R.; Hoffman, D. P.; Park, M.; Mathies, R. A. Difference Bands in Time-Resolved Femtosecond Stimulated Raman Spectra of Photoexcited Intermolecular Electron Transfer from Chloronaphthalene to Tetracyanoethylene. *J. Phys. Chem. A* **2018**, *122*, 3594-3605.

(8) McHale, J. L. *Molecular Spectroscopy*; Prentice-Hall: Upper Saddle River, NJ, 1999.

(9) Oscar, B. G.; Liu, W.; Zhao, Y.; Tang, L.; Wang, Y.; Campbell, R. E.; Fang, C. Excited-State Structural Dynamics of a Dual-Emission Calmodulin-Green Fluorescent Protein Sensor for Calcium Ion Imaging. *Proc. Natl. Acad. Sci. U. S. A.* **2014**, *111*, 10191-10196.

(10) Petrone, A.; Cimino, P.; Donati, G.; Hratchian, H. P.; Frisch, M. J.; Rega, N. On the Driving Force of the Excited-State Proton Shuttle in the Green Fluorescent

Protein: A Time-Dependent Density Functional Theory (TD-DFT) Study of the Intrinsic Reaction Path. *J. Chem. Theory Comput.* **2016**, *12*, 4925-4933.

(11) Wang, Y.; Tang, L.; Liu, W.; Zhao, Y.; Oscar, B. G.; Campbell, R. E.; Fang, C. Excited State Structural Events of a Dual-Emission Fluorescent Protein Biosensor for Ca^{2+} Imaging Studied by Femtosecond Stimulated Raman Spectroscopy. *J. Phys. Chem. B* **2015**, *119*, 2204-2218.

(12) Stephens, P. J.; Devlin, F. J.; Chabalowski, C. F.; Frisch, M. J. Ab Initio Calculation of Vibrational Absorption and Circular Dichroism Spectra Using Density Functional Force Fields. *J. Phys. Chem.* **1994**, *98*, 11623-11627.

(13) Gritsenko, O. V.; Schipper, P. R. T.; Baerends, E. J. Exchange and Correlation Energy in Density Functional Theory: Comparison of Accurate Density Functional Theory Quantities with Traditional Hartree–Fock Based Ones and Generalized Gradient Approximations for the Molecules Li_2, N_2, F_2. *J. Chem. Phys.* **1997**, *107*, 5007-5015.

(14) Frisch, M. J.; Trucks, G. W.; Schlegel, H. B.; Scuseria, G. E.; Robb, M. A.; Cheeseman, J. R.; Scalmani, G.; Barone, V.; Mennucci, B.; Petersson, G. A.; et al. *Gaussian 09*, Revision B.1; Gaussian, Inc.: Wallingford, CT, 2009.

(15) Fang, C.; Frontiera, R. R.; Tran, R.; Mathies, R. A. Mapping GFP Structure Evolution During Proton Transfer with Femtosecond Raman Spectroscopy. *Nature* **2009**, *462*, 200-204.

(16) Barclay, M. S.; Quincy, T. J.; Williams-Young, D. B.; Caricato, M.; Elles, C. G. Accurate Assignments of Excited-State Resonance Raman Spectra: A Benchmark Study Combining Experiment and Theory. *J. Phys. Chem. A* **2017**, *121*, 7937-7946.

Chapter 4 Transient electronic and vibrational signatures during reversible photoswitching of a cyanobacteriochrome photoreceptor

Published in: **Sean R. Tachibana**, Longteng Tang, Cheng Chen, Liangdong Zhu, Yuka Takeda, Keiji Fushimi, Travis K. Seevers, Rei Narikawa, Moritoshi Sato, and Chong Fang* **(2021)** "Transient electronic and vibrational signatures during reversible photoswitching of a cyanobacteriochrome photoreceptor", *Spectrochim. Acta A*, 250, 119379. DOI: 10.1016/j.saa.2020.119379.

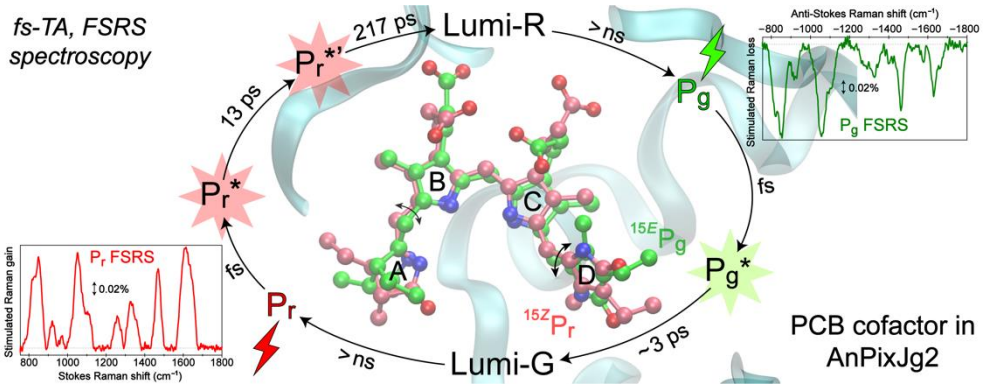

"It is difficult to understand the universe if you only study one planet." – Miyamoto Musashi

4.1 Abstract

Cyanobacteriochromes (CBCRs) are an emerging class of photoreceptors that are distant relatives of the phytochromes family. Unlike phytochromes, CBCRs have gained popularity in optogenetics due to their highly diverse spectral properties spanning the UV to near-IR region and only needing a single compact binding domain. AnPixJg2 is a CBCR that can reversibly photoswitch between its red-absorbing ($^{15Z}P_r$) and green-absorbing ($^{15E}P_g$) forms of the phycocyanobilin (PCB) cofactor. To reveal primary events of photoconversion, we implemented femtosecond transient absorption spectroscopy with a homemade LED box and a miniature peristaltic pump flow cell to track transient electronic responses of the photoexcited AnPixJg2 on molecular time scales. The 525 nm laser-induced P_g-to-P_r reverse conversion exhibits a ~3 ps excited-state lifetime before reaching the conical intersection (CI) and undergoing further relaxation on the 30 ps time scale to generate a long-lived Lumi-G ground state intermediate en route to P_r. The 650 nm laser-induced P_r-to-P_g forward conversion is less efficient than reverse conversion, showing a longer-lived excited state which requires two steps with ~13 and 217 ps time constants to enter the CI region. Furthermore, using a tunable ps Raman pump with broadband Raman probe on both the Stokes and anti-Stokes sides, we collected the pre-resonance ground-state femtosecond stimulated Raman spectroscopy (GS-FSRS) data with mode assignments aided by quantum calculations. Key vibrational marker bands at ~850, 1050, 1615, and 1649 cm^{-1} of the P_r conformer exhibit a notable blueshift to those of the P_g conformer inside AnPixJg2, reflecting the PCB chromophore terminal D (major) and A (minor) ring twist along the primary photoswitching reaction coordinate. This integrated

ultrafast spectroscopy and computational platform has the potential to elucidate photochemistry and photophysics of more CBCRs and photoactive proteins in general, providing the highly desirable mechanistic insights to facilitate the rational design of functional molecular sensors and devices.

4.2 Introduction

Photosensing proteins allow living organisms to detect light and convert incident photons into a biochemical response [1]. Almost all proteins can absorb light in the UV region due to the presence of aromatic amino acids such as tyrosine, tryptophan, or phenylalanine, but the ability to detect visible to near-IR light is desirable for bioimaging [2-4] and optogenetic applications [5-8]. Besides the photoreceptors found in the eyes of animals, phytochromes and cyanobacteriochromes (CBCRs) are the best known visible light receptors [9-11]. Phytochromes share the conserved PAS (Per/ARNT/Sim), GAF (cGMP-phosphodiesterase/adenylate cyclase/formate hydrogen lyase transcription activator FhlA), and PHY (phytochrome-specific) domains, wherein the GAF domain is responsible for covalently binding a linear tetrapyrrole (bilin) chromophore that is necessary for light detection [1]. The PAS-GAF-PHY architecture is required for a functional photocycle in canonical phytochromes. In contrast, CBCRs only require the GAF domain for proper chromophore binding and photoconversion (e.g., regulating the phototaxis of cells), which allows for a more desirable size for application purposes. Some of the most common bilin chromophores are phycocyanobilin (PCB, found in algae and cyanobacteria), phytochromobilin (PΦB, found in plants), and biliverdin IXα (BV, a

mammalian-intrinsic chromophore) that allow this superfamily to obtain a diverse spectral property from the UV to near-IR region. Upon photoexcitation, these photosensors undergo a *Z*/*E* isomerization at the C15=C16 bond (by the D-ring) of the cofactor chromophore (Fig. 4.1b) [9,12]. As these photosensors undergo the light-induced conversion, they adopt a Lumi-intermediate state where the chromophore resides in a twisted conformational state but the overall protein has not fully relaxed to establish the new chromophore environment.

In the phytochrome and CBCR family, many proteins share similar chromophores and GAF domains, yet they are able to display different spectral properties and dynamics. Previous studies of a popular cyanobacterial phytochrome, Cph1, have reported the ultrafast dynamics for P_r/P_{fr} (red/far-red) photoconversion [9,13,14]. Dasgupta et al. reported a major 3 ps time constant responsible for the initial *Z*-to-*E* isomerization at the C15=C16 bond of the bilin prosthetic group [9]. The isomerization leads to production of Lumi-R* (the asterisk indicates the electronic excited state) population that decays to the Lumi-R ground state on the ~30 ps time scale. A closely related CBCR, NpR6012g4, was studied by Kim et al. via ultrafast spectroscopy of both photoconversion ($P_g \leftrightarrow P_r$) processes [15,16], invoking heterogeneous ground-state populations that photoconvert on different time scales. Overall, the forward ($^{15Z}P_r$ to $^{15E}P_g$) photoconversion exhibits a longer excited-state lifetime and reaches the conical intersection (CI) after ~75 ps to 1 ns. The reverse ($^{15E}P_g$ to $^{15Z}P_r$) photoconversion shows a shorter excited-state lifetime and reaches the CI after ~2 ps. When comparing the photoconversion of P_r to P_g in CBCR with P_r to P_{fr} in Cph1, they share the same cofactor 15*Z*-to-15*E* isomerization but differ in the

hypso/bathochromic shift, quantum yield (see Section 3.3 below), and change of LUMO energy. For the P_r-to-P_g transition, the LUMO is destabilized whereas the P_r-to-P_{fr} photosensors show a stabilized LUMO [17].

In this work, we investigated one of the first described hypsochromic red/green CBCR GAF2 protein encoded from *Anabaena* sp. PCC7120 (AnPixJg2) [18,19]. Under ambient light, AnPixJg2 adopts a mix of red light-absorbing ($^{15Z}P_r$) and green light-absorbing ($^{15E}P_g$) species, with the superscripts highlighting the photoinduced *Z*/*E* isomerization of a key double bond (C15=C16, Fig. 4.1b) adjacent to the most flexible D-ring of the chromophore (i.e., between the 15*Z* isomer at the resting "red" state and the 15*E* isomer at the photoproduct "green" state). By exciting AnPixJg2 with red or green light, the protein photoconverts to the P_g and P_r states in a reversible manner. Although AnPixJg2 has its size advantage over the bulkier phytochromes, AnPixJg2 utilizes PCB as its chromophore which is biologically unavailable in mammalian cells. In addition, AnPixJg3 (GAF3) is photo-inactive whereas AnPixJg4 (GAF4) shows P_r-to-P_g photoconversion and rapid P_g-to-P_r dark reversion [8,18]. Therefore, mechanistic insights into the structure and dynamics of key residues, which play important roles for photoconversion, would enable protein engineers to identify photoactive GAF domains through amino acid sequencing, site-specific mutagenesis, and targeted evolution. Previous nanosecond studies on AnPixJ has provided information of four intermediates formed on the nanosecond to millisecond time scales [20], but deeper insights into the primary photodynamic events on even shorter time scales would allow for a fuller picture of photoconversion that leads to function. To help remedy these shortcomings with fundamental understanding, we have implemented a series of studies, first of

which utilized femtosecond transient absorption (fs-TA) and global analysis, followed by the wavelength-tunable ground-state femtosecond stimulated Raman spectroscopy (GS-FSRS) and quantum calculations to delineate the ultrafast dynamics of both photoswitching processes between P_r and P_g states of AnPixJg2.

4.3 Experimental Material and Methods

4.3.1 Protein expression

The His-tagged AnPixJg2 (amino acid positions 221–397) and AnPixJg2_BV4 inserted into pET28a vector (Novagen) have been constructed in the previous studies [18,21]. These plasmids were transferred into the *Escherichia coli* strain C41 (Cosmo Bio) harboring phycocyanobilin (PCB) synthetic system (pKT271-C0185) or biliverdin (BV) synthetic system (pKT270) for protein expression [22,23]. The bacterial cells were grown on Lysogeny Broth (LB) agar medium at 37 °C and selected by kanamycin and chloramphenicol (each final concentration, 20 μg mL^{-1}). The selected cells were cultured in 1 L LB medium at 37 °C until the cell optical density at 600 nm was reached at 0.4–0.8. Subsequently, isopropyl β-D-1-thiogalactopyranoside (final concentration, 0.1 mM) was added into the culture media and these cells were cultured at 18 °C overnight to induce the protein expression.

4.3.2 Protein extraction and purification

After protein expression was induced, the culture broth was centrifuged at 5,000 g for 15 min to collect cells and then frozen at –80 ºC. The cells were suspended in a

lysis buffer (20 mM HEPES-NaOH pH=7.5, 0.1 M NaCl, and 10% (w/v) glycerol) and disrupted by Emulsiflex C5 high-pressure homogenizer at 12,000 psi (Avestin, Inc.). The mixtures were centrifuged at 165,000 g for 30 min to remove pellets. The collected solutions were filtered through a 0.2 μm cellulose acetate membrane. Followed by the addition of imidazole (final concentration, 30 mM), the solution was loaded onto a nickel-affinity His-trap column (GE Healthcare) using an ÄKTAprime plus (GE Healthcare). After washing the column with the lysis buffer containing 30 to 100 mM imidazole, His-tagged proteins were purified using the lysis buffer containing 100 to 400 mM imidazole with a linear gradient system (1 mL/min, total 15 min). The purified proteins were incubated with 1 mM EDTA on ice for 1 h and then dialyzed against the lysis buffer to remove imidazole and EDTA.

4.3.3 LED box design and flow cell methods

The homemade 3D-printed box measures 10 × 10 × 6 cm^3 (L × W × H) with a 5-mm-diameter hole centered on each side [24]. The sample holder was printed at the box center, ~4 cm away from the LEDs inserted through the holes on four sides. Four Broadcom Limited 5 mm through-hole cyan LEDs centered at 505 nm were used to photoconvert P_g to P_r, operated at 3.2 V and 20 mA per LED. The P_r-to-P_g photoconversion used four VCC 5 mm though-hole red LEDs centered at 650 nm working at 2.1 V and 20 mA per LED. The measured irradiation power of the four 505 nm and 650 nm LEDs at the sample holder is ~3.2 mW and 1.0 mW, respectively. The CBCR sample was circulated from the LED box to a 1-mm-pathlength quartz flow cell using a Gikfun 12V DC peristaltic pump. A 1 × 2 mm (ID x OD) uxcell silicone tubing

was used to keep the total loop volume of ~1.8 mL. AnPixJg2 was kept in its dominant P_r or P_g forms under constant illumination of 505 or 650 nm LEDs, respectively. Fresh P_r or P_g sample solution was continuously flowed into the laser beam path in the optical setup to observe the photoconversion process via time-resolved electronic spectroscopy and collect the associated ground-state vibrational spectra (*vide infra*).

The flow rate was calculated by measuring the time (83 s) to flow 10 mL sample solution at 0.12 mL/s. Given the flow cell dimension of $0.8 \times 0.1 \times 4$ cm^3 (L × W × H) with a total volume of 0.3 mL (48-Q-1, Starna Cells), the top surface area is 0.08 cm^2, so the distance that solution can flow through the cell per second is 1.5 cm. The diameter of laser focal point at the sample was measured to be ~150 μm (0.015 cm), hence it takes ~10 ms to completely refresh the sample within the entire laser spot. Since each spectral data point was collected in our experiments with 3,000 laser shots (see Section 2.4 below) at 1 kHz repetition rate, recording the signal consecutively in the chopper on and off cycle, there are 5 laser pulses acting as the pump (with the corresponding probe) before the sample solution becomes completely replenished, then repeated for 300 times to increase the signal-to-noise ratio. Though the excited sample solution may have a very small percentage of transient photoswitching products (e.g., Lumi-R or Lumi-G as detailed in Section 3 below) within each five-pump-pulse cycle, while the pump wavelength has a weak overlap with the absorption of the intermediates (Lumi-G or Lumi-R) or final products (P_r or P_g, see Fig. 4.1a), the reported ultrafast electronic spectra on the femtosecond to nanosecond time scales are not affected and thus accurately reflect the chromophore dynamics under investigation.

4.3.4 Steady-state electronic spectroscopy

The steady-state absorption spectra of CBCR samples in buffer solution housed in a 1-mm-pathlength quartz cuvette (Spectrosil 1-Q-1, Starna Cells) were collected by a Thermo Scientific Evolution 201 UV/Visible spectrophotometer. The protein sample concentration was set at OD≈1 per mm for the 648 nm absorption peak under ambient conditions (see Figs. 4.1a and 4.6 in Section 4.7). Meanwhile, the steady-state emission spectra of the protein samples in buffer were examined using a Shimadzu RF-6000 spectrofluorophotometer, wherein the arc lamp was also used for the excitation-dependent absorbance measurements (Fig. 4.8, see Section 4.7). For each case, the excitation slit width was set to 5.0 nm and a mirror was placed on the back to allow for the excitation light to reflect back and cover the full area of the sample quartz cuvette. Before each data collection, the sample was exposed under ambient light for 5 min to fully convert back to the native state. The sample was then photoexcited for 1 min before promptly collecting the absorption spectrum. All other ambient lights in the lab were turned off to minimize any back photoconversion. All the experiments were performed at room temperature and 1 atm pressure.

In the Narikawa lab, UV/Visible absorption spectra of the newly prepared proteins were recorded with a Shimadzu UV-2600 spectrophotometer at room temperature. Monochromatic light at various wavelengths for inducing photoconversion was generated by an Opto-Spectrum Generator (Hamamatsu Photonics, Inc.): P_g form, at 540 nm; P_r form, at 650 nm (see Fig. 4.6 in Section 4.7).

4.3.5 Femtosecond transient absorption (fs-TA) spectroscopy and femtosecond stimulated Raman spectroscopy (FSRS)

Time-resolved light-induced electronic responses of the CBCR cofactor were collected via a fs-TA setup with ultrafast laser pulses from a Ti:sapphire-based regenerative laser amplifier (Legend-Elite-USP-1K-HE, Coherent, Inc.) seeded by a Ti:sapphire-based oscillator (Mantis-5, Coherent, Inc.). The fundamental output laser pulse train has a center wavelength of ~800 nm, average power of ~3.70 W, and repetition rate of 1 kHz, which was split up to generate the tunable fs actinic pump (ca. 480–720 nm) for photoexcitation, ps Raman pump (ca. 480–720 nm), and fs supercontinuum white light (SCWL) probe [25,26]. In particular, we used a home-built two-stage noncollinear optical parametric amplifier (NOPA) to generate the 525 and 650 nm actinic pump with ~0.3 mW average power for fs-TA experiments, initiating the $P_g \rightarrow P_r$ and $P_r \rightarrow P_g$ processes, respectively. Temporal compression of the actinic pump was achieved by a chirped mirror pair (DCM-12, 400–700 nm, Laser Quantum, Inc.). The broadband probe beam was created by focusing a small portion of the fundamental laser pulses on a 2-mm-thick quartz cuvette filled with deionized water, followed by temporal compression via a chirped mirror pair (DCM-9, 450–950 nm, Laser Quantum, Inc.). The pump and probe beams were focused on the sample solution in a 1-mm-thick quartz flow cell (see Section 2.2), and the cross-correlation time between the incident fs pump and probe pulses was measured to be ~120 fs in methanol housed in the 1-mm-thick quartz cuvette. A motorized linear translation stage (NRT150, Thorlabs, Inc.) was used to precisely control the time delay up to 900 ps for the preceding actinic pump (versus the probe fixed in time).

Using the aforementioned fs laser amplifier system, the light-induced vibrational responses of the CBCR cofactor were collected via FSRS methodology in the electronic ground state (S_0). The ps Raman pump was generated by a home-built three-stage NOPA system, which consists of one fs-NOPA and spectral filter that produce the ps tunable seed pulse as well as a subsequent two-stage ps-NOPA for intensity amplification, while the ps 400 nm pump pulses were generated by a home-built second harmonic bandwidth compressor (SHBC) of the fs 800 nm fundamental laser pulses [27]. Using a neutral density filter, we set the output ps Raman pump power to ~2 mW at 500, 596, 633, and 678 nm (specific wavelengths used in FSRS experiments). In addition, we implemented the conventional FSRS setup with a ps, ~2 mW, 792 nm Raman pump to achieve a pre-resonance condition while minimizing spectral overlap with the P_g and P_r absorption bands (hence photoswitching behavior, see Figs. 4.6 and 4.7 in Section 4.7). All the laser pulses were parallel polarized.

In the fs-TA and FSRS setups, a phase-locked optical chopper (Newport 3501) was inserted in the beam path of the actinic pump and Raman pump, respectively. Time zero was set when either pump pulse is coincident with the SCWL probe pulse at the focusing point on the sample cell. The transmitted probe was collimated and focused into an imaging spectrograph (IsoPlane SCT-320, Princeton Instruments, Inc.) with a reflective grating (300 grooves/mm, 300 nm blaze wavelength for TA; 1200 grooves/mm, 500 nm blaze wavelength for FSRS) for dispersed detection and an integrated front-illuminated CCD array camera (PIXIS:100F, Princeton Instruments, Inc.) at the exit plane. To improve the signal-to-noise ratio, we used 3,000 laser shots per point and six sets in fs-TA (hence 9,000 spectra averaged at each time delay point),

and 3,000 laser shots per point and 60 sets in FSRS (hence 90,000 spectra averaged for each ground-state Raman spectrum) [28]. To overlay the GS-FSRS spectra collected on the Stokes and anti-Stokes sides for comparison, the Raman intensity and Raman shift axes need to be multiplied by –1 for the latter case [28,29].

4.3.6 Quantum calculations

The vibrational normal mode frequencies of the PCB cofactor of AnPixJg2 in the electronic ground state (S_0) were calculated *in vacuo* with density functional theory (DFT) at the RB3LYP level using Gaussian 16 software [30]. The PCB chromophore in P_r form was directly taken from the reported crystal structure of AnPixJg2 (PDB ID:3W2Z) [19]. The two propionate ($–C_2H_4COO^-$) groups on the B and C rings were removed and capped with methyl ($–CH_3$) groups to avoid calculation complexation, while proper numbers of hydrogen atoms were added to the chemical structure using GaussView 6. The total number of charges is +1 (i.e., a protonated nitrogen site on the C ring). To mimic structural restraints from the PCB local environment in the GAF2-binding pocket, two bridge-dihedral angles between the C and D rings were fixed to their values in the reported crystal structure before optimization. The PCB structure was first optimized with 3-21G basis sets, further optimized with 6-31G, then 6-31G(d,p) basis sets, followed by the vibrational frequency calculation in the resting state (i.e., P_r). Due to the lack of crystal structure with PCB in the P_g state of AnPixJg2, we adopted the P_g crystal structure of Slr1393g3 (PDB ID: 5M82) [31], which is also a red/green CBCR [32] and in close relationship with AnPixJg2 [11]. The PCB chromophore structure therein shows both twisting of the D and A rings. Therefore, the

two dihedral angles between A and B rings were also fixed, in addition to the two dihedral angles between C and D rings, before geometric optimization. The P_g molecular structure was then optimized and vibrational frequencies were calculated following the same steps as calculations for the P_r structure to provide an informative comparison between these two conformers. The Raman spectra were exported with 10 cm^{-1} half width at half height (HWHH) and 9 cm^{-1} step size as well as a frequency scaling factor of 0.97 [33,34] to juxtapose with the experimental FSRS spectra collected in the electronic ground state of the respective PCB conformers in AnPixJg2 (*vide infra*).

4.4 Results and Discussion

4.4.1 Steady-state and time-resolved electronic spectroscopy

In order to keep AnPixJg2 in the P_r or P_g conformers, a home-built LED box was made that fits four 5 mm through-hole LEDs with a center wavelength of 505 or 650 nm. Approximately 2 mL of AnPixJg2 in buffer was kept at the center of the LED box with an OD of ~1/mm at the P_r absorption peak (~650 nm, see Fig. 4.1a). The sample was pumped into a flow cell so no LED light could be scattered into the optical setup for fs-TA and FSRS experiments, while allowing for new fresh sample to be flown in (see Sections 2.2 and 2.3). In fs-TA setup, the photoconversion reaction was initiated using the fs-actinic pump centered at 525 nm (Fig. 4.1a, green dashed) and 650 nm (Fig. 4.1a, red dashed) for the $P_g \rightarrow P_r$ and $P_r \rightarrow P_g$ process, respectively. As a control, the sample was placed in the actinic pump beam path before it was focused (to less than 150 μm diameter at the sample spot [35], see Section 2.2) and we observed a

clear color change within seconds, indicating that the fs actinic pump pulse train is capable of photoswitching AnPixJg2 between conformers.

Starting from time zero of photoexcitation, the $P_g \rightarrow P_r$ reaction shows three major features at ~690, 620, and 544 nm (Fig. 4.2a). The negative band around 544 nm is attributed to the ground-state bleaching (GSB) of the photoexcited P_g population that overlaps with the residual scattering from the actinic pump (see Fig. 4.8a in Section 4.7). A probe-dependent fit was taken at the bluer 504 nm (Fig. 4.2c, blue) to retrieve clearer GSB dynamics without significant influence from the pump scattering at 525 nm and the rising excited-state absorption (ESA) band around 595 nm (tentatively assigned here, see below for details). Since the GSB recovery was tracked on the blue edge with a reduced signal-to-noise ratio (thus hindering an accurate assessment of the long-time recovery percentage on the tens of ps to hundreds of ps time scales), only major dynamic components of ~100 fs and 5 ps were retrieved. The 5 ps time constant is consistent with other reported $^{15E}P_g$-to-$^{15Z}P_r$ conversions in similar CBCRs [16], which is longer than the ca. 1–3 ps observed for the PCB cofactor in Cph1 phytochrome reverse and forward photoconversions [9,14].

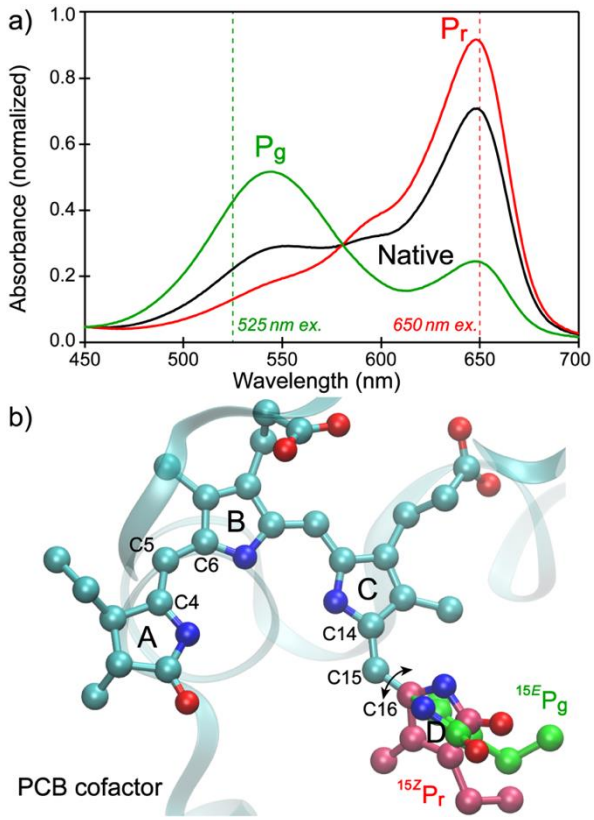

Fig. 4.1. Steady-state absorption profiles of the AnPixJg2 cofactor. (a) Ground-state electronic absorption spectra of the AnPixJg2-PCB native (black), $^{15Z}P_r$ (red), and $^{15E}P_g$ (green) species normalized at 280 nm, obtained upon 1 min irradiation of ambient white light, 505 nm LEDs, and 650 nm LEDs, respectively. The P_r form has a λ_{max}=648 nm and a shoulder at 592 nm while the P_g form has a λ_{max}=544 nm. The actinic pump wavelengths in TA experiments are noted by dashed lines. (b) Crystal structure of the PCB cofactor in the P_r state (PDB ID: 3W2Z) and illustration of the D-ring twist in the P_g state inside the protein pocket (a model structure based on Slr1393g3, PDB ID: 5M82; see Graphical Abstract for directly overlaid structures). The light-induced $P_r \rightarrow P_g$ switching thus represents a primary photoreaction with *Z*-to-*E* isomerization of the chromophore with twisting (black curved arrows, D-ring colored from red to green by ~90° for illustration) around the C15=C16 bridge between the C/D rings. Carbon, nitrogen, and oxygen atoms are shown as cyan, blue, and red spheres, respectively, while hydrogen atoms are omitted for simplicity.

The dominant positive band around 692 nm corresponds to the P_g* ESA (the asterisk denotes the electronic excited state, e.g., the first singlet excited state S_1) most likely from S_1 to S_2 because the band reaches maximum intensity close to time zero and is located on the red edge (i.e., lower energy side of the spectral detection window). Another P_g* feature that starts from time zero is the negative band at ~649 nm, which represents the downward stimulated emission (SE) transition from S_1 to S_0. Both P_g* bands (ESA and SE) decay within tens of ps in the TA contour plot (Fig. 4.2a) with ~3.5 and 2.8 ps time constants (Fig. 4.2b, red and Fig. 4.2c, green) that largely match the P_g GSB recovery component of ~5 ps, supporting a peaked CI that bifurcates into different species [36,37]. This few-ps time scale likely involves local orientational relaxation of the chromophore D-ring and its immediate vicinity. The longer 22 and 32 ps decay components of the P_g* ESA and SE bands are attributed to the relaxation of the photoconverted species after the CI, while the additional ~1.6 ns decay of the P_g* SE band probes the (weak) fluorescence lifetime back to P_g.

The most interesting feature in the photoinduced $P_g \rightarrow P_r$ transition is the rise of a long-lived absorption band around 595 nm. This transient band appears after several ps with the retrieved time constants of ~120 fs (decay), 3.1 ps (rise), 19 ps (rise), and 1 μs (decay) (Fig. 4.2b, black). The sub-ps component overlaps with the above-mentioned GSB and SE bands, resulting in a gradual signal rise from the negative to positive region. In contrast to the P_g* ESA band at 692 nm that diminishes after ~50 ps, the long-lived characteristic of the 595 nm positive band suggests that it is more likely associated with a ground-state population of Lumi-G. The 1 μs decay time constant was used to estimate the Lumi-G lifetime that extends well beyond our

detection time window (see Section 2.4). For corroboration, Fukushima and coworkers identified two metastable ground-state intermediates for the P_g-to-P_r photoconversion within ~50 ns and 190 μs [20]. The 3.1 ps rise component corresponds to the P_g* species moving into the CI, which closely matches the decay of both the P_g* ESA (3.5 ps) and SE (2.8 ps) as well as the GSB recovery (5 ps). The slight 19 ps rise component could represent further relaxation of Lumi-G that is evident by the noticeable blueshift of the ~600 nm absorption band (Fig. 4.2a) [38], also in accord with the 22–32 ps time constants retrieved from the P_g* decay dynamics (Fig. 4.2b,c).

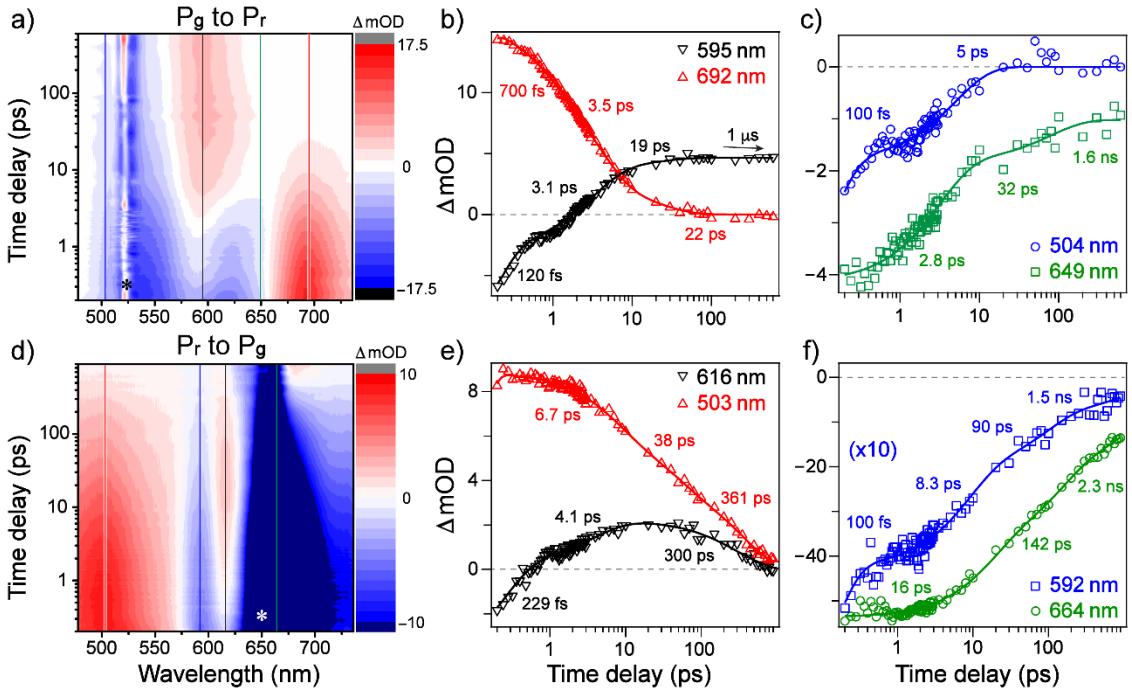

Fig. 4.2. Time-resolved electronic spectra during reversible photoswitching processes of AnPixJg2. The fs-TA contour plot of (a) $P_g \rightarrow P_r$ and (d) $P_r \rightarrow P_g$ transition was collected using a 525 nm actinic pump with 650 nm LEDs and 650 nm actinic pump with 505 nm LEDs, respectively. Colored vertical lines correspond to the specific spectral region for the probe-dependent least-squares fits (b, c, e, and f). The 592 nm data points and fit (f, blue) are scaled by a factor of 10 for better visual comparison to the much stronger 664 nm data plot (f, green). In both photoswitching cases of the PCB cofactor, scattering from the actinic pump (denoted by the asterisks in panels a and d) was largely removed by subtracting the –2 ps TA trace from the subsequent time-resolved TA traces (raw spectra shown in Fig. 4.8 in Section 4.7).

For the $P_r \rightarrow P_g$ conversion, the fs-TA 2D contour plot (Fig. 4.2d) exhibits a longer P_r* lifetime (than the P_g* lifetime in Fig. 4.2a) since the initial bands reaching maximum around time zero fully decay away after hundreds of ps. In particular, the prominent P_r* features include the 503 nm ESA and 664 nm SE bands, which exhibit pure decay time constants of ~6.7, 38, and 361 ps (Fig. 4.2e, red) and ~16 ps, 142 ps,

and 2.3 ns (Fig. 4.2f, green). The 664 nm SE band mainly probes the fluorescence pathway of P_r* back to P_r that was previously reported to be centered at 670 nm [20]. The much weaker, narrow, negative band at 592 nm could be assigned to GSB due to its proximity to a shoulder peak within the P_r ground-state absorption (GSA) band (Fig. 4.1a). Notably, in contrast to the aforementioned 595 nm absorption band in Fig. 4.2a, we observed the distinct rise and decay of a narrow 616 nm absorption band in Fig. 4.2d. The short-lived characteristic is indicative of an excited-state species that we denote as a P_r*' intermediate via continuous structural evolution of the PCB chromophore [39]. The strongly overlapped TA bands hinder a clearer identification of the intermediate state. However, previous QM/MM studies of AnPixJg2 [40] as well as spectroscopic studies on other CBCR and phytochrome systems [9,12,15] suggest that P_r*' could have a deprotonated chromophore in an unrelaxed protein pocket (i.e., as a transient precursor to the intermediate Lumi-R state with a deprotonated PCB chromophore [20]). Further excited-state vibrational studies (e.g., tunable FSRS) are needed to track proton transfer dynamics [25,28] and shed more light on P_r*' (e.g., whether a change of protonation state occurs on the ~10 ps time scale as shown in Fig. 4.2e,f), though recent work has supported a fully protonated chromophore in both equilibrium forms (i.e., after protein relaxation hosting the isomerized cofactor) [41-43].

By comparing the TA dynamics that emerge from initial photoexcitation, the hundreds of fs time constants (100–229 fs) can only be extracted from the GSB recovery at 592 nm (Fig. 4.2f, blue) and initial decay at the neighboring still-negative 616 nm band (Fig. 4.2e, black). The other retrieved time constants from the highly

overlapped bands show a weighted average that could involve multiple steps of P_r* relaxation on the ps-to-ns time scales. The P_r*-to-P_r*' transition occurs on the 6.7–16 ps time scales as these time constants can be correlated with the P_r*' rise component (4.1 ps, Fig. 4.2e, black). Furthermore, the 361 ps decay component (from the 503 nm ESA band of P_r*, Fig. 4.2e, red) and 300 ps decay component (from the 616 nm ESA band of P_r*', Fig. 4.2e, black) represent the excited-state populations that enter the CI for photoconversion. This assignment is supported by previous TA experiments on a similar red/green CBCR, NpR6012g4, where Kim and coworkers found 55 and 345 ps lifetimes that generate the photoproduct Lumi-R state [15]. The GSB recovery dynamics at 592 nm (Fig. 4.2f, blue) largely match the main GSB decay time constants at 648 nm of ~100 fs, 11 ps, 91 ps, and 1.5 ns. On the red side of the 648 nm GSB band is the 664 nm SE band that overlaps with a weak fluorescence band of P_r (see Fig. 4.8 in Section 4.7). Even after subtracting the actinic pump scattering, the 648 nm GSB and 664 nm SE signal (Fig. 4.2d, dark blue region) was ~10 times larger than other spectral features, therefore the color scale was fixed to better resolve the weaker TA bands. Temporal evolution of these strong negative features in the ca. 625–700 nm region can be better viewed in the raw time-stacked TA spectra (Fig. 4.8 in Section 4.7).

To further dissect the overlapped TA spectra and elucidate the underlying reaction species, global analysis can fit the data to a postulated multi-population model to obtain the respective concentration and time constants [44,45]. A series of linear differential equations is used on a target model to be numerically solved and yield the best results. The evolution-associated difference spectra (EADS) implement multiple

sequential states to extract time constants from spectral evolution during a reaction; however, it does not directly give the species-specific rate constants that describe the evolution of populations from one to another [44,46]. Decay-associated difference spectra (DADS) describe the data in a parallel model with each species decaying with a distinct lifetime [47,48]. Using both schemes for the fs-TA spectra of AnPixJg2, the singular value decomposition suggested a four-component model (Fig. 4.3) that was validated by having more components that only fit the early-time coherent artifacts or fewer components that lead to averaged longer time constants. In general, the sequential reaction model should work well here as a stepwise isomerization mechanism was proposed in related red/green CBCR systems [12,20].

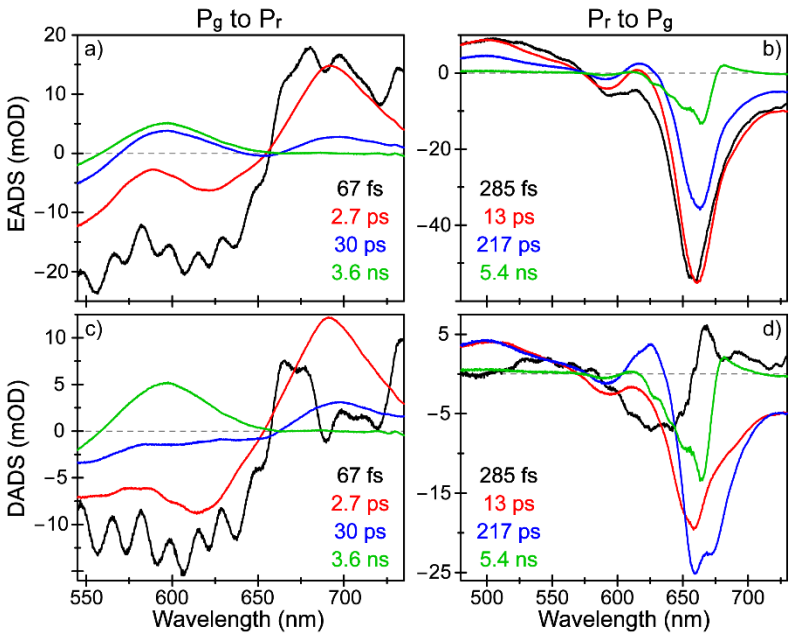

Fig. 4.3. Global analysis of fs-TA spectra during reversible photoswitching processes of AnPixJg2. The probe window for $P_g \rightarrow P_r$ transition (a, c) was truncated on the blue side (~545 to 735 nm) to remove the residual pump scattering (525 nm) that interferes with analysis. The spectra are ordered from fastest to slowest time constants in black, red, blue, to green with the corresponding lifetimes listed in the inset. For the $P_r \rightarrow P_g$ transition (b, d), the full probe window from ~490 to 735 nm was considered due to the pronounced 664 nm SE band at the red side of the residual pump scattering (650 nm). The EADS (a, b) and DADS (c, d) yield complementary information about the underlying species and reaction kinetics that manifest key spectral changes of the photoexcited PCB cofactor.

Reminiscent of the probe-dependent fits in Fig. 4.2a-c, the P_g-to-P_r global analysis yields similar time constants of ~70 fs, 2.7 ps, 30 ps, and 3.6 ns (Fig. 4.3a,c). As the black trace evolves to red, the P_g* ESA, SE, and GSB features become more refined as the wave packet moves out of the Franck-Condon region. The red-to-blue evolution exhibits a pronounced decrease in the initial P_g* species and rise of the

ground-state Lumi-G, mainly evinced by the dramatic TA signal sign change below ~650 nm. The rise of the Lumi-G species and recovery of the GSB band corroborate the assignment of the 2.7 ps time constant to the P_g* species moving through a CI (Fig. 4.4a). The blue-to-green transition with a 30 ps lifetime shows a complete decay of the P_g* ESA band above 650 nm with a slight rise of the Lumi-G absorption band, as well as further recovery of the GSB band below 570 nm. This dynamic component indicates that both the photoreactant P_g and the photoproduct Lumi-G populations are accumulating on a similar time scale after the CI crossing of the P_g* species, again supporting a peaked CI [9,36]. The DADS spectra with less spectral overlap from concurrent species show a cleaner blue trace with no positive band below 650 nm, substantiating the 30 ps relaxation of nascent ground-state species. The longest 3.6 ns time constant is associated with the decay of Lumi-G and a near complete recovery of the GSB, likely involving the chromophore subpopulations that undergo other radiative and nonradiative relaxation pathways [49]. Because our time window is currently limited to 900 ps (see Section 2.4 above), longer time constants are less reliable and are usually averaged in the fs-TA spectral analysis.

As expected, the P_r-to-P_g conversion also exhibits the Franck-Condon relaxation from black to red traces in Fig. 4.3b,d, involving a notable redshift of the SE band. The red-to-blue transition with a 13 ps lifetime shows further redshift of the P_r* SE band at ~664 nm and blueshift of the ESA band at ~503 nm, suggesting that blue trace remains in the electronic excited state. Accordingly, the intermediate P_r*' band rises (see the blue trace positive band around 620 nm) but decays away with the 217 ps time constant (Fig. 4.4b) that likely involves local solvation and surrounding protein

residue side chains dynamics [39,41,50,51], while the cofactor accessibility to aqueous phase was demonstrated using the FTIR difference spectrum in H_2O or D_2O medium [20] and the change of solvent accessibility to the cofactor pocket was shown during ns-to-μs molecular dynamics (MD) simulations [41,50]. This short-lived feature substantiates the excited-state population as an intermediate before the CI. The last 5.4 ns component (green trace) shows the residual GSB and fluorescence lifetime (SE decay), while we observed a small positive band around 680 nm (also visible in Fig. 4.2d above 675 nm at later time points) that is redder than GSB at 648 nm. Therefore, this stage likely has contributions from Lumi-R photoproduct species on the electronic ground state after the C15=C16 bond isomerization (see Fig. 4.4b), reminiscent of the aforementioned Lumi-G species, albeit with much less transition oscillator strength in the red region [12,20]. Since some of the initial chromophore populations were photoconverted to a new conformer state in our spectroscopic measurements, a long-lived GSB signal is expected for both conversion processes as full recovery occurs on the much longer time scales of microseconds to milliseconds [9,20].

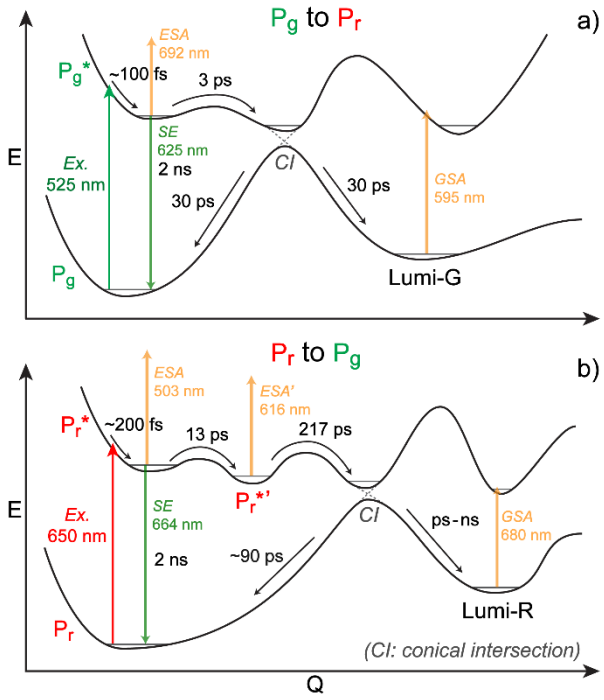

Fig. 4.4. Potential energy surface for the (a) P_g to P_r and (b) P_r to P_g photoconversion of AnPixJg2. The photoexcitation, ESA, SE, and GSA transitions are represented by vertical arrows with characteristic center wavelengths listed from fs-TA spectra. The arrow length is illustrative and does not exactly scale to the energy gap. Average time constants from the probe-dependent and global analysis are denoted by the curved or tilted arrows connecting reaction species. The nuclear coordinate Q along the D-ring isomerization coordinate is part of a multidimensional landscape that likely involves continuous solvation dynamics and polar residue side-chain motions [39].

Based on TA spectral analysis, we sketch the potential energy surface of the AnPixJg2 PCB cofactor in Fig. 4.4a and b for the P_g-to-P_r and P_r-to-P_g transitions, respectively. As P_g is excited to P_g* by the 525 nm actinic pump, the initially relaxed P_g* efficiently crosses a small barrier toward the S_1/S_0 CI on the ~3 ps time scale. At the CI, the P_g* population can continue twisting to produce a long-lived Lumi-G species wherein the chromophore resembles P_r, or twist back to repopulate the P_g ground state on a similar time scale of ~30 ps (Figs. 4.2b,c and 4.3a,c). On the other

hand, the P_r-to-P_g photoconversion exhibits a notably longer excited-state lifetime due to higher transition barriers and the production of a P_r*' intermediate with ~13 ps time constant (Figs. 4.2e,f and 4.3b,d). From P_r*', there remains a large barrier to cross before reaching the S_1/S_0 CI to partially produce the Lumi-R species. The P_r* population is shown to be more fluorescent than P_g* (see the larger and longer-lived SE band in Fig. 4.3b,d than that in Fig. 4.3a,c) as it was the only species to show some fluorescence before quickly converting to P_g in our spectroscopic experiments. To increase the fluorescence quantum yield for bioimaging applications, an enhancement of the H-bonding network around the D-ring or steric hindrance may help [49] (see Fig. 4.9 in Section 4.7 for the chromophore local environment), although it could also decrease the reversible photoswitching quantum yield that may well benefit super-resolution imaging [24,52,53].

4.4.2 Resonance-enhanced ground-state stimulated Raman spectroscopy

To shed more light on the atomic structures of PCB conformers before and after photoconversion (see Fig. 4.10 in Section 4.7 for illustration), we performed GS-FSRS experiments to obtain vibrational signatures of the P_g and P_r species. Given the recent elucidation of local relaxations caused by side chain motions and solvation rather than the structural heterogeneity in a related bacteriophytochrome and CBCR [39,54], we consider FSRS a suitable method to distinguish the solvation dynamics (from excited-state FSRS that tracks the non-equilibrium vibrational dynamics) and structural heterogeneity (from ground-state FSRS that records the equilibrium vibrational features) [28,55,56]. Herein, various Raman pump wavelengths and accompanying

broadband Raman probe on the Stokes and anti-Stokes sides were implemented to explore the resonance Raman enhancement effects on the converting species of AnPixJg2 (see Figs. 4.11 and 4.12 in Section 4.7). Overall, the P_g vibrational peaks exhibit a frequency blueshift as compared to the P_r species mainly above 1200 cm^{-1}, in accordance with a more twisted conformation (hence less electronic conjugation across the PCB tetrapyrrole-ring system) in the green-absorbing P_g state [41,43]. To visualize the associated vibrational motions, the density functional theory (DFT)-based Gaussian calculations were performed at B3LYP level with a 6-31G(d,p) basis set (Section 4.3.6). The calculated Raman spectra show a similar trend to the GS-FSRS data with P_g peaks blue-shifted from P_r peaks (see Fig. 4.5) mainly in the high-frequency region, with Raman modes above 1600 cm^{-1} tracking the C-D ring and A-B ring methine bridge C=C stretching motions (Table 4.1) [9,20].

In particular, strong Raman modes at ~1615 and 1649 cm^{-1} in P_r shift to 1630 and 1665 cm^{-1} in P_g, demonstrating the blueshift of 15 and 16 cm^{-1}, respectively. The 1649 and 1665 cm^{-1} modes were assigned to the A-B methine bridge C=C stretch and C–H rocking with A-ring N–H rocking motions (Table 4.1). The blueshift of this mode from P_r to P_g is due to the A-ring twist (see Fig. 4.10 and Table 4.2 in Section 4.7) that disrupts its H-bonding interactions with the nearby Asp291 and Trp289 (Fig. 4.9 in section 4.7). The main 1615 and 1630 cm^{-1} modes for P_r and P_g species, respectively, involve the C-D methine bridge C=C stretch and C–H rocking with D-ring N-H rocking and C=C stretch. As the D-ring twists more significantly (by ~155°), it most likely breaks the H-bond with Tyr352 and π-π stacking with Trp289, causing the mode frequency blueshift from the ground-state P_r to P_g.

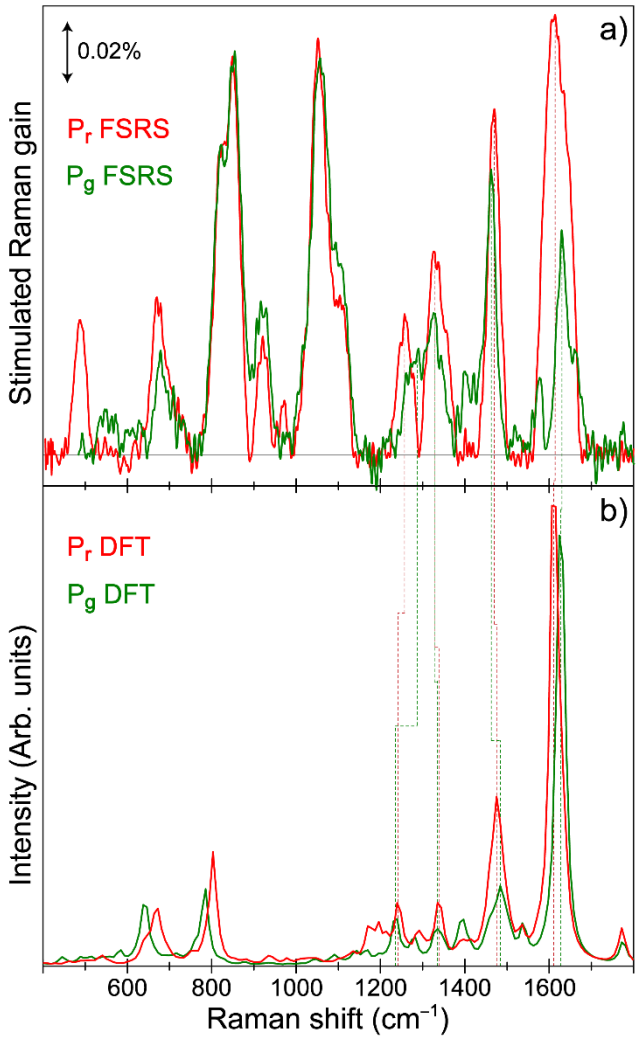

Fig. 4.5. GS-FSRS of the P_r (red) and P_g (green) conformers of AnPixJg2. The P_r measurement used 505 nm LEDs, 596 nm Raman pump, and Raman probe on the Stokes side. The P_g measurement used 650 nm LEDs, 678 nm Raman pump, and Raman probe on the anti-Stokes side. For the anti-Stokes FSRS spectrum of P_g, the Raman shift and peak intensity axes were multiplied by –1 for direct comparison with the Stokes FSRS of P_r. Vertical dotted lines depict peak frequency shifts from the experimental to DFT-calculated (frequency scaling factor of 0.97 applied) Raman spectra.

Velazquez Escobar and coworkers previously conducted resonance Raman (RR) of AnPixJg2 using a 1064 nm continuous-wave Raman pump and cooling the

sample to –140°C [41] while the red-light-induced photoconversion of AnPixJg2 occurs above –80°C. Raman pump was off-resonance from the P_r and P_g ground-state absorption, and their spectra closely match our calculated Raman spectra (Fig. 4.5b). The RR spectra also showed a blueshift of the 1630 cm^{-1} mode that was assigned to the C-D methine bridge C=C stretch, with the higher-frequency shoulder assigned to the A-B methine bridge C=C stretch. One of the main differences between the RR at low temperature and GS-FSRS spectra at room temperature lies in two strong bands at ~850 and 1050 cm^{-1} in Fig. 4.5a, which are also essentially absent in the calculated off-resonance Raman spectra (Fig. 4.5b). The specific Raman pump used in FSRS could resonantly enhance these specific modes that are vibronically coupled to the electronic transition [29,49,57], since the ~850 and 1050 cm^{-1} modes involve the C-D bridge-H out-of-plane (HOOP) motion [9,13] and D-ring deformations (Table 4.1), they display significant Huang-Rhys factors and nuclear displacement from the ground to excited state [13,49] and have been observed in previous FSRS measurements of the excited PCB chromophore in Cph1. In particular, the HOOP mode was proposed to be an integral component of the excited-state reaction coordinate toward a C15=C16 isomerized state on the ~3 ps time scale [9], reminiscent of Fig. 4.4a.

Meanwhile, although the Raman pump wavelength was tuned across the P_r and P_g absorption bands that are separated by over 100 nm, the Raman pump could still photoconvert the sample to a mixed state (Fig. 4.7 in Section 4.7) while the LEDs' power was not sufficient for a full conversion to pure starting species (Fig. 4.1a). Though an exact match is not expected between the low-temperature off-resonance RR and room-temperature pre-resonance FSRS spectra, we have identified key vibrational

signatures of P_r and P_g that support both the D- and A-ring twist after photoconversion (see Fig. 4.10 in Section 4.7 for PCB twisting geometries), and resonance conditions that can be further optimized with a strategic combination of tunable Raman pump and probe pulses (Figs. 4.11 and 4.12 in Section 4.7).

Notably, the calculated Raman intensities do not match the experimental values mainly due to the mode-dependent change of resonance conditions using tunable FSRS [29,49,58] and limitation of DFT calculations only focusing on the PCB chromophore here (Fig. 4.10 in Section 4.7) without explicit treatment of the protein pocket. In our experiments, various Raman pump wavelengths were used in order to obtain Raman spectrum of a pure P_g or P_r population (e.g., see Fig. 4.11 for P_g). Surprisingly, each Raman pump resulted in a similar Raman spectrum despite the use of 505 or 650 nm LEDs to generate P_r or P_g species (Fig. 4.12). To find the cause of this dilemma, the sample was inserted in the actinic pump and Raman pump beam path to see if any photoconversion occurs. Both pumps were able to convert the sample as evinced by a clear color change upon the passage of light. To further investigate the photoconversion of AnPixJg2, we used a fluorimeter arc lamp and a UV/Visible spectrophotometer to excite the sample at different wavelengths and collect the absorption spectra therein (Fig. 4.7). The finding confirmed that Raman pump overlapping with any ground-state absorption features of AnPixJg2 can induce photoswitching to various extents and cause a mixed population of P_g and P_r. As a result, the 678 nm Raman pump anti-Stokes FSRS with 650 nm LEDs (Fig. 4.5, green) and 596 nm Raman pump Stokes FSRS with 505 nm LEDs (Fig. 4.5, red) represent a mixed population with predominant P_g and P_r conformers, respectively. For this reason, AnPixJg2 represents a rather special case that

a pre-resonance enhancement condition cannot be directly used to increase the signal-to-noise ratio of a target species [56], because another species would be readily generated that absorbs more than 100 nm away (see Figs. 4.1 and 4.7). Therefore, though the calculations of GS-FSRS spectrum under pre-resonance conditions [59-61] could be helpful to identify key Franck-Condon active modes and yield a better prediction of Raman peak intensities over a broad spectral window (e.g., from low- to high-frequency modes in Fig. 4.5b), the applicability of such calculations for the P_g and P_r characterization in AnPixJg2 with swift photoswitching remains limited due to key experimental challenges (Figs. 4.7 and 4.12) in obtaining the accurate pre-resonance spectrum of pure P_g and P_r species for a rigorous comparison.

Like AnPixJg2, Slr1393g3 is a red/green-photoswitching CBCR with its P_g crystal structure reported (5M82, see Section 4.3.6) [31], while both CBCRs share the same PCB chromophore with conserved residues around the chromophore (Fig. 4.9) [19]. The illustrative D and A ring twist between the P_g and P_r conformers may shed some light on the photoswitching process with the D-ring likely twisting on the excited state and A-ring twist on the ground state. This could be due to the change of single- and double-bond character in the excited versus ground state [62,63]. As a conjugated molecule undergoes a π-π^* electronic excitation, a double bond typically adopts more single-bond character, thus allowing it to twist more freely when compared to the ground state. In consequence, after AnPixJg2 is excited, the D-ring twist along the C15=C16 bond constitutes the main reaction coordinate for the cofactor crossing a CI into the ground Lumi state, wherein the A-ring twist along the C5–C6 bond further relaxes the protein on longer time scales with a large-scale conformational change of

the surrounding protein pocket and H-bonding network. This reaction stage well beyond the aforementioned ultrafast time scales achieves localization of the π-orbital on PCB in an equilibrated nonplanar conformation of the tetrapyrrole ring system [20] and completes the photoconversion from one absorbing state to another (P_r to P_g, or P_g to P_r). Such a reaction process is also corroborated by local environment of the cofactor chromophore as crystal structures for phytochromes and CBCRs show less tight packing around the D-ring, so there could be more conformational freedom about the C15 methine bridge than about the C5 or C10 methine bridges (see Figs. 4.1b and 4.10 for the atomic numbering of PCB cofactor) [10,11].

4.4.3 Ground-state heterogeneity and photoconversion quantum yield

The heterogeneity of the ground-state population of CBCRs and phytochromes has brought a vast amount of spectroscopic techniques [12,13,15,64,65] and simulations [40,66] to determine how many subpopulations each species has as well as how their dynamics differ. The heterogeneity in phytochromes and CBCRs points toward a common feature that could be linked to a functional role in nature or evolution advantage. As for AnPixJg2 in solution, Scarbath-Evers et al. implemented MD simulations on a 1 μs time scale in correlation with experimental ^{13}C cross-polarization magic-angle spinning NMR spectroscopy that uncovered two sub-states in P_r where the D-ring adopts two different isomers [50]. This finding is also in line with Kim et al. reporting their TA and global analysis data on a similar red/green CBCR, NpR6012g4, tracking two $^{15Z}P_r$ subpopulations that photoconvert to ^{15E}Lumi-R species on separate time scales of ~75 ps and 1 ns [15]. On the other hand, Rao and coworkers recently

published QM/MM calculations on AnPixJg2 where the D-ring heterogeneity could be mainly governed by the protonation states of histidine residues around the chromophore [40]. Therefore, we surmise that the highly overlapped TA spectra observed during the P_r-to-P_g photoconversion of AnPixJg2 (Fig. 4.2d) are likely due to a heterogeneous ground-state population that produces Lumi-R on the hundreds of ps to few ns time scales (Figs. 4.2f and 4.3b). Different subpopulations in P_r could also be the cause of the ground-state shoulder peak at ~592 nm (Fig. 4.1a) and the resulting GSB band (Fig. 4.2d), as well as the mismatch between the apparent time constants and the retrieved time constants from global analysis on the basis of a homogeneous model for dominant species (Fig. 4.4b). Based on the current GS-FSRS data of the P_g and P_r species of AnPixJg2 with a series of Raman pump, Raman probe, and LED wavelengths (Fig. 4.12), the Raman peak widths are similar across a spectral window over ~1100 cm^{-1} for both P_g and P_r species, which suggests that the structural heterogeneity remain largely unchanged before and after the reversible photoswitching events.

Looking forward, an actinic-pump-dependent TA and FSRS experiment with tunable Raman pump wavelengths would help to uncover the number of ground-state subpopulations and their photoconversion dynamics [13,39]. Moreover, the time-resolved excited-state FSRS will be implemented in future studies on the PCB cofactor along with a newly engineered AnPixJg2_BV4 with just four mutated residues in the protein pocket (e.g., Fig. 4.9 that plays a critical role on the ultrafast photochemistry and function of the photosensory unit) which can bind the BV cofactor (see Section 2.1) for mammalian cell applications [21]. Preliminary TA results of AnPixJg2_BV4 (PCB) in our lab showed altered time constants on the ps-to-ns time scales and a more

homogeneous population in the P_r state due to a less restrictive and more flexible chromophore pocket (versus AnPixJg2), which will be reported in a subsequent publication. In particular, similar pre-resonance and off-resonance conditions (as in Figs. 4.11 and 4.12) will be implemented for AnPixJg2_BV4 (PCB) to directly compare with AnPixJg2 (PCB) to gain further insights into the correlation between structural heterogeneity and Raman peak width, aided by the excited-state dynamics of Raman peaks that could report on local relaxation at the active site as well as subpopulations of the chromophore (hence enabling an evaluation of the dominant factor) [24,56].

The photoconversion quantum yield for AnPixJg2 has yet to be reported, but based on the phylogenetically related NpR6012g4, the P_r-to-P_g photoconversion should be close to 40% [15], consistent with the CI-branching and generation of various ground-state intermediates depicted in Fig. 4.4b. The rather efficient photoconversion (more than canonical phytochromes at <15% [9,12]) was observed upon irradiating the sample with multiple types of light (*vide supra*). Previous TA work on a four-ring molecular photoswitch (1,2-dithienyl-1,2-dicyanoethene, 4TCE) showed that the GSB recovery dynamics on the 40 ps time scale could be used to obtain the *trans*-to-*cis* isomerization yield [67]. However, this approach is much less applicable for AnPixJg2 due to a significant overlap between transient GSB and GSA bands (Fig. 4.2a) or GSB and ESA bands (Fig. 4.2d), the significantly larger isomerization time constant (Fig. 4.4b), as well as the lack of direct observation of the final photoproducts P_r and P_g beyond Lumi-G and Lumi-R in Fig. 4.4a and b, respectively, within our experimental time window of 600–900 ps (Fig. 4.2). Furthermore, the ps narrowband Raman pump

pulse can cause the sample to photoconvert, making it rather challenging to find an optimal resonance condition that would enhance the P_r and P_g species separately (see Fig. 4.12). All excitations, even at 800 nm center wavelength, can convert AnPixJg2 from the native state to a different mixed population state (Fig. 4.7), thus prompting us to further select a suitable combination of LEDs, Raman pump, and Raman probe to collect reliable GS-FSRS spectrum of a specific conformer (e.g., P_g in Fig. 4.11, and P_r in Fig. 4.5) with key vibrational signatures.

Comparing the ultrafast photoconversion processes revealed in this work to previously studied phytochromes and CBCRs [9,15,16], a common trend emerges where the forward reaction exhibits a longer-lived excited state as it moves from a stable conformer to a meta-stable conformer. In particular, both the ground- and excited-state energetics need to be considered to map out the potential energy landscape for photoconversion. The longer-lived excited state naturally corresponds to more complex relaxation pathways before it produces the photointermediate or Lumi-R state (e.g., Fig. 4.4b). With the reverse photoconversion, moving away from a meta-stable conformer with less chromophore tetrapyrrole-ring π-conjugation [43] helps the system to relax across a smaller barrier en route to the Lumi intermediate. The TA-uncovered major lifetimes of ~3 and 30 ps for P_g* species (Fig. 4.4a) and ~13 and 217 ps for P_r* species (Fig. 4.4b) are congruent with the primary decay time constants of fluorescence at 42 ps and 200 ps for APg_{543}* (same as P_g*, emission peak at 610 nm) and APr_{648}* (same as P_r*, emission peak at 670 nm), respectively [20]. In both cases, the excited-state reaction barriers naturally involve the D-ring flipping motions, concomitant with

ultrafast motions of the surrounding solvent molecules and residue side chains that underlie the chromophore-protein interactions in real time [54,56].

4.5 Conclusions

In summary, we have performed the wavelength-tunable fs-TA and GS-FSRS studies of both the forward ($^{15Z}P_r$ to $^{15E}P_g$) and reverse ($^{15E}P_g$ to $^{15Z}P_r$) photoconversion of a CBCR AnPixJg2 in buffer solution at room temperature, essentially tracking the protein-chromophore interactions on intrinsic molecular time scales. The forward reaction exhibits a longer-lived excited state and requires two distinct steps with ~13 and 217 ps time constants before reaching the CI to form the photoproduct (Lumi-R). Conversely, the reverse reaction exhibits a much faster excited-state decay and takes a dominant ~3 ps step to cross a small barrier to reach the CI, allowing us to resolve the Lumi-G accumulation on the 30 ps time scale within our detection time window. The primary photochemical reaction coordinate has been attributed to a facile C15=C16 bond isomerization that occurs on ultrafast time scales inside a tightly packed yet highly dynamic chromophore pocket, which supports photoconversion via S_1/S_0 CIs.

Besides gaining fundamental insights into the reversible photoswitching processes of PCB cofactor in AnPixJg2 upon electronic excitation, we have also provided vibrational signatures of the red-absorbing ground state versus green-absorbing photoproduct via resonance Raman enhancement across the visible to near-IR region. A strategic combination of the continuous-wave LEDs, ps Raman pump wavelengths, and fs Raman probe on the Stokes or anti-Stokes side allows us to reveal a common blueshift of the high-frequency Raman modes from the P_r to P_g species,

corroborated by quantum chemistry calculations of the respective ground-state chromophore structure involving a major D-ring twist and minor A-ring twist between the P_r and P_g conformers. We envision that the deciphered mechanistic information at molecular level with correlated electronic and vibrational signatures on ultrafast time scales can enable the targeted design of photosensory units in protein matrix from the bottom up, achieving desirable properties in imaging and optogenetic applications from color tuning, brightness, stability, to photoswitching efficiency, reversibility, and signal contrast in more realistic environments.

4.6 References

[1] M. Ikeuchi, T. Ishizuka, Cyanobacteriochromes: a new superfamily of tetrapyrrole-binding photoreceptors in cyanobacteria, Photochem. Photobiol. Sci. 7 (2008) 1159-1167. https://doi.org/10.1039/B802660M.

[2] X. Shu, A. Royant, M.Z. Lin, T.A. Aguilera, V. Lev-Ram, P.A. Steinbach, R.Y. Tsien, Mammalian expression of infrared fluorescent proteins engineered from a bacterial phytochrome, Science 324 (2009) 804-807. https://doi.org/10.1126/science.1168683.

[3] G.S. Filonov, K.D. Piatkevich, L.-M. Ting, J. Zhang, K. Kim, V.V. Verkhusha, Bright and stable near-infrared fluorescent protein for *in vivo* imaging, Nat. Biotechnol. 29 (2011) 757-761. https://doi.org/10.1038/nbt.1918.

[4] K.D. Piatkevich, F.V. Subach, V.V. Verkhusha, Engineering of bacterial phytochromes for near-infrared imaging, sensing, and light-control in mammals, Chem. Soc. Rev. 42 (2013) 3441-3452. https://doi.org/10.1039/C3CS35458J.

[5] N.C. Rockwell, Y.-S. Su, J.C. Lagarias, Phytochrome structure and signaling mechanisms, Annu. Rev. Plant Biol. 57 (2006) 837-858. https://doi.org/10.1146/annurev.arplant.56.032604.144208.

[6] M.-H. Ryu, M. Gomelsky, Near-infrared light responsive synthetic c-di-GMP module for optogenetic applications, ACS Synth. Biol. 3 (2014) 802-810. https://doi.org/10.1021/sb400182x.

[7] F. Pennacchietti, A. Losi, X.-l. Xu, K.-h. Zhao, W. Gärtner, C. Viappiani, F. Cella, A. Diaspro, S. Abbruzzetti, Photochromic conversion in a red/green cyanobacteriochrome from *Synechocystis* PCC6803: quantum yields in solution and photoswitching dynamics in living *E. coli* cells, Photochem. Photobiol. Sci. 14 (2015) 229-237. https://doi.org/10.1039/C4PP00337C.

[8] K. Fushimi, G. Enomoto, M. Ikeuchi, R. Narikawa, Distinctive properties of dark reversion kinetics between two red/green-type cyanobacteriochromes and their application in the photoregulation of cAMP synthesis, Photochem. Photobiol. 93 (2017) 681-691. https://doi.org/10.1111/php.12732.

[9] J. Dasgupta, R.R. Frontiera, K.C. Taylor, J.C. Lagarias, R.A. Mathies, Ultrafast excited-state isomerization in phytochrome revealed by femtosecond stimulated Raman spectroscopy, Proc. Natl. Acad. Sci. U. S. A. 106 (2009) 1784-1789. https://doi.org/10.1073/pnas.0812056106.

[10] N.C. Rockwell, J.C. Lagarias, A brief history of phytochromes, ChemPhysChem 11 (2010) 1172-1180. https://doi.org/10.1002/cphc.200900894.

[11] K. Fushimi, R. Narikawa, Cyanobacteriochromes: photoreceptors covering the entire UV-to-visible spectrum, Curr. Opin. Struct. Biol. 57 (2019) 39-46. https://doi.org/https://doi.org/10.1016/j.sbi.2019.01.018.

[12] P.W. Kim, L.H. Freer, N.C. Rockwell, S.S. Martin, J.C. Lagarias, D.S. Larsen, Second-chance forward isomerization dynamics of the red/green cyanobacteriochrome NpR6012g4 from *Nostoc punctiforme*, J. Am. Chem. Soc. 134 (2012) 130-133. https://doi.org/10.1021/ja209533x.

[13] K.M. Spillane, J. Dasgupta, J.C. Lagarias, R.A. Mathies, Homogeneity of phytochrome Cph1 vibronic absorption revealed by resonance Raman intensity analysis, J. Am. Chem. Soc. 131 (2009) 13946-13948. https://doi.org/10.1021/ja905822m.

[14] Y. Yang, K. Heyne, R.A. Mathies, J. Dasgupta, Non-bonded interactions drive the sub-picosecond bilin photoisomerization in the Pfr state of phytochrome Cph1, ChemPhysChem 17 (2016) 369-374. https://doi.org/10.1002/cphc.201501073.

[15] P.W. Kim, L.H. Freer, N.C. Rockwell, S.S. Martin, J.C. Lagarias, D.S. Larsen, Femtosecond photodynamics of the red/green cyanobacteriochrome NpR6012g4 from *Nostoc punctiforme*. 1. Forward dynamics, Biochemistry 51 (2012) 608-618. https://doi.org/10.1021/bi201507k.

[16] P.W. Kim, L.H. Freer, N.C. Rockwell, S.S. Martin, J.C. Lagarias, D.S. Larsen, Femtosecond photodynamics of the red/green cyanobacteriochrome NpR6012g4 from *Nostoc punctiforme*. 2. Reverse dynamics, Biochemistry 51 (2012) 619-630. https://doi.org/10.1021/bi2017365.

[17] C. Song, R. Narikawa, M. Ikeuchi, W. Gärtner, J. Matysik, Color tuning in red/green cyanobacteriochrome AnPixJ: photoisomerization at C15 causes an

excited-state destabilization, J. Phys. Chem. B 119 (2015) 9688-9695. https://doi.org/10.1021/acs.jpcb.5b04655.

[18] R. Narikawa, Y. Fukushima, T. Ishizuka, S. Itoh, M. Ikeuchi, A novel photoactive GAF domain of cyanobacteriochrome AnPixJ that shows reversible green/red photoconversion, J. Mol. Biol. 380 (2008) 844-855. https://doi.org/https://doi.org/10.1016/j.jmb.2008.05.035.

[19] R. Narikawa, T. Ishizuka, N. Muraki, T. Shiba, G. Kurisu, M. Ikeuchi, Structures of cyanobacteriochromes from phototaxis regulators AnPixJ and TePixJ reveal general and specific photoconversion mechanism, Proc. Natl. Acad. Sci. U. S. A. 110 (2013) 918-923. https://doi.org/10.1073/pnas.1212098110.

[20] Y. Fukushima, M. Iwaki, R. Narikawa, M. Ikeuchi, Y. Tomita, S. Itoh, Photoconversion mechanism of a green/red photosensory cyanobacteriochrome AnPixJ: time-resolved optical spectroscopy and FTIR analysis of the AnPixJ-GAF2 domain, Biochemistry 50 (2011) 6328-6339. https://doi.org/10.1021/bi101799w.

[21] K. Fushimi, T. Miyazaki, Y. Kuwasaki, T. Nakajima, T. Yamamoto, K. Suzuki, Y. Ueda, K. Miyake, Y. Takeda, J.-H. Choi, H. Kawagishi, E.Y. Park, M. Ikeuchi, M. Sato, R. Narikawa, Rational conversion of chromophore selectivity of cyanobacteriochromes to accept mammalian intrinsic biliverdin, Proc. Natl. Acad. Sci. U. S. A. 116 (2019) 8301-8309. https://doi.org/10.1073/pnas.1818836116.

[22] K. Mukougawa, H. Kanamoto, T. Kobayashi, A. Yokota, T. Kohchi, Metabolic engineering to produce phytochromes with phytochromobilin, phycocyanobilin, or phycoerythrobilin chromophore in *Escherichia coli*, FEBS Lett. 580 (2006) 1333-1338. https://doi.org/https://doi.org/10.1016/j.febslet.2006.01.051.

[23] K. Miyake, K. Fushimi, T. Kashimoto, K. Maeda, W. Ni Ni, H. Kimura, M. Sugishima, M. Ikeuchi, R. Narikawa, Functional diversification of two bilin reductases for light perception and harvesting in unique cyanobacterium *Acaryochloris marina* MBIC 11017, FEBS J. 287 (2020) 4016-4031. https://doi.org/10.1111/febs.15230.

[24] T.D. Krueger, L. Tang, L. Zhu, I.L. Breen, R.M. Wachter, C. Fang, Dual illumination enhances transformation of an engineered green-to-red

photoconvertible fluorescent protein, Angew. Chem. Int. Ed. 59 (2020) 1644-1652. https://doi.org/10.1002/anie.201911379.

[25] W. Liu, Y. Wang, L. Tang, B.G. Oscar, L. Zhu, C. Fang, Panoramic portrait of primary molecular events preceding excited state proton transfer in water, Chem. Sci. 7 (2016) 5484-5494. https://doi.org/10.1039/C6SC00672H.

[26] L. Tang, L. Zhu, M.A. Taylor, Y. Wang, S.J. Remington, C. Fang, Excited state structural evolution of a GFP single-site mutant tracked by tunable femtosecond-stimulated Raman spectroscopy, Molecules 23 (2018) 2226. https://doi.org/10.3390/molecules23092226.

[27] L. Zhu, W. Liu, C. Fang, A versatile femtosecond stimulated Raman spectroscopy setup with tunable pulses in the visible to near infrared, Appl. Phys. Lett. 105 (2014) 041106. https://doi.org/10.1063/1.4891766.

[28] C. Fang, L. Tang, B.G. Oscar, C. Chen, Capturing structural snapshots during photochemical reactions with ultrafast Raman spectroscopy: from materials transformation to biosensor responses, J. Phys. Chem. Lett. 9 (2018) 3253–3263. https://doi.org/10.1021/acs.jpclett.8b00373.

[29] K. Roy, S. Kayal, F. Ariese, A. Beeby, S. Umapathy, Mode specific excited state dynamics study of bis(phenylethynyl)benzene from ultrafast Raman loss spectroscopy, J. Chem. Phys. 146 (2017) 064303. https://doi.org/10.1063/1.4975174.

[30] M.J. Frisch, G.W. Trucks, H.B. Schlegel, G.E. Scuseria, M.A. Robb, J.R. Cheeseman, G. Scalmani, V. Barone, G.A. Petersson, H. Nakatsuji, X. Li, M. Caricato, A.V. Marenich, J. Bloino, B.G. Janesko, R. Gomperts, B. Mennucci, H.P. Hratchian, J.V. Ortiz, A.F. Izmaylov, J.L. Sonnenberg, D. Williams-Young, F. Ding, F. Lipparini, F. Egidi, J. Goings, B. Peng, A. Petrone, T. Henderson, D. Ranasinghe, V.G. Zakrzewski, J. Gao, N. Rega, G. Zheng, W. Liang, M. Hada, M. Ehara, K. Toyota, R. Fukuda, J. Hasegawa, M. Ishida, T. Nakajima, Y. Honda, O. Kitao, H. Nakai, T. Vreven, K. Throssell, J. J. A. Montgomery, J.E. Peralta, F. Ogliaro, M.J. Bearpark, J.J. Heyd, E.N. Brothers, K.N. Kudin, V.N. Staroverov, T.A. Keith, R. Kobayashi, J. Normand, K. Raghavachari, A.P. Rendell, J.C. Burant, S.S. Iyengar, J. Tomasi, M. Cossi, J.M. Millam, M. Klene, C. Adamo, R. Cammi,

J.W. Ochterski, R.L. Martin, K. Morokuma, O. Farkas, J.B. Foresman, D.J. Fox, *Gaussian 16, Revision A.03*, in, Gaussian, Inc., Wallingford, CT, 2016.

[31] X. Xu, A. Höppner, C. Wiebeler, K.-H. Zhao, I. Schapiro, W. Gärtner, Structural elements regulating the photochromicity in a cyanobacteriochrome, Proc. Natl. Acad. Sci. U. S. A. 117 (2020) 2432-2440. https://doi.org/10.1073/pnas.1910208117.

[32] X.-L. Xu, A. Gutt, J. Mechelke, S. Raffelberg, K. Tang, D. Miao, L. Valle, C.D. Borsarelli, K.-H. Zhao, W. Gärtner, Combined mutagenesis and kinetics characterization of the bilin-binding GAF domain of the protein Slr1393 from the cyanobacterium *Synechocystis* PCC6803, ChemBioChem 15 (2014) 1190-1199. https://doi.org/10.1002/cbic.201400053.

[33] A.P. Scott, L. Radom, Harmonic vibrational frequencies: an evaluation of Hartree−Fock, Møller−Plesset, quadratic configuration interaction, density functional theory, and semiempirical scale factors, J. Phys. Chem. 100 (1996) 16502-16513. https://doi.org/10.1021/jp960976r.

[34] J.P. Merrick, D. Moran, L. Radom, An evaluation of harmonic vibrational frequency scale factors, J. Phys. Chem. A 111 (2007) 11683-11700. https://doi.org/10.1021/jp073974n.

[35] W. Liu, F. Han, C. Smith, C. Fang, Ultrafast conformational dynamics of pyranine during excited state proton transfer in aqueous solution revealed by femtosecond stimulated Raman spectroscopy, J. Phys. Chem. B 116 (2012) 10535-10550. https://doi.org/10.1021/jp3020707.

[36] T. Kumpulainen, B. Lang, A. Rosspeintner, E. Vauthey, Ultrafast elementary photochemical processes of organic molecules in liquid solution, Chem. Rev. 117 (2017) 10826-10939. https://doi.org/10.1021/acs.chemrev.6b00491.

[37] M.A. Taylor, L. Zhu, N.D. Rozanov, K.T. Stout, C. Chen, C. Fang, Delayed vibrational modulation of the solvated GFP chromophore into a conical intersection, Phys. Chem. Chem. Phys. 21 (2019) 9728-9739. https://doi.org/10.1039/C9CP01077G.

[38] L. Tang, C. Fang, Nitration of tyrosine channels photoenergy through a conical intersection in water, J. Phys. Chem. B 123 (2019) 4915-4928. https://doi.org/10.1021/acs.jpcb.9b03464.

[39] D. Wang, X. Li, S. Zhang, L. Wang, X. Yang, D. Zhong, Revealing the origin of multiphasic dynamic behaviors in cyanobacteriochrome, Proc. Natl. Acad. Sci. U. S. A. 117 (2020) 19731-19736. https://doi.org/10.1073/pnas.2001114117.

[40] A.G. Rao, C. Wiebeler, S. Sen, D.S. Cerutti, I. Schapiro, Histidine protonation controls structural heterogeneity in the cyanobacteriochrome AnPixJg2, bioRxiv (2020) 2020.2008.2021.260158. https://doi.org/10.1101/2020.08.21.260158.

[41] F. Velazquez Escobar, T. Utesch, R. Narikawa, M. Ikeuchi, M.A. Mroginski, W. Gärtner, P. Hildebrandt, Photoconversion mechanism of the second GAF domain of cyanobacteriochrome AnPixJ and the cofactor structure of its green-absorbing state, Biochemistry 52 (2013) 4871-4880. https://doi.org/10.1021/bi400506a.

[42] N.C. Rockwell, S.S. Martin, S. Lim, J.C. Lagarias, J.B. Ames, Characterization of red/green cyanobacteriochrome NpR6012g4 by solution nuclear magnetic resonance spectroscopy: a protonated bilin ring system in both photostates, Biochemistry 54 (2015) 2581-2600. https://doi.org/10.1021/bi501548t.

[43] C. Wiebeler, A.G. Rao, W. Gärtner, I. Schapiro, The effective conjugation length is responsible for the red/green spectral tuning in the cyanobacteriochrome Slr1393g3, Angew. Chem. Int. Ed. 58 (2019) 1934-1938. https://doi.org/10.1002/anie.201810266.

[44] I.H.M. van Stokkum, D.S. Larsen, R. van Grondelle, Global and target analysis of time-resolved spectra, Biochim. Biophys. Acta 1657 (2004) 82-104. https://doi.org/http://doi.org/10.1016/j.bbabio.2004.04.011.

[45] J.J. Snellenburg, S.P. Laptenok, R. Seger, K.M. Mullen, I.H.M. van Stokkum, Glotaran: a Java-based graphical user interface for the R-package TIMP, J. Stat. Softw. 49 (2012) 1-22. https://doi.org/10.18637/jss.v049.i03.

[46] A.R. Holzwarth, Chapter 5: Data Analysis of Time-Resolved Measurements, in: J. Amesz, A.J. Hoff (Eds.) Biophysical Techniques in Photosynthesis, Kluwer Academic Publishers; Springer, Dordrecht, Netherlands, 1996, pp. 75-92.

[47] K.C. Toh, E.A. Stojkovic, I.H.M. van Stokkum, K. Moffat, J.T.M. Kennis, Proton-transfer and hydrogen-bond interactions determine fluorescence quantum yield and photochemical efficiency of bacteriophytochrome, Proc. Natl. Acad. Sci. U. S. A. 107 (2010) 9170-9175. https://doi.org/10.1073/pnas.0911535107.

[48] C. Chen, L. Zhu, S.A. Boulanger, N.S. Baleeva, I.N. Myasnyanko, M.S. Baranov, C. Fang, Ultrafast excited-state proton transfer dynamics in dihalogenated non-fluorescent and fluorescent GFP chromophores, J. Chem. Phys. 152 (2020) 021101. https://doi.org/10.1063/1.5138666.

[49] C. Fang, L. Tang, C. Chen, Unveiling coupled electronic and vibrational motions of chromophores in condensed phases, J. Chem. Phys. 151 (2019) 200901. https://doi.org/10.1063/1.5128388.

[50] L.K. Scarbath-Evers, S. Jähnigen, H. Elgabarty, C. Song, R. Narikawa, J. Matysik, D. Sebastiani, Structural heterogeneity in a parent ground-state structure of AnPixJg2 revealed by theory and spectroscopy, Phys. Chem. Chem. Phys. 19 (2017) 13882-13894. https://doi.org/10.1039/C7CP01218G.

[51] E. Claesson, W.Y. Wahlgren, H. Takala, S. Pandey, L. Castillon, V. Kuznetsova, L. Henry, M. Panman, M. Carrillo, J. Kübel, R. Nanekar, L. Isaksson, A. Nimmrich, A. Cellini, D. Morozov, M. Maj, M. Kurttila, R. Bosman, E. Nango, R. Tanaka, T. Tanaka, L. Fangjia, S. Iwata, S. Owada, K. Moffat, G. Groenhof, E.A. Stojković, J.A. Ihalainen, M. Schmidt, S. Westenhoff, The primary structural photoresponse of phytochrome proteins captured by a femtosecond X-ray laser, eLife 9 (2020) e53514. https://doi.org/10.7554/eLife.53514.

[52] D. Bourgeois, V. Adam, Reversible photoswitching in fluorescent proteins: a mechanistic view, IUBMB Life 64 (2012) 482-491. https://doi.org/10.1002/iub.1023.

[53] K. Nienhaus, G.U. Nienhaus, Fluorescent proteins for live-cell imaging with super-resolution, Chem. Soc. Rev. 43 (2014) 1088-1106. https://doi.org/10.1039/C3CS60171D.

[54] D. Wang, Y. Qin, M. Zhang, X. Li, L. Wang, X. Yang, D. Zhong, The origin of ultrafast multiphasic dynamics in photoisomerization of bacteriophytochrome, J.

Phys. Chem. Lett. 11 (2020) 5913-5919. https://doi.org/10.1021/acs.jpclett.0c01394.

[55] C. Fang, R.R. Frontiera, R. Tran, R.A. Mathies, Mapping GFP structure evolution during proton transfer with femtosecond Raman spectroscopy, Nature 462 (2009) 200-204. https://doi.org/10.1038/nature08527.

[56] C. Fang, L. Tang, Mapping structural dynamics of proteins with femtosecond stimulated Raman spectroscopy, Annu. Rev. Phys. Chem. 71 (2020) 239-265. https://doi.org/10.1146/annurev-physchem-071119-040154.

[57] B.G. Oscar, C. Chen, W. Liu, L. Zhu, C. Fang, Dynamic Raman line shapes on an evolving excited-state landscape: insights from tunable femtosecond stimulated Raman spectroscopy, J. Phys. Chem. A 121 (2017) 5428-5441. https://doi.org/10.1021/acs.jpca.7b04404.

[58] C. Chen, L. Zhu, C. Fang, Femtosecond stimulated Raman line shapes: dependence on resonance conditions of pump and probe pulses, Chin. J. Chem. Phys. 31 (2018) 492-502. https://doi.org/10.1063/1674-0068/31/cjcp1805125.

[59] A.B. Myers, R.A. Mathies, Resonance Raman Intensities: A Probe of Excited-State Structure and Dynamics, in: T.G. Spiro (Ed.) Biological Applications of Raman Spectroscopy, John Wiley & Sons, Inc., New York, 1987, pp. 1-58.

[60] M.S. Barclay, T.J. Quincy, D.B. Williams-Young, M. Caricato, C.G. Elles, Accurate assignments of excited-state resonance Raman spectra: a benchmark study combining experiment and theory, J. Phys. Chem. A 121 (2017) 7937-7946. https://doi.org/10.1021/acs.jpca.7b09467.

[61] P.C. Andrikopoulos, Y. Liu, A. Picchiotti, N. Lenngren, M. Kloz, A.S. Chaudhari, M. Precek, M. Rebarz, J. Andreasson, J. Hajdu, B. Schneider, G. Fuertes, Femtosecond-to-nanosecond dynamics of flavin mononucleotide monitored by stimulated Raman spectroscopy and simulations, Phys. Chem. Chem. Phys. 22 (2020) 6538-6552. https://doi.org/10.1039/C9CP04918E.

[62] C.A. Guido, D. Jacquemin, C. Adamo, B. Mennucci, On the TD-DFT accuracy in determining single and double bonds in excited-state structures of organic molecules, J. Phys. Chem. A 114 (2010) 13402-13410. https://doi.org/10.1021/jp109218z.

[63] I.V. Polyakov, B.L. Grigorenko, E.M. Epifanovsky, A.I. Krylov, A.V. Nemukhin, Potential energy landscape of the electronic states of the GFP chromophore in different protonation forms: electronic transition energies and conical intersections, J. Chem. Theory Comput. 6 (2010) 2377-2387. https://doi.org/10.1021/ct100227k.

[64] C. Song, G. Psakis, C. Lang, J. Mailliet, W. Gärtner, J. Hughes, J. Matysik, Two ground state isoforms and a chromophore *D*-ring photoflip triggering extensive intramolecular changes in a canonical phytochrome, Proc. Natl. Acad. Sci. U. S. A. 108 (2011) 3842-3847. https://doi.org/10.1073/pnas.1013377108.

[65] P.W. Kim, N.C. Rockwell, S.S. Martin, J.C. Lagarias, D.S. Larsen, Heterogeneous photodynamics of the P_{fr} State in the cyanobacterial phytochrome Cph1, Biochemistry 53 (2014) 4601-4611. https://doi.org/10.1021/bi5005359.

[66] S. Kaminski, G. Daminelli, M.A. Mroginski, Molecular dynamics simulations of the chromophore binding site of *Deinococcus radiodurans* bacteriophytochrome using new force field parameters for the phytochromobilin chromophore, J. Phys. Chem. B 113 (2009) 945-958. https://doi.org/10.1021/jp8047532.

[67] J. Zhou, X. Guo, H.E. Katz, A.E. Bragg, Molecular switching via multiplicity-exclusive *E*/*Z* photoisomerization pathways, J. Am. Chem. Soc. 137 (2015) 10841-10850. https://doi.org/10.1021/jacs.5b07348.

4.7 Supplemental Information

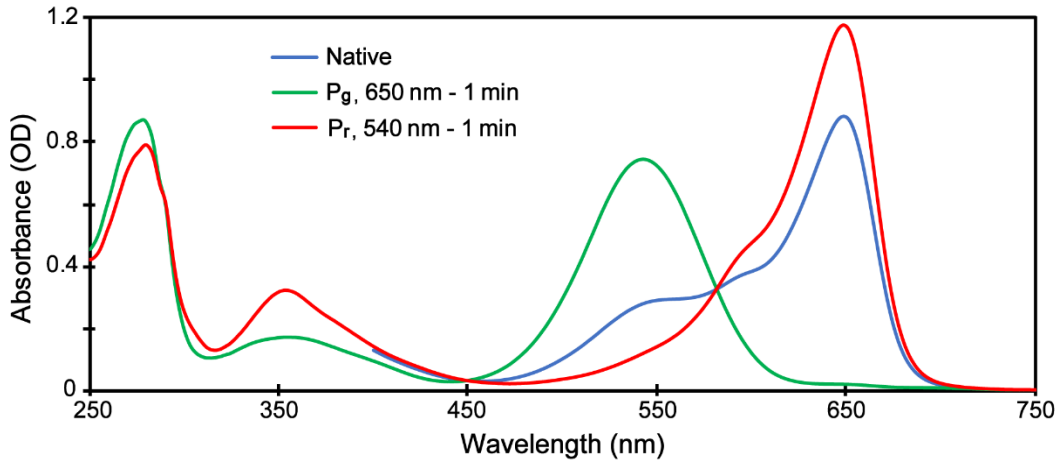

Fig. 4.6. Steady-state electronic absorption spectra of AnPixJg2 native (wild-type, blue), P_r (red), and P_g (green) forms that were provided by the Narikawa group before shipping. Native state shows the equilibrium species when kept under ambient light. The P_r and P_g species were obtained by 540 and 650 nm light irradiation for 1 minute, respectively, before immediately collecting the spectrum. The P_r and P_g species achieve almost full conversion after 1 minute of irradiation.

In comparison to the steady-state absorption spectra collected by the Narikawa group [1], the conversion in our lab (Fig. 4.1a) was not as complete due to the power achieved by our LEDs (see Section 4.4. in above). A new LED box will be printed with at least 16 LEDs to increase the overall irradiation power at the sample. The partial conversion (~80%, particularly for $P_r \rightarrow P_g$) should not affect our fs-TA data because the actinic pump excites a specific species while the data collection scheme only tracks the spectral difference due to those excited-state populations (as well as ground state bleaching, see Section 4.4). Moreover, our actinic pump wavelengths were selected to not overlap with the other species (see vertical dashed lines at 525 and 650 nm in Fig. 4.1a). Due to the evidence of a heterogeneous ground-state population (see Section

4.3.5), the actinic pump placement would discriminate which subpopulation is effectively excited. This is evident in the P_g-to-P_r photoconversion where the 525 nm actinic pump is on the blue side of the 544 nm P_g absorption peak, similar to Kim and coworkers' TA experiment on the red/green CBCR NpR6012g4 using a 500 nm actinic pump [2]. Notably, the blue-side (500 nm) excitation of $^{15E}P_g$ leads to a sub-ps and 2 ps time constants in producing a ^{15Z}Lumi-G species whereas the red-side (575 nm) excitation yields a longer 5 ps time constant.

The raw TA time-stacked plots (Fig. 4.8 below) exhibit distinct spectral features in association with the photoinduced $P_r \rightarrow P_g$ and $P_g \rightarrow P_r$ processes of AnPixJg2 in solution. In particular, for the $P_r \rightarrow P_g$ TA spectra (Fig. 4.8b), the dominant negative ~664 nm stimulated emission band exhibits clear decay dynamics, in accordance with the 2D contour plot in Section 4.4 (Fig. 4.2d).

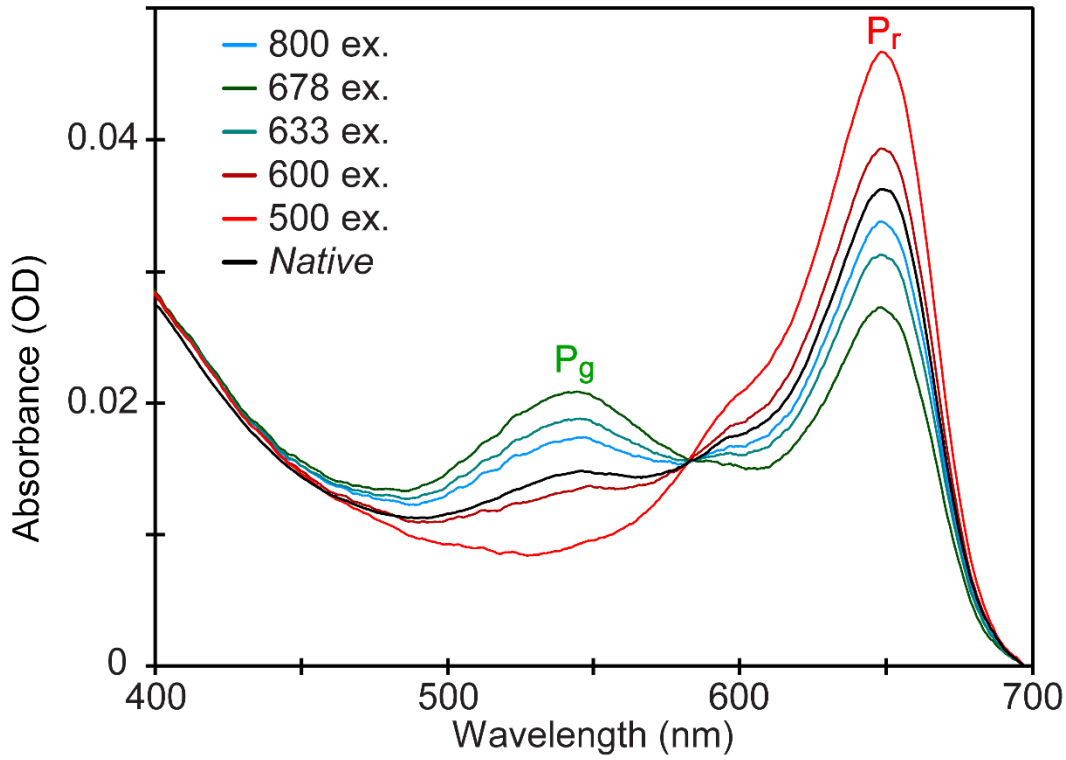

Fig. 4.7. Steady-state electronic absorption spectra of AnPixJg2 samples after being excited by the arc lamp in a Shimadzu RF-6000 spectrofluorophotometer. The excitation wavelengths were selected on the basis of Raman pump wavelengths in FSRS measurements that would resonantly enhance the P_g and P_r ground-state species (see Section 4.4 and Fig. 4.12 below). A dilute AnPixJg2 in buffer solution sample was put in a 1-mm-pathlength quartz cuvette and placed in the excitation beam path inside the spectrofluorophotometer. For each trial, AnPixJg2 sample was allowed to recover under ambient light to the native species (black) before each specific wavelength excitation (800, 678, 633, 600, 500 nm) for 1 min. All the tested excitation light can photoconvert the native species to more P_r (red) or P_g (green) species as shown by the color-coded spectra.

In particular, the protein sample was photoconverted to its native state by placing it under ambient light for five minutes and collecting the absorption spectrum to keep the starting population consistent (Fig. 4.7, black trace). The sample was then placed

in the fluorimeter with a mirror placed on the opposite side of the excitation to back-reflect and disperse the excitation light across the whole sample cell. Any excitation redder of ~630 nm can photoconvert AnPixJg2 to P_g (Fig. 4.7, green-like colors), whereas the 600 and 500 nm excitation photoconverts to P_r (Fig. 4.7, red-like colors). This result means that essentially any excitation within the absorption band of a certain species could cause photoconversion, and the extent of such conversion is dependent on the light irradiation bandwidth and power. The most unexpected photoconversion was observed with 800 nm excitation (cyan trace in Fig. 4.7), which seems to be outside of the P_r absorption band (Fig. 4.6) but still causes a slight $P_r \rightarrow P_g$ conversion.

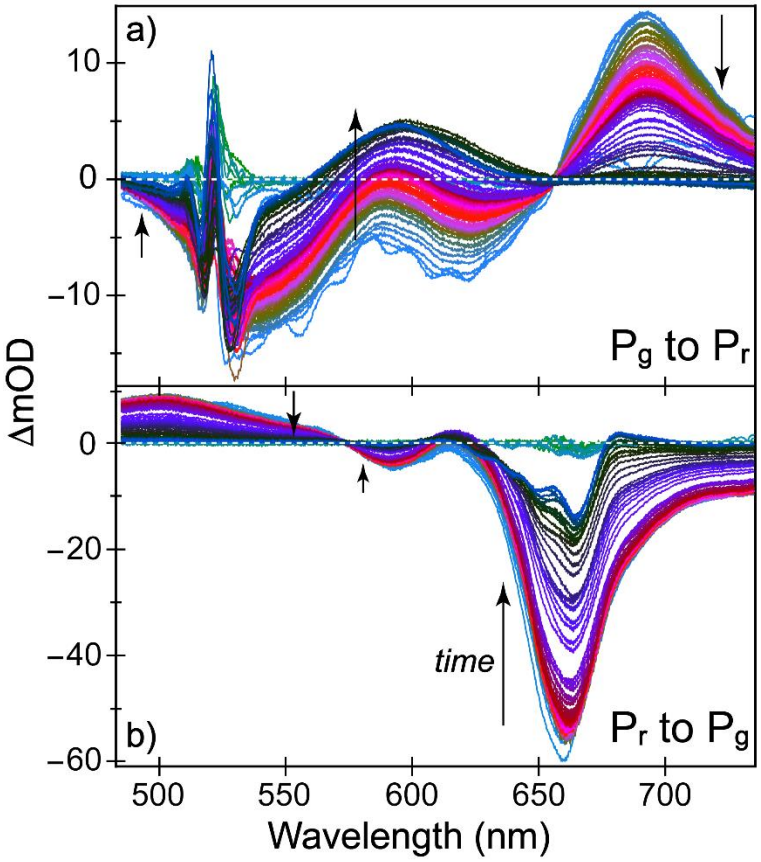

Fig. 4.8. Raw experimental time-stacked fs-TA spectra of (a) P_g to P_r and (b) P_r to P_g transition of AnPixJg2. The –2 ps time delay data trace was subtracted from the subsequent time-resolved data traces (up to 900 ps as displayed by the color-coded lines) to remove the pump light scattering at 525 and 650 nm to initiate the P_g-to-P_r (panel a) and P_r-to-P_g (panel b) transitions, respectively. Vertical arrows denote time evolution of the TA traces at representative spectral regions (see Fig. 4.2 in Section 4.4 for the 2D contour plots and associated probe-dependent dynamics with least-squares fits that retrieve the underlying time constants). The observed ultrafast electronic responses mainly arise from the photoexcited CBCR cofactor PCB chromophore. The removal of pump scattering in panel b is effective hence the full detection spectral window can be used without the need to truncate the red side.

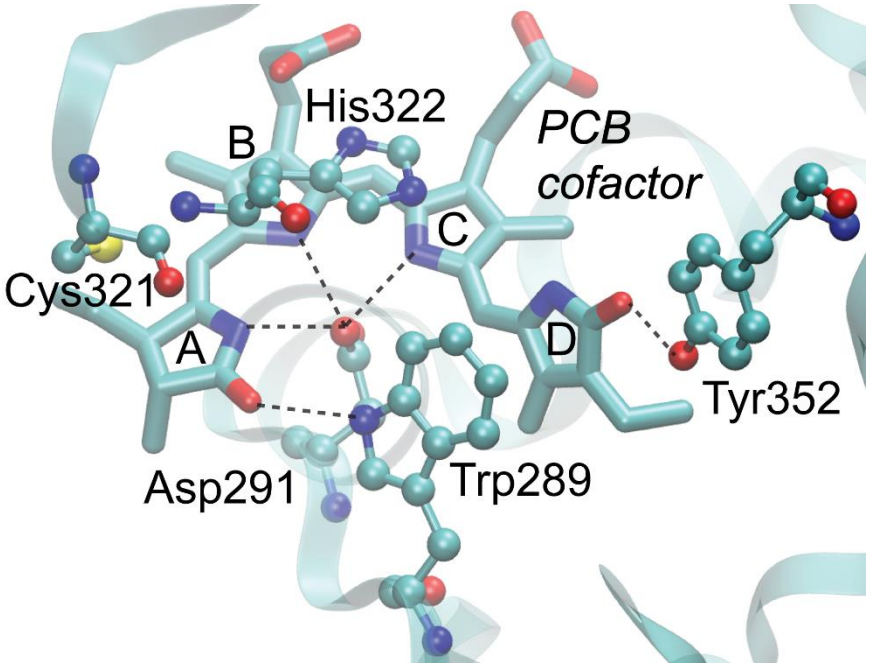

Fig. 4.9. Crystal structure of AnPixJg2 (PBD ID: 3W2Z) [3] in the P_r state with key residues surrounding the PCB cofactor. The canonical Cys321 within the GAF domain covalently binds PCB (closest to the A ring) with His322 keeping the B and C rings in a coplanar geometry. Representative H-bonding interactions are shown by dashed lines between the chromophore and key residues in its vicinity. AnPixJg2 is a typical expanded red/green (XRG) CBCR GAF domain that covalently attaches to PCB and exhibits reversible photoconversion between a 15*Z*-isomer (P_r, shown here) and a 15*E*-isomer (P_g, see Fig. 4.10 below for illustration).

Notably, these polar or aromatic residues are highly conserved between AnPixJg2 that binds PCB and the recently engineered AnPixJg2_BV4 (H293Y, F308T, H318Y, I336V; residues 308 and 336 located in close proximity to the C ring) that binds the biliverdin cofactor (see Section 4.4.1 above) [1]. Therefore, such an elaborate network with electronic interactions (including the directional H-bonding) and steric constraints is essential to stabilize the cofactor chromophore conformation and maintain function

(e.g., these versatile red/green CBCRs that differ from the red/far-red phytochromes) in the protein matrix, particularly regarding the cofactor binding pocket.

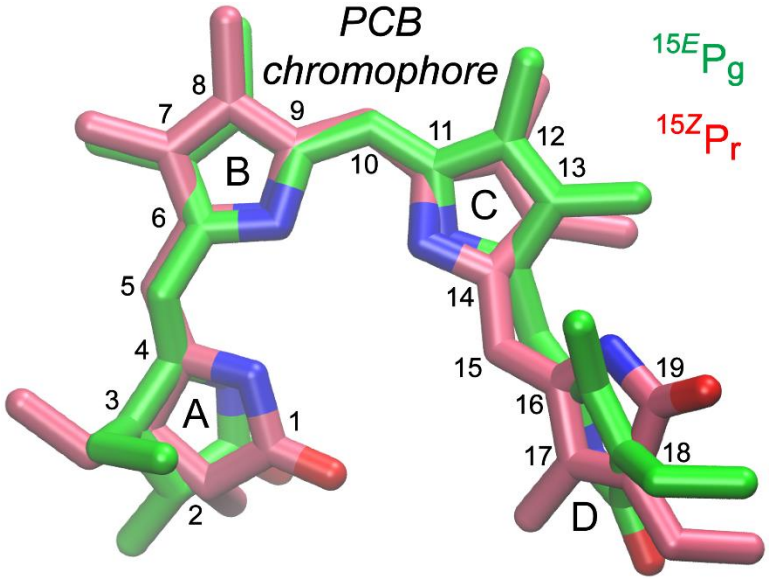

Fig. 4.10. Overlaid calculated structures that represent the P_g (green) and P_r (red) conformers of the PCB cofactor of AnPixJg2. The atomic numbering (1-19) of carbon atoms of the tetrapyrrole-ring system is shown. Besides the primary C15=C16 double bond *Z*-to-*E* transition at the D ring (dihedral angle change by ~155°, a clear change of the D-ring position with respect to the tetrapyrrole-ring plane), notable twisting of the C5–C6 bond between the A/B rings is apparent (dihedral angle change by ~72°, see Table 4.2 below) [4].

Interestingly, a previous molecular dynamics (MD) study of AnPixJg2 in solution on the 1 μs time scale showed more change of the A-B methine bridge single bond (C5–C6) than the double bond (C4=C5) between two conformational sub-states,

causing a decreased coplanarity of the A-ring with respect to the tetrapyrrole ring plane [5]. See Section 4.3.6 above for our computational work details to obtain the ground-state equilibrium state with certain frozen coordinates in Gaussian software [6]. The chromophore remains protonated (at the C-ring nitrogen site) for these two calculations, in accordance with recent work [7,8].

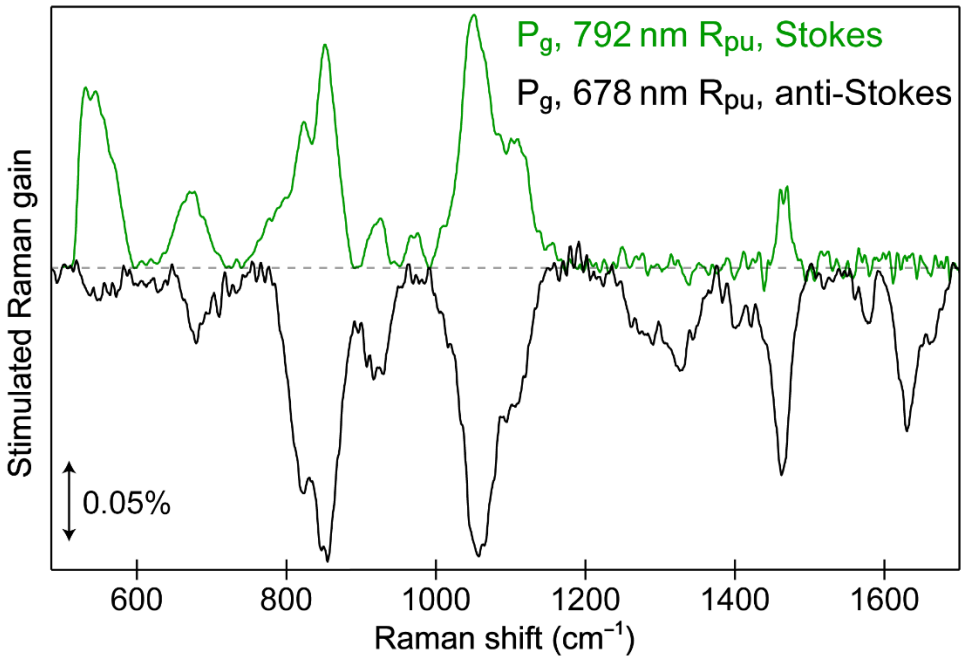

Fig. 4.11. Ground-state (GS-)FSRS spectra of the P_g species of AnPixJg2 with 792 nm Raman pump (R_{pu}) and broadband Raman probe on the Stokes side (green, stimulated Raman gain) as well as 678 nm R_{pu} and broadband Raman probe on the anti-Stokes side (black, stimulated Raman loss, frequency axis multiplied by –1 for direct overlay with the green trace). The double-headed arrow represents the Raman gain magnitude of 0.05%.

Notably, both GS-FSRS experiments with different R_{pu} wavelengths used the freshly prepared sample solution via a flow cell connected to an LED box with 650 nm LEDs, which maintain AnPixJg2 in the P_g state. Although the 792 nm R_{pu} does not significantly overlap with the P_g or P_r absorption bands (Fig. 4.1a) while inducing some photoconversion (Fig. 4.7), which should record Raman features of a mostly pure P_g state, the off-resonance condition and weak Raman probe photon counts in the far-red region leads to compromised information in the high-frequency region where crucial C=C, C=N, and C=O vibrations occur (e.g., see largely absent peaks in green trace above 1200 cm^{-1}). Nevertheless, other Raman modes mostly match between the two spectra above.

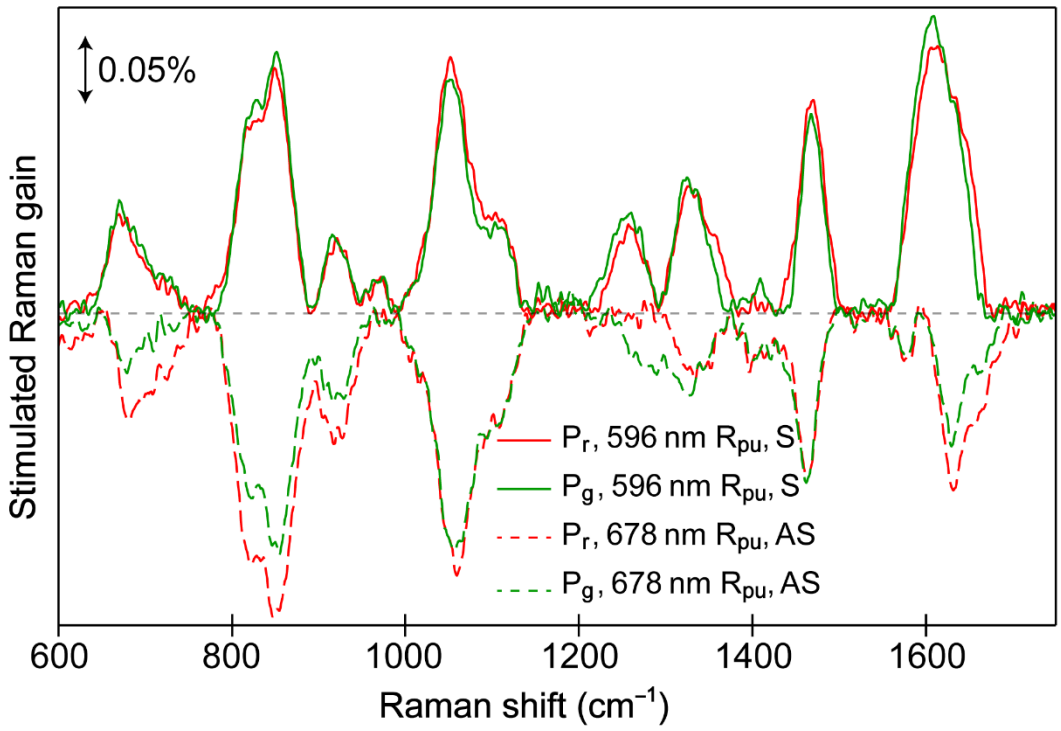

Fig. 4.12. Tunable GS-FSRS of the P_g and P_r species of AnPixJg2. Narrowband Raman pump at 596 nm (solid) and 678 nm (dashed) with broadband Raman probe on the Stokes and anti-Stokes sides lead to the recorded Raman spectra of the sample irradiated by 650 nm (green) and 505 nm (red) LEDs. The double-headed arrow represents the stimulated Raman gain magnitude of 0.05%.

Although 650 nm LEDs convert and maintain AnPixJg2 in the P_g state, two R_{pu} wavelengths at 596 nm (green solid) and 678 nm (green dashed) result in different GS-FSRS with noticeable peak frequency shifts (e.g., above 1400 cm^{-1}). Interestingly, even with different starting species of P_r and P_g in association with different LEDs (red vs. green), R_{pu} becomes the dominant factor for the recorded spectra since there are only slight intensity changes with no significant Raman shifts (i.e., green solid spectrum matches red solid spectrum, green dashed spectrum matches red dashed spectrum).

Such a phenomenon could be rationalized by the photoconverting capability of R_{pu}: 596 and 678 nm generates more P_r and P_g species, respectively (Fig. 4.7). The high-frequency modes manifest larger frequency and intensity changes (P_r vs. P_g) than the low-frequency modes.

Notably, vibrational mode changes are expected between P_r and P_g states because the chromophore D-ring isomerizes and breaks the adjacent H-bonds and π-π stacking interactions to various extents (see Fig. 4.1b in Section 4.4 and Figs. 4.9-4.10 above) [9]. Though our LEDs may not achieve complete photoconversion and a mixed population still exists, the visual color change of the sample solution with significant absorption spectral change indicates that the dominant species of P_r or P_g can be achieved by specific light excitation as used in our experiments.

Table 4.1. Experimental Raman mode frequencies and assignments aided by quantum calculations

GS-FSRS [a]	DFT calc. (unscaled) [b]	Vibrational mode assignment (major)
P_r		
1649	1621 (1671)	A-B methine bridge C_4=C_5 stretch and C–H rock with A-ring N–H rock
1615 [c]	1609 (1659)	C-D methine bridge C_{15}=C_{16} stretch and C–H rock with D-ring N–H rock and C=C stretch
1469	1486 (1532)	B & C-ring deformation with N–H rock
1327	1340 (1381)	B-C bridge C–H rocking with C & D-ring N–H rock and ring deformation
1258	1242 (1280)	Bridge C–H rocking with all N–H rocking
1052	1046 (1078)	D-ring deformation with strong CH_3 bending motions
850	803 (828)	C-D bridge C–H wagging, small C–H rocking in B-C bridge
673	673 (694)	Collective C–C conjugated wagging with C–H wagging
P_g D-ring twist ~155° & A-ring twist ~76°		
1665	1634 (1685)	A-B methine bridge C_4=C_5 stretch and C–H rock with A-ring N–H rock
1630 [c]	1622 (1672)	C-D methine bridge C_{15}=C_{16} stretch and C–H rock with D-ring N–H rock and C=C stretch
1461	1487 (1533)	B & C-ring deformation with N–H rock
1328	1332 (1373)	B-C bridge C–H rocking with C & D-ring N–H rock and ring deformation
1258	1236 (1274)	Bridge C–H rocking with all N–H rocking
1056	1047 (1079)	D-ring deformation with strong CH_3 bending motions
854	785 (809)	C-D bridge C–H wagging, small C–H rocking in B-C bridge
680	643 (663)	C-D methine bridge and D-ring wagging with some A-ring wagging

[a] The experimental GS-FSRS peak frequencies validated by tunable R_{pu} wavelengths and detailed comparison between the Stokes and anti-Stokes spectra of P_g and P_r species of AnPixJg2. The broad Raman bands are fit by multiple gaussian profiles [10] with their center frequencies noted.

[b] Vibrational normal mode frequencies of the P_r and P_g species of the PCB chromophore were calculated from the geometrically optimized structure in the

electronic ground state (S_0) using density functional theory (DFT, see Section 4.3.6 above) in Gaussian 16 [6]. The frequency scaling factor was 0.97 to compare the off-resonance calculation results [11,12] to the GS-FSRS experimental values [13,14]. The match between experimental and calculated frequencies for the low-frequency modes is less than satisfactory due to the collective nature of skeletal motions and their higher dependence on protein local environment that we did not explicitly model [15,16]. The blueshift of the C=C stretching modes from P_r to P_g is a "vibrational" staple for the AnPixJg2 photoconversion [17,18].

[c] There is a small shoulder peak to the lower-frequency side of this main peak, at ~1579 cm^{-1}, that exhibits a largely unchanged frequency in P_r and P_g (indicating that the PCB cofactor remains protonated upon reaching the equilibrated ground state) [10,18]. This peak was attributed to an in-phase N–H in-plane bending (rocking) motion of the B- and C-ring nitrogen atoms [18], which is red-shifted from similar motions involving the D-ring nitrogen atom (i.e., 1615 cm^{-1} in P_r, and 1630 cm^{-1} in P_g).

Table 4.2. Bridge dihedral angles involving terminal pyrrole rings of the PCB cofactor in various CBCR conformers

	A/B NCCC DB [a]	A/B CCCN SB [a]	C/D NCCC SB [a]	C/D CCCN DB [a]
P_r (3W2Z) [b]	0.380	10.576	– 147.893	26.955
P_g (5M82) [b]	7.488	– 61.077	– 109.810	– 178.439
$P_r \rightarrow P_g$ change [c]	7.108	71.653	38.083	154.606

[a] The columns designate dihedral angels (°) of the methine bridges between specific chromophore rings, listing four atoms (e.g., NCCC and CCCN) that make up the specific dihedral angle and the pertinent chemical bond being a single bond (SB) or double bond (DB).

[b] The P_r and P_g conformers of PCB cofactors were taken from the crystal structures of (PDB ID) 3W2Z and 5M82, respectively. 3W2Z reports the P_r crystal structure of AnPixJg2, while 5M82 is the crystal structure of the photoproduct state of GAF3 from Slr1393 of *Synechocystis* sp. PCC6803, a similar red-green switching CBCR like AnPixJg2. Since the dihedral angles between A and B rings were not fixed for the P_r calculation (Section 4.3.6), the resultant A/B-ring DB and SB dihedral angles in the geometrically optimized structure were 4.616° and 15.344°, respectively.

[c] For the P_r to P_g transition, the D ring twists by ~155° along the C_{15}=C_{16} bond (going through 180°/–180° as the preferred twisting route to also avoid steric hindrance with the adjacent C-ring methyl group, see Fig. 4.10; the largest magnitude of dihedral angle change within this table) and ~38° via the C_{14}–C_{15} single bond (see Figs. 4.1b and 4.10 for structural illustration). In contrast, the A ring does not twist as much with ~7° along the C_4=C_5 double bond and ~72° along the C_5–C_6 single bond, largely matching a previous work running 15-ns MD simulations on the photoproduct state of AnPixJg2 and obtaining the associated dihedral angle changes of ~6.4° and 30.3° [18]. Note that the magnitudes of the dihedral angle changes are tabulated in this row. The D-ring twist was found to contribute more than the A-ring to the photoproduct color tuning [8].

4.8 Supplemental References

[1] K. Fushimi, T. Miyazaki, Y. Kuwasaki, T. Nakajima, T. Yamamoto, K. Suzuki, Y. Ueda, K. Miyake, Y. Takeda, J.-H. Choi, H. Kawagishi, E.Y. Park, M. Ikeuchi, M. Sato, R. Narikawa, Rational conversion of chromophore selectivity of cyanobacteriochromes to accept mammalian intrinsic biliverdin, Proc. Natl. Acad. Sci. U. S. A. 116 (2019) 8301-8309. https://doi.org/10.1073/pnas.1818836116.

[2] P.W. Kim, L.H. Freer, N.C. Rockwell, S.S. Martin, J.C. Lagarias, D.S. Larsen, Femtosecond photodynamics of the red/green cyanobacteriochrome NpR6012g4 from *Nostoc punctiforme*. 2. Reverse dynamics, Biochemistry 51 (2012) 619-630. https://doi.org/10.1021/bi2017365.

[3] R. Narikawa, T. Ishizuka, N. Muraki, T. Shiba, G. Kurisu, M. Ikeuchi, Structures of cyanobacteriochromes from phototaxis regulators AnPixJ and TePixJ reveal general and specific photoconversion mechanism, Proc. Natl. Acad. Sci. U. S. A. 110 (2013) 918-923. https://doi.org/10.1073/pnas.1212098110.

[4] E. Claesson, W.Y. Wahlgren, H. Takala, S. Pandey, L. Castillon, V. Kuznetsova, L. Henry, M. Panman, M. Carrillo, J. Kübel, R. Nanekar, L. Isaksson, A. Nimmrich, A. Cellini, D. Morozov, M. Maj, M. Kurttila, R. Bosman, E. Nango, R. Tanaka, T. Tanaka, L. Fangjia, S. Iwata, S. Owada, K. Moffat, G. Groenhof, E.A. Stojković, J.A. Ihalainen, M. Schmidt, S. Westenhoff, The primary structural photoresponse of phytochrome proteins captured by a femtosecond X-ray laser, eLife 9 (2020) e53514. https://doi.org/10.7554/eLife.53514.

[5] L.K. Scarbath-Evers, S. Jähnigen, H. Elgabarty, C. Song, R. Narikawa, J. Matysik, D. Sebastiani, Structural heterogeneity in a parent ground-state structure of AnPixJg2 revealed by theory and spectroscopy, Phys. Chem. Chem. Phys. 19 (2017) 13882-13894. https://doi.org/10.1039/C7CP01218G.

[6] M.J. Frisch, G.W. Trucks, H.B. Schlegel, G.E. Scuseria, M.A. Robb, J.R. Cheeseman, G. Scalmani, V. Barone, G.A. Petersson, H. Nakatsuji, X. Li, M. Caricato, A.V. Marenich, J. Bloino, B.G. Janesko, R. Gomperts, B. Mennucci, H.P. Hratchian, J.V. Ortiz, A.F. Izmaylov, J.L. Sonnenberg, D. Williams-Young, F. Ding, F. Lipparini, F. Egidi, J. Goings, B. Peng, A. Petrone, T. Henderson, D.

Ranasinghe, V.G. Zakrzewski, J. Gao, N. Rega, G. Zheng, W. Liang, M. Hada, M. Ehara, K. Toyota, R. Fukuda, J. Hasegawa, M. Ishida, T. Nakajima, Y. Honda, O. Kitao, H. Nakai, T. Vreven, K. Throssell, J. J. A. Montgomery, J.E. Peralta, F. Ogliaro, M.J. Bearpark, J.J. Heyd, E.N. Brothers, K.N. Kudin, V.N. Staroverov, T.A. Keith, R. Kobayashi, J. Normand, K. Raghavachari, A.P. Rendell, J.C. Burant, S.S. Iyengar, J. Tomasi, M. Cossi, J.M. Millam, M. Klene, C. Adamo, R. Cammi, J.W. Ochterski, R.L. Martin, K. Morokuma, O. Farkas, J.B. Foresman, D.J. Fox, *Gaussian 16, Revision A.03*, in, Gaussian, Inc., Wallingford, CT, 2016.

[7] N.C. Rockwell, S.S. Martin, S. Lim, J.C. Lagarias, J.B. Ames, Characterization of red/green cyanobacteriochrome NpR6012g4 by solution nuclear magnetic resonance spectroscopy: a protonated bilin ring system in both photostates, Biochemistry 54 (2015) 2581-2600. https://doi.org/10.1021/bi501548t.

[8] C. Wiebeler, A.G. Rao, W. Gärtner, I. Schapiro, The effective conjugation length is responsible for the red/green spectral tuning in the cyanobacteriochrome Slr1393g3, Angew. Chem. Int. Ed. 58 (2019) 1934-1938. https://doi.org/10.1002/anie.201810266.

[9] C. Fang, L. Tang, C. Chen, Unveiling coupled electronic and vibrational motions of chromophores in condensed phases, J. Chem. Phys. 151 (2019) 200901. https://doi.org/10.1063/1.5128388.

[10] C. Fang, L. Tang, B.G. Oscar, C. Chen, Capturing structural snapshots during photochemical reactions with ultrafast Raman spectroscopy: from materials transformation to biosensor responses, J. Phys. Chem. Lett. 9 (2018) 3253–3263. https://doi.org/10.1021/acs.jpclett.8b00373.

[11] J. Neugebauer, M. Reiher, C. Kind, B.A. Hess, Quantum chemical calculation of vibrational spectra of large molecules—Raman and IR spectra for Buckminsterfullerene, J. Comput. Chem. 23 (2002) 895-910. https://doi.org/10.1002/jcc.10089.

[12] C. Chen, L. Zhu, M.S. Baranov, L. Tang, N.S. Baleeva, A.Y. Smirnov, I.V. Yampolsky, K.M. Solntsev, C. Fang, Photoinduced proton transfer of GFP-inspired fluorescent superphotoacids: principles and design, J. Phys. Chem. B 123 (2019) 3804-3821. https://doi.org/10.1021/acs.jpcb.9b03201.

[13] A.P. Scott, L. Radom, Harmonic vibrational frequencies: an evaluation of Hartree−Fock, Møller−Plesset, quadratic configuration interaction, density functional theory, and semiempirical scale factors, J. Phys. Chem. 100 (1996) 16502-16513. https://doi.org/10.1021/jp960976r.

[14] J.P. Merrick, D. Moran, L. Radom, An evaluation of harmonic vibrational frequency scale factors, J. Phys. Chem. A 111 (2007) 11683-11700. https://doi.org/10.1021/jp073974n.

[15] S. Gozem, F. Melaccio, H.L. Luk, S. Rinaldi, M. Olivucci, Learning from photobiology how to design molecular devices using a computer, Chem. Soc. Rev. 43 (2014) 4019-4036. https://doi.org/10.1039/c4cs00037d.

[16] C. Fang, L. Tang, Mapping structural dynamics of proteins with femtosecond stimulated Raman spectroscopy, Annu. Rev. Phys. Chem. 71 (2020) 239-265. https://doi.org/10.1146/annurev-physchem-071119-040154.

[17] Y. Fukushima, M. Iwaki, R. Narikawa, M. Ikeuchi, Y. Tomita, S. Itoh, Photoconversion mechanism of a green/red photosensory cyanobacteriochrome AnPixJ: time-resolved optical spectroscopy and FTIR analysis of the AnPixJ-GAF2 domain, Biochemistry 50 (2011) 6328-6339. https://doi.org/10.1021/bi101799w.

[18] F. Velazquez Escobar, T. Utesch, R. Narikawa, M. Ikeuchi, M.A. Mroginski, W. Gärtner, P. Hildebrandt, Photoconversion mechanism of the second GAF domain of cyanobacteriochrome AnPixJ and the cofactor structure of its green-absorbing state, Biochemistry 52 (2013) 4871-4880. https://doi.org/10.1021/bi400506a.

Chapter 5 An Engineered Biliverdin-Compatible Cyanobacteriochrome Enables a Unique Ultrafast Reversible Photoswitching Pathway

Published in: **Sean R. Tachibana**, Longteng Tang, Liangdong Zhu, Yuka Takeda, Keiji Fushimi, Yoshibumi Ueda, Takahiro Nakajima, Yuto Kuwasaki, Moritoshi Sato, Rei Narikawa, and Chong Fang* **(2021)** "An Engineered Biliverdin-Compatible Cyanobacteriochrome Enables a Unique Ultrafast Reversible Photoswitching Pathway", *Int. J. Mol. Sci.*, 22 (10), 5252. DOI: 10.3390/ijms22105252.

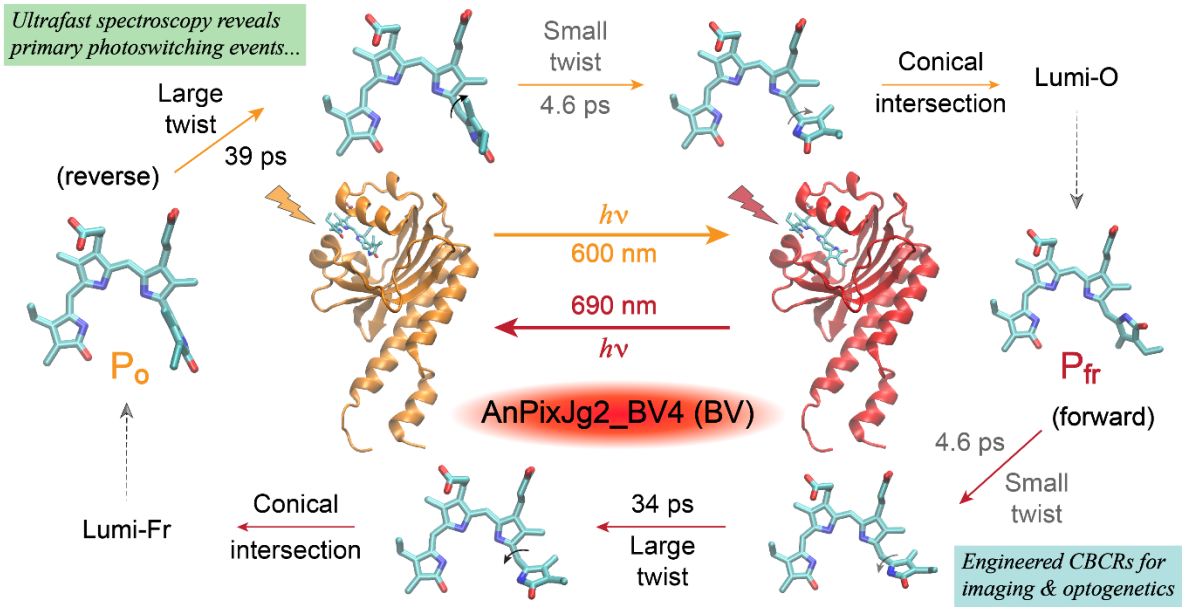

"Perception is strong and sights weak. In strategy, it is important to see distant things as if they were close and to take a distanced view of close things." – Miyamoto Musashi

5.1 Abstract

Cyanobacteriochromes (CBCRs) are promising optogenetic tools for their diverse absorption properties with a single compact cofactor-binding domain. We previously uncovered the ultrafast reversible photoswitching dynamics of a red/green photoreceptor AnPixJg2, which binds phycocyanobilin (PCB) that is unavailable in mammalian cells. Biliverdin (BV) is a mammalian cofactor with a similar structure to PCB but exhibits redder absorption. To improve the AnPixJg2 feasibility in mammalian applications, AnPixJg2_BV4 with only four mutations has been engineered to incorporate BV. Herein, we implemented femtosecond transient absorption (fs-TA) and ground state femtosecond stimulated Raman spectroscopy (GS-FSRS) to uncover transient electronic dynamics on molecular time scales and key structural motions responsible for the photoconversion of AnPixJg2_BV4 with PCB (Bpcb) and BV (Bbv) cofactors in comparison with the parent AnPixJg2 (Apcb). Bpcb adopts the same photoconversion scheme as Apcb, while BV4 mutations create a less bulky environment around the cofactor D ring that promotes a faster twist. The engineered Bbv employs a reversible clockwise/counterclockwise photoswitching that requires a two-step twist on ~5 and 35 ps time scales. The primary forward $P_{fr} \rightarrow P_o$ transition displays equal amplitude weights between the two processes before reaching a conical intersection. In contrast, the primary reverse $P_o \rightarrow P_{fr}$ transition shows a 2:1 weight ratio of the ~35 ps over 5 ps component, implying notable changes to the D-ring-twisting pathway. Moreover, we performed pre-resonance GS-FSRS and quantum calculations to identify the Bbv vibrational marker bands at ~659, 797, and 1225 cm^{-1}. These modes reveal a stronger H-bonding network around the BV cofactor A ring with

BV4 mutations, corroborating the D-ring-dominant reversible photoswitching pathway in the excited state. Implementation of BV4 mutations in other PCB-binding GAF domains like AnPixJg4, AM1_1870g3, and NpF2164g5 could promote similar efficient reversible photoswitching for more directional bioimaging and optogenetic applications, and inspire other bioengineering advances.

5.2 Introduction

Phytochromes, bacteriophytochromes, and cyanobacteriochromes (CBCRs) are among a superfamily of linear tetrapyrrole (bilin chromophore that is metabolically derived from heme) binding photoswitching proteins [1-3]. In nature, these proteins act as photosensing and signaling units that allow organisms to detect and respond to light from the UV to near-IR range [4-8]. Previous efforts have engineered these proteins as both non-invasive optogenetic tools [9-11] and fluorescent tags in vivo [12,13]. CBCRs have shown to be a versatile tool in optogenetic applications by requiring only a single compact domain for incorporation of the cofactor chromophore, the photosensing unit that can be considered as the active site [3,14]. Recently, we have studied a red/green-absorbing ($^{15Z}P_r/^{15E}P_g$) hypsochromic CBCR named AnPixJg2 using the wavelength-tunable femtosecond transient absorption (fs-TA) and ground-state femtosecond stimulated Raman spectroscopy (GS-FSRS) [15]. We uncovered the initial ultrafast dynamics as the phycocyanobilin (PCB cofactor in protein matrix) photoswitches from the P_g to P_r and P_r to P_g conformers in a reversible manner (controlled by a combination of actinic laser pump pulses and continuous-wave/cw LEDs). The nomenclature of *Z* and *E* refers to the C-D ring methine bridge C15=C16 configuration in the *cis* and *trans*

state, respectively. The $P_g \rightarrow P_r$ conversion exhibits a more downhill reaction with a ~3 ps lifetime to reach a conical intersection (CI) and relaxes into a Lumi-G state on the ~30 ps time scale. In contrast, the $P_r \rightarrow P_g$ conversion shows a longer-lived excited state with ~13 and 217 ps time constants to reach a CI, which takes much longer time to further relax in the ground state of Lumi-R and beyond.

Although AnPixJg2 has shown to be an efficient photoswitching protein, some major drawbacks involve the lack of PCB in mammalian cells and a green absorbing ($^{15E}P_g$) form outside the optimal biological window, which render it less ideal for mammalian applications. Many protein engineers have drawn inspirations from similar photoswitching proteins such as bacteriophytochromes, which incorporate the biliverdin (BV) cofactor that is intrinsic in mammalian cells. BV also red-shifts the absorption profiles of both conformational states due to a larger electronic conjugation than the PCB molecular framework [16]. Unlike CBCRs, bacteriophytochromes require three domains as a large photosensory core module with global structural preferences for BV incorporation and are typically used as fluorescent probes due to their higher fluorescence quantum yield [17]. In contrast, CBCRs that incorporate PCB as the cofactor exhibit low binding affinity for BV due to the double-bond carbon that cysteine (e.g., Cys321) covalently binds to (see Figure 5.1A–C). The different binding sites shift the cofactor location in the pocket, which decreases binding and protein expression [18].

To expand the functional space of CBCRs, the canonical AnPixJg2 has been engineered to accept the BV cofactor (AnPixJg2_BV4) with a solved crystal structure (PDB: 5ZOH) [18]. This advance was achieved by mutating four key residues around

the cofactor pocket (H293Y, F308T, H318Y, and I336V). The BV incorporation red-shifts the red/green absorption to a far-red/orange absorption profile. The overall structure of AnPixJg2 with PCB cofactor (Apcb for short) and AnPixJg2_BV4 with BV cofactor (Bbv for short) was shown to be quite similar. The major structural difference was identified to be the BV cofactor shifted by ~0.75 Å due to the canonical Cys321 covalently binding at the $C3^2$ instead of $C3^1$ in PCB (Figure 5.1A,B versus C). Although shifted in Bbv, five crucial residues responsible for cofactor stability (W289, D291, R301, H322, and Y352) were also shown to be highly conserved in the cofactor vicinity. Of the four mutations (H293Y, F308T, H318Y, and I336V), F308T and I366V were found to be the most crucial for BV incorporation and expression. Both of these residues are located near cofactor C and D rings that reduce steric hindrance upon the BV-acceptable mutations. Besides achieving spatially compact residues, F308T and H318Y both contribute to better stabilize the C ring propionate group through H-bonding. The same BV4 mutations were also demonstrated in several other PCB GAF domains with clearly improved BV-binding efficiencies [18].

Since internal conversion between the spin-allowed electronic states typically occurs on ultrafast time scales that precedes fluorescence events on the nanosecond (ns) time scale [19], the tracking of Bbv cofactor ultrafast dynamics could uncover how the BV4 mutations affect the photoswitching pathways in real time. We implemented a systematic study using fs-TA with global analysis, and GS-FSRS with quantum calculations of AnPixJg2_BV4 with PCB cofactor (Bpcb for short), Apcb, and Bbv. These unique CBCR samples allow for a direct comparison of the same cofactor in different pockets (Apcb vs. Bpcb), and different cofactors in the same pocket (Bpcb vs.

Bbv). Correlating the effects of the BV4 mutations and BV cofactor on reversible photoswitching pathways with primary electronic and structural events in the non-equilibrium regime could facilitate future rational design of CBCRs, photoswitching proteins with cofactors, and other functional photochromic systems in general.

5.3 Experimental Material and Methods

5.3.1 Protein expression

The His-tagged AnPixJg2_BV4 inserted into pET28a vector (Novagen) was constructed in our previous study [18]. The plasmid was transferred into the E. coli strain C41 (Cosmo Bio) harboring the PCB synthetic system (pKT271-C0185) or BV synthetic system (pKT270) for protein expression. The bacterial cells were grown on Lysogeny Broth (LB) agar medium at 37 °C and selected by kanamycin and chloramphenicol (each final concentration set at 20 μg/mL), then cultured in 1 L LB medium at 37 °C until the cell optical density (OD) at 600 nm reached a range of 0.4–0.8. Isopropyl β-D-1-thiogalactopyranoside (IPTG at final concentration of 0.1 mM) was then added into the culture media and these cells were cultured at 18 °C overnight to induce protein expression.

5.3.2 Protein extraction and purification

After protein expression was induced, the culture broth was centrifuged at 5,000 *g* for 15 min to collect cells and then frozen at –80 °C. The cells were suspended in a lysis buffer (20 mM HEPES–NaOH at pH=7.5, 0.1 M NaCl, and 10% (w/v) glycerol)

and disrupted by Emulsiflex C5 high-pressure homogenizer at 12,000 psi (Avestin, Inc.), The 4-(2-hydroxyethyl)piperazine-(2-ethanesulfonic acid) or HEPES aqueous buffer solution was used because it has higher stability in maintaining the physiological pH values of cell culture media despite changes in CO_2 concentration. The mixtures were then centrifuged at 165,000 *g* for 30 min to remove pellets, and the collected solutions were filtered through a 0.2 μm membrane. After adding imidazole (30 mM final concentration), the solution was loaded onto a nickel-affinity His-trap column (GE Healthcare). After washing with lysis buffer containing 30–100 mM imidazole, the His-tagged proteins were purified using lysis buffer containing 100–400 mM imidazole with a linear gradient system (1 mL/min) for 15 min. The purified proteins were incubated with 1 mM EDTA on ice for 1 h and then dialyzed against the lysis buffer to remove the residual imidazole and EDTA. This detailed process to make Bpcb (green/red) and Bbv (orange/far-red) samples in this work was identical to the one we used to prepare Apcb (green/red) samples [15], and all the CBCR samples were prepared in the aforementioned HEPES buffer solution at physiological pH (7.5) and the specific concentrations (see Table 5.1 in Section 4.1 below) for all the steady-state and time-resolved spectroscopic measurements as reported herein.

5.3.3 Femtosecond transient absorption (fs-TA) and ground-state femtosecond stimulated Raman spectroscopy (GS-FSRS) with various light irradiation conditions

Our fs-TA and GS-FSRS setups have been built upon a Ti:sapphire-based laser oscillator (Mantis-5, Coherent, Inc.) and regenerative amplifier (Legend Elite-USP-

1K-HE, Coherent, Inc.), which produce fundamental pulses of ~800 nm center wavelength, 3.7 W average power, and 35 fs duration at 1 kHz repetition rate [57,63]. Tunable fs photoexcitation pulses were generated through a home-built two-stage noncollinear optical parametric amplifier (NOPA) [64]. The desired output wavelength was selected in the first NOPA by overlapping a supercontinuum white light (SCWL) and a 400 nm pump, which were generated by focusing a portion of the fundamental pulses on a thin sapphire crystal and a BBO crystal, respectively. This output pulse was used as the seed and further amplified by the second NOPA with a stronger 400 nm pump. The probe pulse was also an SCWL but generated through a 2-mm-thick quartz cell filled with deionized water to extend to a bluer spectral region than the sapphire plate [31]. The actinic pump and probe pulses were temporally compressed via chirped-mirror pairs DCM-12 (400–700 nm) and DCM-9 (450–950 nm, Laser Quantum, Inc.), respectively [15]. The laser beam size at the focus for the actinic pump was measured to be ~150 μm in diameter. The pump-probe delay was controlled by a 150 mm motorized linear translation stage (NRT150, Thorlabs, Inc.) that enables a detection time window of ~1 ns. To ensure sufficient data points across the entire time window for subsequent spectral analysis up to the ns time scale (see Figure 5.3 and Figure 5.7), we collected a total of 110 time delay points between –2 ps and 600 ps (taking every 100 ps from 100 to 600 ps, hence 6 points on the long time scale) for the Bpcb $P_g \rightarrow P_r$ transition (Figure 5.2A), and a total of 138 time delay points between –2 ps and 900 ps (every 50 ps from 100 to 900 ps, hence 17 points on the long time scale) for the Bpcb $P_r \rightarrow P_g$, Bbv $P_o \rightarrow P_{fr}$, and Bbv $P_{fr} \rightarrow P_o$ transitions (Figure 5.2C,B,D). In particular, for the probe-dependent fits of TA marker bands for Bbv (Figure 5.7B and 5.7D), we fit

the long time constant within a numerical range from ~1–5 ns, and found that the best fits to go through 17 data points from time delay of 100 to 900 ps without large offsets were achieved with a ~3 ns time constant. These characteristic values were corroborated by global analysis results (see Figure 5.3C,G and 5.3D,H), which show a ~10% increase of root-mean-square deviation (RMSD) if the ns time constant was removed from the fits. This systematic retrieval of time constants and amplitudes in Figure 5.7 in association with fs-TA data in Figure 5.2 substantiates all our reaction models in Figure 5.5, further supported by our FSRS data in Figure 5.4 (see Section 5.4).

Before each fs-TA experiment, the CBCR sample solution inside a 2 mL microcentrifuge tube was kept in a home-built 3D-printed black box and irradiated with LEDs of a certain wavelength for 5 min to ensure that all protein samples were converted to the desired state. The detail of the 3D LED box can be found in our previous report [15]. The sample solution was then circulated through a 1-mm-pathlength quartz flow cell (48-Q-1, Starna Cells) positioned in the laser beam path. During the experiments, the power of actinic pump that can convert the sample was set at ~0.3 mW while the LEDs were constantly on to ensure the sample return to their initial states after the laser-induced conversion. Detailed combinations of the pump and LED wavelengths are listed in Table 5.1 (see below) as a handy summary for experimental conditions that yield major results in this work.

For GS-FSRS experiments (note that “femtosecond” in the FSRS terminology does not restrict it to excited-state measurements using a preceding actinic pump, so only the Raman ps-pump-fs-probe pair is required for a ground-state measurement),

the ~4 mW, 2 ps Raman pump with 803 nm center wavelength was directly produced from a portion of the laser fundamental output through a home-built reflective-grating-slit-based spectral filter [63]. This pump wavelength was shown to lead to minimal photoconversion that could generate a mixed P_g/P_r population of AnPixJg2 [15] so we can focus on the more pure conformer state under specific cw light irradiation conditions (see Figure 5.4). Raman pump was chopped at half of the laser repetition rate (500 Hz). The Raman probe was generated via a 2-mm-thick sapphire crystal plate (instead of a water-filled cuvette) due to its capability of producing stronger redder photons up to ~920 nm [31,63]. The same quartz flow cell and LED boxes were used. Both the Stokes and anti-Stokes GS-FSRS spectra were collected for a direct comparison and confirmation of Raman peak frequencies [20,49]. Since both fs-TA and GS-FSRS signals were generated along the probe direction, the probe beam passing through the sample solution was collimated and focused into a spectrograph (IsoPlane SCT-320, Princeton Instruments, Inc.) with the reflective grating selected for TA (300 grooves/mm, 300 nm blaze wavelength) or FSRS (600 grooves/mm, 1 μm blaze wavelength), then imaged at the exit focal plane onto a front-illuminated CCD array camera (PIXIS:100F, Princeton Instruments, Inc.) with data output to a computer and further processing and storage by a custom LabVIEW suite. The obtained GS-FSRS data can be directly compared with the DFT calculation results of the cofactor molecule (see below) [15,20].

5.3.4 Quantum calculations

Ground state vibrational normal modes of the BV cofactor of AnPixJg2_BV4 mutant were calculated using Gaussian 16 software [52] at the DFT RB3LYP level of theory *in vacuo*. To generate the initial input of BV in the P_{fr} form for calculation, the chromophore structure was first taken from the reported crystal structure (PDB ID: 5ZOH) [18], then proper numbers of hydrogen atoms were added and the two propionate groups on the B and C rings were cut and capped with methyl groups [15,45] in GaussView6. The structure was optimized with a series of basis sets from 3-21G, 6-31G to 6-31G(d,p), followed by vibrational frequency calculation of the geometrically optimized structure.

To investigate the effect of structural restraints of the chromophore on the calculation results, we examined a few different combinations of fixing the dihedral angles (e.g., CCCC and CCCN) and bridge angles (i.e., the CCC angle along the methine bridge) between the chromophore rings: no angles were fixed between the four rings; two dihedral angles between C/D rings and the bridge angle between B/C rings were fixed; four dihedral angles between A/B, and C/D rings as well as the bridge angle between B/C rings were fixed; and all six dihedral angles between A/B/C/D rings were fixed. The outcome of fixing all six dihedral angles of the cofactor matches the experimental results the best. Due to no crystal structure of BV in the P_o form, the dihedral angle closer to the D ring (around the C15=C16 bond, see Figure 5.1C) in the $^{15Z}P_{fr}$ form from crystal structure (PDB ID: 5ZOH) [18] was twisted to 180° (to represent the $^{15E}P_o$ conformer, also see Graphical Abstract) and all six dihedral angles between the four rings were then fixed. The same calculation steps as those for the P_{fr}

form were followed. Due to the lack of accurate modeling of the pertinent interactions or related crystal structures with the P_o conformer (especially for the translocated cofactor with a still-twisted A ring versus the P_{fr} conformer [18]), there is a poor match between the calculated and observed Raman spectrum of the P_o state, hence we focus on the more reliable mode assignment of the P_{fr} state (see Figure 5.12 and Table 5.2). The Raman spectrum was exported with 7 cm^{-1} half widths at half height (HWHH) and 1 cm^{-1} step size. A scaling factor of 0.97 was used [15,65] for the low and high-frequency regions to better match the experimental FSRS spectra (see Figure 5.4).

5.4 Results and Discussion

5.4.1 Steady-state electronic spectroscopy with altered structural contexts in CBCR pockets

In line with our previous study [15], a home-built LED box that fits four 5 mm through-hole LEDs was implemented to keep the samples in their respective conformers for all the spectroscopic experiments. LEDs with center wavelengths at 505, 600, and 650 nm were used to convert CBCRs to the $^{15Z}P_r$, $^{15Z}P_{fr}$, and $^{15E}P_g$ conformers, respectively, and maintain those species in the sample reservoir during fs-TA and GS-FSRS experiments. To achieve conversion toward the $^{15E}P_o$ conformer of Bbv, a tungsten lamp with a 650 nm longpass filter was used since our available LEDs did not convert the CBCR sample fast enough. The sample solution was then peristaltically pumped into a flow cell to prevent the LED irradiation from interfering with ultrafast spectroscopic measurements and also allow fresh sample solution to be flowed continuously, so refreshed samples always reach the laser irradiation spot for

spectral data collection. For fs-TA experiments (see detailed results in Section 2.2 below), a 525 and 650 nm actinic pump (~100 fs duration [20]) was used to excite the P_g and P_r conformers, respectively, of both Apcb and Bpcb (Figure 5.1D and E). For Bbv, due to the red-shifted ground state absorption profile, a 600 and 690 nm actinic pump (~100 fs duration) was implemented to excite the P_o and P_{fr} conformers (15*E* and 15*Z* isomers), respectively (Figure 5.1F).

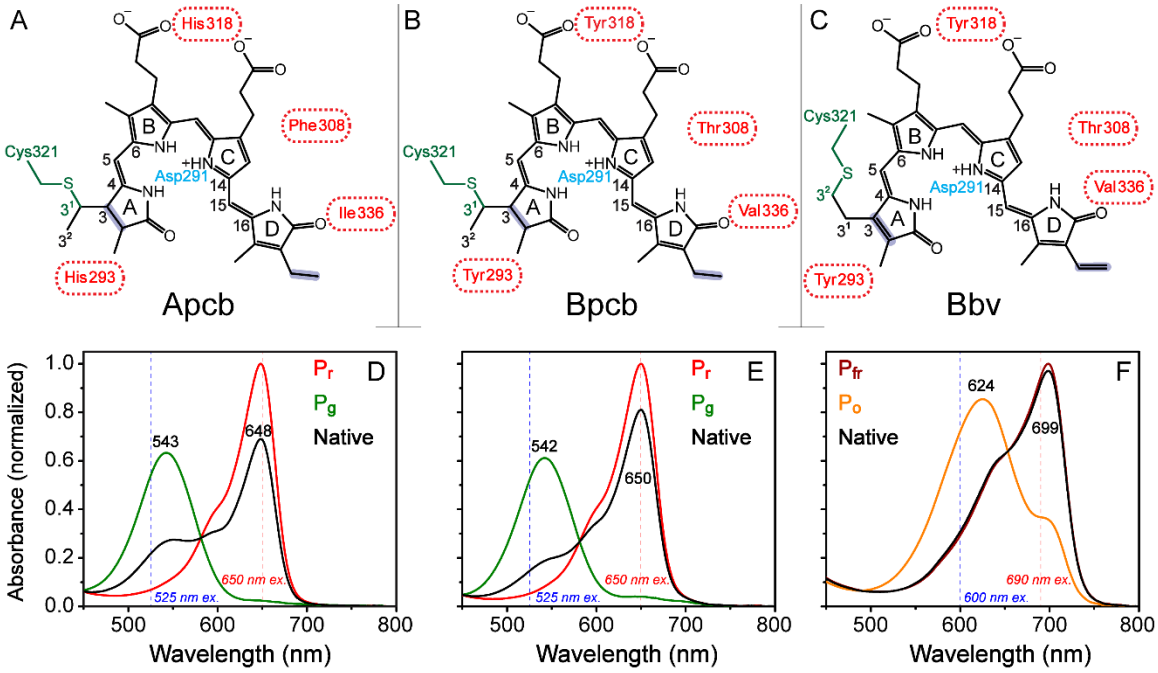

Figure 5.1. Representative chromophore and surrounding protein residues of (A) AnPixJg2_PCB, (B) AnPixJg2_BV4_PCB, and (C) AnPixJg2_BV4_BV. The associated native/dark-adapted states of $^{15Z}P_r$, $^{15Z}P_r$, and $^{15Z}P_{fr}$ are depicted. Four residues responsible for the BV incorporation are shown (red) with Cys321 (green) that covalently binds cofactor to protein pocket. Key changes to cofactor conjugation are highlighted by purple shades with Asp291 (cyan) as an important H-bonding partner to A, B, and C rings. The absorption spectra of (D) Apcb, (E) Bpcb, and (F) Bbv are normalized to the reddest-absorbing species. Sample spectra were collected after ambient light, 505 nm LED, 650 nm LED, 600 nm LED, and a tungsten lamp with 650 nm longpass filter irradiation for 5 min for the native (black), P_r (red), P_g (green), P_{fr} (dark red), and P_o (orange) species, respectively. The actinic pump wavelengths for fs-TA experiments are labeled by vertical dashed blue and red lines in each panel.

The steady-state electronic absorption spectrum of the native CBCR conformer was the first spectrum collected and the sample in buffer solution was allowed to equilibrate under ambient light for 5 min. Afterwards, the converted/target species was generated by specific light irradiation (see Table 5.1) for 5 min due to accumulated photoswitching from the starting species under a cw-light source [15]. Each spectrum was fitted using Gaussian peaks to identify major peak positions of 648/543, 650/542, and 699/624 nm for the Apcb P_r/P_g, Bpcb P_r/P_g, and Bbv P_{fr}/P_o conformers, respectively. Based on the spectra of native conformers, the BV4 mutations seem to promote a more homogeneous ground-state population as evidenced by the predominant P_r and P_{fr} forms of Bpcb and Bbv, respectively (Figure 5.1E,F, black traces). Upon comparison of the P_r and P_g absorption spectra of Apcb and Bpcb (Figure 5.1D,E, red and green traces), the BV4 mutations also cause a larger energy difference from 543/648 nm (~2984 cm^{-1}) to 542/650 nm (~3066 cm^{-1}). More importantly, the extended π-conjugation of Bbv cofactor molecular framework (Figure 5.1C) improves its π-π stacking with Trp289 [18] that contributes to the notably redder absorption of both P_o and P_{fr} states (Figure 5.1F, orange and dark red traces) than P_g and P_r states in Apcb as well as Bpcb (Figure 5.1D,E).

Table 5.1. Laser and LED irradiation conditions for the CBCR reversible photoswitching studies.

Sample	**Initial state**	**LED (nm)**	**Investigated state transition**	**Fs-actinic pump (nm)**	**Optical density (OD/mm)** [a]
Bpcb	P_g	650	$P_g \rightarrow P_r$	525	0.8
Bpcb	P_r	505	$P_r \rightarrow P_g$	650	0.8
Bbv	P_o	650 and above [b]	$P_o \rightarrow P_{fr}$	600	0.43
Bbv	P_{fr}	600	$P_{fr} \rightarrow P_o$	690	0.43

[a] Measured at the reddest-absorbing peak of the thermally equilibrated/dark-adapted state (see Figure 5.1D-F).
[b] Generated by a tungsten lamp with a 650 nm longpass filter.

5.4.2 Time-resolved electronic spectroscopy tracks reversible photoswitching of PCB and BV cofactors in the AnPixJg2_BV4 pocket

The time-resolved electronic spectra of CBCRs in buffer solution using ultrafast laser pulses (Figure 5.2) track the cofactor molecular population as it evolves on the excited-state potential energy surface (PES). There are four characteristic features in the fs-TA spectra: excited-state absorption (ESA), hot ground-state absorption (HGSA), ground-state bleaching (GSB), and stimulated emission (SE). Both ESA and HGSA bands are positive whereas GSB and SE bands are negative. The GSB feature overlaps with the ground state absorption band (see Figure 5.1D-F) which distinguishes it from the typically red-shifted SE and HGSA features. Notably, the measured TA signal intensity for Bpcb photoswitching processes (ca. ±18 mOD, OD is optical density, Figure 5.2A,C) is similar to that for Apcb at a similar sample concentration (OD≈0.8 per mm at the P_r absorption peak) [15], whereas the less concentrated Bbv (OD≈0.4 per mm at the P_{fr} absorption peak, see Table 5.1 in Section 2.1 above) displays much stronger TA intensity (~2–2.5 fold, Figure 5.2B,D). This result implies a larger excited-state transition oscillator strength [21,22] of the more conjugated BV cofactor than PCB cofactor in the CBCR pocket (see Figure 5.1) [18].

For corroboration, the raw experimental time-stacked fs-TA spectra (Figure 5.6) exhibit the ultrafast dynamics of key electronic features, and the probe-dependent signal intensity (±5 nm of peak wavelength, see Figure 5.7) least-squares fits yield multiple exponentials with characteristic time constants and amplitude weights [23]. Since the protein cofactor photoswitching process typically involves excited state intermediates undergoing parallel and/or sequential transitions, the observed broad

spectral features could be highly overlapped so the retrieved time constants from the probe-dependent fits may be convoluted or combined into an averaged value. Therefore, it is imperative to analyze and compare the least-squares fits with the associated time constants and amplitude weights for multiple TA marker bands to identify common features for the excited-state chromophores (see each panel in Figure 5.7 for a specific photoswitching process in various CBCR samples under study).

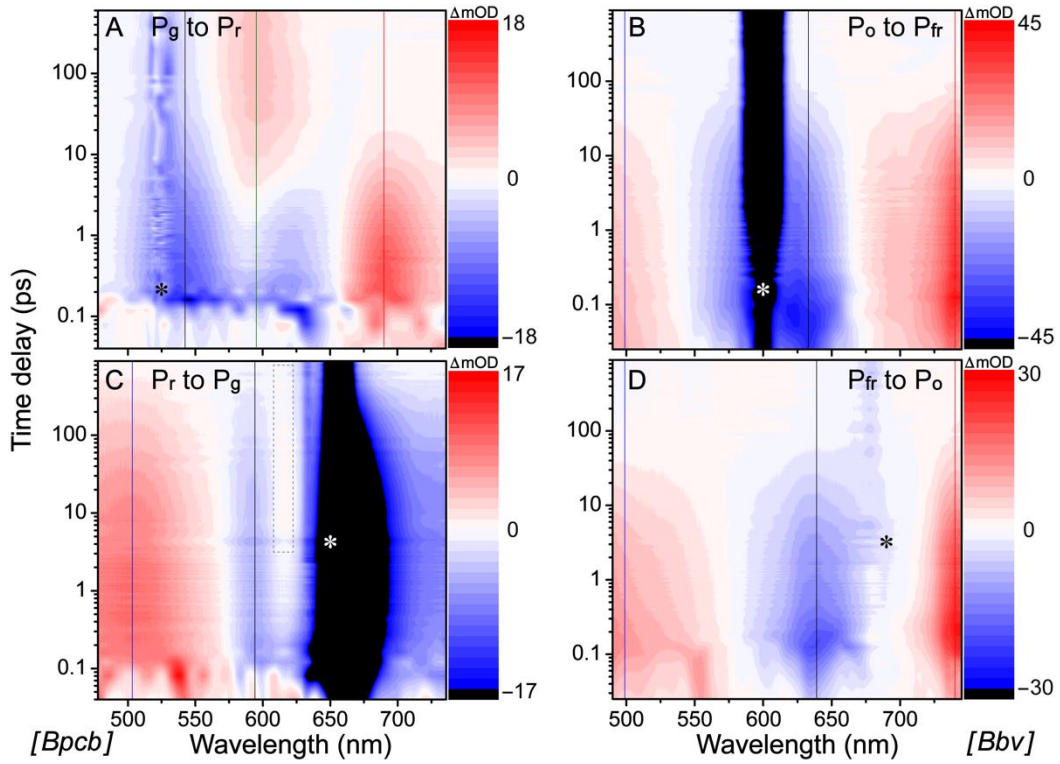

Figure 5.2. Time-resolved electronic spectra during reversible photoswitching of Bpcb and Bbv in buffer solution. The fs-TA 2D-contour plots of (A) Bpcb $P_g \rightarrow P_r$, (C) Bpcb $P_r \rightarrow P_g$, (B) Bbv $P_o \rightarrow P_{fr}$, and (D) Bbv $P_{fr} \rightarrow P_o$ transitions were collected using a 525 nm actinic pump with 650 nm LEDs, 650 nm actinic pump with 505 nm LEDs, 600 nm actinic pump with 650 nm longpass-filtered tungsten lamp, and 690 nm actinic pump with 600 nm LEDs, respectively, up to 900 ps after electronic excitation. Strong scattering from the pump beam (specific location marked by the asterisk in each panel) was largely removed by subtracting the –2 ps TA trace from the subsequent traces, although residual scattering can be clearly seen in black (panels B and C). A weak positive band (light red color) is marked by the dashed rectangle at late times in panel C. Key probe regions for dynamic analysis of the TA marker bands are highlighted by the color-coded vertical lines in each panel (see the associated least-squares fits with retrieved time constants in Figure 5.7).

To help deconvolute the underlying cofactor species with pertinent time constants, global analysis was implemented to analyze TA data within the entire

detection spectral and time window, allowing a holistic representation of the excited state electronic dynamics. The global analysis method typically employs two different models, evolution-associated difference spectrum (EADS) and decay-associated difference spectrum (DADS) [24]. In short, EADS uses multiple sequential states to model the spectra whereas DADS uses a parallel model with each species decaying with distinct lifetimes, which could provide complementary information for the complex TA data with overlapping spectral bands. The –2 ps (time delay, meaning that the probe pulse precedes the actinic pump pulse by 2 ps, hence serving as a useful background) TA spectrum was subtracted from the subsequent data traces to remove the strong scattering signal (some residuals can still be seen in Figure 5.2). During global analysis in Glotaran [25], the pump scattering was either set to zero if the feature was in the middle of the window or the window was trimmed when the scattering was at the edge so it would not interfere with the least-squares fits of the chromophore spectral features (Figure 5.3). Notably, the retrieved components from global analysis do not necessarily correspond to distinct molecular species, rather, they represent a mathematical description of the spectral data with characteristic separable components and time constants in capturing the chromophore electronic dynamics.

The fs-TA spectral 2D-contour plot (Figure 5.2A) and global analysis results (Figure 5.3A,E) of Bpcb $P_g \rightarrow P_r$ photoconversion exhibit three major features that appear at the photoexcitation time zero: ~542 nm GSB (matching the steady-state absorption peak of P_g state in Figure 5.1E), 620 nm SE, and 690 nm ESA. These features correspond to the P_g* (the asterisk denotes excited state) population. There is also rise of a positive feature around 595 nm that persists beyond the typical excited-

state lifetime, hence it was assigned as an HGSA band of Lumi-G [15]. The 542 nm GSB band shows recovery dynamics of ~350 fs (10%), 3.5 ps (45%), 31 ps (29%), and 1 μs (16%) (Figure 5.7A, black trace). The representative 1 μs component was used to model the long-lived population that does not return to original ground state within our detection time window. The most pronounced 690 nm ESA band shows clear decay dynamics with ~400 fs (9%), 4 ps (68%), and 27 ps (23%) time constants (Figure 5.7A, red trace), which is accompanied by a clear rise of the 595 nm HGSA that has been attributed to the Lumi-G species of PCB cofactor in the "hot" electronic ground state [15]. Due to spectral overlap in the visible spectral region, the probe-dependent fit of the 595 nm band yields a ~200 fs (25%) and 3.4 ps (37%) decay of the initial negative feature (Figure 5.7A, green trace, reminiscent of the adjacent GSB band dynamics) and a 21 ps (11%) rise of the Lumi-G HGS species that becomes apparent after ~4 ps (see the summary PES scheme below). The ~1 μs (27%) decay component was necessary for the fit since the long-lived signal eventually diminishes well beyond our current detection time window (see Methods in Section 3.3 below; a good separation of time constants allows the retrieval of longer time constants) [15].

Global analysis of the TA spectra for the photoinduced Bpcb $P_g \rightarrow P_r$ conversion requires five components to achieve a satisfactory fit, wherein the initial component fits a large coherent artifact with <5 fs lifetime (much lower than our cross-correlation time of ~120 fs [15,26]) so it was removed from the figure to focus on major electronic dynamics of the protein cofactor (see Figure 5.3A,E). The retrieved lifetimes were <100 fs, 4.2 ps, 20 ps, and 3 ns that largely match the probe-dependent fits (Figure 5.7A). The sub-ps time constant is known to be Franck-Condon (FC) relaxation as the

photoexcited wavepacket moves across the PES after electronic excitation [15,19,27,28]. This ultrafast step can be seen as clear and distinct features emerge in EADS (Figure 5.3A) and DADS (Figure 5.3E, black to blue trace). The 4.2 ps component likely tracks a partial twisting motion of the D ring in P_g* as it moves toward a CI, consistent with literature and the well-accepted D-ring twist along the photoswitching coordinate [15,29]. This interpretation is also supported by the loss of P_g* ESA and SE bands at ~690 and 620 nm (Figure 5.3A,E, blue to green trace), and the associated large amplitude weight that suggests a dominant relaxation pathway to the ground state. After the CI passage, the population diverges into two pathways. First, the twisted P_g* can continue to twist and reach the Lumi-G state as the primary photoproduct species, which is evident by the ~21 ps rise of the Lumi-G HGSA band (Figure 5.3A,E, green to magenta trace; Figure 5.7A, green trace). Second, the twisted P_g* can reverse-twist back to P_g in the ground state as indicated by the ~31 ps GSB band recovery (Figure 5.7A, black trace). The ~3 ns component from global analysis and ~1 μs component from the probe-dependent fits are representative of a weak fluorescence process and further protein-pocket-facilitated cofactor motions as Lumi-G fully converts to P_r in the electronic ground state [15,30].

The Bpcb $P_r \rightarrow P_g$ TA spectra (Figure 5.2C) and global analysis (Figure 5.3B,F) show clear P_r* modes with an ESA band around ~520 nm and two GSB bands at 594 and 650 nm, with the latter two bands matching the main ground state absorption peak and its bluer vibronic shoulder (Figure 5.1E, red trace). The strong scattering from 650 nm actinic pump made the probe-dependent fits in that region unreliable (see black shade in Figure 5.2 and orange asterisk in Figure 5.6C). We thus fit the cleaner 594 nm

GSB band recovery dynamics with ~150 fs (34%), 4.7 ps (20%), 118 ps (30%), and 1 ns (16%) time constants (Figure 5.7C, black trace). Meanwhile, the 503 nm ESA band exhibits similar intensity decay time constants of ~4.8 ps (13%), 254 ps (57%), and 2.5 ns (6%) but also requires a 28 ps (24%) component for a satisfactory fit (Figure 5.7C, blue trace). The retrieval of two intermediate time constants (28 and 254 ps) instead of one 118 ps time constant (from GSB recovery) or 111 ps (from global analysis of the spectra within the detection window, see below) could be due to more complex dynamics when higher-lying electronic excited states are involved (e.g., the 503 nm ESA band due to the $S_1 \rightarrow S_n$ transition) [20,31], although the general time scale of ~110–120 ps is consistent for the PCB cofactor excited-state relaxation along the S_1 PES.

Notably, there is a discernible rise and decay of a positive band around ~615 nm (see Figure 5.2C, dashed rectangle box) which resembles the fs-TA data of Apcb [15] and could be attributed to a slightly twisted excited-state intermediate (P_r*'). To reduce the pump scattering effect and confirm the delayed onset of this specific ESA band, we performed a control experiment using a dilute Bpcb sample (OD≈0.2/mm at the P_r state absorption peak, about a quarter of the Bpcb sample concentration listed in Table 5.1 and presented in Figure 5.2C) and observed clear dynamics of a ~618 nm band with a much reduced scattering signal to the red side (Figure 5.8). The 743 nm SE band shows similar decay dynamics to the bluer GSB band at 594 nm (Figure 5.7C). The overall cofactor excited-state decay dynamics of Bpcb are faster than Apcb (see Section 5.4.5 below for a detailed comparison), suggesting that smaller residues in the

chromophore vicinity of AnPixJg2_BV4 mutant [18] allow for faster ring-twisting events (likely accompanied by local environment relaxation) of the PCB cofactor [32].

Global analysis of the Bpcb $P_r \rightarrow P_g$ TA spectra yields ~150 fs, 4.5 ps, 111 ps, and 4.1 ns lifetimes. As discussed above, the 150 fs component reflects FC dynamics of the P_r* species while the 4.5 ps component tracks the P_r*$\rightarrow P_r$*' transition. This key assignment was made previously in the Apcb $P_r \rightarrow P_g$ conversion by a pronounced rise and decay of the 616 nm ESA band of P_r*' species [15]. However, the more significant overlap with a stronger GSB band (versus that in Apcb) makes it more difficult to reliably fit the weak 615 nm P_r*' ESA band dynamics of Bpcb. Nevertheless, transient spectral signatures of the P_r*' state is evident from global analysis (Figure 5.3B,F, blue to green trace, see the black arrow) and the pertinent ~620 nm ESA band decays away on the 111 ps time scale, which likely corresponds to the non-equilibrium molecular movement toward a peaked CI [27,33] that can repopulate the original ground state and convert to the Lumi-R state [15,29]. Notably, the CI is also evident from the dominant loss of excited-state features with the 111 ps lifetime (Figure 5.3B,F, green to magenta trace), while the longer-lived 4.1 ns component with an SE band redder than ~670 nm (Figure 5.2C, with a more pronounced SE peak at ~743 nm in the dilute CBCR sample in Figure 5.8) is likely owing to the fluorescence transition from P_r* [15,29]. Overall, the $P_r \rightarrow P_g$ conversion is less efficient than the $P_g \rightarrow P_r$ conversion since the majority of excited-state species return to the original ground state [15,29,34], in accord with the observed longer lifetimes and the lack of prominent new TA features emerging at late times after 650 nm photoexcitation (see Figures 5.2C and 5.3B).

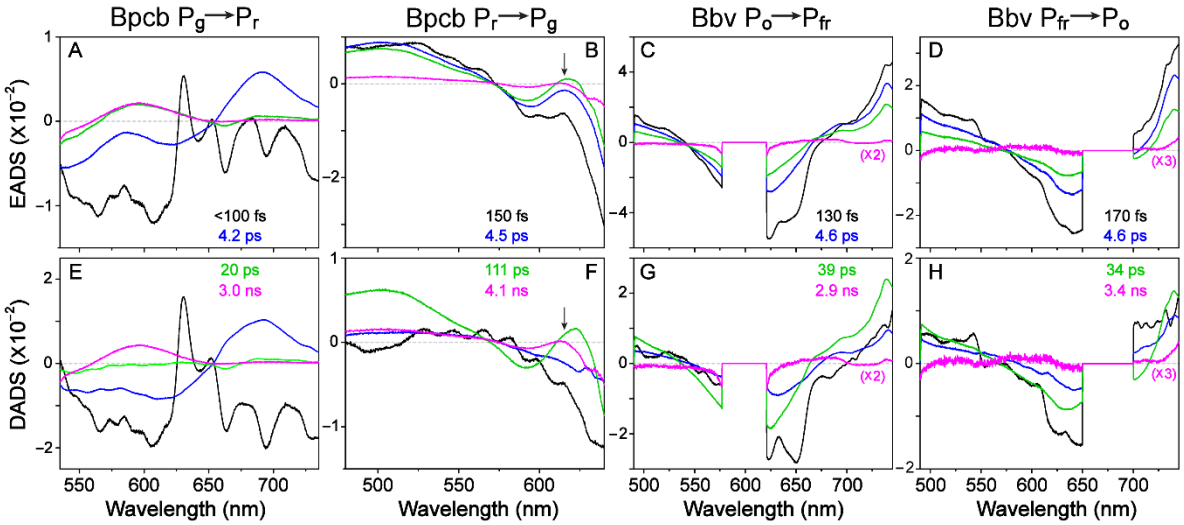

Figure 5.3. Global analysis of the fs-TA spectra during CBCR photoswitching processes. The underlying EADS/DADS of Bpcb $P_g \rightarrow P_r$, Bpcb $P_r \rightarrow P_g$, Bbv $P_o \rightarrow P_{fr}$, and Bbv $P_{fr} \rightarrow P_o$ transitions are shown in panels (A)/(E), (B)/(F), (C)/(G), and (D)/(H), respectively. The retrieved spectra are ordered from fastest to slowest lifetimes in black, blue, green to magenta traces, with the associated lifetimes color-coded and listed in insets. To remove pump scattering effect on data analysis, the probe window was truncated when the scattering signal was on the edge of detection window (panels A, B, E, F) or scattering region was set to zero (panels C, D, G, H). Black arrows in panels B,F show a weak ESA band at ~615 nm.

For comparison, the fs-TA spectra of the newly engineered Bbv exhibit similar features for both the $P_o \rightarrow P_{fr}$ and $P_{fr} \rightarrow P_o$ transitions (Figure 5.2B and D), which differ from the PCB cases (Figure 5.2A and C). Although the observed TA bands are shifted in wavelength, they both exhibit a blue ESA band at the edge of our spectral window (<500 nm), a GSB band in the middle region (around 633 and 639 nm for $P_o \rightarrow P_{fr}$ and $P_{fr} \rightarrow P_o$ transitions, respectively, see Figure 5.6B and D), and a strong red ESA band (>740 nm). An expanded spectral window to the bluer or redder probe regions is required to determine the exact locations for the blue and red ESA peaks, however, the

increased similarity between the TA signatures of BV's P_{fr} and P_o states vs. PCB's P_r and P_g states indicates the major effect of the intrinsic cofactor electronic structure, which likely causes the largely unchanged TA bands that are consistent with much less energy separation between the two conformers in BV (624 and 699 nm in Figure 5.1F, ~1719 cm^{-1}) vs. PCB (542 and 650 nm in Figure 1E, ~3066 cm^{-1}). These common TA features in Figure 5.2B and D mainly track the P_o* and P_{fr}* electronic dynamics because they appear at the photoexcitation time zero and decay away with no clear wavelength shifts. It is notable that the P_{fr} GSB band around 690 nm overlaps with the pump scattering that is largely removed for TA analysis (Figure 5.6D). Interestingly, all the least-squares fits of excited state dynamics show similar time constants for both conversions of the BV cofactor (Figure 5.7B and D), which differs significantly from the PCB cofactor counterparts (Figure 5.7A and C). For the $P_o \rightarrow P_{fr}$ conversion, the probe-dependent fits expose ~125 fs (43%), 4.6 ps (18%), and 32 ps (39%) time constants for the 499 nm ESA band, ~150 fs (48%), 4.6 ps (17%), 39 ps (34%), and 2.9 ns (1%) time constants for the 633 nm GSB band, and ~125 fs (27%), 4.6 ps (23%), 39 ps (49%), and 2.9 ns (1%) time constants for the 740 nm ESA band (see Figure 5.7B). Similar dynamic components are apparent for these TA bands that report on the common excited-state decay pathways of a presumably homogeneous P_o* population [35-37] as discussed in detail below.

For the $P_{fr} \rightarrow P_o$ conversion, the corresponding probe-dependent fits expose ~125 fs (35%), 4.8 ps (27%), 39 ps (37%), and 3.4 ns (1%) time constants for the 499 nm ESA band, ~129 fs (50%), 4.6 ps (21%), 37 ps (28%), and 3.4 ns (1%) for the 639 nm GSB band, and ~130 fs (31%), 4.9 ps (31%), 36 ps (34%), and 3 ns (4%) time

constants for the 740 nm ESA band (see Figure 5.7D), which reflect the common excited-state decay pathways of a presumably homogeneous P_{fr}* population. Note that such a systematic analysis of independent measurements on reversible photoswitching processes of the same CBCR sample (e.g., Bbv with specific light irradiation conditions listed in Table 5.1 in Section 2.1 above) substantiates the robustness of the aforementioned time constants and amplitude weights for the underlying dynamic components retrieved after an actinic pump. As further corroboration, global analysis of the $P_o \rightarrow P_{fr}$ (Figure 5.3C,G) and $P_{fr} \rightarrow P_o$ (Figure 5.3D,H) transitions also output similar time constants of ~130 and 170 fs, 4.6 and 4.6 ps, 39 and 34 ps, and 2.9 and 3.4 ns, respectively. Similar to the Bpcb $P_g \rightarrow P_r$ conversion case (Figure 5.3A,E), the fit for a large coherent artifact was removed in the reversible photoswitching between P_o and P_{fr} states of Bbv to retrieve the intrinsic underlying time constants along the excited-state PES of the protein cofactor. Moreover, though the EADS show the blue trace (4.6 ps lifetime) decaying into green trace (~35 ps lifetime, Figure 5.3C,D), the corresponding DADS show the green trace intensity higher than blue trace in both ESA regions (below 550 nm and above 720 nm, Figure 5.3G,H). This finding is indicative of some deviations from a simple kinetic model that the 4.6 ps component precedes the 35 ps component (see below).

To confirm these key observations and results for the Bbv photoswitching mechanisms, we performed the following control experiments. (1) Fs-TA data sets were collected at least twice with the freshly prepared protein samples on different days in the laser lab to ensure reproducibility. (2) The steady-state absorption spectra of the P_o and P_{fr} conformers were taken before and after every TA experiment to confirm that

the protein samples maintain their photoswitching capabilities. (3) Control TA experiments using 600 nm actinic pump with 600 nm LEDs (Figure 5.9A) and 704 nm actinic pump with the 650 nm longpass-filtered tungsten lamp (Figure 5.9B) were conducted to ensure that the TA data in Figure 4.2B and D were not just collecting the same conformer or mixed species. (4) A visual confirmation was achieved that the actinic pump could convert the protein samples by holding the sample cuvette in the beam path before it was focused [15]. (5) A redder actinic pump at 704 nm was used and similar TA features were observed for the $P_{fr} \rightarrow P_o$ transition (see Figure 5.10 and Figure 5.2D). With all these strategic, useful, and interwoven control experiments substantiating the aforementioned results, the observed similar dynamics of the $P_o \rightarrow P_{fr}$ and $P_{fr} \rightarrow P_o$ transitions infer a very alike or even "purely" reversible excited-state pathway of the BV cofactor in AnPixJg2_BV4.

The major differences between the aforementioned reversible photoswitching dynamics are the amplitude weights of the two intermediate components retrieved on the ps time scale. The $P_o \rightarrow P_{fr}$ conversion (Figure 5.7B) shows about half the weight for the ~5 ps component (18%, 17%, and 23%) compared to the ~35 ps component (39%, 34%, and 49%) for the blue ESA, GSB, and red ESA bands, respectively. In contrast, for the corresponding TA marker bands, the $P_{fr} \rightarrow P_o$ conversion (Figure 5.7D) shows approximately equal weights for the ~5 ps (27%, 21%, and 31%) and ~35 ps (37%, 28%, and 34%) components. This experimental finding poses two interesting questions. (1) Why does Bbv exhibit similar photoswitching dynamics in both directions whereas the Apcb and Bpcb $P_g \rightarrow P_r$ and $P_r \rightarrow P_g$ conversions show different excited-state pathways? (2) Why are the amplitude weights of two largely conserved

intermediate ps time constants the major differentiating factor between the Bbv $P_o \rightarrow P_{fr}$ and $P_{fr} \rightarrow P_o$ photoconversion?

5.4.3 Altered excited-state dynamics arise from an interplay between PCB or BV cofactor and AnPixJg2 or AnPixJg2_BV4 on ultrafast time scales

To answer these fundamental questions, we first examined the differences between PCB and BV cofactors in the AnPixJg2_BV4 pocket. The location-shifted BV cofactor in the BV4 pocket moves the A ring closer to its H-bonding partners Asp291 and Trp289 [18]. The distance between the cofactor A ring nitrogen atom and the Asp291 oxygen atom decreases from ~1.95 Å in the Apcb P_r state crystal structure (PDB ID: 3W2Z) [8] to 1.76 Å in the Bbv P_{fr} state crystal structure (PDB ID: 5ZOH at 1.60 Å resolution) [18]. The distance between the cofactor A ring carbonyl oxygen and the Trp289 nitrogen is ~0.21 Å closer in Bbv (2.76 Å) than Apcb (2.97 Å). The closer H-bonding partners and the extra electron density in the A ring would effectively restrict it from large twisting motions, while a slight twist of the A ring has been reported as a component in the photoconversion process [15,37,38]. By better stabilizing the A ring inside the protein pocket, more of the photoconverting energy could be localized at the D ring with a reversible clockwise/counterclockwise twist (i.e., along the same isomerization pathway but in opposite directions) by reducing motions away from the D ring.

As the D ring twists, there are two dihedral angles that correlate with the conversion between P_{fr} and P_o conformers. The dihedral closer to the D ring (D-dihedral) likely causes a smaller twisting motion than the dihedral closer to the C ring

(C-dihedral, see Figure 5.1A-C), since the D-dihedral twist is a volume-conserving motion whereas the C-dihedral twist likely increases the volume [39-41]. Upon excitation of P_{fr} to P_{fr}*, the conjugated double bonds acquire more single-bond character and vice versa [33,42,43], in accord with previous studies showing that the C15=C16 bond (directly connecting to the D ring) is responsible for the major twisting between the 15*Z*/*E* conformers [44-46]. By analyzing both dihedral angles for the available Apcb P_r state and Bbv P_{fr} state crystal structures, the C-dihedral (CCCC) around the bridge single bond (36.08° vs. 51.12°) is more twisted in Bbv whereas the D-dihedral (CCCN) around the bridge double bond (26.96° vs. 0.83°) is more twisted in Apcb from the pyrrole ring plane [8,15,18]. The BV4 mutations, specifically the more critical F308T and I336V, help to accommodate the shifted cofactor around the D ring due to less bulky residues [18]. Notably, if we attribute the observed 4.6 and 34 ps in the Bbv $P_{fr} \rightarrow P_o$ photoconversion (Figure 5.3D) to the small-scale D-dihedral and large-scale C-dihedral twisting motions, respectively, we could then expect a smaller and larger time constant from the cofactor TA dynamics in Apcb due to the aforementioned starting geometry. Indeed for the C-dihedral twist, we observed a 217 ps component for the Apcb $P_r \rightarrow P_g$ transition [15], and a 111 ps component for the Bpcb $P_r \rightarrow P_g$ transition (Figure 5.3B) likely owing to an intermediate geometry of the D ring in between the Apcb P_r and Bbv P_{fr} conformers. In contrast, for the D-dihedral twist on the few ps time scale, it is less sensitive to the initial geometry alone mainly due to its close interaction with an adjacent Val336 or Ile336 (in Bbv, Bpcb or Apcb, see Figure 5.1A-C) that could affect the faster time constant (in preparation for the subsequent larger twist motion) [20,47].

It is likely that Bpcb also takes advantage of the extra space around the cofactor and adopts a slightly shifted orientation from Bbv. The larger area around the D ring also explains the overall faster photoswitching dynamics in Bpcb than Apcb [32]. The slightly slower ~4 ps component in Bpcb $P_g \rightarrow P_r$ than ~3 ps in Apcb $P_g \rightarrow P_r$ conversion [15] can be explained by the shifted PCB cofactor in the AnPixJg2_BV4 pocket which would bring the D ring closer to Val336 and somewhat hinder the initial smaller twist (i.e., D-dihedral). Although the smaller twisting motion becomes slower, the larger twist (i.e., C-dihedral) occurs faster in the $P_g \rightarrow P_r$ photoconversion of Bpcb (~20 ps) than Apcb (~30 ps), both retrieved from global analysis of the corresponding TA spectra after 525 nm photoexcitation. We note that the larger twist occurs in the electronic ground state past the CI, likely owing to the metastable P_g* species that undergoes a more downhill and efficient process than the more "trapped" P_r* species that requires both twisting processes in the electronic excited state [15,29]. Interestingly for the latter case, the $P_r \rightarrow P_g$ photoconversion of Bpcb (~4.5 and 111 ps) also occurs faster than Apcb (~13 and 217 ps) involving presumably small and large ring-twisting motions of the protein cofactor, both retrieved from global analysis of the corresponding TA spectra after 650 nm photoexcitation [15].

For Bbv, because the photoswitching pathways are fully reversible with largely conserved time constants, the amplitude weights from the TA signal intensity fits become crucial in gaining mechanistic insights into the excited-state pathways. Since Bpcb does not exhibit such a reversible TA pattern during photoswitching, the observed "fully reversible" pathway seems to be unique to Bbv (i.e., both AnPixJg2_BV4 pocket and BV cofactor are needed). The probe-dependent least-squares fits implement a

parallel model of multiple processes with a common time zero, although it does not mean that the fastest component occurs first. By inspecting the Apcb and Bpcb photoswitching scheme, the 3–4 and 20–30 ps components likely represent the aforementioned small and large twisting processes, respectively, although the detailed assignments to excited- or ground-state dynamics need to come from the TA spectral analysis. The amplitude weight of each time constant is representative of how dominant the associated pathway is for energy dissipation. Since the Bbv TA bands emerge around photoexcitation time zero and then decay, while the peak wavelength remain largely unshifted up to 900 ps (Figure 5.2B,D), the observed TA band intensity dynamics likely track the excited-state population change along the ring-twisting coordinates. Notably, a larger twist could cause a larger change of the electronic transition oscillator strength for the resultant conformation than that of a smaller twist, which may contribute to the apparent TA band intensity decay dynamics. We thus focus on the change of amplitude weight ratios instead of exact weights for ensuing analysis.

In the $P_{fr} \rightarrow P_o$ conversion of Bbv, the equal weights of the ~5 ps and 35 ps components (Figure 5.7D) suggest that a 5 ps smaller twisting motion would populate the P_{fr}*' state before undergoing the 35 ps larger twisting motion en route to the CI. The less energy-consuming and more facile 5 ps twist could reduce the chances of other nonradiative pathways that compete with the 35 ps twist, while the initial small twist out of the more stabilized P_{fr} state may be required to help the D ring move away from the adjacent Val336 to allow more room for the subsequent large twist in the excited state (Figure 5.1C). In the $P_o \rightarrow P_{fr}$ conversion of Bbv, an unexpected observation that the ~35 ps larger twist being twice as dominant as the 5 ps smaller twist implies that

the larger twisting motion occurs first. The more energy-consuming and less facile 35 ps twist would bring the excited state closer to the ground state, allowing for more nonradiative processes to compete with the smaller twist. This would effectively cause the weight of the smaller twisting component to drop in comparison with the larger twist [20,21]. After the smaller twist, the remaining population could pass through a CI and continue to undergo cofactor ring twist and the surrounding protein pocket relaxation to reach the isomerized state (see Section 5.4.5 below and Graphical Abstract following the Chapter title for illustration). We note that if we attributed the ~5 and 35 ps to inhomogeneous species of P_o* undergoing excited-state energy relaxation in parallel, then it would be presumptuous to explain the same time constants from two inhomogeneous subpopulations of P_{fr}* because the two conformer states have different cofactor conformations in their respective surrounding protein pockets upon electronic excitation [8,38].

In both Bbv conversions, most of the population returns to the original ground state. The lack of a long-lived GSB recovery is evident (Figure 5.7B,D) that per excitation pulse, the TA signal from any photoconverted population is likely within our signal-to-noise ratio. Although having an apparently lower photoconversion efficiency than Apcb, Bbv still exhibit a fast photoconversion and can operate effectively under cw or ambient light sources for potential optogenetic applications [3,7,17].

5.4.4 Ground state femtosecond stimulated Raman spectroscopy sheds light on structural factors that rationalize the unique reversible photoswitching pathways in Bbv

To help elucidate the atomic structures of Bpcb and Bbv conformers, GS-FSRS experiments were performed to obtain the vibrational signatures of Apcb, Bpcb, and Bbv (Figure 5.4). Respective LEDs were implemented to collect the Apcb P_r and P_g (Figure 5.4A), Bpcb P_r and P_g (Figure 5.4B), as well as Bbv P_{fr} and P_o conformers (Figure 5.4C). With the pre-resonance ps 803 nm Raman pump, the fs broadband Raman probe on the Stokes side was used to effectively prevent notable dispersive line shapes of the cofactor chromophore [20,48]. The collected spectra in Figure 5.4A match our previous experimental results on Apcb using various Raman pump wavelengths at 792, 678, and 596 nm with Raman probe on the Stokes or anti-Stokes sides [15]. As a control experiment, we also collected the anti-Stokes FSRS spectra with a bluer Raman probe than the Raman pump (Figure 5.11) [22,48,49], which exhibit much stronger peaks due to the resonance enhancement achieved by the Raman probe with respect to the ground state absorption peaks of P_{fr} (699 nm) and P_o (624 nm), further confirming the vibrational peak frequencies in S_0 [28,48,50,51]. Using the Gaussian software [52], density functional theory (DFT) calculations at B3LYP level with 6-31G(d,p) basis sets were performed on the BV cofactor to visualize the vibrational normal modes (see Experimental Methods in Section 3.4 below). A frequency scaling factor 0.97 was applied to match the DFT-calculated spectrum to the GS-FSRS spectrum of the Bbv P_{fr} conformer (Figure 5.12). The discrepancy in the Raman peak intensities is likely due to the DFT calculations only treating the cofactor

quantum mechanically *in vacuo* without the protein pocket. More accurate hybrid quantum mechanics/molecular mechanics (QM/MM) methods would help model the CBCR protein with the embedded cofactor as a whole [37,45,53,54] which could complement our experimental capabilities in ultrafast laser spectroscopy. The description of major vibrational modes of the P_{fr} state can be seen in Table 5.2.

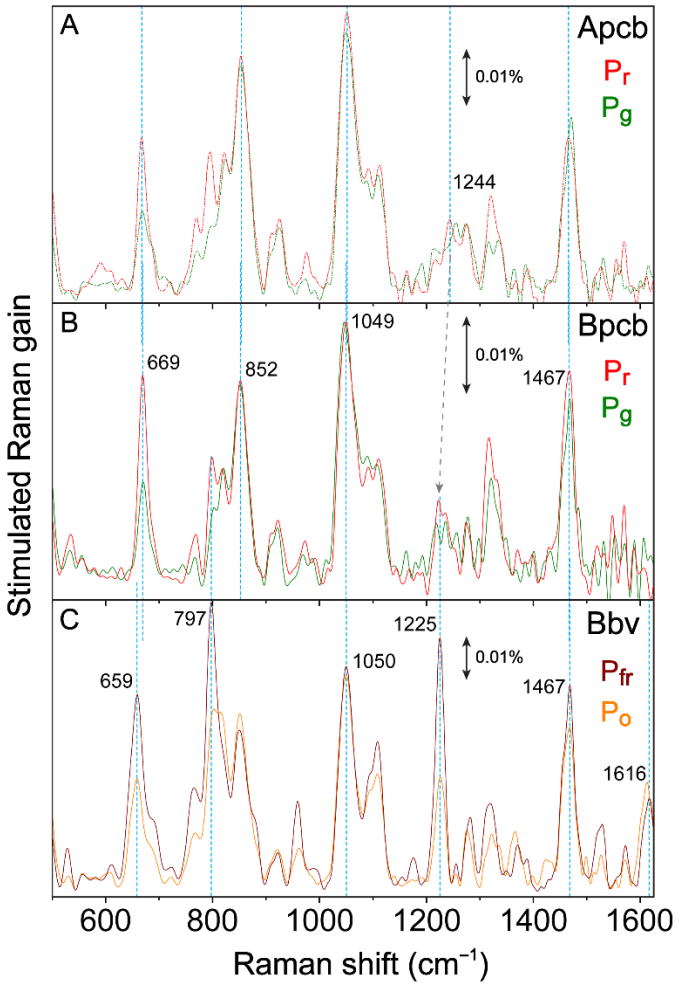

Figure 5.4. Raman signatures of various cofactors in related CBCR conformers. GS-FSRS spectra of (A) Apcb and (B) Bpcb P_r (red) and P_g (green) species using 505 and 650 nm LEDs, respectively, as well as (C) Bbv P_{fr} (dark red) and P_o (orange) species using 600 nm LEDs and a 650 nm longpass-filtered tungsten lamp. The ps 803 nm Raman pump was used to minimize the pump-induced conversion of the cofactor species, with the fs Raman probe set at the Stokes side. Vertical dotted lines and a dashed arrow denote the peak frequency shifts between key vibrational modes of related CBCR cofactors. The double-headed arrows denote the stimulated Raman gain magnitude of 0.01% in each panel.

Overall, Apcb, Bpcb, and Bbv share marker bands common to bilin photosensors at ~1051 and 1466 cm^{-1} [35,55]. PCB and BV cofactors exhibit similar vibrational motions with small frequency shifts (Figure 5.4). The 1051 cm^{-1} mode is localized to the D-ring deformation with strong C–H sidechain wagging. Meanwhile, the 1466 cm^{-1} mode is attributed to the B and C ring-deformation and CH_3 rocking. Both of these modes are stabilized by the conserved His322, Trp289, and Tyr352 in the CBCR pocket [18]. The overall higher intensity of the red-absorbing species (P_r in Apcb and Bpcb, and P_{fr} in Bbv) is attributed to better resonance enhancement with the 803 nm Raman pump. Moreover, the similar peak intensity at ~1050 cm^{-1} for P_o and P_{fr} of Bbv while most other modes display reduced intensities in P_o can be rationalized by the vibronic coupling matrix that yields the mode-dependent change of resonance conditions [15,20], which indicates the importance of light-induced D-ring motions that connect these conformers. Key differences between the vibrational spectra of PCB (Figure 5.4A,B) and BV (Figure 5.4C) can be seen by the red-shifted modes around 660 and 800 cm^{-1}, and in the 1200–1400 cm^{-1} region.

The ~660 cm^{-1} peak region reveals key differences in electronic conjugation between the PCB and BV cofactors. This Raman mode involves collective C–C and C–H wagging motions in the conjugated cofactor ring system. A frequency redshift of 10 cm^{-1} from the ~669 cm^{-1} mode in Apcb and Bpcb (Figure 5.4A,B) to 659 cm^{-1} mode in Bbv (Figure 5.4C) is rationalizable by two extra double bounds in the A and D rings of Bbv cofactor (see Figure 5.1C). In Bbv, the peak doublet around 825 cm^{-1} shows a clear blueshift of the lower-frequency mode from P_{fr} (797 cm^{-1}) to P_o (809 cm^{-1}). Since the associated vibrational motions involve N–H wagging from the A, B, and C rings with

C–H wagging on the CD bridge [15,55], the frequency blueshift is likely due to a twisted D ring that disrupts the H-bonding of Trp289 to A ring. In Apcb and Bpcb, the lack of a strong peak around 800 cm^{-1} could be attributed to a different H-bonding network of the A ring with reduced electric polarizability (one less double bond). In the 1200–1400 cm^{-1} region, Bbv exhibits a prominent 1225 cm^{-1} mode. In Bpcb and Apcb, this mode is weak but displays a noticeable redshift from Apcb to Bpcb (~1244 to 1225 cm^{-1}, see the tilted arrow from Figure 5.4A to B). In both PCB and BV calculations [15], since this mode involves delocalized N–H rocking and AB bridge C–H rocking motions, the clear peak enhancement in Bbv (Figure 5.4C) further corroborates the shifted, stronger H-bonded A ring in the more conjugated BV cofactor. The redshift in Bpcb compared to Apcb is also consistent with the BV4 mutations that allow the PCB cofactor to adopt a slightly shifted position inside the protein pocket and establish better H-bonding interactions, yet the largely unchanged Raman peak intensity around 1235 cm^{-1} indicates that the mode-dependent electric polarizability is dictated by the intrinsic chromophore electronic structure (see the clear peak intensity ratio and line width change from Figure 5.4A,B to C) [20,29].

5.4.5 Contrasting excited-state potential energy surfaces for reversible photoswitching of PCB and BV cofactors in the AnPixJg2_BV4 pocket

With all the correlated electronic and vibrational signatures from steady-state to time-resolved regime [15,20], we could sketch the overall reversible photoswitching pathways of Bpcb and Bbv (Figure 5.5). Bpcb adopts the similar reaction scheme as Apcb as the BV4 mutations do not affect the major pathways of the embedded cofactor.

The less bulky residues (particularly Thr308 and Val336, Figure 5.1B) in Bpcb allow the D ring more room to twist, decreasing the excited-state dynamics time constants [15,36]. In the Bpcb $P_g \rightarrow P_r$ conversion (Figure 5.5A), the P_g* species undergoes FC relaxation on the ~100 fs time scale, then approaches a CI on the ~4.2 ps time scale. The slightly shifted cofactor in Bpcb makes the initial twist slightly slower than that in Apcb (~2.7 ps) [15]. After the CI, the cofactor population likely continues twisting to the converted Lumi-G state or twisting back to P_g on the 20–30 ps time scales. This step is evident by a ~20 ps component in the Lumi-G rise (HGSA at ~595 nm in Figure 5.2A) and a ~30 ps component in the GSB recovery (Figure 5.7A). As for the opposite $P_r \rightarrow P_g$ conversion (Figure 5.5C), after FC relaxation the P_r* species transitions into a twisted P_r*' intermediate with a 4.5 ps time constant, which requires further ring twists into a CI on the 111 ps time scale. The P_r*' state can be seen by the transient rise and decay of a weak ESA band around 615 nm (Figure 5.2C and Figure 5.8), corroborated by a stronger ESA band around 616 nm with similar dynamics for the same PCB cofactor inside the AnPixJg2 pocket (i.e., Apcb) [15].

On the long time scale, since the 3–4 ns minor component from global analysis of Bpcb (Figure 5.3A,B,E,F) is an average value of all the long processes going beyond our current time window of ~1 ns, the pertinent contributors could be fluorescence from P_g* species (see the 620 nm SE band in Figure 5.2A and PES in Figure 5.5A) or P_r* species (see the >670 nm SE band in Figure 5.2C and PES in Figure 5.5C), and the long-lasting photoproduct state that does not return to the original ground state on this time scale (e.g., Lumi-G in Figure 5.5A and Lumi-R in Figure 5.5C). In analogy, the similar ~3 ns minor component from global analysis of Bbv (Figure 5.3C,D,G,H) could

involve weak fluorescence from P_o* and P_{fr}* species plus the long-lasting photoproduct states Lumi-O and Lumi-Fr in Figure 5.5B and 5.5D, respectively. It is interesting to note that these minor components with 1–4% amplitude weights were consistently retrieved from both the red ESA band (~740 nm) and GSB band (633–639 nm) of Bbv (Figure 5.7B,D), indicating that a small percentage of the excited-state population goes from the excited state to the original ground state on the ~3 ns timescale (a typical radiative transition lifetime), which could be due to the aforementioned weak fluorescence component. The absence of a prominent SE band could be due to spectral overlap with the strong and broad ESA band on the red side (Figure 5.2B,D and Figure 5.3C,G,D,H), and any mismatch between the ESA and GSB dynamics could imply some deviations from a direct S_1-to-S_0 transition. These long-time-scale processes could benefit from future in-depth studies with other experimental and computational techniques (see below) that are beyond the scope of this work.

Notably, the engineered Bbv undergoes a more "purely" reversible photoswitching pathway as reflected by the highly conserved excited-state time constants from either conformer of the cofactor. The $P_{fr} \rightarrow P_o$ conversion (Figure 5.5D) adopts a similar scheme to the $P_r \rightarrow P_g$ conversion of the PCB samples from the thermally equilibrated state to the metastable state. The similarly weighted ~4.6 and 34 ps time constants infer that the 4.6 ps small-scale twisting motion occurs prior to the 34 ps larger twist, which is characteristic of the D-dihedral change acting as a preparatory step [28,56] for the C-dihedral change (see details in Section 2.3 above). In contrast, starting from the metastable state with a more downhill relaxation, the higher-weighted ~39 ps larger twisting motion could generate a P_o*' species that is

energetically closer to the ground state, which allows for other nonradiative processes (depicted by a vertically downward gray arrow in Figure 5.5B) to more effectively compete with the 4.6 ps small-scale twist leading into to a CI region before the Lumi-O formation. Given this kinetic scheme, we do not expect a significant accumulation of transient P_o*' species since the 4.6 ps outgoing rate is much faster than the 39 ps incoming rate, which likely explains the lack of clear TA features from the P_o*' species. As a result, the observed TA dynamics (Figure 5.2B) mainly reflect the ultrafast multi-exponential decay of P_o* species (Figure 5.5B), consistent with kinetic models with reversible reactions connecting all the transient species. In particular, the DADS feature with a 4.6 ps lifetime (Figure 5.3G) does not reflect the P_o*' species *per se*, instead, it mathematically tracks the 4.6 ps kinetic component (along the P_o*'-to-CI pathway) with a similar spectral profile as the initial ~130 fs and subsequent 39 ps components (i.e., P_o* species) as shown in the EADS analysis (Figure 5.3C).

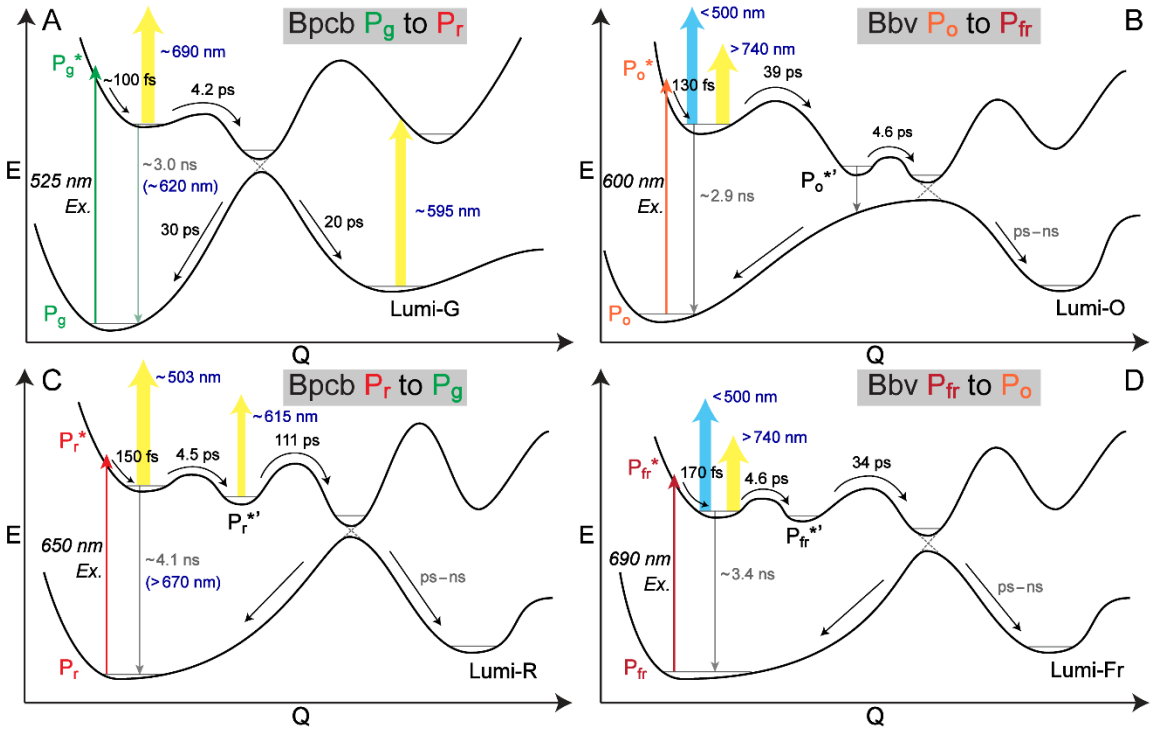

Figure 5.5. Representative potential energy surfaces of Bpcb (A) $P_g \rightarrow P_r$, (C) $P_r \rightarrow P_g$, and Bbv (B) $P_o \rightarrow P_{fr}$, (D) $P_{fr} \rightarrow P_o$ photoconversion. The photoexcitation (Ex.), ESA, SE, GSB, and HGSA transitions are illustrated by the color-coded vertical arrows. The arrow lengths are not drawn to scale with the exact energy gaps. Reaction scheme is denoted by curved arrows with characteristic time constants retrieved from global analysis of the corresponding TA spectra in Figures 5.2 and 5.3. A minor fluorescence component is shown by a dim downward arrow. The ps–ns time scales for Lumi state formation in panels B–D indicate a long-lived state beyond our detection time window. The horizontal axis "Q" represents the dominant cofactor ring-twisting motions that could change as time progresses after photoexcitation, while the protein environment continuously contributes to the nuclear motions.

Recent reports on the ultrafast dynamics of a red/far-red bathy bacteriophytochrome named PaBphP that binds BV inside the GAF domain (part of a classical PAS-GAF-PHY architecture) [32,36] provide a useful comparison. The forward $^{15Z}P_r \rightarrow {}^{15E}P_{fr}$ photoconversion utilizes a two-step process on the excited state

with a 2–207 ps local environment (e.g., protein residue sidechains, internal/trapped water molecules [55-57], elaborate H-bonding networks) relaxation and a 375 ps isomerization to the CI [32]. For comparison, the reverse $P_{fr} \rightarrow P_r$ photoconversion (with higher bond strain/distortion to release) goes through an excited-state bifurcation on the much faster ~1 and 4 ps time scales where both wavepackets reach the CI [36]. The pertinent few-ps photoisomerization step around the C15=C16 bond that significantly shifts the cofactor D-ring with respect to a nearby protein pocket residue is consistent with our assignment of the 3–5 ps component to the D-dihedral/small-scale twisting motion (see Section 2.3 above). By evaluating the conformational differences between P_{fr} and P_r states of PaBphP via X-ray crystallography, the BV cofactor exhibits distinct conformations of the A, B, C, and D rings [58], which underlie the significant difference between forward and reverse pathways mediated by different residues in the extensively rearranged H-bonding network. In sharp contrast, stabilizing the A, B, and C rings through largely conserved H-bonding and π-π stacking (e.g., between Trp289 and D ring) in the BV4 pocket [18] could therefore allow a rather unique and "purely" reversible photoconversion pathway of the BV cofactor (between the P_o and P_{fr} states of Bbv, Figure 5.1F) as observed in this work (Figures 5.2, 5.3, 5.6, and 5.7). Notably, the focus here is the elucidation of reversible photoswitching between distinct (not necessarily pure) conformers in the protein pocket.

The more homogeneous, thermally equilibrated populations of Bpcb and Bbv could also be related to the protonation state of the adjacent His322 [37]. QM/MM calculations indicate that the His322 protonation state is a trigger for structural heterogeneity. In the crystal structure of the P_{fr} state of AnPixJg2_BV4 [18], His322

shares two H-bonding partners: one is the B ring propionate, the other is a local water molecule that also H-bonds to the D ring nitrogen site (–NH group). The His318Tyr mutation in BV4 removes the original H-bond between His318 and the B ring propionate in AnPixJg2 [8] and would thus increase the H-bonding interaction between B ring and His322 [18]. For the other H-bonding partner, since both PCB and BV cofactors undergo some position shift in the BV4 pocket, the D ring likely has more tendency to move away from His322. The resultant singly protonated state of His322 (as an H-bond donor to the B ring propionate) would support a more homogeneous cofactor population [37], which is evident from the "native" steady-state electronic absorption spectra that show Bbv (Figure 5.1F, black trace) being more homogeneous than Bpcb (Figure 5.1E, black trace). The homogeneous population also supports Bbv in adopting a sequential kinetic model instead of a parallel model to undergo excited-state electronic and structural relaxation of the BV cofactor with continuous active-site motions in S_1 [30,32], followed by slower thermal relaxation events of the chromophore and protein matrix in the electronic ground state (S_0). By exciting a mostly homogeneous ground state population, it is unlikely to have the transient wavepacket branch into different pathways with notably different time constants (e.g., ~5 and 35 ps) that both reach the CI.

Meanwhile, the P_o conformer of Bbv is likely more homogeneous due to its higher absorption peak than the P_g conformers of Apcb and Bpcb (Figure 5.1F orange trace vs. Figure 5.1D,E green traces, all relative to their corresponding redder-absorbing peaks), because a larger extinction coefficient could be indicative of a more stabilized P_o state of Bbv. For corroboration, implementing the BV4 mutation to

AnPixJg4 (the fourth GAF domain of AnPixJ) leads to a rapid P_o-to-P_{fr} dark reversion that is ~400-fold faster than that of AnPixJg2_BV4 (Bbv), while the relative P_o/P_{fr} absorption peak intensity ratio (0.65, peak wavelengths at 628 nm/700 nm) [18] is indeed smaller in AnPixJg4_BV4 than that in Bbv (0.85, peak wavelengths at 624 nm/699 nm, Figure 5.1F). The BV-binding efficiency of AnPixJg4_BV4 (44%) is also significantly lower than AnPixJg2_BV4 (75%). Further investigation of AnPixJg4_BV4 using a similar combination of fs-TA and GS-FSRS to this work could help to unveil the mechanistic origin for the fourth GAF domain to exhibit greatly accelerated dark reversion on the ground state, shedding light on the effect of cofactor-protein-pocket interplay on the apparent TA features versus the thermally equilibrated P_{fr} state. Knowledge about the effects of specific attributes around the cofactor and how they contribute to the overall photoswitching dynamics would enable protein engineers to effectively tailor these photoswitching proteins for specific applications.

To further decipher the multidimensional [20,56,57] photoswitching dynamics, we expect the improved molecular dynamics (MD) simulation methods with higher accuracy and longer duration [26,37,55,57,59] and other spectroscopic techniques to paint a holistic and accurate portrait as the molecular system is excited, photoconverting, and relaxing back to its thermally stable dark-adapted state [29,55]. Since the metastable light-adapted P_o and P_g crystal structures are challenging to obtain, QM/MM methodology has advanced in closely matching the calculated absorption spectra of protein conformers with their experimental counterparts, including recent successes on a similar red/green absorbing CBCR named Slr1393g3 with its P_r and P_g crystal structures both solved [38,54]. By implementing similar QM/MM calculations

on Bbv, more accurate vibrational and structural insights into the P_o conformer could be gained to augment our current understanding of the P_{fr} conformer (Figure 5.4 and Table 5.2) with its available crystal structure [18]. Moreover, a systematic calculation of the excited-state free energies of the BV cofactor with various D-ring twisting geometries and intermediates (see Section 2.3 above) in the protein pocket can shed more light on the ultrafast reversible photoswitching pathway between the P_o and P_{fr} conformers of AnPixJg2_BV4.

In addition, an expanded spectroscopic toolset from ultrafast regime (typically fs-to-ns time scales as reported here) to the more macroscopic time scales (ns-to-ms or longer) could better identify long-lived or later intermediates (e.g., Lumi-G and Lumi-R in Apcb and Bpcb, and Lumi-O and Lumi-Fr in Bbv), which may dictate the forward/reverse reaction speed and yield [5,29,60,61]. These Lumi states are likely similar to the photoproduct species in our current experiments on the ns time scale (Figure 5.5), however, they require further protein relaxation and chromophore pocket rearrangement on the electronic ground state to eventually reach the final product state. For example, a TA setup with pulsed (100 ns) LED-based broadband probe has expanded the time window from ns to ms and identified two intermediates between Lumi-G_2 and P_r after 532 nm excitation of P_g of NpR6012g4 [62], and recent applications in conjunction with fs-TA were able to elucidate a series of meta states that emerge after the Lumi state formation in AnPixJg2 as well as NpR6012g4 with a strong sequence homology (both are canonical red/green CBCRs) [61]. In aggregate, by combining multiple techniques such as TA, FSRS, QM/MM, X-ray crystallography, and NMR, the resultant comprehensive information can delineate the complex

photoconversion of CBCRs and other photosensing proteins as they convert from one state to another on various time scales. Such a more complete understanding of the working mechanisms of these fascinating nanomachines can help bioengineers to better predict, design, prepare, and tune the next generation of bioimaging and optogenetic toolsets to advance life sciences and improve human health.

5.5 Conclusions

In summary, we systematically investigated Apcb, Bpcb, and Bbv as related CBCRs in aqueous buffer solution using the steady-state and time-resolved (fs-to-ns time scales) spectroscopic techniques, and revealed that the strategic BV4 mutations allow more room for the protein cofactor to shift and twist, achieve a more homogeneous native population of the embedded cofactor, and conserve the reversible photoconversion pathways as primary forward and reverse reaction events. When BV is incorporated into the AnPixJg2_BV4 pocket, the extended electronic conjugation along with the BV translocation essentially stabilize the A ring through an improved H-bonding network at the active site. The resulting conformational stability allows the ultrafast photoswitching dynamics to be more localized at the cofactor D ring, which undergoes characteristic small and large-scale D-ring twisting motions with ~5 and 35 ps time constants upon photoexcitation. These primary events effectively lead to a clockwise/counterclockwise reversible pathway (en route to the S_1-S_0 CI, followed by further relaxation in S_0) between the $^{15Z}P_{fr}$ and $^{15E}P_o$ conformers. With the red-shifted absorption and emission properties, the targeted and effective BV4 mutation thus enables CBCRs to be visualized and regulated in deep mammalian tissues. The

aforementioned more directional and controllable reversible photoconversion as the "central dogma" of phytochromes [2] for a homogeneous cofactor population (in the photosensory unit) could provide more collective and strong driving forces for the downstream signaling and regulatory events (e.g., transcription, motility). Given the vast CBCR family with various functions and properties, ultrafast electronic and vibrational spectroscopic toolsets with complementary long-time-delay spectroscopic techniques, as well as MD and QM/MM calculations will continue to represent a powerful characterization platform in delineating the photoconversion mechanisms on molecular time scales and more generally, unlocking the design space and potential from the bottom up for light-driven molecular machines for diverse applications.

5.6 References

1. Wu, S.-H.; Lagarias, J.C. Defining the bilin lyase domain: Lessons from the extended phytochrome superfamily. *Biochemistry* **2000**, *39*, 13487-13495.

2. Rockwell, N.C.; Su, Y.-S.; Lagarias, J.C. Phytochrome structure and signaling mechanisms. *Annu. Rev. Plant Biol.* **2006**, *57*, 837-858.

3. Ikeuchi, M.; Ishizuka, T. Cyanobacteriochromes: A new superfamily of tetrapyrrole-binding photoreceptors in cyanobacteria. *Photochem. Photobiol. Sci.* **2008**, *7*, 1159-1167.

4. Hirose, Y.; Shimada, T.; Narikawa, R.; Katayama, M.; Ikeuchi, M. Cyanobacteriochrome CcaS is the green light receptor that induces the expression of phycobilisome linker protein. *Proc. Natl. Acad. Sci. U. S. A.* **2008**, *105*, 9528-9533.

5. Narikawa, R.; Fukushima, Y.; Ishizuka, T.; Itoh, S.; Ikeuchi, M. A novel photoactive GAF domain of cyanobacteriochrome AnPixJ that shows reversible green/red photoconversion. *J. Mol. Biol.* **2008**, *380*, 844-855.

6. Rockwell, N.C.; Lagarias, J.C. A brief history of phytochromes. *ChemPhysChem* **2010**, *11*, 1172-1180.

7. Rockwell, N.C.; Martin, S.S.; Lagarias, J.C. Red/green cyanobacteriochromes: Sensors of color and power. *Biochemistry* **2012**, *51*, 9667-9677.

8. Narikawa, R.; Ishizuka, T.; Muraki, N.; Shiba, T.; Kurisu, G.; Ikeuchi, M. Structures of cyanobacteriochromes from phototaxis regulators AnPixJ and TePixJ reveal general and specific photoconversion mechanism. *Proc. Natl. Acad. Sci. U. S. A.* **2013**, *110*, 918-923.

9. Piatkevich, K.D.; Subach, F.V.; Verkhusha, V.V. Engineering of bacterial phytochromes for near-infrared imaging, sensing, and light-control in mammals. *Chem. Soc. Rev.* **2013**, *42*, 3441-3452.

10. Ryu, M.-H.; Gomelsky, M. Near-infrared light responsive synthetic c-di-GMP module for optogenetic applications. *ACS Synth. Biol.* **2014**, *3*, 802-810.

11. Ziegler, T.; Möglich, A. Photoreceptor engineering. *Front. Mol. Biosci.* **2015**, *2*, 30.

12. Shu, X.; Royant, A.; Lin, M.Z.; Aguilera, T.A.; Lev-Ram, V.; Steinbach, P.A.; Tsien, R.Y. Mammalian expression of infrared fluorescent proteins engineered from a bacterial phytochrome. *Science* **2009**, *324*, 804-807.

13. Filonov, G.S.; Piatkevich, K.D.; Ting, L.-M.; Zhang, J.; Kim, K.; Verkhusha, V.V. Bright and stable near-infrared fluorescent protein for *in vivo* imaging. *Nat. Biotechnol.* **2011**, *29*, 757-761.

14. Narikawa, R.; Muraki, N.; Shiba, T.; Ikeuchi, M.; Kurisu, G. Crystallization and preliminary X-ray studies of the chromophore-binding domain of cyanobacteriochrome AnPixJ from *Anabaena* sp. PCC 7120. *Acta Cryst. Sect. F* **2009**, *F65*, 159-162.

15. Tachibana, S.R.; Tang, L.; Chen, C.; Zhu, L.; Takeda, Y.; Fushimi, K.; Seevers, T.K.; Narikawa, R.; Sato, M.; Fang, C. Transient electronic and vibrational signatures during reversible photoswitching of a cyanobacteriochrome photoreceptor. *Spectrochim. Acta A* **2021**, *250*, 119379.

16. Auldridge, M.E.; Forest, K.T. Bacterial phytochromes: More than meets the light. *Crit. Rev. Biochem. Mol. Biol.* **2011**, *46*, 67-88.

17. Oliinyk, O.S.; Chernov, K.G.; Verkhusha, V.V. Bacterial phytochromes, cyanobacteriochromes and allophycocyanins as a source of near-infrared fluorescent probes. *Int. J. Mol. Sci.* **2017**, *18*, 1691.

18. Fushimi, K.; Miyazaki, T.; Kuwasaki, Y.; Nakajima, T.; Yamamoto, T.; Suzuki, K.; Ueda, Y.; Miyake, K.; Takeda, Y.; Choi, J.-H., *et al.* Rational conversion of chromophore selectivity of cyanobacteriochromes to accept mammalian intrinsic biliverdin. *Proc. Natl. Acad. Sci. U. S. A.* **2019**, *116*, 8301-8309.

19. Kennis, J.T.M.; Groot, M.-L. Ultrafast spectroscopy of biological photoreceptors. *Curr. Opin. Struct. Biol.* **2007**, *17*, 623-630.

20. Fang, C.; Tang, L.; Chen, C. Unveiling coupled electronic and vibrational motions of chromophores in condensed phases. *J. Chem. Phys.* **2019**, *151*, 200901.

21. McHale, J.L. *Molecular spectroscopy*. Prentice-Hall: Upper Saddle River, NJ, 1999.

22. Chen, C.; Liu, W.; Baranov, M.S.; Baleeva, N.S.; Yampolsky, I.V.; Zhu, L.; Wang, Y.; Shamir, A.; Solntsev, K.M.; Fang, C. Unveiling structural motions of a highly fluorescent superphotoacid by locking and fluorinating the GFP chromophore in solution. *J. Phys. Chem. Lett.* **2017**, *8*, 5921–5928.

23. Chen, C.; Zhu, L.; Boulanger, S.A.; Baleeva, N.S.; Myasnyanko, I.N.; Baranov, M.S.; Fang, C. Ultrafast excited-state proton transfer dynamics in dihalogenated non-fluorescent and fluorescent GFP chromophores. *J. Chem. Phys.* **2020**, *152*, 021101.

24. van Stokkum, I.H.M.; Larsen, D.S.; van Grondelle, R. Global and target analysis of time-resolved spectra. *Biochim. Biophys. Acta* **2004**, *1657*, 82-104.

25. Snellenburg, J.J.; Laptenok, S.P.; Seger, R.; Mullen, K.M.; van Stokkum, I.H.M. Glotaran: A Java-based graphical user interface for the R-package TIMP. *J. Stat. Softw.* **2012**, *49*, 1-22.

26. Tang, L.; Zhang, S.; Zhao, Y.; Rozanov, N.D.; Zhu, L.; Wu, J.; Campbell, R.E.; Fang, C. Switching between ultrafast pathways enables a green-red emission ratiometric fluorescent-protein-based Ca^{2+} biosensor. *Int. J. Mol. Sci.* **2021**, *22*, 445.

27. Kumpulainen, T.; Lang, B.; Rosspeintner, A.; Vauthey, E. Ultrafast elementary photochemical processes of organic molecules in liquid solution. *Chem. Rev.* **2017**, *117*, 10826-10939.

28. Fang, C.; Tang, L.; Oscar, B.G.; Chen, C. Capturing structural snapshots during photochemical reactions with ultrafast Raman spectroscopy: From materials transformation to biosensor responses. *J. Phys. Chem. Lett.* **2018**, *9*, 3253–3263.

29. Fukushima, Y.; Iwaki, M.; Narikawa, R.; Ikeuchi, M.; Tomita, Y.; Itoh, S. Photoconversion mechanism of a green/red photosensory cyanobacteriochrome AnPixJ: Time-resolved optical spectroscopy and FTIR analysis of the AnPixJ-GAF2 domain. *Biochemistry* **2011**, *50*, 6328-6339.

30. Wang, D.; Li, X.; Zhang, S.; Wang, L.; Yang, X.; Zhong, D. Revealing the origin of multiphasic dynamic behaviors in cyanobacteriochrome. *Proc. Natl. Acad. Sci. U. S. A.* **2020**, *117*, 19731-19736.

31. Tang, L.; Wang, Y.; Zhu, L.; Lee, C.; Fang, C. Correlated molecular structural motions for photoprotection after deep-UV irradiation. *J. Phys. Chem. Lett.* **2018**, *9*, 2311-2319.

32. Wang, D.; Qin, Y.; Zhang, M.; Li, X.; Wang, L.; Yang, X.; Zhong, D. The origin of ultrafast multiphasic dynamics in photoisomerization of bacteriophytochrome. *J. Phys. Chem. Lett.* **2020**, *11*, 5913-5919.

33. Taylor, M.A.; Zhu, L.; Rozanov, N.D.; Stout, K.T.; Chen, C.; Fang, C. Delayed vibrational modulation of the solvated GFP chromophore into a conical intersection. *Phys. Chem. Chem. Phys.* **2019**, *21*, 9728-9739.

34. Kim, P.W.; Freer, L.H.; Rockwell, N.C.; Martin, S.S.; Lagarias, J.C.; Larsen, D.S. Femtosecond photodynamics of the red/green cyanobacteriochrome NpR6012g4 from *Nostoc punctiforme*. 2. Reverse dynamics. *Biochemistry* **2012**, *51*, 619-630.

35. Spillane, K.M.; Dasgupta, J.; Lagarias, J.C.; Mathies, R.A. Homogeneity of phytochrome Cph1 vibronic absorption revealed by resonance Raman intensity analysis. *J. Am. Chem. Soc.* **2009**, *131*, 13946-13948.

36. Wang, D.; Qin, Y.; Zhang, S.; Wang, L.; Yang, X.; Zhong, D. Elucidating the molecular mechanism of ultrafast Pfr-state photoisomerization in bathy bacteriophytochrome PaBphP. *J. Phys. Chem. Lett.* **2019**, *10*, 6197-6201.

37. Rao, A.G.; Wiebeler, C.; Sen, S.; Cerutti, D.S.; Schapiro, I. Histidine protonation controls structural heterogeneity in the cyanobacteriochrome AnPixJg2. *Phys. Chem. Chem. Phys.* **2021**, *23*, 7359-7367.

38. Xu, X.; Höppner, A.; Wiebeler, C.; Zhao, K.-H.; Schapiro, I.; Gärtner, W. Structural elements regulating the photochromicity in a cyanobacteriochrome. *Proc. Natl. Acad. Sci. U. S. A.* **2020**, *117*, 2432-2440.

39. Gepshtein, R.; Huppert, D.; Agmon, N. Deactivation mechanism of the green fluorescent chromophore. *J. Phys. Chem. B* **2006**, *110*, 4434-4442.

40. Jung, Y.O.; Lee, J.H.; Kim, J.; Schmidt, M.; Moffat, K.; Šrajer, V.; Ihee, H. Volume-conserving *trans–cis* isomerization pathways in photoactive yellow protein visualized by picosecond X-ray crystallography. *Nat. Chem.* **2013**, *5*, 212-220.

41. Chang, J.; Romei, M.G.; Boxer, S.G. Structural evidence of photoisomerization pathways in fluorescent proteins. *J. Am. Chem. Soc.* **2019**, *141*, 15504-15508.

42. Guido, C.A.; Jacquemin, D.; Adamo, C.; Mennucci, B. On the TD-DFT accuracy in determining single and double bonds in excited-state structures of organic molecules. *J. Phys. Chem. A* **2010**, *114*, 13402-13410.

43. Polyakov, I.V.; Grigorenko, B.L.; Epifanovsky, E.M.; Krylov, A.I.; Nemukhin, A.V. Potential energy landscape of the electronic states of the GFP chromophore in different protonation forms: Electronic transition energies and conical intersections. *J. Chem. Theory Comput.* **2010**, *6*, 2377-2387.

44. Dasgupta, J.; Frontiera, R.R.; Taylor, K.C.; Lagarias, J.C.; Mathies, R.A. Ultrafast excited-state isomerization in phytochrome revealed by femtosecond stimulated Raman spectroscopy. *Proc. Natl. Acad. Sci. U. S. A.* **2009**, *106*, 1784-1789.

45. Wiebeler, C.; Rao, A.G.; Gärtner, W.; Schapiro, I. The effective conjugation length is responsible for the red/green spectral tuning in the cyanobacteriochrome Slr1393g3. *Angew. Chem. Int. Ed.* **2019**, *58*, 1934-1938.

46. Liu, Y.; Chen, Z.; Wang, X.; Cao, S.; Xu, J.; Jimenez, R.; Chen, J. Ultrafast spectroscopy of biliverdin dimethyl ester in solution: Pathways of excited-state depopulation. *Phys. Chem. Chem. Phys.* **2020**, *22*, 19903-19912.

47. Fang, C.; Tang, L. Mapping structural dynamics of proteins with femtosecond stimulated Raman spectroscopy. *Annu. Rev. Phys. Chem.* **2020**, *71*, 239-265.

48. Chen, C.; Zhu, L.; Fang, C. Femtosecond stimulated Raman line shapes: Dependence on resonance conditions of pump and probe pulses. *Chin. J. Chem. Phys.* **2018**, *31*, 492-502.

49. Liu, W.; Tang, L.; Oscar, B.G.; Wang, Y.; Chen, C.; Fang, C. Tracking ultrafast vibrational cooling during excited state proton transfer reaction with anti-Stokes and Stokes femtosecond stimulated Raman spectroscopy. *J. Phys. Chem. Lett.* **2017**, *8*, 997–1003.

50. Frontiera, R.R.; Shim, S.; Mathies, R.A. Origin of negative and dispersive features in anti-Stokes and resonance femtosecond stimulated Raman spectroscopy. *J. Chem. Phys.* **2008**, *129*, 064507.

51. Umapathy, S.; Lakshmanna, A.; Mallick, B. Ultrafast Raman loss spectroscopy. *J. Raman Spectrosc.* **2009**, *40*, 235-237.

52. Frisch, M.J.; Trucks, G.W.; Schlegel, H.B.; Scuseria, G.E.; Robb, M.A.; Cheeseman, J.R.; Scalmani, G.; Barone, V.; Petersson, G.A.; Nakatsuji, H., *et al. Gaussian 16, Revision A.03*, Gaussian, Inc.: Wallingford, CT, 2016.

53. Mroginski, M.A.; von Stetten, D.; Escobar, F.V.; Strauss, H.M.; Kaminski, S.; Scheerer, P.; Günther, M.; Murgida, D.H.; Schmieder, P.; Bongards, C., *et al.* Chromophore structure of cyanobacterial phytochrome Cph1 in the Pr state: Reconciling structural and spectroscopic data by QM/MM calculations. *Biophys. J.* **2009**, *96*, 4153-4163.

54. Wiebeler, C.; Schapiro, I. QM/MM benchmarking of cyanobacteriochrome Slr1393g3 absorption spectra. *Molecules* **2019**, *24*, 1720.

55. Velazquez Escobar, F.; Utesch, T.; Narikawa, R.; Ikeuchi, M.; Mroginski, M.A.; Gärtner, W.; Hildebrandt, P. Photoconversion mechanism of the second GAF domain of cyanobacteriochrome AnPixJ and the cofactor structure of its green-absorbing state. *Biochemistry* **2013**, *52*, 4871-4880.

56. Fang, C.; Frontiera, R.R.; Tran, R.; Mathies, R.A. Mapping GFP structure evolution during proton transfer with femtosecond Raman spectroscopy. *Nature* **2009**, *462*, 200-204.

57. Oscar, B.G.; Liu, W.; Zhao, Y.; Tang, L.; Wang, Y.; Campbell, R.E.; Fang, C. Excited-state structural dynamics of a dual-emission calmodulin-green fluorescent protein sensor for calcium ion imaging. *Proc. Natl. Acad. Sci. U. S. A.* **2014**, *111*, 10191-10196.

58. Yang, X.; Kuk, J.; Moffat, K. Conformational differences between the Pfr and Pr states in *Pseudomonas aeruginosa* bacteriophytochrome. *Proc. Natl. Acad. Sci. U. S. A.* **2009**, *106*, 15639-15644.

59. Scarbath-Evers, L.K.; Jähnigen, S.; Elgabarty, H.; Song, C.; Narikawa, R.; Matysik, J.; Sebastiani, D. Structural heterogeneity in a parent ground-state structure of AnPixJg2 revealed by theory and spectroscopy. *Phys. Chem. Chem. Phys.* **2017**, *19*, 13882-13894.

60. Xu, X.-L.; Gutt, A.; Mechelke, J.; Raffelberg, S.; Tang, K.; Miao, D.; Valle, L.; Borsarelli, C.D.; Zhao, K.-H.; Gärtner, W. Combined mutagenesis and kinetics characterization of the bilin-binding GAF domain of the protein Slr1393 from the cyanobacterium *Synechocystis* PCC6803. *ChemBioChem* **2014**, *15*, 1190-1199.

61. Kirpich, J.S.; Chang, C.-W.; Franse, J.; Yu, Q.; Escobar, F.V.; Jenkins, A.J.; Martin, S.S.; Narikawa, R.; Ames, J.B.; Lagarias, J.C., *et al.* Comparison of the forward and reverse photocycle dynamics of two highly similar canonical red/green cyanobacteriochromes reveals unexpected differences. *Biochemistry* **2021**, *60*, 274-288.

62. Gottlieb, S.M.; Corley, S.C.; Madsen, D.; Larsen, D.S. Note: A flexible light emitting diode-based broadband transient-absorption spectrometer. *Rev. Sci. Instrum.* **2012**, *83*, 056107.

63. Liu, W.; Han, F.; Smith, C.; Fang, C. Ultrafast conformational dynamics of pyranine during excited state proton transfer in aqueous solution revealed by femtosecond stimulated Raman spectroscopy. *J. Phys. Chem. B* **2012**, *116*, 10535-10550.

64. Zhu, L.; Liu, W.; Fang, C. A versatile femtosecond stimulated Raman spectroscopy setup with tunable pulses in the visible to near infrared. *Appl. Phys. Lett.* **2014**, *105*, 041106.

65. Merrick, J.P.; Moran, D.; Radom, L. An evaluation of harmonic vibrational frequency scale factors. *J. Phys. Chem. A* **2007**, *111*, 11683-11700.

5.7 Supplemental Information

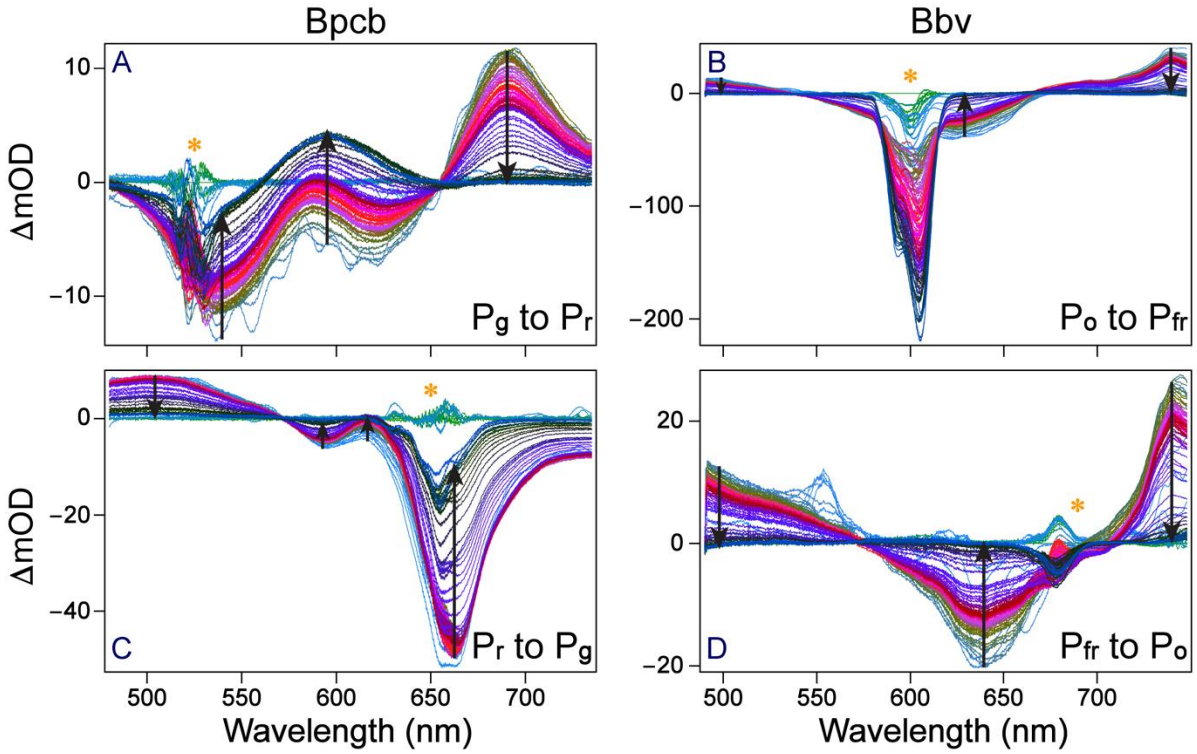

Figure 5.6. Raw experimental fs-TA spectra of (A) Bpcb $P_g \rightarrow P_r$, (C) Bpcb $P_r \rightarrow P_g$, (B) Bbv $P_o \rightarrow P_{fr}$, and (D) Bbv $P_{fr} \rightarrow P_o$ transitions. The Bpcb $P_g \rightarrow P_r$ and $P_r \rightarrow P_g$ spectral data were collected using a 525 nm actinic pump with 650 nm LEDs and 650 nm actinic pump with 505 nm LEDs, respectively. The Bbv $P_o \rightarrow P_{fr}$ and $P_{fr} \rightarrow P_o$ spectral data were collected using a 600 nm actinic pump with 650 nm longpass-filtered tungsten lamp and 690 nm actinic pump with 600 nm LEDs, respectively. The –2 ps TA trace was subtracted from all the subsequent traces to effectively remove strong scattering signals around the actinic pump wavelengths (denoted by the orange asterisk in each panel) [1]. Representative black arrows highlight the dynamic trend of transient electronic marker bands as time progresses up to 900 ps (except for 600 ps in panel A) within the probe spectral window. All the time-resolved electronic spectroscopic measurements were performed for various CBCRs in aqueous buffer solution at room temperature (see Section 5.3 above).

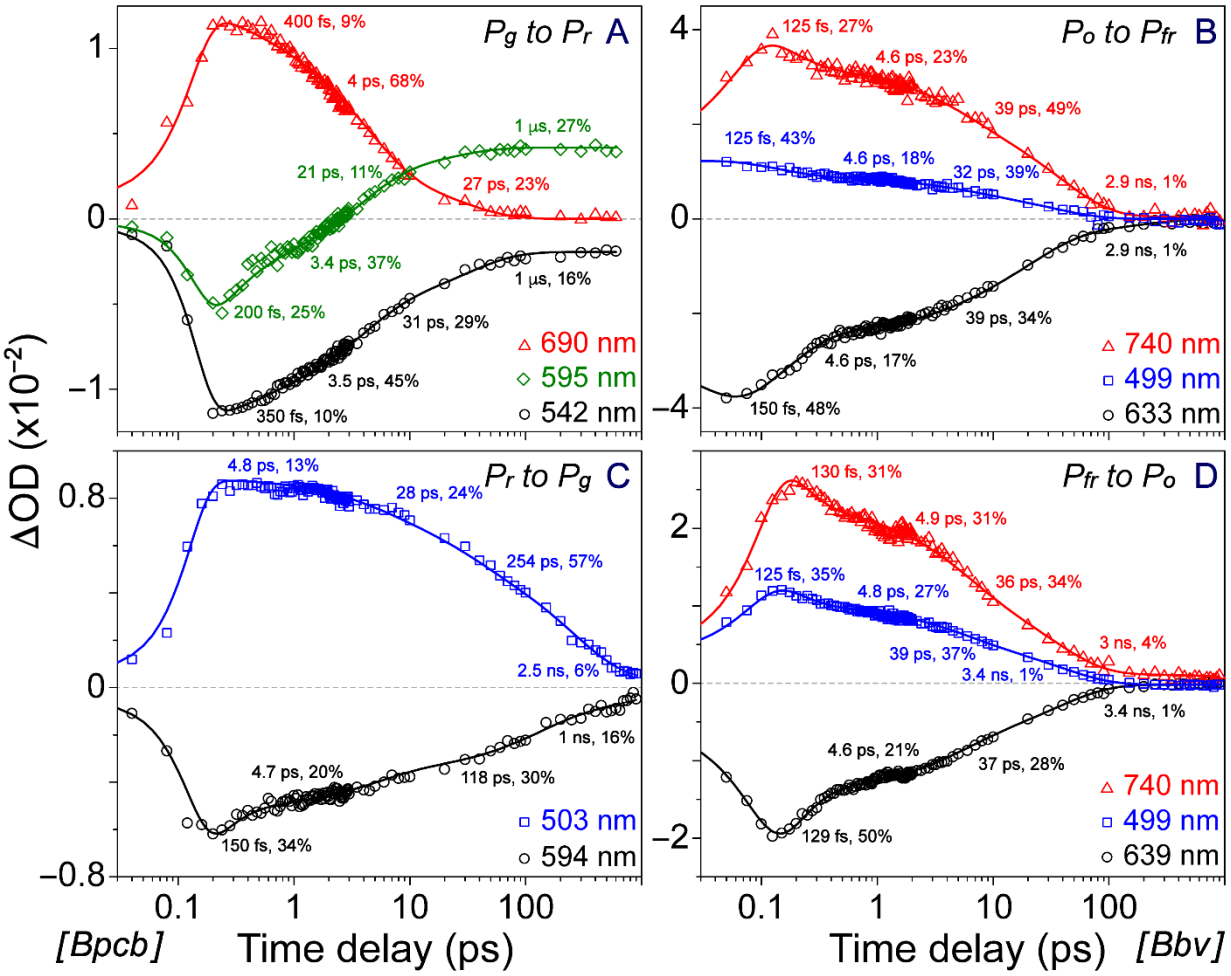

Figure 5.7. Probe-dependent fits of (A) Bpcb $P_g \rightarrow P_r$, (C) Bpcb $P_r \rightarrow P_g$, (B) Bbv $P_o \rightarrow P_{fr}$, and (D) Bbv $P_{fr} \rightarrow P_o$ transitions. The integrated TA signal intensity area was taken ±5 nm from the listed center wavelengths and least-squares fit using weighted (percentage shown) exponential decay components. The Bpcb $P_g \rightarrow P_r$ and $P_r \rightarrow P_g$ spectral data were collected using a 525 nm actinic pump with 650 nm LEDs and 650 nm actinic pump with 505 nm LEDs, respectively. The Bbv $P_o \rightarrow P_{fr}$ and $P_{fr} \rightarrow P_o$ spectral data were collected using a 600 nm actinic pump with 650 nm longpass-filtered tungsten lamp and 690 nm actinic pump with 600 nm LEDs, respectively. All the fs-TA experiments were performed for CBCRs in buffer at room temperature. The locations for these specific probe wavelengths in the broadband TA spectra of various CBCR photoswitching processes can be visualized by the color-coded vertical solid lines in Figure 5.2A–D (see Section 5.4).

Notably, these probe-dependent fits yield characteristic time constants with amplitude weights that facilitate interpretations of excited-state processes, corroborated by global analysis (Figure 5.3), particularly for the long time constant (~3 ns) with 1–4% amplitude weight of Bbv (Figure 5.7B,D).

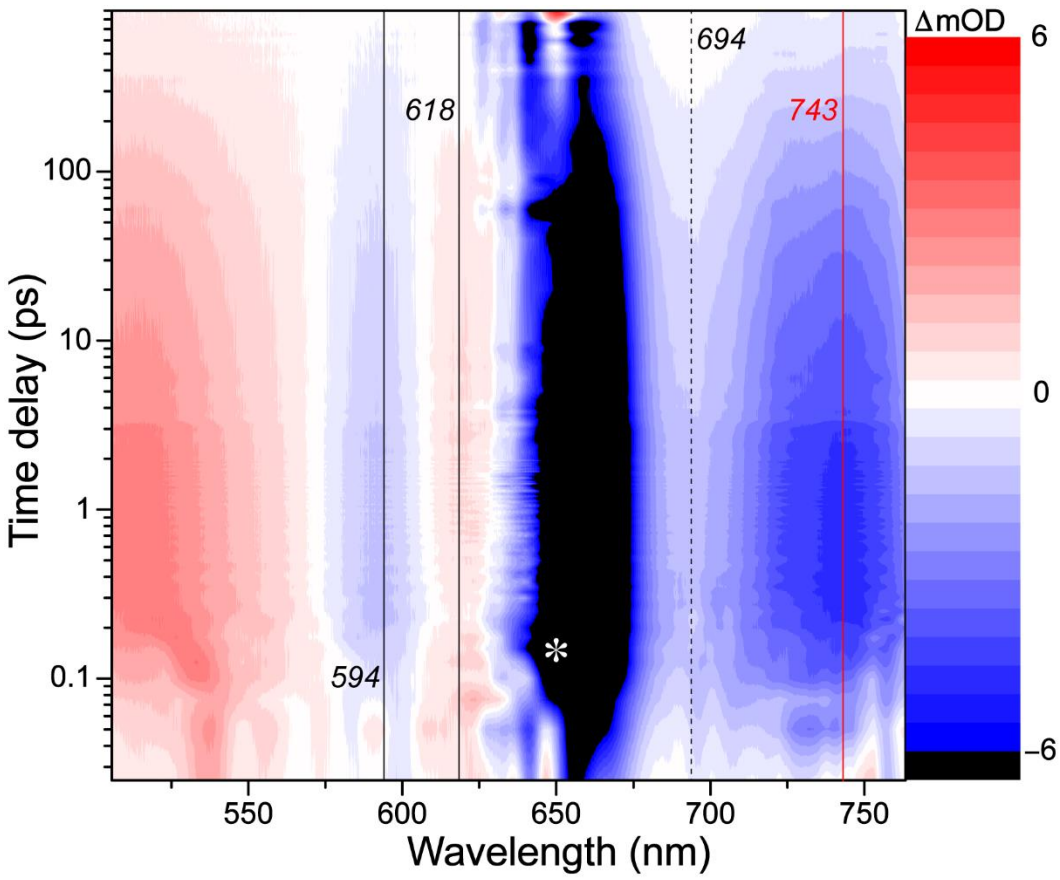

Figure 5.8. Control plots of fs-TA spectra for dilute Bpcb $P_r \rightarrow P_g$ conversion. The actinic pump at 650 nm was used in conjunction with the 505 nm LEDs, while the white light probe was generated using a sapphire crystal plate (to cover the region for redder photons, see Section 5.3.3 above). The Bpcb concentration was ~0.2 OD per mm measured at the absorption peak of the steady-state P_r species. Besides the prominent ESA band below ~550 nm, the GSB/ESA/SE bands around 594/618/743 nm are labeled and denoted by black/black/red vertical solid lines. The white asterisk marks the pump scattering around 650 nm. The black dashed line at 694 nm may be indicate of a weak HGSA band of Lumi-R that emerges at later times (still overlapped with the pump scattering on the blue side and residual SE band on the red side) [1,2]. GSB, ground-state bleaching; ESA, excited-state absorption; SE, stimulated emission; HGSA, hot ground-state absorption.

In comparison with the much higher concentration of Bpcb sample in buffer solution, the much reduced scattering from the 650 nm Raman pump as well as less GSB band intensity in that region allows a clearer observation of the ESA band around 618 nm, which could be attributed to an intermediate electronic excited state that we termed as P_r*' (see Figure 5.5C in Section 5.4).

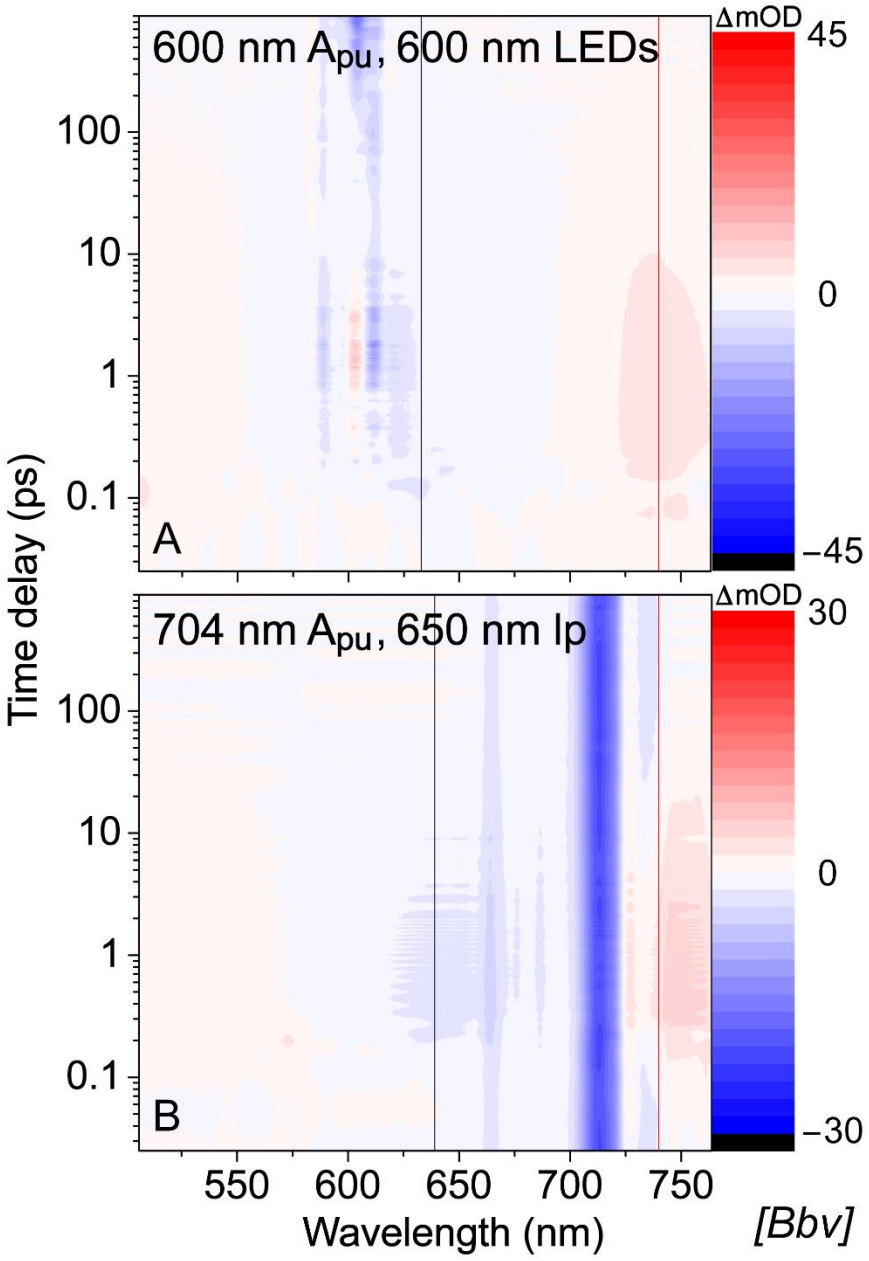

Figure 5.9. Control plots of fs-TA spectra for Bbv reversible photoswitching. Contour plots of the fs-TA spectra of Bbv in buffer solution following (A) 600 nm actinic pump (A_{pu}) with 600 nm LEDs and (B) 704 nm actinic pump with 650 nm longpass (lp)-filtered tungsten lamp up to 900 ps time delay. Vertical red/black lines denote 740/633 nm probe wavelengths in panel A and 740/639 nm probe wavelengths in panel B for comparison to Figure 5.2B and D in Section 5.4

Notably, since the 600 nm LEDs convert Bbv to its P_{fr} state (see Figure 5.1F) with no significant P_o population, the 600 nm A_{pu} cannot effectively initiate the $P_o \rightarrow P_{fr}$ conversion. Therefore, on similar intensity and time scales, TA features in Figure 5.9A are much smaller than those in Figure 5.2B. In particular, the prominent GSB band around 633 nm or 700 nm (Figure 5.2B) is negligible in Figure 5.9A. Moreover, the 600 nm A_{pu} does not create a mixed P_o/P_{fr} population at the time zero of photoexcitation, which would otherwise display complex overlapping electronic bands [1]. In analogy, since the 650 nm lp-filtered tungsten lamp converts Bbv to its P_o state (Figure 5.1F) with no significant P_{fr} population, the 704 nm Apu cannot effectively initiate the $P_{fr} \rightarrow P_o$ conversion. The residual TA signals in Figure 5.9A and B correspond to a small P_o and P_{fr} population that remains unconverted by the LED box or lp-filtered tungsten lamp, respectively, which resemble the spectral patterns in Figure 5.2B and D. These carefully designed and analyzed control experiments further confirm the robustness of major TA data which track the reversible photoswitching processes between the P_o and P_{fr} conformers of Bbv on the sub-nanosecond time scale (see Section 5.4), with the intended reversible photoswitching processes under investigation (i.e., not the pureness of each conformer state, but the light-induced transitions between the specific excited-state species in both directions).

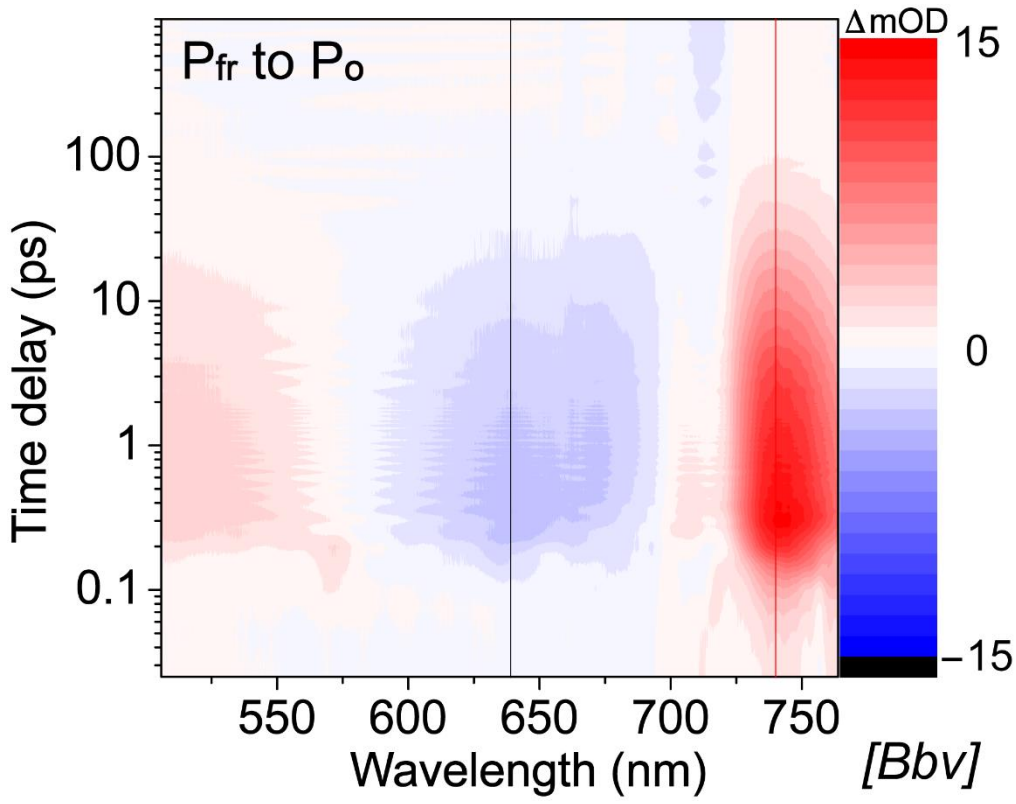

Figure 5.10. Contour plot of fs-TA spectra for the Bbv $P_{fr} \rightarrow P_o$ conversion upon 704 nm excitation. Experimental conditions were kept the same as Figure 5.2D except that the actinic pump was tuned from 690 nm to the redder 704 nm. Black and red vertical lines denote the probe wavelengths of 639 and 740 nm for a direct comparison with TA features in Figure 5.2D (Section 5.4).

Notably, the observed TA spectral pattern and retrieved time constants in Figure 5.10 match those in Figure 5.2D regarding the Bbv $P_{fr} \rightarrow P_o$ conversion (with 600 nm LEDs), while the reduced TA signal intensity with 704 nm pump is likely due to less sample concentration for this experiment (OD≈0.2/mm, with the cofactor having similar absorption intensity at 704 and 690 nm, see dark red trace in Figure 5.1F) [3]. This important result provides further evidence that the 690 and 704 nm actinic pump pulses excite a homogeneous P_{fr} population of the BV cofactor inside AnPixJg2_BV4 pocket (see Section 5.4) [4-6].

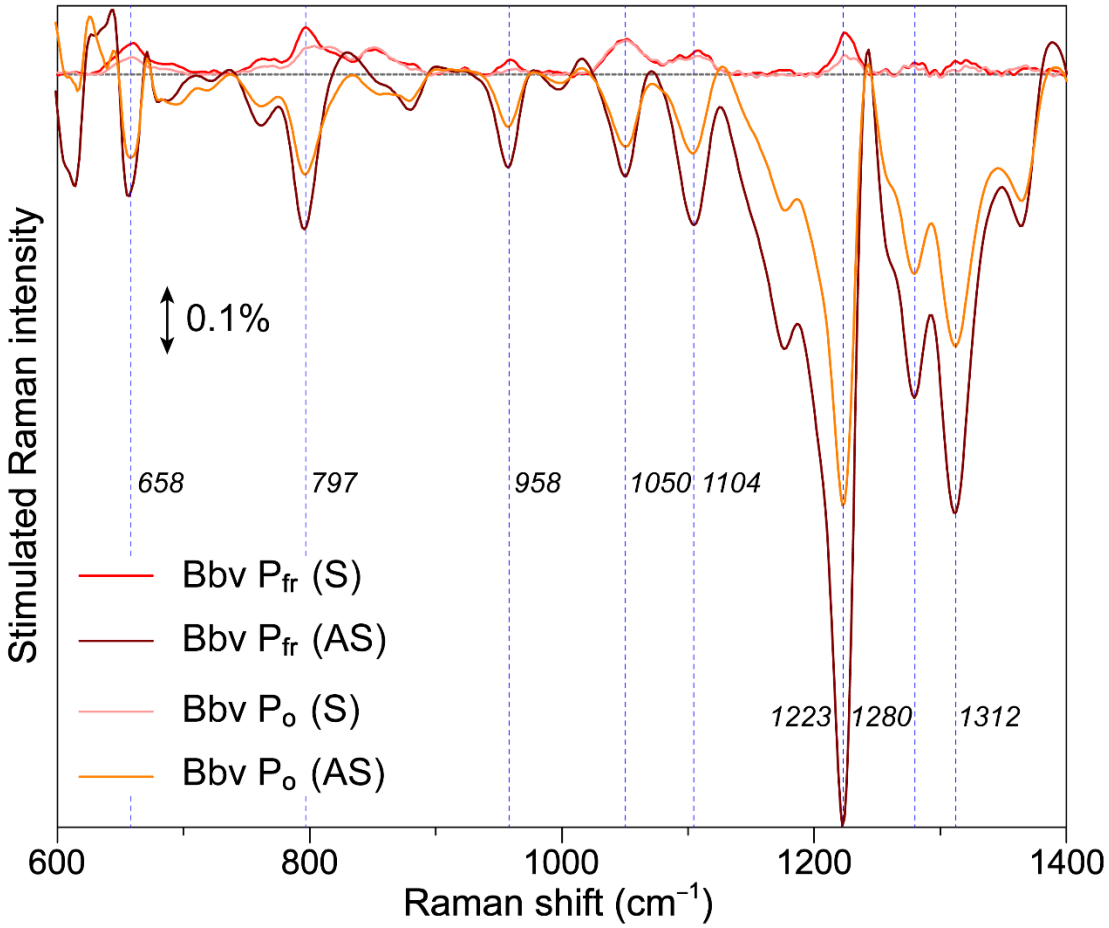

Figure 5.11. Comparison of the Stokes and anti-Stokes FSRS of Bbv in buffer solution. Using 803 nm Raman pump and Raman probe on the Stokes (S) and anti-Stokes (AS) side, the ground-state FSRS spectra of the Bbv P_{fr} conformer and P_o conformer are overlaid in one graph with the S (red)/AS (dark red) spectra and S (pink)/AS (orange) spectra shown with positive/negative-going peaks (as Raman gain/loss), respectively. The frequency axis of the AS spectrum is multiplied by (–1) to match that of the S spectrum. Vertical blue dashed lines highlight the mostly identical peak frequencies despite the significant intensity difference between the S and AS spectra of both Bbv conformers. The stimulated Raman gain magnitude of 0.1% is shown by the double-headed arrow.

Notably, some dispersive spectral line shapes are visible for the anti-Stokes FSRS, although the peak intensity enhancement is significant due to a better overlap

between the bluer Raman probe (than the 803 nm Raman pump) and the ground state absorption band of the P_{fr} species. This effect is less dramatic for the P_o species that has an absorption peak (624 nm) bluer than the P_{fr} species (699 nm, see Figure 5.1F).

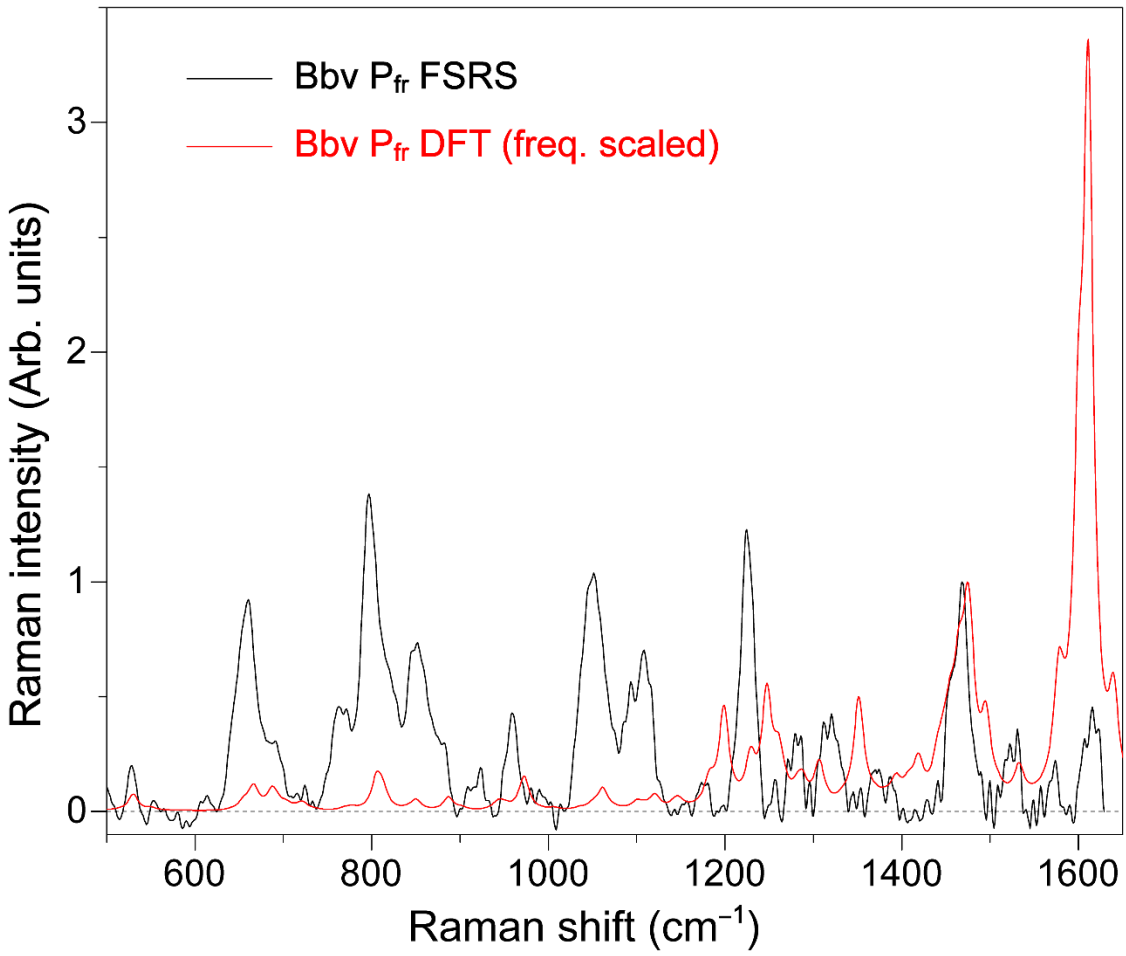

Figure 5.12. Overlay of the experimental GS-FSRS of Bbv P_{fr} state using 600 nm LEDs, 803 nm ps Raman pump, and redder Raman probe on the Stokes side (black) and the DFT-calculated Raman spectrum [7] using the BV cofactor taken from the crystal structure (PDB ID: 5ZOH) [4]. Both spectra were normalized at the ~1467 cm^{-1} mode for better comparison. A frequency scaling factor of 0.97 was used to match the experimental and calculated Raman spectra [1,8,9].

In comparison with our previous GS-FSRS experiment on the PCB cofactor in AnPixJg2 (Apcb) using a bluer Raman pump wavelength (596 nm) and Raman probe

on the Stokes side wherein a prominent 1615 cm^{-1} mode was observed for the P_r form [1], the much weaker ~1616 cm^{-1} mode of the BV cofactor P_{fr} form in AnPixJg2_BV4 (Bbv, also see Figure 5.4C in Section 5.4) in this work is due to weak probe photon counts redder than ~920 nm in supercontinuum white light generated by focusing fs ~800 nm laser pulses onto a thin sapphire plate [3,10]. Future work using a redder white light with the ~800 nm Raman pump or the current white light with a bluer Raman pump could provide more spectral data in the high-frequency (>1600 cm^{-1}) region.

Table 5.2. Raman mode assignment of the BV cofactor P_{fr} state.

GS-FSRS (cm^{-1})	DFT calc. (cm^{-1}) (unscaled, cm^{-1})[a]	Vibrational mode assignment (major)
P_{fr}		
1616	1610 (1660)	CD methine bridge C15=C16 stretch and C–H rock with D ring N–H rock and C=C stretch
1467	1465 (1510)	B and C ring deformation with N–H rock, sidechain CH_3 bending
1225	1238 (1276)	A, B, and C ring deformation with N–H rock and AB methine bridge C–H rock
1103	1102 (1136)	B and C ring deformation with C–H bridge rock
1050	1051 (1083)	D ring deformation with strong sidechain C–H wagging
853	850 (876)	C & D ring N–H rocking with C–C stretching of the C and D ring, and methine bridge bending
797	805 (830)	ABC ring N–H wagging with CD methine bridge C–H wagging
659	657 (677)	Collective C–C conjugated wagging with C–H wagging

[a] The vibrational normal mode frequencies were calculated using the BV cofactor from Bbv crystal structure (PDB ID: 5ZOH) [4] with the C and D ring propionate groups replaced with methyl caps [1,11]. The density functional theory (DFT)-calculated vibrational frequencies were multiplied by a 0.97 scaling factor. The experimental Raman mode frequencies were determined by least-squares fitting the GS-FSRS spectrum with gaussian-profile peaks above the signal-to-noise ratio (see Figure 5.4C in Section 5.4) [12,13].

5.8 Supplemental References

1. Tachibana, S.R.; Tang, L.; Chen, C.; Zhu, L.; Takeda, Y.; Fushimi, K.; Seevers, T.K.; Narikawa, R.; Sato, M.; Fang, C. Transient electronic and vibrational signatures during reversible photoswitching of a cyanobacteriochrome photoreceptor. *Spectrochim. Acta A* **2021**, *250*, 119379.
2. Kirpich, J.S.; Chang, C.-W.; Franse, J.; Yu, Q.; Escobar, F.V.; Jenkins, A.J.; Martin, S.S.; Narikawa, R.; Ames, J.B.; Lagarias, J.C., *et al.* Comparison of the forward and reverse photocycle dynamics of two highly similar canonical red/green cyanobacteriochromes reveals unexpected differences. *Biochemistry* **2021**, *60*, 274-288.
3. Zhu, L.; Liu, W.; Fang, C. A versatile femtosecond stimulated Raman spectroscopy setup with tunable pulses in the visible to near infrared. *Appl. Phys. Lett.* **2014**, *105*, 041106.
4. Fushimi, K.; Miyazaki, T.; Kuwasaki, Y.; Nakajima, T.; Yamamoto, T.; Suzuki, K.; Ueda, Y.; Miyake, K.; Takeda, Y.; Choi, J.-H.; Kawagishi, H,; Park, E.Y.; Ikeuchi, M.; Sato, M.; Narikawa, R. Rational conversion of chromophore selectivity of cyanobacteriochromes to accept mammalian intrinsic biliverdin. *Proc. Natl. Acad. Sci. U. S. A.* **2019**, *116*, 8301-8309.
5. Wang, D.; Qin, Y.; Zhang, M.; Li, X.; Wang, L.; Yang, X.; Zhong, D. The origin of ultrafast multiphasic dynamics in photoisomerization of bacteriophytochrome. *J. Phys. Chem. Lett.* **2020**, *11*, 5913-5919.

6. Rao, A.G.; Wiebeler, C.; Sen, S.; Cerutti, D.S.; Schapiro, I. Histidine protonation controls structural heterogeneity in the cyanobacteriochrome AnPixJg2. *Phys. Chem. Chem. Phys.* **2021**, *23*, 7359-7367.

7. Frisch, M.J.; Trucks, G.W.; Schlegel, H.B.; Scuseria, G.E.; Robb, M.A.; Cheeseman, J.R.; Scalmani, G.; Barone, V.; Petersson, G.A.; Nakatsuji, H., *et al. Gaussian 16, Revision A.03*, Gaussian, Inc.: Wallingford, CT, 2016.

8. Scott, A.P.; Radom, L. Harmonic vibrational frequencies: An evaluation of Hartree−Fock, Møller−Plesset, quadratic configuration interaction, density functional theory, and semiempirical scale factors. *J. Phys. Chem.* **1996**, *100*, 16502-16513.

9. Merrick, J.P.; Moran, D.; Radom, L. An evaluation of harmonic vibrational frequency scale factors. *J. Phys. Chem. A* **2007**, *111*, 11683-11700.

10. Dubietis, A.; Tamošauskas, G.; Šuminas, R.; Jukna, V.; Couairon, A. Ultrafast supercontinuum generation in bulk condensed media. *Lith. J. Phys.* **2017**, *57*, 113-157.

11. Wiebeler, C.; Rao, A.G.; Gärtner, W.; Schapiro, I. The effective conjugation length is responsible for the red/green spectral tuning in the cyanobacteriochrome Slr1393g3. *Angew. Chem. Int. Ed.* **2019**, *58*, 1934-1938.

12. Oscar, B.G.; Liu, W.; Zhao, Y.; Tang, L.; Wang, Y.; Campbell, R.E.; Fang, C. Excited-state structural dynamics of a dual-emission calmodulin-green fluorescent protein sensor for calcium ion imaging. *Proc. Natl. Acad. Sci. U. S. A.* **2014**, *111*, 10191-10196.

13. Fang, C.; Tang, L.; Oscar, B.G.; Chen, C. Capturing structural snapshots during photochemical reactions with ultrafast Raman spectroscopy: From materials transformation to biosensor responses. *J. Phys. Chem. Lett.* **2018**, *9*, 3253–3263.

Chapter 6 Experimental Advances

"You should not have a favorite weapon. To become over-familiar with one weapon is as much a fault as not knowing it sufficiently well." – Miyamoto Musashi

6.1 LED Box

In studying photoconvertible and photoswitchable systems that have multiple populations with different ground state absorption profiles, we needed a way to reliably control the molecular species to be probed by ultrafast spectroscopy. Initially, an LED flashlight was mounted behind the cuvette cell irradiating the sample concurrently with the laser pulses. This brought concern in what energy state the system is excited from, interactions with the LED and laser, and possible light bleed into the spectrometer.

To overcome these experimental concerns, a 3D-printed LED box was designed and built to irradiate a sample well that would be flown into an external quartz cuvette in the laser beampath. This setup required three major components: **1.** Design and build a box to house the suitable amount of LEDs, sample vial, and tubing for the flow cell; **2.** Construct a low volume (<2 mL) flow cell; **3.** Build the electronics to control the LEDs and flow cell pump. The box was designed in three parts. The first was an outer box without a top with a gap on one of the top corners to allow the tubing and wires to

be routed. This acted as the outer shell of the box to reduce light bleed and prevent the LEDs from shorting. The outer box also had a sample holder in the center of the box that consisted of four cylindrical supports with a ring large enough to hold a microcentrifuge tube in the center. The second piece was the LED insert that was a box with no top or bottom. The insert was designed to sit in a lip in the outer box shell and have holes drilled in to wire as many LEDs as needed. This insert was designed to have multiple inserts printed for quick swapping of LED wavelengths. The final part was a lid for the top of the black box.

Constructing the low-volume flow cell was needed since commercially available options were expensive and typically used to precision dosing at low volumes. The pump and peristaltic head was sourced from an inexpensive peristaltic pump readily available on Amazon.com. The motor and pump head could later be upgraded with a higher quality but still affordable pump, and gears to attach to the rollers and motor drive shaft. This will change the cheap friction-driven design to a geared design for a more reliable flow of sample solution. The low volume was achieved by the small pump head and also modifying the interior radial to accommodate a 2 × 1 mm silicon tubing. Reducing the tube size, moving the pump and sample reservoir closer to the sample cuvette location can reduce the overall volume loop to ~1.6 mL. In our typical experiments, 1.8 – 2 mL total sample volume is recommended to have enough excess sample in the reservoir.

The LEDs were powered through a variable DC power supply for different LED configurations and types. All LEDs were configured with four parallel strands wired in

series. This allowed for the same voltage output no matter how many rows of LEDs (sets of 4) were added.

6.2 Low-Temperature Flow Cell

The low-temperature flow cell was developed as a need to study solution samples well below 0 °C. One of the major problems in collecting spectra at low temperature is the buildup of condensation that will scatter the probe light, thus making the spectral data unreliable. To overcome the condensation problem, a 3D-printed box was designed to have two quartz windows and a quick disconnect gas valve. The prototype box was designed to be purged with inert gas (e.g., N_2) to remove the water/moisture inside the box and flow in cold sample.

All the connections to the box were sealed with either silicon or proto putty (silicon and cornstarch) to prevent any moisture from leaking in. The box was designed in two parts, the main body and the lid. The main body had two cut-outs for the quartz windows that were recycled from damaged cuvettes. The window cut-outs had a lip for the quartz to sit and be glued in with silicon and proto putty. The side close to the pump had three holes. Two of the holes were for the flow cell tubing that was sealed with silicon and the other was for a bolt to hold a post to attach to the sample stage. The bottom of the box had a bolt to mount the 3D-printed cuvette holder inside the box and another hole to pass a thermos probe through. The top of the box has a channel to hold the proto putty and act as an O-ring with the lid. The lid had a hole for the quick detach valve to purge the box with nitrogen.

For the cold bath, the exposed tubing for the peristaltic pump loop had an external tube placed on top (double tubing design) for insulation and mitigate condensation. The sample reservoir was placed inside a metal vacuum insulated bowl (available from Amazon). Depending on the temperature needed, the cold bath could be liquid nitrogen, dry ice and solvent mixture, or ice bath. To keep the reservoir at an equilibrium temperature, a small motor with a long shaft and plastic propeller can be used to constantly mix the sample. In order to accurately record the temperature, thermo probes were placed in the sample reservoir and inserted inline on the out let of the cuvette cell. Typical non-viscous samples would have a temperature difference of ~1–2 °C whereas more viscous samples would see a larger difference of ~5–10 °C. Currently, the lowest temperature achieved inside the box was down to –80°C, however, with highly viscous samples we could achieve ca. –40 °C for the flowing solution sample.

Some improvements for the low-temperature setup would be to convert the prototype box from a plastic 3D-printed build to machined metal. This way the box will be more robust to help with the laser alignment during the experimental setup. The metal box would also allow for better securement of the lid. Moreover, by implementing proper O-rings and a valve for the bottom of the box, this would create a better seal and potentially save cost on having to constantly flow nitrogen gas during experiments.

Chapter 7 Perspectives and Outlook

"The true science of martial arts means practicing them in such a way that they will be useful at any time, and to teach them in such a way that they will be useful in all things."
– Miyamoto Musashi

In this dissertation, a homebuilt, state-of-the-art vibrational spectroscopy technique called femtosecond stimulated Raman spectroscopy (FSRS) in conjunction with femtosecond transient absorption (fs-TA) were used to investigate the intrinsic molecular mechanisms of potential biomedical tools. First, the excited-state proton transfer (ESPT) dynamics was elucidated of a single Pro377Arg point mutation in a calcium ion (Ca^{2+}) biosensor named GEM-GECO1-P377R. The P377R changed the original blue-green emission-ratiometric biosensor to an excitation-ratiometric biosensor. Unlike the hydrophobic proline, the hydrophilic arginine facilitated ESPT but also introduces a more photosensitive excited state intermediate that is prone to photodegradation.

Second, the ultrafast photoswitching dynamics of a cyanobacteriochrome (CBCR) photoreceptor was elucidated on the intrinsic molecular timescales. The parent AnPixJg2 with phycocyanobilin (PCB) cofactor (Apcb for short) and the mutated AnPixJg2_BV4 with PCB (Bpcb for short) share similar photoswitching dynamics. In AnPixJg2_BV4 with the biliverdin cofactor (Bbv for shot), the enlarged conjugation shifts the thiol attachment to the protein pocket by one bond and red-shifts the ground

state electronic absorption. Taken together, Bbv exhibits a unique reversible photoswitching pathway in a clockwise/counter-clockwise manner inside the protein pocket on ultrafast timescales prior to the dominant Lumi-state formation.

7.1 Photodimerization of Vivid and its Engineered Magnets

Vivid (VVD) is a natural photoreceptor derived from the LOV2 domain and incorporates flavin adenine dinucleotide (FAD) as a cofactor.[1,2] Many of these photoreceptors have been proven to modify protein activity with light. This provides researchers a powerful approach in controlling cell signaling, gene expression, and morphology.[3-9] The small size and the abundance of FAD in mammalian cells makes VVD desirable for human applications. Under blue light irradiation, VVD switches from a monomer to a homodimer. Although VVD is a promising photoreceptor, the homodimerization, slow switch-off kinetics (half-life $t_{1/2}\approx 2.8$h),[10-12] and low dimerization affinity can be further tuned. In order to make VVD a viable optogenetic tool, Kawano and co-workers engineered Magnet variants,[1] which introduced charged residues (nMag with negatively charged residues and pMag with positively charged residues) at the dimerizing interface. This advance allowed electrostatic discrimination to prevent homodimerization and promote heterodimerization. Kawano and co-workers also found key residues that are crucial for the switch-off and binding affinity.

By implementing the state-of-the-art fs-TA and FSRS techniques, we expect to elucidate the photoswitching and initial dimerization mechanisms on the intrinsic molecular timescales (fs to ns). We will first study the isolated FAD chromophore in

biological buffer to act as a baseline. To study VVD and the Magnets, the LED flow cell can allow precise control in observing the dynamics of the dimer versus monomer.

7.2 Experimental Advances

Many of the experimental advances have been covered in Chapter 6. In brief, upgrades to current experimental tools such as the low-temperature flow cell and LED box can be made to further improve the original crude design. The low-temperature flow cell can use more robust materials like aluminum or steel to create the enclosing box. This would allow for a more rigid and supportive box to have better consistency in the setup. One of the major components would be the implication of proper gaskets and valves for purging the box. If sealed properly, the low-temperature box could also be designed to hold a vacuum as another method of removing moisture from air.

As for the LED box, the simple box design allows for users to create any LED array for application purposes. A possible upgrade to the LED flow cell is to add a T-valve to load and unload samples. By having a T-valve, this could eliminate the need for a sample reservoir and enable a semi-closed loop flow cell. The pump head could be 3D-printed to fit the LEDs inside to reduce the loop volume and length.

"There is nothing outside of yourself that can ever enable you to get better, stronger, richer, quicker, or smarter. Everything is within. Everything exists. Seek nothing outside of yourself." – Miyamoto Musashi

7.3 References

(1) Kawano, F.; Suzuki, H.; Furuya, A.; Sato, M. *Nature Communications* **2015**, *6*, 6256.

(2) Kawano, F.; Aono, Y.; Suzuki, H.; Sato, M. *PLOS ONE* **2013**, *8*, e82693.

(3) Tyszkiewicz, A. B.; Muir, T. W. *Nature Methods* **2008**, *5*, 303.

(4) Shimizu-Sato, S.; Huq, E.; Tepperman, J. M.; Quail, P. H. *Nature biotechnology* **2002**, *20*, 1041.

(5) Kennedy, M. J.; Hughes, R. M.; Peteya, L. A.; Schwartz, J. W.; Ehlers, M. D.; Tucker, C. L. *Nature Methods* **2010**, *7*, 973.

(6) Wang, X.; Chen, X.; Yang, Y. *Nature Methods* **2012**, *9*, 266.

(7) Crefcoeur, R. P.; Yin, R.; Ulm, R.; Halazonetis, T. D. *Nature Communications* **2013**, *4*, 1779.

(8) Motta-Mena, L. B.; Reade, A.; Mallory, M. J.; Glantz, S.; Weiner, O. D.; Lynch, K. W.; Gardner, K. H. *Nature Chemical Biology* **2014**, *10*, 196.

(9) Toettcher, J. E.; Gong, D.; Lim, W. A.; Weiner, O. D. *Nature Methods* **2011**, *8*, 837.

(10) Zoltowski, B. D.; Schwerdtfeger, C.; Widom, J.; Loros, J. J.; Bilwes, A. M.; Dunlap, J. C.; Crane, B. R. *Science (New York, N.Y.)* **2007**, *316*, 1054.

(11) Zoltowski, B. D.; Crane, B. R. *Biochemistry* **2008**, *47*, 7012.

(12) Zoltowski, B. D.; Vaccaro, B.; Crane, B. R. *Nature Chemical Biology* **2009**, *5*, 827.